UNIVERSITAT DE BARCELONA

Periodic time dependent Hamiltonian systems and applications

Marc Jorba-Cuscó

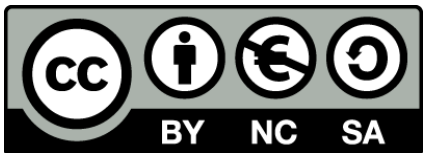

Periodic time dependent Hamiltonian systems and applications

Marc Jorba-Cuscó

A Thesis submitted
for the degree of Doctor in Mathematics

Advisors: **Àngel Jorba Monte and Ariadna Farrés Basiana**
Tutor: **Àngel Jorba Monte**

Programa de Doctorat de Matemàtiques.
Departament de Matemàtiques i Informàtica
Universitat de Barcelona

Barcelona, December 2018

UNIVERSITAT DE BARCELONA

Certifico que la present memòria ha estat
realitzada per en Marc Jorba Cuscó
en el Departament de Matemàtiques i Informàtica
sota la meva direcció.

Desembre de 2018, Barcelona.
Ángel Jorba Monte

Contents

Agraïments

Em sento enormement privilegiat d'haver pogut desenvolupar la tesi doctoral en les condicions en què ho he fet. No podria haver imaginat un millor context ni un ambient més amigable. En la realització d'aquesta tesi m'he topat amb molts bons moments i alguns, no molts, de de dolents És moment de mirar enrere i d'agrair a tots aquelles persones que han compartit aquests moments amb mi.

En primer lloc, m'agradaria dedicar unes paraules als meus directors de Tesi, l'Ariadna i l'Àngel. Si hagués de fer una llista de totes les coses que he après de vosaltres, aquesta dissertació doblaria el seu volum, quelcom que segurament no seria del tot convenient.

T'agraeixo, Ariadna, la passió que m'has inculcat ~~pels dibuixos bonics~~ per l'astrodinàmica. Treballar amb tu, sempre ha estat estimulant i particularment divertit. T'agraeixo també els teus esforços per reconduir les meves disgregacions creatives, evitant que el treball de tots aquests anys hagi acabat en un absolut desastre. En perspectiva, sento que t'hauria d'haver fet molt més cas. T'agraeixo moltíssim haver mantingut una accessibilitat total tot i les circumstàncies No tinc la intenció de plegar veles i espero que seguirem navegant plegats durant molt de temps. Em sento enormement orgullós de ser el teu primer estudiant de tesi i espero que en vinguin molts més i que siguin més talentosos que jo, doncs, crec que tens una gran quantitat de coneixement que transmetre.

A tu, Àngel, t'agraeixo la exagerada quantitat de temps que m'has dedicat, fins i tot, quan no en tenies. Gràcies per tenir la porta del teu despatx sempre oberta, literalment i, sobretot, figuradament. Parlar de matemàtiques, de programació o, en general de ciència amb tu ~~mola que t'hi c~~ és un veritable plaer. Parlar de qualsevol cosa, de fet, aprofito també per agrair-te tots els consells sobre temes que no tenen res a veure amb les matemàtiques. T'agraeixo també la llibertat que m'has donat per enfocar la meva recerca segons els meus capricis tot i que em portessin a errors que necessitava cometre per créixer com a investigador. Ets un enorme referent. Si tingués aptituds per la política, em presentaria a alcalde de Olesa de Montserrat només per nomenar-te fill predilecte (necessitava acabar això amb una broma dolenta ja que m'estava posant molt intens).

Narcís, ets el ~~putu amo~~ col·lega més *gunter da barsiria. La dinamica ans unesh i ans unira senpra astem par deu blessed aka pec banait. Sharaut cunpany i guan lof par la squashi. A*

la crackhouse totaldia. Ja diuen que no hi ha res més bonic que l'amistat entre dos idiotes.

Joba Joan, quan tinguis una estona hem de parlar d'uns temes. L'únic que et puc dir és que segueixis així, en general ~~i que et pillis un fogo per les nits d'estiu~~. Ha estat un autèntic plaer compartir despatx amb tu, quan no estaves voltant pel món, vull dir.

Parlant de companys de despatx, gràcies, Dani per aquells primers dos anys en què em vas transmetre el teu coneixement infinit de gnuplot (jo vaig assumir el què vaig poder) i per introduir-me en el món de *La rueda del tiempo*. Lectura que m'ha acompanyat durant els últims mesos d'escriptura de la tesi. I també moltes gràcies al *Canelillu* que no vas ser company de despatx però t'hi passaves el dia i, jo què sé, per mi és com si ho fossis. I fes-me cas d'una vegada, juga al *Dark Souls*.

Un agraïment molt especial a la llista de col·laboradors: A la Núria Fagella i el Joan Carles Tatjer, quina odissea d'article, per favor. Però ara ja està acabat, no? Ja tinc moltes ganes de començar el següent. Gràcies també al Pepe Rosales amb qui he compartit la millor i la pitjor cara de les formes normals. M'agrada molt el teu estil de programar i prometo que, com a homenatge, et copiaré algunes decisions de disseny. Merci monsieur Dubois for trying to teach me quantum mechanics. I hope that the invariant manifolds will make you rich or, at least, very happy. We ~~bloody~~ did it! Best regards also for Cristel, Turgay and Simon. It has been a pleasure to discuss with you all.

M'agradaria recordar també als membres del xalet (i alguns de l'edifici històric), tots ells responsables de l'esperit científic que s'hi respira: A en Carles Simó, em sento especialment orgullós de formar part del teu arbre genealògic. Tots nosaltres, els teus descendents, estarem encantats d'aportar el nostre gra de sorra per perpetuar el teu llegat. A l'Arturo Vieiro, gràcies per no portar la conta de tots els cafès als que m'has convidat. Me n'alegro molt de com ha acabat tot. A l'Àlex Haro, gràcies per *La fundación* i per haver-me guiat pel meravellós món dels dominis rectificables. A en Gerard Gómez, gràcies per la seva amabilitat i disposició a discutir qualsevol qüestió referent a l'astrodinàmica. A l'Ernest Fontich gràcies per la teva amabilitat, vas ser tu qui em va posar en contacte amb l'Àngel quan era un estudiant de màster. Suposo que no cal ni dir l'enorme impacte que això ha tingut en la meva vida. A en Jaume Timoneda, gràcies per la feina de manteniment de software. És impossible agrair-t'ho prou.

Una abraçada molt forta per la resta de companys que m'heu acompanyat durant aquests anys: Susanna, Miquel, Luque, Fabrizzio, Zubin, Gladston, Begoña, Carlos, Roc, Marta, Giulia, Eloi, Dani, President Jarque. També als meus companys de la universitat autònoma, gràcies pels memes, Rojas, Bachiller i Xitnoc. Segur que em deixo algú i em sap greu però és que si no, no acabo mai.

Moltes gràcies als meus pares per haver-me donat l'oportunitat d'estudiar i de realitzar-me professionalment i com a persona. Aquesta tesi és també vostra. I gràcies a les meves germanes per tenir-me en tant alta consideració tot i que estic bastant segur de no merèixer-

ho.

Gràcies Reshi. T'anyorem molt, Fetuccini.

Finalment gràcies a la Núria, per tot. Estem compartint un camí vital. Un camí que només podria recórrer amb tu. Aquesta tesi forma part d'aquest camí i et pertany tant com a mi. Gràcies per acceptar aquesta part meva que m'allunya de les persones. En aquells moments on em sento lluny de tothom, tu ets al meu costat recordant-me que ja no estic sol. Valen, deixo de fer-me el poeta. Moltes gràcies, *xurri*. T'estimo.

Resum en Català

Les equacions diferencials Hamiltonianes indueixen sistemes dinàmics governats per una llei de conservació. Si no depèn del temps, la quantitat conservada, la funció Hamiltoniana, és constant quan s'avalua al llarg d'una trajectòria del sistema. Donada $H \in \mathcal{C}^r(\mathbb{R} \times \mathbb{R}^{2n}, \mathbb{R})$, $r \geq 1$, una funció diferenciable, un sistema dinàmic continu que té per camp de velocitats

$$\begin{aligned} \dot{Q} &= \frac{\partial}{\partial P} H(t, Q, P), \\ \dot{P} &= -\frac{\partial}{\partial Q} H(t, Q, P), \end{aligned} \tag{1}$$

es diu de n graus de llibertat. La variable Q denota les coordenades de posició mentre que P denota les de moment. Quan la funció Hamiltoniana depèn del temps, t, es diu que el sistema associat és no autònom, en cas contrari el sistema és autònom.

Una solució de la equació diferencial (1) $\varphi : \mathbb{R} \mapsto \mathbb{R}^{2n}$ es pot escriure com

$$\dot{\varphi} = J \nabla H(\varphi),$$

$$J = \begin{pmatrix} 0 & I \\ -I & 0 \end{pmatrix},$$

on I és la matriu identitat de dimensió n. L'estructura geomètrica de l'espai de fase es manifesta en certes propietats molt específiques de les trajectòries, per exemple, el flux d'un sistema Hamiltonià preserva la mesura d'una regió donada de l'espai de fase. En particular, un sistema Hamiltonià no pot tenir atractors ni repulsors.

Aquesta tesi versa sobre sistemes Hamiltonians no autònoms que depenen periòdicament del temps. Hom pot, en tal cas, pensar la variable temporal com un angle. Aquesta variable angular augmenta el nombre de graus de llibertat en una meitat, és per això que es diu que els sistemes Hamiltonians que depenen periòdicament del temps tenen n graus i mig de llibertat.

L'aplicació estroboscòpica, la que s'obté avaluant el flux del sistema al període del camp de velocitats, és una eina estàndard emprada en l'estudi d'equacions diferencials que depenen periòdicament del temps. En cas que el sistema original sigui Hamiltonià, l'aplicació estroboscòpica és un difeomorfisme $P : \mathbb{R}^{2n} \mapsto \mathbb{R}^{2n}$ que preserva l'estructura simplèctica:

$$DP^T JDP = J.$$

D'una aplicació tal, se'n diu simplèctica.

Les aplicacions simplèctiques són la versió discreta dels sistemes Hamiltonians La majoria de propietats que manifesten les trajectòries dels sistemes Hamiltonians també s'observen en les trajectòries, obtingues a través de la iteració d'una certa condició inicial sota l'acció de P, de les aplicacions estroboscòpiques

En el món de les aplicacions, és comú que els sistemes Hamiltonians que depenen periòdicament del temps siguin, de fet, pertorbacions periòdiques de sistemes autònoms En tal cas, l'espai de fase del sistema pertorbat hereta l'estructura del no pertorbat: genèricament, les estructures quasi periòdiques del sistema autònom adquireixen la freqüència de la pertorbació.

Les estructures invariants d'un sistema dinàmic organitzen el comportament límit de les solucions del sistema i. e. aquestes estructures són l'esquelet de la dinàmica Els objectes invariants, així com els seu comportament normal, s'han d'analitzar amb cura si es vol tenir una comprensió profunda de la dinàmica

En la majoria de problemes que provenen de les diferents ciències naturals, els sistemes són no integrables, depenen de paràmetres i hom no té cap control sobre els valors D'Aquests Això fa certament difícil la tasca d'estudiar-los des de un punt de vista teòric. És en aquest context on els mètodes numèrics aporten esdevenen eines indispensables per a l'estudi dels sistemes dinàmics

Continguts d'aquesta dissertació

Aquesta tesi està estructurada en dues parts. En la primera estudiem, en abstracte, diferents varietats invariants que apareixen en sistemes Hamiltonians que depenen periòdicament del temps. Aquesta primera part, en centrem, majoritàriament, en els algorismes i implementacions de mètodes numèrics per calcular tals objectes. També incloem un estudi teòric que, per ser un context molt més simple, considerem sistemes no Hamiltonians. En la segona part recollim una sèrie de problemes relatius a la mecànica celeste, l'astrodinàmica i a la física de partícules que es poden abordar tot fent servir les eines desenvolupades en la primera part.

Primera part: Estudi d'estructures invariants

- **El mètode no autònom de les transformades de Lie:** Les formes normals són, simplificant el llenguatge, una presentació minimalista d'un sistema Hamiltonià adaptada per capturar certes propietats interessants. Una punt un de vista simple i intuïtiu és el següent: Les propietats d'un cert sistema es poden llegir en la expansió de Taylor de la seva funció Hamiltoniana. Si un sistema Hamiltonià H verifica unes certes hipòtesis, aleshores es pot transformar, mitjançant canvis de variables simplèctics a un sistema de la forma

$$\bar{H} = N + \mathcal{R},$$

  on N és un polinomi que tan sols conté monomis que codifiquen les propietats que volem capturar i $\mathcal{R}$ és un residu petit.

  En el Capítol 1 d'aquesta tesi tractem la generalització del clàssic mètode de les transformades de Lie adaptat al cas de Hamiltonians que depenen periòdicament del temps. En particular, adaptem l'esmentat mètode al càlcul de formes normals al voltant d'òrbites periòdiques.

- **El mètode de la parametrització en aplicacions estroboscòpiques:** El mètode de la parametrització és un conjunt de tècniques enfocades a l'estudi de les varietats invariants de sistemes dinàmics. Degut a la seva formulació constructiva, el mètode és adequat tant per encarar qüestions teòriques com per dissenyar algorismes eficients. Emprant el mètode de la parametrització hom és capaç de provar l'existència de, i a la vegada calcular, varietats invariants de tot tipus fins i tot si no es coneix completament la dinàmica interna.

  En el Capítol 2 adaptem el mètode de la parametrització per calcular varietats estables i inestables de punts fixos d'aplicacions estroboscòpiques. En el camí, utilitzem la tècnica del transport de jets per produir expansions d'ordre alt de aplicacions estroboscòpiques.

- **Càlcul de corbes invariants:** Els tors invariants tenen una importància capital en l'estudi dels sistemes Hamiltonians. Els de dimensió màxima són l'objecte bàsic central estudiat per la teoria KAM i poden ser emprats, per exemple, per demostrar l'estabilitat local de punts d'equilibri el·líptics en sistemes autònoms de dos graus de llibertat. Els tors invariants de dimensió baixa, juntament amb les seves varietats invariants també tenen un rol destacat en la organització de les trajectòries en l'espai de fase.

  En el Capítol 3 explorem un conegut mètode de càlcul de corbes invariants, tors invariants d'una dimensió. El capítol tracta els algorismes i implementació d'un mètode de Newton adaptat al càlcul de corbes invariants la dinàmica interna de les quals és una rotació rígida irracional. Expliquem també com calcular el comportament lineal

normal de tals corbes així com les varietats estables i inestables associades a les direccions hiperbòliques. Finalment, tractem un mètode de continuació adaptat al càlcul de famílies de corbes invariants en aplicacions simplèctiques.

- **Sistemes quasi periòdics al pla complex:** Els sistemes quasi-periòdicament forçats esdevenen models molt útils per tractar fenòmens en diversos camps de les ciències naturals. També apareixen quan es considera la dinàmica lineal al voltant d'una corba invariant, com en el Capítol 3. Sortint del context Hamiltonià, els sistemes quasi-periòdicament forçats han motivat una literatura rica que avarca l'existència d'atractors, en alguns casos, no regulars. És habitual, en el si d'aquests sistemes, estudiar els mecanismes de destrucció de corbes invariants i els conjunts invariants residuals. La no reductibilitat, i. e. la impossibilitat de tractar l'aproximació lineal de la corba invariant com una matriu de coeficients constants, hi juga un paper fonamental.

  En el Capítol 4 ens traslladem al pla complex i sortim del context Hamiltonià. Estudiem des del punt de vista teòric, i en aquesta situació més senzilla, els sistemes quasi-periòdicament forçats lineals del pla complex. En particular, donem sengles classificacions lineals i topològiques dels mateixos i caracteritzem la no reductibilitat Aquesta classificació s'estén als sistemes afins en cas de que aquests tinguin una corba invariant. Acabem el capítol estudiant un mecanisme de fracalització que té lloc en la transició d'una classe atractora no reductible a una classe repulsora no reductible

Segona part: Aplicacions

- **Models periòdics del sistema Terra-Lluna:** La dinàmica d'una petita partícula en el sistema Terra-Lluna és un tema candent en el camp de l'astrodinàmica. Conèixer l'estructura dinàmica de tal sistema serà determinant a l'hora de dissenyar missions de tot tipus: des de L'establiment d'una base a la cara de la Lluna fins a l'observació de l'espai profund mitjançant telescopis orbitals.

  El model més comú per descriure la dinàmica en el sistema Terra-Lluna és el Problema Restringit dels Tres Cossos (PRTC). En aquesta simplificació del problema dels tres cossos, s'assumeix que hi ha dos objectes màssics primaris, la Terra i la Lluna, i una partícula test que no consta de massa, és a dir, la seva presència no afecta la trajectòria de la Terra i la Lluna i, per tant, aquestes es mouen seguint una solució del problema de dos cossos. El model RPTC és un sistema Hamiltonià autònom amb tres graus de llibertat i té una mancança notable: no considera l'efecte de la gravetat del sol.

  En el Capítol 5 exposem les propietats més importants de dos models alternatius al RPTC que sí que tenen en compte la gravetat del Sol: El Problema Bicircular (PBC) i el Problema Quasi-Bicircular (PQBC). El primer, el PBC, assumeix un moviment de

Terra, Lluna i Sol que no verifica les lleis de Newton, és a dir, és no coherent. El segon, el PQBC, és una versió coherent del primer. El PBC és un model adequat per descriure certes regions del sistema Terra-Lluna però no ho és en d'altres.

- **Veles solars al sistema Terra-Lluna:** Una vela solar és un mitjà de propulsió de naus espacials que es basa en l'efecte de la Pressió de la Radiació Solar (PRS), la força que transmet un paquet de fotons al impactar en un cos. Aquesta força creix amb la relació entre l'àrea exposada de l'objecte i la seva massa: un objecte amb gran àrea però lleuger rebrà una quantitat més gran de moment per part de la Llum. La reflectivitat de l'objecte també hi juga un paper molt important. Com més reflectant sigui, més acceleració deguda a la PRS. Seguint aquestes idees, el concepte de vela solar resulta natural: Una gran superfície altament reflectant i molt lleugera.

  Encara que l'acceleració creada per la vela és molt més petita que la que proveeix un propulsor convencional, és contínua i il·limitada mentre que la vela no es deteriori. Aquestes particularitats es poden emprar pel disseny de missions amb vela que serien inconcebibles mitjançant propulsors tradicionals. En el nostre cas, fem servir un sistema Hamiltonià que depèn periòdicament del temps i de sengles paràmetres, l'efectivitat i l'orientació de la vela.

  En el Capítol 6 estudiem com l'espai de fase del sistema Terra-Lluna depèn del paràmetres de la vela. En particular, estudiem la geometria de les famílies de punts fixos que reemplacen els punts d'equilibri Lagrangians en el sistema Terra-Lluna. Ens fixem també en el comportament lineal i les bifurcacions. Per construir els models, fem servir les pautes marcades en el Capítol 5.

- **Pressió de radiació solar i els núvols libracionals:** L'any 1961, l'astrònom polonès K. Kordylewsky va detectar la presència de núvols densos de pols espacial en la proximitat dels punts de libració triangulars del sistema Terra-Lluna. Es podria dir que aquest descobriment era esperat, en efecte, l'existència de asteroides Troians en els punts triangulars del sistema Sol-Júpiter feien pensar en altres regions estables de tipus similar.

  Les observacions de Kordylewsky són tècnicament difícils de reproduir i, de fet, al llarg de tots aquests anys, diferents astrònoms han escrit articles explicant resultats negatius en els intents de replicar els experiments del polonès. Aquesta dificultat intrínseca al problema es pot explicar des del punt de vista dinàmic: Els punts triangulars del sistema Terra-Lluna no són estables. Tampoc són extremadament inestables, endemés, algunes zones properes als punts triangulars són estables a la pràctica. Aquestes consideracions apareixen en alguns, no tots, dels articles de la literatura que intenten donar una visió teòrica del fenomen És encara més comú el fet que s'ignori l'efecte de la PRS.

En el Capítol 7 investiguem l'efecte de petites dosis de PRS en unes certes regions d'estabilitat conegudes. En particular observem que, encara que l'acceleració proporcionada per la PRS sigui baixa, aquesta pot tenir un impacte notable en aquestes regions d'estabilitat.

- **La dinàmica de les recol·lisions de partícules:** La física d'altes energies és un camp que s'ocupa d'entendre els blocs fonamentals que constitueixen la matèria i la radiació. Les col·lisions entre partícules han estat, des del descobriment de l'àtom, mecanismes fonamentals per entendre la composició d'aquests. Quan un àtom és excitat per un làser, alguns dels electrons poden ser expulsats lluny del nucli i, per efecte de la interacció de Coulomb, poden ser recapturats després d'una llarga excursió. Aquest fenomen es coneix com recol·lisió.

  Els mecanismes que indueixen electrons a la recol·lisió han estat estudiats des del punt de vista dels sistemes dinàmics. El moviment d'un electró proper a un àtom excitat per un làser es pot modelar com un sistema Hamiltonià forçat periòdicament on el terme periòdic correspon a l'acció del làser. Emperò, el cas en que a l'electró se'l permet moure's en un espai unidimensional és l'únic en que s'ha proposat un escenari on una estructura invariant del sistema organitza els electrons que recol·lisionen amb l'àtom.

  En el Capítol 8 estudiem l'escenari dos dimensional. En particular, som capaços de trobar un mecanisme de recol·lisió, relacionat amb una varietat invariant de dimensió tres, que explica totes les trajectòries que recol·lisionen. Aquest nou escenari és consistent amb el cas unidimensional estudiat anteriorment.

Introduction

A dynamical system is one that evolves with time. This definition is so diffuse that seems to be completely useless, however, gives a good insight of the vast range of applicability of this field of Mathematics has. It is hard to track back in the history of science to find the origins of this discipline. The works by Fibonacci, in the twelfth century, concerning the population growth rate of rabbits can be already considered to belong to the above mentioned field. Newton's legacy changed the prism through the humankind watched the universe and established the starting shot of several areas of knowledge including the study of differential equations. Newton's second law relates the acceleration, the second derivative of the position of a body with the net force acting upon it. The formulation of the law of universal gravitation settled the many body problem, the fundamental question around the field of celestial mechanics has grown. Newton itself solved the two body problem, providing an analytical proof of Kepler's laws. In the subsequent years a number of authors, among of them Euler and Lagrange, exhausted Newton's powerful ideas but none of them was able to find a closed solution of the many body problem. By the end of the nineteenth century, Poincaré changed again the point of view: The french mathematician realized that the many body problem could not be solved in the sense his predecessors expected, however, many other fundamental questions could be addressed by studying the solutions of not quantitatively but by means of their geometrical and topological properties. The ideas that bloomed in Poincaré's mind are nowadays a source of inspiration for modern scientist facing problems located along all the spectrum of human knowledge.

Hamiltonian systems are central to the study of dynamical systems. These are governed by a conservation law. If the conserved quantity, the so called Hamiltonian function, does not depend on time, it is constant when it is evaluated along the trajectories of the system. As a matter of fact, a Hamiltonian smooth function $H = H(t, Q, P)$, where t denotes the time and $(Q, P) \in \mathbb{R}^{2n}$, determines the evolution of the system through the associated first

order differential equation

$$\dot{P} = -\frac{\partial}{\partial Q} H(t, Q, P),$$
$$\dot{Q} = \frac{\partial}{\partial P} H(t, Q, P).$$

Here, the integer n is named the number of degrees of freedom of the Hamiltonian systems, the coordinates Q are the positions and P are refereed as the momenta. When the Hamiltonian function does not depend on the time variable t, the system is said to be **autonomous**, otherwise, it is called **nonautonomous**.

The phase space, has dimension twice the degrees of freedom of the system and displays a very specific geometrical property: It has a symplectic structure. That is, a solution of a Hamiltonian system $t \mapsto \varphi(t) \in \mathbb{R}^{2n}$ can be written as

$$\dot{\varphi} = J \nabla H(\varphi),$$

where

$$J = \begin{pmatrix} 0 & I \\ -I & 0 \end{pmatrix},$$

and I is the identity matrix of dimension n. This geometrical structure induces properties on the solutions of the systems, in particular, the flow preserves the Lebesgue measure of regions of phase space and, therefore, Hamiltonian systems do not have attractors.

Let us focus, for the moment being, in autonomous Hamiltonians. When these have n conserved quantities, $I_1, I_2, \ldots, I_n$ whose gradients are linearly independent at each point of the phase space and are in involution;

$$\sum_{j=1}^{n} \left(\frac{\partial I_k}{\partial Q_j} \frac{\partial I_l}{\partial P_j} - \frac{\partial I_k}{\partial P_j} \frac{\partial I_l}{\partial Q_j} \right) = 0 \quad \text{if } k \neq l;$$

for each $k, l \in \{1, \ldots, n\}$, are said to be **integrable**. The phase space of such systems is foliated by n-dimensional invariant sets. When these sets are a compact connected manifold, they are diffeomorphic to the torus of dimension n.

Many problems in physics (and other sciences) can be modeled by means of Hamiltonian systems, moreover, a large number of those models are perturbations of integrable Hamiltonians. It is natural to address the question of whether the invariant tori of integrable systems persist under perturbation. This problem was originally undertaken by Kolmogorov [Kol54] and, later, completed by Arnold [Arn63a, Arn63b] and Moser [Mos62]. The set of results concerning this issue is nowadays known as KAM theory [1]. The solution of the problem

[1] KAM theory is still a hot topic today and it has been generalized to systems that are not Hamiltonians.

was that most, in a measure theory sense, of the invariant tori persist. The size of the perturbation needed to destroy each torus depends (among other hypotheses) on arithmetical properties of its vector of basic frequencies. The space let by the tori after their destruction contains with chaotic motion, trajectories which, even though they are deterministic, seem to obey some kind of randomness.

This thesis is concerned with nonautonomous Hamiltonian systems whose time dependence is periodic and, by using a suitable rename, one can think of the temporal variable as an angular one. This angular variables rises by a half the number of degrees of freedom, henceforth, periodic time dependent Hamiltonian systems are said to be of n and a half degrees of freedom. A standard tool to study periodically time dependent Hamiltonian systems is the so-called **stroboscopic map** i.e. the map obtained by evaluating the flow of the system at the period of the Hamiltonian function. The stroboscopic map of a periodically time dependent Hamiltonians is a diffeomorphism P of the phase space that preserve the symplectic structure

$$DP^T JDP = J.$$

Symplectic maps are the discrete counterpart to Hamiltonian systems. Most of the properties of Hamiltonians systems can also be derived for maps, in particular, the measure of regions of the phase space is preserved by iteration under a symplectic map. When $n = 1$, the set of symplectic maps coincides with the set of Area Preserving Maps (APM), those whose differential matrix has determinant equal to one in the whole of the phase space. To study symplectic maps has certain advantages with respect to Hamiltonian differential equations. For instance, the limits of KAM theory are better understood in the case of APM: the destruction of KAM tori occurs by the presence of unstable and stable invariant manifolds related to high period periodic points. The chaotic motion, as well, is induced by the tangles created by the intersection of these manifolds. When KAM tori are destroyed, their remainings are a cantor invariant set, the cantori. The studies on the fate of KAM tori under sufficiently strong perturbations are called Aubry-Mather theory and it is only complete for the case of APM. Notice that one degree of freedom Hamiltonian systems are integrable and their phase space is foliated by invariant tori. The simplest systems in which the dynamics does not consists essentially on invariant tori are one and a half degrees of freedom Hamiltonian systems which, by means of the stroboscopic map, can be regarded as APM.

It is common that periodically time dependent Hamiltonian systems are a periodic perturbation of autonomous systems, it is the case, in fact, of all the systems appearing in this dissertation. The phase space of periodically time dependent perturbations of autonomous systems has an inherited structure. Each quasi-periodic invariant structure gains, generically, the frequency of the perturbation: to perturb periodically in time is to periodically shake the phase space, see [JV97b].

Methodology

Poincaré understood that invariant structures organize the long term behaviour of the solutions of the system. Invariant objects are, therefore, the skeleton of the dynamics. These invariant structures and their linear normal behaviour are to be analyzed carefully and this shall lead to a good insight on global aspects of the phase space.

For nonintegrable systems the task of studying invariant objects and their stability is, in general, a problem which is hard to be handled rigorously. Usually, the hypotheses needed to prove specific statements on the solutions of the systems reduce the applicability of the results. This is especially relevant in physical problems: Indeed, we cannot, for instance, choose the mass of Sun to be sufficiently small.

The advent of the computers changed the way to undertake studies of dynamical systems. The task of writing programs for solving, numerically, problems related to specific examples is, at the present time, as important as theoretical studies. This has two main consequences: On the first hand, more involved models can be chosen to study real problems and this allow us to understand better the relation between abstract concepts and physical phenomena. Secondly, even when facing fundamental questions on dynamics, the numerical studies give us data from which build our theoretical developments.

Nowadays, a large number of commercial (or public) software packages helps scientist to study simple problems avoiding the tedious work to master numerical algorithms and programming languages. These programs are coded to work in the largest possible number of different situations, therefore, they do not have the efficiency that programs written specifically for a certain purpose have. Some of the computations presented in this dissertation cannot be performed by using commercial software or, at least, not in a reasonable amount of time. For this reason, a large part of the work presented here has to do with coding and debugging programs to perform numerical computations. These programs are written to be highly efficient and adapted to each problem. At the same time, the design is done so that specific blocks of the code can be used for other computations, that is, there exist a commitment between efficiency and reusability which is hard to achieve without having full control on the code.

Under these guiding principles we undertake the study of applied dynamical systems according to the following stages: From a particular problem we get a simple model, then perform a number of numerical experiments that permits us to understand the invariant objects of the system, with that information, we can isolate the relevant phenomena and identify the key elements playing a role on it. Next, we try to find an even simpler model in which we can develop theoretical arguments and produce theorems that, with more effort, can be generalized or related to other problems which, in principle, seem to be different to the original one. Paraphrasing Carles Simó, from a physical problem we can take the lift

to the abstract world, use theoretical arguments, come out with conclusions and, finally, lift down to the real world and apply these conclusions to specific problems (maybe not only the original one).

This methodology has been developed in the last decades over the world when it turned out to outstand among the most powerful approaches to cope with problems in applied mathematics. The group of Dynamical Systems from Barcelona has been one of the bulwarks of this development from the late seventies to the present days.

Scope and contents of this dissertation

Following the guidelines presented in the previous section, we concern with several problems, mostly from the field of celestial mechanics but we also deal with a phenomenon coming from high energy physics. All these situations can be modeled by means of periodically time dependent Hamiltonian systems. To cope with those investigations, we develop software which can be used to perform computations in any periodically perturbed Hamiltonian system. We split the contents of this dissertation in two parts. The first one is devoted to general tools to handle periodically time dependent Hamiltonians, even though we fill this first part with a number of illustrating examples, the goal is to keep the exposition in the abstract setting. Most of the contents of Part I deal with the development of software used to be applied in the second part. Some of the software has not been applied to the specific contents of Part II, this is left for future work[2]. We also devote a whole chapter to some theoretical issues that, while are motivated by physical problems, they fall out of the category of periodic time dependent Hamiltonians. This splitting of contents has the intention of reflecting, somehow, the basic methodological principles presented in the previous paragraph, keeping separated the abstract and the physical world but keeping in mind the lift.

Contents of Part I

The non-autonomous Lie tranformation method

Normal forms, roughly speaking, are a minimalist presentation of dynamical systems adapted to capture some relevant properties. The word minimalist means that these systems only have the minimal complexity to display that phenomenon we are interested in. A simple and intuitive point of view to understand better what do we mean is the following: The properties of a system can be read from the Taylor expansion of its associated Hamiltonian function. Symmetries and conservation laws manifest as a vanishing subset of coefficients,

[2]This is developed in the conclusions of the thesis.

the existence of some invariant objects depends on relations between certain coefficients, the appearance of islands of stable motion has to do with resonances that can be read as well from the Taylor expansion of the Hamiltonian function.

Obviously, the systems coming from applications are not in normal form. Provided the systems to verify suitable hypotheses, they can be transformed, by means of changes of variables, to a normal form. For a Hamiltonian H we typically look for a transformation that casts it into

$$\bar{H} = N + \mathcal{R},$$

where N is a polynomial of certain degree which contains only coefficients that lead to the properties we want to capture and $\mathcal{R}$ is a small residue.

The study of normal forms has been enormously relevant to face a number of physical problems. The Birkhoff normal form can be used to study the stability around elliptic points. In the case of two degrees of freedom proving a local KAM theorem around the equilibrium point and in the case of three (or more) degrees of freedom it can be used to derive bounds on the diffusion time, leading not to Lyapunov stability but in effective stability. On the other hand, the partial normal form known as reduction to the centre manifold helps to get rid of hyperbolic direction up to high order. Notice that, in many cases, the hyperbolicity is so large it makes extremely difficult to study the existence of periodic and quasi-periodic solutions. Dispensing with the hyperbolic part is one of the ways to avoid this problem.

Many works concerning Hamiltonian normal forms are focused in capturing properties of the dynamics around equilibrium points, although several works can be found for motion around periodic orbits and also invariant tori. In Chapter 1 we develop a methodology to cope with Hamiltonian normal forms around periodic motion. The main goal of this chapter is the design of the software to perform this kind of computations. By using the public domain package FFTW3, [FJ05] , we are able to produce an efficient arithmetic of Fourier series that increases the velocity of the computation with respect to previous works. Moreover, the software has been designed to be more general, that is, does not use specific symmetries of the Hamiltonian nor the periodic orbit. The goal behind this design is to apply the software to a number of problems in the future. To test the software, we compute the centre manifold of the periodic orbit that replaces the equilibrium point L_1 in the Bicircular Problem. This computation has not been presented in any reference, as far as we know, and it has its own interest by itself. We complete the chapter by writing a theoretical framework that, even it is not new, it helps to explain the implementation and gives formal support to the numerical computations.

The parameterization method on stroboscopic maps

The parameterization method is a unified framework to study invariant manifolds of dynamical systems, see [CFdlL03a, CFdlL03b, CFdlL05a]. Because the way it is formulated, the parameterization method is suited for both, proving the existence of invariant manifolds and computing them. During the last decade this methodology stood out as an excellent tool to fulfill Poincaré's program and get a deep understanding of invariant objects. The book [HCL$^+$16] is an excellent option to get in.

To effectively adapt the framework of the parameterization method to stroboscopic maps we have to deal with high order expansions of such maps. In most of the cases, to get the stroboscopic map, it is mandatory to integrate *numerically* an ordinary differential equation. Henceforth, explicit expressions for high order coefficients are not available.

Automatic differentiation is a tool that permits to produce high order derivatives of elementary expressions. By means suitable properties, one is able to find recurrent formulas for high order derivatives of the most elementary operations: sum, subtraction, product, division, exponential, trigonometric functions... More involved expressions can be obtained combining these basic operations. From the formal point of view, given a function and a point, the information of the values the function takes when it is evaluated near that point is encoded by the Taylor polynomial. The Taylor series of an elementary function, i.e. a function defined by combining elementary operations, can be obtained by performing these elementary operation but on the Taylor expansions. Using these ideas, from any program, we can compute an augmented version of it that produces the derivatives of the output with respect to the input simply replacing the standard arithmetic by an arithmetic of polynomials.

These ideas, applied to a scheme that integrates an ordinary differential equations, are called **jet transport**. With this technique we are able to produce high order expansions of stroboscopic maps which is an unavoidable tool to work the ideas of parameterization method directly in the stroboscopic map.

In Chapter 2 we apply the parameterization method to the computation of stable and unstable manifolds related to fixed points of stroboscopic maps. We discuss both the algorithm and the implementation as well as providing suitable examples to illustrate several difficulties we encounter. There is a section devoted to symplectic maps. Some of the content of this section is convenient to the further discussion of the method. We explain more than the necessary for this particular chapter in order to introduce concepts and notations that are used along this dissertation.

Computation of invariant curves on quasi-periodic skew-products

Invariant tori are invariant structures with a primordial role in Hamiltonian dynamics. As we have mentioned, KAM tori are abundant near an elliptic equilibrium point. KAM tori have

maximal dimension and no room for relevant linear normal behaviour. Lower dimensional invariant tori, however, have linear normal behavior and, henceforth, they may have invariant manifolds attached to it. These invariant manifolds are of higher dimension than the ones related to equilibrium points or periodic orbits. In mechanisms where low codimensionality is relevant, these are the invariant objects that are to be studied.

In time dependent Hamiltonian systems, the simplest invariant objects are the periodic orbits with the same period as the vectorfield. The next level of complexity is the one given by invariant tori of dimension two. Notice that for any tori to be compatible with a periodic time dependent Hamiltonian vectorfield, one of its frequencies has to be the one of the Hamiltonian function. In particular, two dimensional invariant tori appear as invariant curves of the stroboscopic map. When the Hamiltonian is a periodically time dependent perturbation of an autonomous system, the periodic orbits are replaced, if their frequency is not resonant with the one of the perturbation, by two dimensional invariant tori. The extra frequency is the one of the perturbation. Transferring this situation to the stroboscopic map, we obtain a discrete version of the Centre Lyapunov Theorem: Given a fixed point of a stroboscopic map, there is a family of invariant curves growing tangentially to each elliptic direction of the fixed point.

In Chapter 3 we explain how to compute invariant curves of autonomous quasi-periodic skew-products. These are discrete systems with the form

$$\begin{cases} \bar{x} = f(x), \\ \bar{\theta} = \theta + \omega, \end{cases}$$

where x is defined for some open set of $\mathbb{R}^n$ or $\mathbb{C}^n$, θ is an angle defined on the one dimensional torus $\mathbb{T}$ and ω is some irrational number. This kind of systems are relevant in many situations and we will mention some of them later. However, in Chapter 3 we focus on the fact that, an invariant curve of a certain map together with its linear dynamics (in case the last is a quasi-periodic rotation of the one-dimensional torus) can be regarded as quasi-periodic skew-product. We explain, in that chapter, how to compute invariant curves of maps, their linear normal behaviour and the linear approximation to the stable and unstable invariant manifolds. Moreover, we explain a continuation algorithm which is adapted to compute (Lyapunov) families of invariant curves attached to fixed points with some elliptic component. These numerical methods are not new. However, there are two main reasons to include that chapter into this dissertation. The first one is to gather some knowledge that it is split into several papers i.e. this chapter will be used, if necessary, as a reference for the author. The second is more relevant for the purpose of this dissertation: When studying the linear normal behaviour of invariant curves we introduce the concept of reducibility, to be studied later in Chapter 4 from a theoretical point of view. As we will stress later, Chapter 3 acts as a

motivation for Chapter 4. Moreover, the algorithm for the continuation of invariant curves will be used in each chapter of Part II.

Complex skew-products

We have already introduced the concept of quasi-periodic skew-product. These, when they are non-autonomous, are also known as quasi-periodically driven systems and model many physical situations: from problems in celestial mechanics to quantum physics, passing thought electronics. A skew-product has the general form

$$\begin{cases} \bar{x} = f(x, \theta), \\ \bar{\theta} = \theta + \omega, \end{cases}$$

that it, the dynamics on the direction x, in general, depends on θ. If ω is rational, the case we are interested in, the simplest invariant objects those systems have are invariant curves. As we have suggested several times by now, the linear normal behaviour around the invariant objects is as important as the object itself. The normal behaviour around an invariant curve is given by a linear-skew product.

Recall that, in the periodic case, Floquet Theory states that a linear differential equation with periodic coefficients can be reduced, by means of a periodic change of variables, to constant coefficients[3]. The situation for the quasi-periodic case is much more involved: There is no general answer for the question of reducibility in the quasi-periodic case although there are remarkable partial results.

To cope with the problem of reducibility, in all of its generality, from the theoretical point of view is a hard task. However, we can keep studying partial cases, simpler situations in which we have fewer elements playing a role and it is easier to establish relations between them. This is the reason why we restrict ourselves to the complex case which is a middle ground between the real one-dimensional and two-dimensional cases.

In Chapter 4 we are concerned with the dynamics of linear skew products of the complex plane. These are maps $F_{\mu,\omega} : \mathbb{T} \times \mathbb{C} \to \mathbb{T} \times \mathbb{C}$ of the form

$$\begin{cases} \tilde{z} = a(\theta) z, \\ \tilde{\theta} = \theta + \omega, \end{cases} \tag{2}$$

where $\theta \in \mathbb{T} \mapsto a(\theta) \in \mathbb{C} \setminus \{0\}$ is a smooth map.

[3]Notice that we are dealing with discrete dynamical systems and classical Floquet theory holds for continuous systems, however, the classical results we refer to are easily transferred to the setting of discrete dynamics.

Our first goal is to classify linear skew products. We consider linear and topological conjugacies which preserve the skew product structure and we show the different equivalence classes. Two relevant indicators in this classification are the Lyapunov exponent and the winding number of the skew product, defined as the winding number of the curve $\theta \mapsto a(\theta)$ w.r.t. the origin, and denoted by $\mathrm{wind}(a, 0)$. The simplest dynamics is the one given by the class of reducible skew products. In this context, we show that reducibility can be characterized by the winding number being equal to zero. More generally, we show that any linear system can be written in a normal form that depends on the winding number and the Lyapunov exponents.

The dynamics of general (nonlinear) skew products is a well known topic in dynamical systems that has been considered by several authors (see, for instance, [Sta97, Jor01, Gle02]), and very often specifically to study the existence of invariant curves, the fractalization phenomenon and the existence of Strange Non-chaotic Attractors (SNAs) [PMR98, PNR01b, Jäg03, HS06, Jäg07, JNOT07, JT08, Bje09]. In linear systems, the invariant curve is given by $z = 0$ and, hence, it always exists. For this reason, let us consider a small modification of a linear skew product, given by the so called affine skew products,

$$\begin{cases} \tilde{z} = a(\theta, \mu)z + c(\theta, \mu), \\ \tilde{\theta} = \theta + \omega, \end{cases} \tag{3}$$

If (3) has an invariant curve, then it can be reduced to the form (2) by translating the curve to the origin and, hence, the classification we have obtained for linear systems can be extended to affine systems. An interesting situation happens when (3), for some value of the parameter μ, has no invariant curve. A natural question is then the following: if the parameter moves from a value for which there is an invariant curve to another value for which there is no invariant curve, how does this curve disappears? We will see that, in this case, the curve may exhibit a fractalization process[4] as the parameter varies. Even further, we show that this process appears in a simple family of skew-products.

Contents of Part II

Periodic models for the Earth-Moon system

The motion of a test particle in the proximity of Earth and Moon is a hot topic in astrodynamics. The list of potential applications that could be benefited from a deep understanding of the natural dynamics near Earth and Moon is long and it is increasing day by day. Let us mention, for instance, the possibility of setting of an extraterrestrial hub, the exploration

[4]We avoid to give an accurate definition of fractalization here. See Chapter 4 for a suitable discussion.

in-situ of natural resources, deep space exploration by means of telescopes, new solutions for the delicate issue of space debris, end-of-life strategies adapted to the natural dynamics and, probably the most recent examples, the study of mini-moons, small objects captured (temporarily) which orbit around Earth.

The simplest model that describes the motion of a small particle in the Earth-Moon system is the Restricted Three Body Problem (RTBP). The very specific properties of the Earth-Moon system, such as the large mass ratio between Moon and Earth; the eccentricity of the motion of the primaries or the uniformly large effect of Sun's gravity, are certainly not well captured by the Earth-Moon RTBP. It is natural, therefore, to look for a more sophisticated model. Sun's gravitational acceleration upon the test particle is the most relevant force ignored by the RTBP, at least if a large vicinity of Earth and Moon is considered. In this situation, the gravity of Sun acts as a periodic perturbation of the RTBP.

In Chapter 5 we propose two models that introduce Sun's gravity in different ways. The first model, the so-called Bicircular Problem (BCP), considers only the direct effect of Sun's gravity on the test particle and not on Earth and Moon. For that reason, the three primaries, Earth, Moon and Sun, move following trajectories that do not verify Newton's laws. In particular, Earth and Moon move along a circular orbit around their centre of masses while the Earth-Moon barycentre move along another (coplanar) circular orbit with Sun around the centre of masses of the whole system.

The second model studied in Chapter 5 is the Quasi-Bicircular Problem (QBCP). This model is build to be a coherent version of the BCP. Besides being coherent, this new model introduces an effect that is ignored by the BCP: the non-constant distance between Earth and Moon. The QBCP is a restricted model in which the trajectories followed by the primaries are a solution of the Three Body Problem for the Earth-Moon-Sun parameters which is planar and close to bicircular.

The main goal of Chapter 5 is to compare the BCP and the QBCP and provide guidelines to decide under what circumstances each model is to be used (depending on the problem considered). To do so we provide a description of the most relevant dynamical properties around the triangular, using the BCP, and collinear points, under the QBCP.

Solar Sailing in the Earth-Moon system

Solar sail is a novel way of propelling spacecrafts. The basic principle behind solar sails is that photons, acting as particles, push matter when impacting upon it. This phenomenon is known as Solar Radiation Pressure (SRP). The acceleration a body can get from SRP depends on its mass, its area and its reflectivity. The lightest, largest and more reflective the body is, the larger the acceleration induced by SRP will be. A propeller designed according to these ideas has to be a large and light mirror and, also, the probe itself has to be light.

The acceleration provided by SRP is, usually, much smaller than the one achieved by means of a traditional propeller. However, this acceleration is continuous and only limited by the lifespan of the sail. Stress that, because the SRP acts at any given time[5], the trajectories that follow solar sails are different to the probes following the natural dynamics determined by the gravitational forces and, eventually, getting some suitable thrust.

In Chapter 6 we are concerned with the motion of a solar sail in the Earth-Moon system. Notice that, as it acts upon the sail depending on the position of Sun, the acceleration due to SRP depends periodically on time with the period of Sun. Any model for the motion of a test particle in the Earth-Moon system can be augmented to include the effect of SRP. Taking advantage on the results of Chapter 5, we augment the BCP and the QBCP with SRP to describe the motion of a solar sail in the Earth-Moon system. As long as we know, the works related to this thesis, are the first to include the effect of Sun's gravity when studying the dynamics of a solar sail near Earth and Moon.

The acceleration of SRP upon the sail depends on three parameters, the effectivity of the sail (which captures, essentially, its area-to-mass ratio) and the yaw and pitch angles. Because the period of SRP term is the same as Sun's, the augmented models are, as in the case of BCP and QBCP, periodic perturbations of the RTBP. Therefore, the libration points are replaced by periodic orbits, what we call **dynamical equivalents**. The goal of Chapter 6 is to study how these equivalents to the libration equilibria change with respect the parameters of the sail. We are interested in bifurcations and how these orbits are related when the parameters are moved. We also concern about the motion in some extended region around some interesting periodic orbits.

As most of the works in the literature deal with models that do not include the effect of Sun's gravity, we also provide a comparison with the model used in these works, the model obtained when augmenting the RTBP to include SRP. We show that there are remarkable differences between the models, especially near the collinear points L_1 and L_2.

Solar Radiation Pressure and Libration Clouds

In 1961 the polish astronomer K. Kordylewsky reported the presence of dense clouds of space dust in the proximity of the Earth-Moon triangular points. Somehow, this finding was expected: The presence of Trojan asteroids located in the Sun-Jupiter triangular points made the scientific community opened to the existence of objects near the Earth-Moon triangular points.

The observations by Kordylewsky are technically hard to reproduce and many negative reports have appeared during the years discarding the presence of dust in the Earth-Moon

[5]In this thesis we will not consider the effect of shadows of Earth and Moon.

triangular points. Recently Slíz-Balogh, Barta and Horváth published the last works (up to now), see [SBBH18, SBBH19] and the discussion seems far to be closed.

The (geometrically defined) triangular points in the real Earth-Moon system are unstable. The Bicircular Problem captures this fact and, as it is discussed in Chapter 5, can be used, as a first approach, to undertake a study on the dynamics of the Earth-Moon triangular points. In [Jor00], À. Jorba investigates out-of-plane regions of effective stability induced by (sticky) elliptic invariant tori.

In Chapter 7 we provide a preliminary study on the effect Solar Radiation Pressure on the out-of-plane regions of effective stability reported in [Jor00]. In particular, this chapter is directed to hightlight the huge impact of SRP has in the BCP. To illustrate this fact we focus on very small values of the lightness number. We would like to notice that, as the particles that are expected to populate these regions have a high area-to-mass ratio, SRP should be taken under consideration.

Recollision of electrons upon an ion

Recollision of particles is among the most relevant issues strong field physics is concerned with. Consider an atom that, by some mechanism, ionizes i.e. an electron abandons the atomic core. Depending on some conditions, the electron may be recaptured by the atom following the Coulomb's laws. When this happens, we say that the electron **recollides** with its parent ion. Recolliding electrons usually return back to the core with a larger kinetic energy than the one they had when abandoning it, this can lead to the triggering of a number of interesting phenomena such as High Harmonic Generation and multiple ionization.

Usually the electron is expelled out the core by the action of a laserfield. The effect of the laser is modeled by means of a periodic function. Near the core, the laser acts as a perturbation of the central problem induced by the (soft) Coulomb potential. The direction along the laser acts is called **polarization direction**. The described interaction between the laser and the Coulomb potential can be modeled by a periodically time dependent Hamiltonian System.

The dynamical mechanism that leads to most of the recolliding trajectories is well understood when the electrons are allowed to move in a one dimensional space (where the phase space is two dimensional). The stable and unstable manifolds of some key hyperbolic periodic orbit drive these trajectories to recollide many times. An essential ingredient for the trajectories to recollide many times is that the manifolds of these key periodic orbits intersect transversely and form a tangle. The chaotic behaviour near the tangle leads to trajectories that recollide a large number of times.

In Chapter 8 we analyze recollision mechanisms when the electrons are allowed to move in two dimensions (and henceforth, the phase space is four dimensional). The role of di-

mensionality is essential for the recollision scenario. Therefore, the one reported in the one dimensional case do not hold in the plane. The goal of Chapter 8 is to introduce a recollision mechanism that can only exists in the two dimensional case, when the direction transversal to the polarization light is considered. We provide numerical evidences of a centre-unstable (centre-stable) manifold driving a region of positive measure of initial conditions to recollision. This recollision scenario has not been, as far as we know, reported in the literature.

Part I

Invariant objects in periodic time dependent Hamiltonians

"Science is knowledge which we understand so well that we can teach it to a computer; and if we don't fully understand something, it is an art to deal with it."

Donald Knuth

"I'm a gambler, a farmboy, and I'm here to take command of your bloody army!"

Matrim Cauthon

1

The non-autonomous Lie Transformation method

Normal forms are a standard tool in mathematics. The idea is to modify a system by means of changes of variables to make it more simple in some determined sense. In dynamical systems and, in particular, Hamiltonian dynamics, normal forms play an important role, indeed, they stood out as a tool to tackle a number of problems, especially in celestial mechanics, see, for instance [GDF$^+$89, GG78, GG85, JS94, Sim89, Sim98].

Let us suppose that we want to understand the motion around some periodic orbit of a T-periodic time dependent Hamiltonian system

$$\begin{array}{rccc} H: & \mathbb{R}^n \times \mathbb{R}^n \times \mathbb{T} & \longrightarrow & \mathbb{R} \\ & (Q, P, \Theta) & \longmapsto & H(Q, P, \Theta), \end{array}$$

where $\mathbb{T} = \mathbb{Z}/T$ and $T = 2\pi/\omega_H$. The linear normal behaviour around the orbit is determined by the eigenvalues of the **monodromy matrix**, the solution of the first order variational equations evaluated at the time T. Due to the symplectic structure of the monodromy matrix, the linear normal behaviour may have a hyperbolic part and a central part. As mentioned, normal forms permit us to simplify the expansion of the Hamiltonian by means of changes of variables. Indeed, one of the common Hamiltonian normal forms consists in killing terms in the Taylor expansion of the Hamiltonian function. Each time a monomial is killed, there is a penalty in terms of the radius of convergence of the resulting series. Therefore it is

recommended to kill the less possible number of terms. In particular, in this chapter, we are interested in a special kind of (semi) normal form called the **centre manifold reduction**.

The hyperbolic part can be interesting to understand several phenomena in dynamics but, usually, takes initial conditions far away from the periodic orbits we want to study. Therefore, it is useful to do a change of variables to uncouple the hyperbolic part and the central part in order to focus on the bonded motion around the periodic orbit. In the literature, this process is called centre manifold reduction. Most of the references are concerned with equilibrium points, see [Jor99, JM99a, Sim96]. Also for the periodic case, see [GJMS93, SGJM95, And98, AS00, And02, GJ01]. These references are devoted to both centre manifold reduction and complete normal forms. Let us mention as well a couple works for quasi-periodic time dependent Hamiltonians, [GJL05, GJ05]. There are two different approaches to deal with centre manifolds. The first, the ones we use in this work, is to perform a number of symplectic changes of variables to uncouple, up to high order, the hyperbolic part and have a relatively simple way to describe the centre motion by fixing the hyperbolic coordinates. Sometimes, this is called normal form style. Another strategy is to compute a parametrization of the manifold. The classical graph transform method [FJ10b] and the more general and powerful parametrization method [BMGLD17] allow to compute expansions of these parametrization up to high order.

As we have mentioned, our approach is the Hamiltonian normal form, that is, we perform changes of variables, not on the vectorfield but on the Hamiltonian function. This has the advantage of reducing the number of equations we have to deal with from $2n$ to one. The disadvantage is that all changes of variables must be canonical. It is not trivial to produce canonical changes, probably the most known method is the Lie transformation method.

This chapter is structured as follows: In Section 1.1 we summarize some results on periodic time dependent Hamiltonian system. We focus on how the classic Hamiltonian formalism is translated to periodic Hamiltonians. In particular we take especial attention on the main elements that play a role in the Lie transformation method: Poisson brackets, canonical changes, the Lie transformation, etc. This section is intended to provide a framework for further discussions.

Section 1.2 explains how to arrange the second order of the Hamiltonian. This means how to handle the linearized flow around the periodic orbit and this matter is handled by the classical Floquet theory. As we need to work with the Hamiltonian function, we discuss the symplectic version of the classical Floquet theory. We draw an sketch of the proof because, even it is something widely known, it is constructive and helps to explain the implementation of the Floquet change of variables in a computer. Section 1.3 concerns with the higher order normal forms. The methodology is presented in rather theoretical way.

In Section 1.4 we focus on the implementation of the previous sections on a computer. We go over the main difficulties encountered as well as discuss tests and validation of software.

The implementation of the software is one of the novelties of this chapter. The program has been coded to be general, we do not use specific symmetries of the Hamiltonian, but we have tried to produce a code that is as efficient as possible. In this regard, we introduce the use of an arithmetic of Fourier series based in fast algorithms to compute the Fast Fourier Transform.

Finally, in Section 1.5 we use the methodology explained in this chapter to compute the centre manifold related to the L_1 periodic orbit of the Bicircular Problem[1]. This allow us to discuss the bifurcation giving rise to the Halo orbits which, in this case, is a bifurcation of invariant tori.

1.1 Periodic time dependent Hamiltonian formalism

This section is concerned about the generalization of some key aspects of autonomous Hamiltonian formalism to periodic time dependent Hamiltonians. In this regard, we review some classical results that provide the theoretical context for the Lie transformation method. The idea is to introduce concepts and results that are used to develop the method. We provide the statement of these classical results but not the proofs. These can be found in any textbook concerning Hamiltonian systems, see, for instance [MH92, Arn78].

Let us fix a frequency ω_H. We assume that we are coping with Hamiltonian systems depending on $(Q, P) \in \mathbb{C}^{2n}$ and periodically on time with period $T = \frac{2\pi}{\omega_H}$. We want to adapt a methodology that works with autonomous Hamiltonians. A simple way to achieve this is to autonomize the system by considering $\Theta = \omega_H t$ as an angular variable and introducing a variable I_Θ, the conjugate action (by definition). Sometimes this new variable is called **ghost action**. We obtain a new Hamiltonian:

$$\bar{H} = \omega_H I_\Theta + H(Q, P, \Theta) \tag{1.1}$$

which is almost the original one. The problem is reduced to an autonomous one, increasing by a half the number of degrees of freedom. However, the simplicity of the I_Θ-dependence of the Hamiltonian has some consequences that are worth to point out. The first one is on the Poisson Bracket.

Definition 1.1.1 (Poisson Bracket)**.** *For functions f and g depending on (Q, P, Θ, I_Θ), the Poisson bracket is defined as*

$$\{f, g\} = \sum_{i=1}^{n} \left[\frac{\partial f}{\partial Q_i} \frac{\partial g}{\partial P_i} - \frac{\partial f}{\partial P_i} \frac{\partial g}{\partial Q_i} \right] + \frac{\partial f}{\partial \Theta} \frac{\partial g}{I_\Theta} - \frac{\partial f}{\partial I_\Theta} \frac{\partial g}{\partial \Theta}.$$

[1]This model is explained in Chapter 5.

Since the ghost action I_Θ has no dynamical meaning and, therefore, has no interest for us we can construct generating functions not depending on I_Θ. Hence, for some H of the form (1.1) and G not depending on I_Θ we have:

$$\begin{aligned}\{H,G\} &= \left[\frac{\partial H}{\partial Q_i}\frac{\partial G}{\partial P_i} - \frac{\partial H}{\partial P_i}\frac{\partial G}{\partial Q_i}\right] - \omega_H \frac{\partial G}{\partial \Theta} \\ &=: \{H,G\}_a - \omega_H \frac{\partial G}{\partial \Theta}.\end{aligned}$$

Let $\mathcal{S}_\mathbb{T} = \mathcal{C}^\omega(\mathbb{C}^{2n}\times\mathbb{T}) \mapsto \mathbb{C}$. For $g, f \in \mathcal{S}_\mathbb{T}$ we define $\mathcal{L}_g f = \{f,g\}$ and $\tilde{\mathcal{L}}_g f = \{f,g\}_a$. Notice that

$$\mathcal{L}_g f = \tilde{\mathcal{L}}_g f - \omega_H \frac{\partial f}{\partial \Theta}.$$

In this particular framework, we can recover the properties of the Poisson Bracket.

Lemma 1.1.2 (Properties of the Poisson Bracket)**.** *For $g, \tilde{f}_1, \tilde{f}_2 \in \mathcal{S}_\mathbb{T}$ and $f_1 = \omega_H I_\Theta + \tilde{f}_1$, $f_2 = \omega_H I_\Theta + \tilde{f}_2$, the following properties hold:*

1. *For $\alpha, \beta \in \mathbb{C}$, $\mathcal{L}_g(\alpha f_1 + \beta f_2) = \alpha \mathcal{L}_g f_1 + \beta \mathcal{L}_g f_2$ (Linearity).*
2. *$\mathcal{L}_g(f_1 f_2) = \mathcal{L}_g(f_1) f_2 + f_1 \mathcal{L}_g(f_2)$ (Leibniz rule).*
3. *$\mathcal{L}_g\{f_1, f_2\} = \{\mathcal{L}_g f_1, f_2\} + \{f_1, \mathcal{L}_g f_2\}$ (Jacobi Identity).*

Definition 1.1.3 (Canonical Change)**.** *A change of variables given by $Q_j = \tilde{Q}_j(q,p)$, $P_j = \tilde{P}_j(q,p)$, $j = 1,\dots,n$, is said to be canonical if*

$$\{\tilde{Q}_j, \tilde{P}_k\} = \delta_{j,k}, \qquad \{\tilde{Q}_j, \tilde{Q}_k\} = 0, \qquad \{\tilde{P}_j, \tilde{P}_k\} = 0.$$

Here $\delta_{j,k} = 1$ if $k = j$ and $\delta_{j,k} = 0$ if $k \neq j$.

Proposition 1.1.4 (Invariance of the Poisson bracket)**.** *The Poisson bracket is invariant under canonical transformations. Moreover a canonical transformation preserves the Hamiltonian structure.*

Definition 1.1.5 (Lie transformation)**.** *For $g, f \in \mathcal{S}_\mathbb{T}$, we define the Lie transformation T_g as*

$$T_g f = \sum_{k=0}^{\infty} \frac{\mathcal{L}_g^k(f)}{k!}$$

Proposition 1.1.6 (Properties of the Lie transformation)**.** *The Lie transformation T_g verifies the following:*

1. $T_g(\alpha f_1 + \beta f_2) = \alpha T_g f_1 + \beta T_g f_2$.
2. $T_g(\{f_1, f_2\} = \{T_g f_1, T_g f_2\}$.
3. $T_g f T_{-g} f = f$.

Proposition 1.1.7. *The Lie transformation is a canonical change of variables.*

The Lie transformation method takes advantage on the fact that T_g is a canonical transformation. Given a Hamiltonian H and a function G, we can consider the transformed Hamiltonian $\bar{H} = T_G H$. If we want the Hamiltonian $\bar{H}$ to have a particular shape, we have to select a suitable function G. This function, is to be called the **generating function**. As a matter of fact, the Lie transformation method consists in, taking into account the desired transformed Hamiltonian (let us call it **normal form**) constructing the generating function that makes the Lie transformation to cast the departing Hamiltonian to the normal form. In this chapter, to apply the Lie transformation method, we assume the original Hamiltonian to have a very specific form:

$$H = H_2(Q, P) + H^{[\geq 3]}(Q, P, \Theta).$$

In particular, we assume the Hamiltonian to start at order 2 and the second order to be independent from the time variable Θ.

We are interested in computing normal forms around a periodic orbit with the same period as the Hamiltonian function. We exclude from our discussion the periodic orbits whose linear normal behaviour has some complex saddle. In particular, during the rest of the chapter, we assume the following hypotheses to be fulfilled.

Hypothesis 1. *Consider a Hamiltonian system with n and a half degrees of freedom $H \in \mathcal{C}^\omega(U \times V \times \mathbb{T}, \mathbb{R})$, where $U, V \subset \mathbb{R}^n$. Assume:*

1. *There exist a T-periodic solution $\psi = (\psi_1, \psi_2) \in \mathcal{C}^\omega(\mathbb{T}, U \times V)$ of the system induced by H.*
2. *There exist a linear change of variables for which the map obtained by the evaluation of the flow at the period reads as:*

$$\begin{pmatrix} u \\ c \\ s \end{pmatrix} \mapsto \begin{pmatrix} \mathcal{U}u \\ \mathcal{C}c \\ \mathcal{S}s \end{pmatrix},$$

where $\mathcal{U}, \mathcal{S} \in GL_d(\mathbb{R})$ are diagonal matrices such that $[\rho(\mathcal{U})]^{-1} < 1$, $\rho(\mathcal{S}) < 1$ and $\mathrm{spec}(\mathcal{C}) \in \mathbb{S}^1 := \{z \in \mathbb{C} || z| = 1\}$.

Translating the periodic orbit to the origin we obtain a new set of coordinates for which the Hamiltonian function does not have terms of first order.

Lemma 1.1.8 (Canceling terms of first order)**.** *Let H be a Hamiltonian fulfilling 1. The Hamiltonian obtained from the change*

$$\begin{cases} Q = \bar{Q} + \psi_1(\Theta), \\ P = \bar{P} + \psi_2(\Theta), \\ \Theta = \bar{\Theta}. \end{cases}$$

has no terms of first order.

Proof. Let us work on the equations of motion. To prove that the new Hamiltonian has no terms of first order is to prove that the origin is an equilibrium point of the associated vectorfield. The new system reads as:

$$\begin{aligned} \dot{\bar{Q}} &= \frac{\partial H}{\partial \bar{P}}\big(\bar{Q} + \psi_1(\Theta), \bar{P} + \psi_2(\Theta), \Theta\big) - \dot{\psi}_1(\Theta), \\ \dot{\bar{P}} &= -\frac{\partial H}{\partial \bar{Q}}\big(\bar{Q} + \psi_1(\Theta), \bar{P} + \psi_2(\Theta), \Theta\big) - \dot{\psi}_2(\Theta). \end{aligned}$$

Since (ψ_1, ψ_2) is an orbit of the system, we have

$$(\dot{\psi}_1, \dot{\psi}_2) = \left(\frac{\partial H}{\partial P}(\psi_1(\Theta), \psi_2(\Theta), \Theta), -\frac{\partial H}{\partial Q}(\psi_1(\Theta), \psi_2(\Theta), \Theta)\right).$$

Moreover $\frac{\partial H}{\partial \bar{Q}} = \frac{\partial H}{\partial Q}$, $\frac{\partial H}{\partial \bar{P}} = \frac{\partial H}{\partial P}$. Evaluating the vectorfield at $\bar{Q} = 0, \bar{P} = 0$ results zero. □

Remark 1.1.9. *We can use also the Lie transformation method to eliminate the terms of first order, see [GJMS93].*

1.2 Symplectic Floquet Theory

In this section we focus on how to transform the second order of the Hamiltonian, that is, the linearization of the vectorfield. The classical Floquet Theory states that a linear ordinary differential equation that depends periodically on time can be transformed, by means of a periodic change of variables, to a system with constant coefficients. If one allows the transformation to be complex, then the period of the change is the same as the period of the equation. If the change is chosen to be real, then, depending on resonances, it may have the period doubled. Let us be more precise: Suppose that we are given a system $\dot{u} = \Gamma(t)u$

with $\Gamma = \mathcal{C}^0(\mathbb{T}, M_n\mathbb{R})$, $\mathbb{T} = T/\mathbb{Z}$ for some $T > 0$. The classical Floquet Theorem assures the existence of a T-periodic change $u = P(t)v$ such that, in these new variables, the system has the form $\dot{v} = Bv$ with B a constant matrix. It is not hard to see that such P solves the initial value problem

$$\dot{P}(t) = \Gamma(t)P(t) - P(t)B, \qquad P(0) = I.$$

From the proof it follows that, if M is the monodromy matrix related to the original system, then $M = \exp(TB)$.

As we are interested in working with a Hamiltonian function, the change of variables must be canonical. The next results is a symplectic version of the Floquet Theorem, stated directly in terms of a Hamiltonian functions which only consists of second order monomials.

Theorem 1.2.1 (The Symplectic Floquet Theorem)**.** *Let us consider a Hamiltonian function:*

$$H(Q, P, \Theta) = Q^T A_1(\Theta)Q + Q^T A_2(\Theta)P + P^T A_3(\Theta)P,$$

where $A_j \in \mathcal{C}^0(\mathbb{T}, M_n\mathbb{C})$ and $A_1(\Theta), A_3(\Theta)$ symmetric matrices for all $\Theta \in \mathbb{T}$. Then, there exist a symplectic, linear and periodic time depending change of variables that casts the original Hamiltonian to

$$\bar{H}(\bar{Q}, \bar{P}) = \bar{Q}^T B_1 \bar{Q} + \bar{Q}^T B_2 \bar{P} + \bar{P}^T B_3 \bar{P},$$

and B_j do not depend on Θ and B_1, B_3 are symmetric matrices.

The proof of this result is provided in [GJMS93]. The proof, as in the classic Floquet Theorem, is constructive and we reproduce (part of) it here. The discussion of the algorithm to compute the Floquet Change is straightforward from the proof.
Let us denote by $\mathrm{SO}(2n)$ the set of symplectic matrices of dimensions $2n \times 2n$. Our main objective is to show that the flow of the Cauchy Problem

$$\dot{P}(\Theta) = \Gamma(\Theta)Q(\Theta) - P(\Theta)B, \qquad P(0) = P_0, \tag{1.2}$$

preserves the symplectic structure of P_0 whenever Q is symplectic for each $\Theta \in \mathbb{T}$ and is also B symplectic. Therefore, we need to show that B, which is essentially a logarithm of the monodromy matrix, can be chosen to be symplectic. We need a preliminary result first.

Lemma 1.2.2 (The inverse of a symplectic matrix)**.** *Let S be a symplectic matrix given by:*

$$S = \begin{pmatrix} S_{11} & S_{12} \\ S_{21} & -S_{11} \end{pmatrix}.$$

Then, the inverse S^{-1} is also symplectic and is given by:

$$S^{-1} = \begin{pmatrix} S_{22}^T & -S_{12}^T \\ S_{21}^T & S_{11}^T \end{pmatrix}.$$

Proof. First we see that S^{-1} has a very particular form:

$$S^T J S = J \iff S^T J = J S^{-1} \iff S^{-1} = -J S^T J,$$

where we have used that $J^2 = -I$. The explicit form of the matrix can be obtained by performing the block products. Moreover,

$$\begin{aligned}(-JS^TJ)^TJ(-JS^TJ) &= J^TSJ^TJJS^TJ \\ J^TSJS^TJ &= -J^TSS^{-1} = -J^T = J.\end{aligned}$$

□

Notice that, generally, to compute the inverse of a matrix is a remarkably expensive operation and should be avoided in any implementation in a computer. However, the inverse of a symplectic matrix can be obtained simply by rearranging blocks and changing some signs. Therefore, it is an almost free operation in terms of computational effort.

The next step is to show that the monodromy matrix of a linear, periodic and symplectic differential equation is also symplectic. The proof of this fact can be obtained from the results in [WN63] using the Lie algebra associated to the symplectic group.

Lemma 1.2.3 (The Monodromy matrix is symplectic)**.** *Consider the Cauchy problem*

$$\dot{Z}(\Theta) = A(\Theta)Z, \qquad Z(0) = Z_0,$$

with $A \in \mathcal{C}^0(\mathbb{T}, \mathrm{SO}(2n)))$ *and* $Z_0 \in \mathrm{SO}(2n)$*. Then, it holds* $Z(\Theta) \in \mathrm{SO}(2n)$ *for all* $\Theta \in \mathbb{T}$*.*

Lemma 1.2.4 (The reduced matrix is symplectic)**.** *Let* B *be a matrix that verifies* $M = \exp(TB)$ *for some* $M \in \mathrm{SO}(2n)$*. Then,* B *can be chosen to be symplectic and with the following block structure:*

$$B = \begin{pmatrix} B_{11} & B_{12} \\ B_{21} & B_{22} \end{pmatrix}, \qquad B_{ij} \in \mathbb{R}^{n\times n},$$

$B_{22} = -B_{11}^T$, $B_{21} = B_{21}^T$, $B_{12} = B_{12}^T$.

Proof. Matrix B is such that $M = \exp(TB)$ with M a symplectic matrix. There exist a change S such that $M = SD_MS^{-1}$, where

$$D_M = \begin{pmatrix} D_m & 0 \\ 0 & D_m^{-1} \end{pmatrix},$$

and $D_m = \mathrm{diag}(\lambda_1, \ldots, \lambda_n)$. Assume the change S to be symplectic, otherwise it can be re-scaled to fulfill that condition. Let D_b be a logarithm of D_m divided by the period. We define:

$$B = SD_BS^{-1}, \qquad D_B = \begin{pmatrix} D_b & 0 \\ 0 & -D_b \end{pmatrix}.$$

Notice that,

1. B is a symplectic matrix:

$$\begin{aligned} B^TJB &= (SD_BS^{-1})^TJ(SD_BS^{-1}) \\ &= S^{-T}D_B^TS^TJSD_BS^{-1} \\ &= D_B^TJD_BS^{-1} = S^{-t}JS^{-1} = J \end{aligned}$$

2. By Lemma 1.2.2 it holds the following block structure for S^{-1}:

$$S = \begin{pmatrix} S_{11} & S_{12} \\ S_{21} & S_{22} \end{pmatrix}, \quad S^{-1} = \begin{pmatrix} S_{22}^T & -S_{12}^T \\ S_{21}^T & S_{11}^T \end{pmatrix},$$

then

$$B = \begin{pmatrix} S_{11}D_bS_{22}^T + S_{12}D_bS_{21}^T & -S_{11}D_bS_{12}^T - S_{12}D_bS_{11}^T \\ S_{21}D_bS_{22}^T + S_{22}D_bS_{21}^T & -S_{21}D_bS_{12}^T - S_{22}D_bS_{11}^T \end{pmatrix}.$$

The set of equalities concerning the sub-matrices of B follows.

□

Proof of Theorem 1.2.1. The Hamiltonian associated to the reduced system $\dot{y} = By$ is

$$H = -\frac{1}{2}\bar{Q}^TB_{21}\bar{Q} + \bar{Q}^TB_{11}\bar{P} - \frac{1}{2}\bar{P}^TB_{12}\bar{P},$$

where we have assumed B has the form discussed in Lemma 1.2.4. Obviously, we have to choose $B_1 = -\frac{1}{2}B_{21}$, $B_2 = B_1^T$ and $B_3 = -\frac{1}{2}B_{12}$. Then both B_1 and B_3 are symmetric matrices. We only need to check that P is symplectic for each time. By construction, the matrix $\exp(TB)$ is a fundamental matrix of the problem $\dot{v} = Bv$, $v(0) = I$. As B is symplectic, $\exp(TB)$ is also symplectic (Lemma 1.2.3). Any fundamental matrix of the original system can be written as $Z(\Theta) = P(\Theta)\exp(TB)$. By Hypothesis $P(0)$ is symplectic and, by Lemma 1.2.2, $\exp(-TB)$ is also symplectic. Therefore, $Z(0)$ is a symplectic matrix and we use Lemma 1.2.3 to conclude that $Z(\Theta)$ is symplectic for all $\Theta \in \mathbb{T}$. Hence $P(\Theta) = Z(\Theta)\exp(-TB)$ is symplectic also for ll $\Theta \in \mathbb{T}$. □

1.2.1 The algorithm

Let us discuss how to translate Theorem 1.2.1 into an algorithm to compute the Floquet change. Let us assume that we are given a linear periodic ODE (in practice this ODE comes from the linearization of some flow around a certain T-periodic orbit:

$$\begin{cases} \dot{u} = Q(\Theta)u, & u(0) = I, \\ \dot{\Theta} = \omega_H. \end{cases} \tag{1.3}$$

Let M be the fundamental matrix, assume that there exist a linear change of variables that casts M to:

$$\begin{pmatrix} \mathcal{U}u & 0 & 0 \\ 0 & \mathcal{C}c & 0 \\ 0 & 0 & \mathcal{S}s \end{pmatrix},$$

where $\mathcal{U}, \mathcal{S} \in M_d(\mathbb{R})$ are diagonal matrices such that $[\rho(\mathcal{U})]^{-1} < 1$, $\rho(\mathcal{S}) < 1$ and $\mathcal{C} \in M_r(\mathbb{C})$ with $\mathrm{spec}(\mathcal{C}) \in \mathbb{S}^1 := \{z \in \mathbb{C} || z| = 1\}$ and all the eigenvalues have multiplicity one. Then, we proceed as follows:

1. We start the computation of the monodromy matrix M of (1.3) by integrating the equation along the period T.

2. Let S be the diagonalizing transformation $M = SD_MS^{-1}$. Due to the Hamiltonian structure of the problem, the columns of S can be scaled such that

$$S^TJS = -\mathrm{i}J, \qquad S^{-1} = -\mathrm{i}JS^TJ.$$

3. Next we compute

   - $\omega_1, \ldots, \omega_r$ such that $\lambda_j^c = e^{\mathrm{i}\omega_i T}$, $\lambda_j^c \in \mathrm{spec}(\mathcal{C})$,
   - and $\alpha_1, \ldots, \alpha_d$ such that $\lambda_j^h = e^{\mathrm{i}\alpha_j T}$, $\lambda_j^h \in \mathrm{spec}(\mathcal{U})$.

   The values ω_j are not uniquely defined. If ω_j is a complex logarithm divided by the period, then any of the values $\pm(\omega_j + \frac{2k\pi}{T})$, $k \in \mathbb{Z}$ is also admissible. Therefore, we have some freedom to choose these values. Defining

$$D_B = \mathrm{diag}(\alpha_1, \ldots, \alpha_d, \mathrm{i}\omega_1, \ldots, \mathrm{i}\omega_r, -\alpha_1, \ldots, -\alpha_d, -\mathrm{i}\omega_1, \ldots, -\mathrm{i}\omega_r)$$

   and $B = SD_BS^{-1}$, we have that B is a real matrix such that $M = e^{BT}$.

4. We integrate the initial value problem

$$\begin{cases} \dot{P}(\Theta) = Q(\Theta)P(\Theta) - P(\Theta)B, \quad P(\Theta) = I, \\ \dot{\Theta} = \omega_H. \end{cases}$$

Remark 1.2.5. *It is advisable to add an extra change of variables that casts B into real Jordan form J_B, let us explain how it is constructed. Recall that $\alpha_1, \ldots, \alpha_d$ are the normalized logarithms* [2] *of the real eigenvalues, $\omega_1, \ldots \omega_r$ are the normalized logarithms of the complex eigenvalues and $d + r = n$. Then,*

$$J_B = \begin{pmatrix} H & E \\ -E & H \end{pmatrix},$$

where H and E are diagonal blocks of size $n \times n$. If $d \neq 0$ and $r \neq 0$, there are not enough α_j's nor ω_j's to fill all the entries of H and E, then the remaining entries are filled with zeros and the values are arranged so the sub-block $(H|E)$ has maximal rank. To compute J_B consider the matrix R defined in the following way: The first n columns are the eigenvectors corresponding to the unstable eigenvalues and the real parts of the eigenvectors related to complex eigenvalues. The remaining columns are filled with the eigenvectors corresponding to the real stable eigenvectors and the imaginary parts of the complex eigenvectors. The columns can be arranged and scaled so the matrix R is symplectic. We also need to compose the changes P and R. The computation of P and the subsequent composition with R can be done at the same time if we integrate the system 1.2 with $P_0 = R$.

Remark 1.2.6. *When computing the normalized logarithms of the complex eigenvalues we have a certain freedom. There is, however a optimal choice for these logarithms. Adding multiples of the vector-field's frequency rotates the change P. This rotation affects the harmonics. The optimal choice logarithms is the one that makes the dominant harmonics to be of lowest degree as possible. That is, we should use this freedom to make the change as close as possible to constant coefficients. In problems which are a perturbation of an autonomous one, we know in advanced that the logarithms are to be chosen as close as possible to the frequencies of the dynamical equivalent of the periodic orbit in the autonomous system.*

Definition 1.2.7 (Real Floquet Normal Form)**.** *Let us consider J_B defined as in Remark 1.2.5. The associated Hamiltonian reads as:*

$$H_{J_B} = \sum_{j=1}^{d} \alpha_j Q_j P_j + \frac{1}{2} \sum_{j=1}^{r} \omega_j (Q_j^2 + P_j^2). \tag{1.4}$$

[2] By normalized, we mean that the logarithms are divided by the period T.

A Hamiltonian with expansion $H = \sum_{k\geq 0} H_k$ such that H_2 has the form (1.4) is said to be in real Floquet normal form.

The real Floquet normal form, is the Hamiltonian related to the linear system induced by the matrix J_B. The point of computing the real normal form is to integrate system (1.2) using real coordinates. Otherwise it would be mandatory to implement a Taylor method handling complex phase spaces. We should replace the real arithmetic of the Taylor method by a complex one. However, in terms of coding time and efficiency, it is much better to cope with real coordinates when integrating system (1.2). However, in the rest of the process, the opposite situation holds. In fact, when performing higher order normal forms we have to solve a number of linear systems. In this context, it is, obviously, more convenient to cope with diagonal systems. Hence, it is advisable to transform the real Floquet normal form to complex coefficients so it is diagonal. We give a discussion on the complexifiying change in Section 1.3.2. For the moment being we provide the definition of complex Floquet normal form, which is the result of applying the complexifying change presented in Section 1.3.2 to the real Floquet normal form.

Definition 1.2.8 (Complex Floquet Normal Form)**.** *A Hamiltonian $H \in \mathcal{C}^\omega(\mathbb{C}^{2n} \times \mathbb{T}, \mathbb{C})$ is said to be in complex Floquet normal form if the second order H_2 reads as follows:*

$$H_2 = \sum_{j=1}^{d} \mathrm{i}\alpha_j \; Q_j P_j + \sum_{j=1}^{r} \omega_j Q_j P_j. \tag{1.5}$$

1.3 Normal form of order larger than two

In this section we are concerned about normal forms of order larger than two (the second order is handled by the Floquet change). First we detail the theoretical setting as well as give accurate definitions of key notions to be used. In this section we name $E = \mathcal{C}^\omega(\mathbb{T}, \mathbb{C})$. The set $\mathcal{K}$ shall denote both E and $\mathbb{C}$. Obviously, $\mathbb{C} \subset E$, we use this notation to make clear when a polynomial depends on time or not.

Notice that we move to complex coordinates, that is, the Hamiltonian function to be transformed is assumed to be a function of complex variables, in particular, whenever we assume some Hamiltonian to be in Floquet Normal form, we are referencing the complex normal form as in Definition 1.2.8.

To produce higher order transformation of the Hamiltonian, we need to work with its Taylor expansion. Henceforth, up to now, any Hamiltonian function is to be represented as a formal series. Mainly, to fulfill our goals, we have to handle two types of formal series, the ones whose coefficients are periodic functions and the ones whose coefficients are complex numbers. Let us give an accurate definition.

Definition 1.3.1 (Formal series)**.** *Let $\mathcal{F}_r^{\mathcal{K}}$ be the space of homogeneous polynomials (in $2n$ variables) of degree r with coefficients in $\mathcal{K} = \mathbb{C}, E$. We define the graded ring of formal series as $\mathcal{F}^{\mathcal{K}} = \bigoplus_{r\geq 0} \mathcal{F}_r^{\mathcal{K}}$.*

An element $f \in \mathcal{F}^{\mathcal{K}}$ shall be written as $\sum_{r\geq 0} f_r$ with $f_r \in \mathcal{F}_r^{\mathcal{K}}$. For the elements f_r we shall use a more explicit notation, $f_r = \sum_{|k|=r} f_k^r Q^{k^1} P^{k^2}$, where:

- $k = (k^1, k^2) \in \mathbb{Z}_+^{2n}$,
- $|k| = \sum_{i=1}^{2n} k_i$,
- $(Q, P) \in \mathbb{C}^{2n}$ and, finally, for $m \in \mathbb{Z}_+^n$ and $Y \in \mathbb{C}^n$, $Y^m = \prod_{i=1}^n Y_i^{m_i}$.

As we have mentioned in previous pages, a normal form is a process in which we simplify a quantity but keeping certain properties in which we are interested. In the case of the Lie transformation method, we produce suitable canonical changes of variables designed to remove particular monomials. There are, however, certain monomials that cannot be eliminated, the resonant ones. The monomials that cannot be eliminated are determined by the coefficients of the Floquet normal form, let us call the vector formed by the coefficients of the Floquet normal form **vector of basic frequencies**. We introduce here the concept of resonant vector.

Definition 1.3.2 (Resonant vector)**.** *The vector of frequencies $\beta = (\beta_1, \ldots, \beta_n)$ is said to be resonant if there exist a nonzero $k \in \mathbb{Z}_+$ such that*

$$\langle \beta, k \rangle = 0.$$

The number $r = |k|$ is the order of the resonance.

The existence of resonances in the vector of basic frequencies plays against the feasibility of certain normal forms. As we will see, if the order of the resonance is higher than the order the normal form to be computed, these resonances have no effect in the process, so any normal form can be carried harmlessly. Notice that the vector of basic frequencies is formed by both the normalized logarithms of the hyperbolic eigenvalues and the normalized logarithms of the elliptic eigenvalues.

Remark 1.3.3 (Change of notation)**.** *Up to now we have named the frequencies associated to hyperbolic eigenvalues as $(\alpha_1, \ldots, \alpha_d)$ and the frequencies associated to the elliptic eigenvalues as $(\omega_1, \ldots, \omega_r)$. Notice that the vector of basic frequencies is given by*

$$(\mathrm{i}\alpha_1, \ldots, \mathrm{i}\alpha_d, \omega_1, \ldots, \omega_r),$$

where, we recall, $r + d = n$. In order to facilitate the subsequent discussion we rename the vector of basic frequencies as

$$\omega = (\omega_1, \ldots, \omega_n).$$

We are aware of the contradicting notation but we hope that this remark will be enough to avoid any confusion to the reader.

Definition 1.3.4 (Module of resonances)**.** *Let $\omega = (\omega_1, \ldots, \omega_n)$, be a vector of basic frequencies. We denote the $\mathbb{Z}$-module of resonances associated to ω as*

$$M_\omega = \{\nu \in \mathbb{Z}_+^{2n} |\ \langle \nu^2 - \nu^1, \omega \rangle = 0.\}$$

We say that the vector ω is non-resonant if $M_\omega = \{0\}$.

Given a Hamiltonian function H in Floquet normal form, the module of resonances associated to H is M_ω where ω is the vector of basic frequencies of H_2 associated to the complex eigenvalues. The module of resonances establishes, as we mentioned, the monomials that cannot be removed of the normal form. Depending on our purposes, we can select a subset from $\mathbb{Z}_+^{2n}$ to be preserved after the transformation process, this set, may have or not some algebraic structure but it must contain the module of resonances. There are other monomials that cannot be removed besides M_ω. Let us provide the definition of the Module of unavoidable resonances, the reason will be clear after the discussion on the construction of the generating function.

Definition 1.3.5 (Module of unavoidable resonances)**.** *We denote the module of unavoidable resonances as*

$$M_u = \{(\nu^1, \nu^2) \in \mathbb{Z}_+^{2n} \mid \nu^1 = \nu^2\}.$$

Definition 1.3.6 (Normal form with respect to M)**.** *Let H be a Hamiltonian and $M \subset \mathbb{Z}_+^{2n}$ containing the module of resonances M_ω associated to H. We say that H is in normal form at order r with respect to M if $H = N^{[\leq r]} + \mathcal{R}^{[>r]}$, where*

$$N^{[\leq r]} = \sum_{|k| \leq r, k \in M} N_k Q^{k^1} P^{k^2}, \qquad \mathcal{R}^{[>r]} = \sum_{|k|>r} R_k Q^{k^1} P^{k^2}.$$

If $N^{[\leq r]} \in \mathcal{F}^{\mathbb{C}}$ we say that the normal form is autonomous and, if $N^{[\leq r]} \in \mathcal{F}^E$ we say that the normal form is non-autonomous.

We refer to $N^{[\leq r]}$ as the truncated normal form of order r and $\mathcal{R}^{[>r]}$ as the rest. As mentioned, the M is used to denote the monomials that are preserved in the normal form and it always has to contain the resonance module: the resonant terms cannot be removed

from the normal form. Anyhow resonant vectors of basic frequencies have measure zero, henceforth, generically speaking $M_\omega = \{0\}$. The set M induces the type of normal form obtained at the end of the process and is defined by some suitable killing criterion, that is, a characterization of the monomials to be removed. When this method is implemented in a computer, maybe it is not advisable to remove all the monomials whose indices are not in M but this will be discussed later. In Definition 1.1.1 we introduce the Poisson bracket which is the main tool to perform canonical transformations. Fixed $g \in \mathcal{F}_{k_1}$, notice that

$$\mathcal{L}_g : \mathcal{F}^{\mathcal{K}}_{k_2} \mapsto \mathcal{F}^{\mathcal{K}}_{k_2+k_1-2}.$$

Let explain how to construct generating functions to fulfill distinct goals using the Lie transformation method. Besides from type of normal form we are interested, we admit also Lie transformations that remove time dependence in all the monomials. We call the transformation that removes time dependence **autonomizing change**. Otherwise, the transformation is called **non-autonomizing**. Notice that, in a non-autonomizing change we can decide to remove some harmonics if that is not harmful. This is to be clarified later.

Proposition 1.3.7 (Construction of the generating function)**.** *Let $H \in \mathcal{C}^\omega(\mathbb{T} \times \mathcal{U}, \mathbb{C})$ and $M \subset \mathbb{Z}^{2n}_+$. Assume:*

1. *H is in Floquet Normal Form with vector of basic frequencies $\omega \neq 0$.*
2. *$M_\omega, M_u \subset M$.*

Then, for a fixed $r \in \mathbb{N}$, there exist $G_{na} \in \bigoplus_{d=3}^r \mathcal{F}^{\mathbb{C}}_d$ and $G_a = \bigoplus_{d=3}^r \mathcal{F}^E_d$ such that.

$$T_{G_{na}} = H_2 + \sum_{2<|k|\leq r, k\in M} N_k + \mathcal{R}^{[>r]}, \quad T_{G_a} = H_2 + \sum_{2<|k|\leq r, k\in M} N'_k + \mathcal{R}'^{[>r]},$$

with $N_k \in \mathcal{F}^E_k$ and $N'_k \in \mathcal{F}^{\mathbb{C}}_k$.

Proof. We construct a generic generating function and then, discuss how to adapt it to fit the requirements of G_{na} (non-autonomizing) and G_a (autonomizing). Since H is supposed to be in Floquet normal form $H_2 \in \mathcal{F}^{\mathbb{C}}_2$. This is the reason why the Hamiltonian should remain untouched up to order 2. Let us suppose that $G = G_{na}, G_a$ exist for $r-1$ and let us construct it for r. We define $G = G^{[<r]} + G^r$ where $G^{[<r]} \in \bigoplus_{d=3}^{r-1} \mathcal{F}^{\mathcal{K}}$ is the generating function for $r-1$. Notice that $T_G H = T_{G^{[<r]}} H + T_{G^r} H$. By induction assumption $T_{G^{[<r]}} H$ is already arranged, we focus on $T_{G^r} H$. We have the following identity:

$$\left[T_{G^r} H\right]^{[=r]} = H^r + \omega_S \frac{\partial G^r}{\partial \Theta} + \{H_2, G^r\}.$$

The rest of the terms are of higher order. At this point, we consider the fact that G^r is a sum of monomials of degree r i.e. $G^r = \sum_{|k|=r} g_k^r(\Theta) Q^{k^1} P^{k^2}$. Applying the linearity of the Poisson Bracket and the fact that H is in Floquet Normal form, we obtain:

$$\{H_2, G^r\} = \sum_{|k|=r} \langle \omega, k^2 - k^1 \rangle g_k^r(\Theta) Q^{k^1} P^{k^2}.$$

Up to now, we have shown that:

$$\left[T_{G^r} H\right]^{[=r]} = H^r + \omega_S \frac{\partial G^r}{\partial \Theta} + \sum_{|k|=r} \langle \omega, k^2 - k^1 \rangle g_k^r(\Theta) Q^{k^1} P^{k^2}.$$

We can solve the equation for each monomial separately. Let us name $\bar{h}_k^r(\Theta)$ the coefficients of the Taylor expansion of the transformed Hamiltonian i.e. $\left[T_{G^r} H\right]^{[=r]} = \sum_{|k|=r} \bar{h}_k^r(\Theta) Q^{k^1} P^{k^2}$. Therefore, for each monomial, we have to solve the following differential equation:

$$\bar{h}_k^r(\Theta) = h_k^r(\Theta) - \omega_S \frac{d}{d\Theta} g_k^r(\Theta) + \langle k^2 - k^1, \omega \rangle g_k^r(\Theta). \tag{1.6}$$

Here, the functions g_k^r are the unknowns and h_k^r are the coefficients of order r of the original Hamiltonian. The functions $\bar{h}_k^r$ can be chosen as desired and this will determine the generating functions. The differential equation (1.6) can be handled by expanding all the functions in Fourier coefficients. In general, the Fourier coefficients of the order r of the generating function are:

$$g_{k,s}^r = \frac{h_{k,s}^r - \bar{h}_{k,s}^r}{\mathrm{i}\omega_H s - \langle k^2 - k^1, \omega \rangle}.$$

Notice that, if $k^2 = k^1$, the average of the generating function is not defined by the previous formula. It has to be taken as zero. Now we specify the generating functions G_{na} and G_a.

If $k \notin M$, the corresponding monomial is to be eliminated. That is, $\bar{h}_k^r \equiv 0$. Then, the Fourier coefficients are chosen as

$$g_{k,s}^r = \frac{h_{k,s}^r}{\mathrm{i}\omega_S s - \langle k^2 - k^1, \omega \rangle} \quad \text{if } s \neq 0,$$
$$g_{k,0}^r = \frac{-h_{k,s}^r}{\langle k^2 - k^1, \omega \rangle} \quad \text{if } k^1 \neq k^2.$$

Notice the appearance of small divisors on the autonomizing change. These small divisors are overcame by the decay of the Fourier coefficients of the functions h_k^r. Hence, at finite order, the resulting expansion is convergent. □

If the initial Hamiltonian function is analytic, the normal form obtained at any finite order is convergent. In general, it is not true that the process taken into all orders results in a convergent series. Even if the truncated process leads into a convergent series, the radius of convergence may be small. This is due to the small divisors appearing in the generating function. These divisors always appear when we decide to remove all the harmonics of the coefficients independently from the choice of M. If we do not want to eliminate the time dependence there are choices of M that avoid small divisors.

Notice that, in the construction of the generating function, we are obligated to select g_r^k to be average free if $k^1 = k^2$. The consequence is that the corresponding term $\bar{h}_r^k$ in the normal form. These are resonances that appear always in the process and coincide with the monomials determined by M_u.

1.3.1 Module for the centre manifold

Definition 1.3.8 (Module of the centre manifold)**.** *We denote the module of the centre manifold as*

$$M_{CM} = \{\nu \in \mathbb{Z}_+^{2n} \mid \nu_1^1 = \nu_1^2, \dots, \nu_d^1 = \nu_d^2\}.$$

Observe that $M_u \subset M_{CM}$. Unlike other normal form processes, the changes of variables in the centre manifold reduction do not look to remove the largest possible number of monomials but the smallest one. This is because the purpose is to describe the largest possible region of the phase space, that is, to produce an expansion with a radius of convergence as large as possible. In M_{CM} we select to eliminate monomials whose exponents in each hyperbolic variable is different from the exponent of his conjugate pair. That is, if $(Q_1, P_1, Q_2, P_2, \dots Q_d, P_d)$ are the hyperbolic variables, we eliminate any monomial containing a factor of the form $Q_i^{k_i^1} P_i^{k_i^2}$ with $k_i^1 \neq k_i^2$. In the case time is also removed, the functions $I_i = Q_i P_i$ $i = 1, \dots, d$ are first integrals of the truncated reduced system.

Lemma 1.3.9. *The functions $I_i = Q_i P_i$ are first integrals of the (autonomous) reduced Hamiltonian. Moreover, as firsts integrals, are independent and in involution.*

Proof. For some $i = 1, \dots, d$, fix I_i. Notice that:

$$\{H, I_i\} = \left[\frac{\partial H}{\partial Q_j}\frac{\partial Q_i P_i}{\partial P_j} - \frac{\partial H}{\partial P_j}\frac{\partial Q_i P_i}{\partial Q_j}\right] - \omega_H \frac{\partial Q_i P_i}{\partial \Theta} = 0.$$

Let us fix $i, j \in \{1, \dots, d\}$ and let I_i and I_j two of the first integrals. Then,

$$\alpha_1 \nabla I_i + \alpha_2 \nabla I_j = (0, \dots \alpha_1 Q_i, \alpha_1 P_i \dots \alpha_2 Q_j, \alpha_2 P_j \dots, 0)$$

and obviously the last vector is zero if and only if $\alpha_1 = \alpha_2 = 0$ hence, the first integrals are independent. On the other hand,

$$\{I_i, I_j\} = (P_i, 0)(0, Q_j)^T - (Q_i, 0)(0, Q_j)^T = 0$$

therefore, the integrals are in involution. □

Remark 1.3.10. *In [AS00, And02] Andreu and Simó use another criterion for the centre manifold. They keep the monomials $\nu \in \mathbb{Z}_+^{2n}$ such that $\nu_1^1 + \nu_1^2 = 1, \ldots \nu_d^1 + \nu_d^2 = 1$. This criterion, preserves more monomials and, therefore, the radius of convergence is slightly larger. However, it does not produces additional first integrals.*

1.3.2 Complexification and realification

In the last section, we work with Hamiltonian systems that are expanded in complex variables. This facilitates the discussion and computation of the normal form as the systems to be solved are diagonal. In applications, we usually work with real Hamiltonians and it is suitable to handle the corresponding manipulations of the normal forms in real coordinates. Let us explain first how to pass from real to complex coordinates. Let $(x, y) \in \mathbb{R}^{2n}$ be real coordinates, we define the complex set of coordinates (Q, P) as

$$x_j = \frac{Q_j + \mathrm{i}P_j}{\sqrt{2}}, \qquad y_j = \frac{\mathrm{i}Q_j + P_j}{\sqrt{2}}, \qquad j = 1, \ldots, n. \tag{1.7}$$

It is simple to check that this is, indeed, a canonical transformation that casts a real Hamiltonian to a complex one. Stress that, in practical implementations, one can compute the expansion of the Hamiltonian directly in these complex coordinates. The realification of the expansion is given by the inverse of (1.7):

$$Q_j = \frac{x_j - \mathrm{i}y_j}{\sqrt{2}}, \qquad P_j = \frac{-\mathrm{i}x_j + y_j}{\sqrt{2}}, \qquad j = 1, \ldots, n. \tag{1.8}$$

1.3.3 Change of variables

Besides from computing the expansion of the normal form, we are also interested in computing the change of variables that cast the coordinates of the normal form to the original coordinates. This can be done for a number of purposes. In this thesis we have used this changes to produce tests on the software, but we refer to [Jor99] (and references therein) for a discussion on how this changes of variables can be used to fulfill many other goals.

Let (q, p) be the original coordinates of the system and (Q, P) the ones defined by the Lie transformation. Then

$$q_i = T_G Q_i, \qquad p_i = T_G P_i, \qquad i = 1, \ldots, n.$$

Notice that this change of variables is done from order 3. The second order is handled by the Floquet change explained in Section 1.2. As the change T_G is the one-time flow of the Hamiltonian G, one only has to change the orientation of the time to get the inverse transformation. This is accomplished by changing the sign of the vectorfield. That is,

$$Q_i = T_{-G} q_i, \qquad P_i = T_{-G} p_i, \qquad i = 1, \ldots, n.$$

Notice that, to compute the change of variables, we only need the generating function, the Floquet change and the periodic orbit. This step can be implemented at the end of the computation of the normal form or in a separated program.

1.3.4 From three and a half degrees of freedom to a family of area preserving maps

Let us focus on a very specific case. Suppose that the original system has three and a half degrees of freedom and a periodic orbit with a single hyperbolic direction. The centre manifold reduction, when the time dependence is removed, reduces the original system, to another Hamiltonian with two degrees of freedom. Typically, one fixes an energy level and uses a Poincaré section to reduce the problem to the study of a family of area preserving maps. The energy is fixed to slice the phase space. This can be done if the Hamiltonian restricted to the centre manifold is positive defined, in that case the levels of energy are diffemorphic to a three sphere, $\{H = h\} \cong \mathbb{S}^3$. Sometimes, the Hamiltonian is not positive defined because the frequencies have opposite signs. The above-mentioned strategy do not work because the levels of energy of the Hamiltonian are not bounded hyperboloid shaped manifolds. The conclusion is that we need another conserved quantity to play the role of the Hamiltonian function. An approximate first integral [Jor99] is perfectly suited to this task. Let us recall how to compute an approximate first interval of a given autonomous Hamiltonian and then, we point out, the advantage of this choice for our situation.

Computation of first integrals: Here we give a short reminding on how to compute an approximate first integral of a given Hamiltonian. For a deeper explanation, remarks on the software implementation performance see [Jor99].

Let us assume that we are given a Hamiltonian H, whose origin is a totally elliptic equilibrium point. Consider the Taylor expansion of the Hamiltonian around the origin

$H = \sum_{j\geq 2} H_j$, where H_j are homogeneous polynomials of degree j. We look for a first integral $F = \sum_{j\geq 2} F_j$, i.e. a function that satisfies $\{H, F\} = 0$. One can solve this equation for F order by order using the following recurrence.

$$\{H_2, F_n\} = -\sum_{j=3}^{n} \{H_j, F_{n-j+2}\}.$$

We stress here that F_2 is not determined by the scheme, therefore it can be freely chosen. This is why an approximated first integral is very suited as a replacement of the Hamiltonian function. Indeed, we can chose F_2 so F is positive defined (for instance, choosing the absolute value of the frequencies of the Hamiltonian as the coefficients of F_2). Then, $\{F = f\} \cong \mathbb{S}^3$ and we can slice the phase space using F.

1.4 Details on the implementation

In this section, we discuss the main aspects of the implementation of this methodology on a computer program. The programs have been written in ANSI C and C++ languages adapting the public software for the computations of normal forms presented in [Jor99]. As we have said, it has also been used the public package [FJ05] to build an efficient arithmetic of Fourier series. In general, the programs are built to be efficient allowing us to provide high order normal forms. As most of ideas used here can be found in [Jor99], we will skip some of the technical details. We recommend the above-mentioned references for a deeper understanding of technical aspects. This section is structured as follows: First we give details on the arithmetic of Fourier-Taylor series, second we comment some aspects on the implementation of the Floquet change. The third point to be addressed is the implementation of the main algorithm and, finally, we discuss tests on software and accuracy.

1.4.1 On Taylor-Fourier series

The main object we have to handle when writing the implementations of the methodology presented in this chapter are homogeneous polynomials whose coefficients are Fourier Series. Here, the Fourier series have complex coefficients and, hence, there are four different arithmetics nested in each operation between two homogeneous polynomials, that is

(1) Real $\mapsto$ (2) Complex $\mapsto$ (3) Fourier Series $\mapsto$ (4) Homogeneous Polynomials.

In order to have a good performance the basic operations between the mathematical objects involved are to be written as efficiently as possible. For the real and complex operations we

use the standard libraries available for ANSI C. The standard arithmetic of complex numbers could be improved, anyhow, we are satisfied with the current performance of the programs. Here we focus on the routines to handle Fourier series and homogeneous polynomials.

The arithmetic of Fourier Series

Let $f \in \mathcal{C}^\omega(\mathbb{T}, \mathbb{C})$. The Fourier coefficients of f are defined as

$$C_k = \frac{1}{2\pi} \int_{\mathbb{T}} f(s) \exp(-\mathrm{i}ks) ds.$$

In the strong regularity condition we are assuming, it is well known that the sequence of partial sums,

$$P_N(\theta) = \sum_{|k|<N} C_k \exp(\mathrm{i}k\theta),$$

converges, uniformly in θ when $N \to \infty$, to f. Moreover, if f is real analytic, the sequence $\{|C_k|\}_{k\in\mathbb{Z}}$ converges to zero exponentially i.e. there exist positive constants M and ρ such that

$$|C_k| \leq M \exp(-|k|\rho).$$

The constants M and ρ depend on f and, in particular, ρ is bounded by the distance of the closest singularity of f (regarded as a holomorphic function) to the real line. If ρ is not too small, the fast decay of the sequence $\{|C_k|\}_{k\in\mathbb{Z}}$ results in the fact that just a few coefficients are needed to describe the function f with a prescribed accuracy. When f is real-valued, it holds that $C_{-k} = \bar{C}_k$, in that case, only half of the coefficients are needed to evaluate the function. A periodic function can be stored in a computer as a finite mesh of points or as a finite set of coefficients. Let us fix a truncation order N, E_N is defined as the space of trigonometric polynomials of degree N, $M = (2N+1)$ and $P_M = \{z = (z_1, \ldots, z_M) \in \mathbb{C}^M\}$. It is trivial to see that, both, E_N and P_M are $\mathbb{C}$ vector spaces of dimension M. The Discrete Fourier transform, $\Gamma_N : P_M \mapsto E_M$, is given by $\Gamma_N(z) = C$, where

$$C_k = \frac{1}{N} \sum_{j=0}^{N-1} z_j \exp\left(-\mathrm{i}k\frac{j}{N}\right),$$

is an isomorphism and its inverse map Γ_N^{-1} is given by $\Gamma_N^{-1}(C) = z$, where

$$z_k = \frac{1}{N} \sum_{j=0}^{N-1} C_j \exp\left(\mathrm{i}k\frac{j}{N}\right),$$

There is an excellent public package by Frigo and Johnson [FJ05]. The FFT is implemented to achieve the computational cost $\mathcal{O}(N \log N)$. We use this software widely in our implementation of the arithmetic of Fourier series. Now, we have an efficient way to pass to coefficients from points (and viceversa). The periodic functions are stored in a structure of the form

```
typedef struct{
        int N;
        double complex *C;
        char mvc;
} sf;
```

The integer indicates the truncation order, the vector of complex numbers contains the coefficients or the mesh of points and the char is a control parameter that encodes whether the array contains points a table of values or Fourier coefficients of the function. The point of this structure is that some operations are suited to be done with the table of values of the function, namely the elementary operations (products, divisions, square roots, etc.) and other are better suited to be performed with the Fourier coefficients, for instance, derivatives, evaluations and norms. Two key functions of the arithmetic are the ones that apply the Fourier transform (or its inverse) if it is required. The direct transformation receives and object of type `sf`, checks the control character `mvc`. In case the array `C` contains points of the table of values, it applies the Fast Fourier Transform on the object and switches the control character, otherwise, it does nothing.

As we have said, each operation of the arithmetic is to be performed over coefficients or values, hence, the first step is to transform between coefficients and values conveniently. Of course, the transformation does not act on the inputs if the corresponding character is in agreement with the output type. After the transformation, the operation is done and the control character of the output is set. In binary operations, obviously, both inputs are to be transformed. This prevents the program to operate objects with different control characters. This is particularly important in operations like the sum, that can be implemented in the same way no matter if the vector contains points or coefficients. In these special operations, we choose to transform the inputs into points as most of the operations have to be performed over the table of values. In general, the arithmetic is designed to perform the least possible number of transformations. In this way, any operation between Fourier Series requires (order of) $N \log N$ operations with complex numbers if previous transformations are required and (order of) N operations with complex numbers if no previous transformation is applied.

Handling Homogeneous Polynomials

The arithmetic of Fourier series is combined with an arithmetic that operates with homogeneous polynomials. We have used the one presented in [Jor99]. There, a deep explanation

o the implementation is given. Here, we discuss the main ideas involved. A homogeneous polynomial of degree k in the variables $(x_0, x_1, \ldots, x_m)$ is an expression

$$P_r = \sum_{|j|=k} p_j x^j$$

where, as usual, $j \in \mathbb{Z}_+^m$, $|j| = j_1 + j_2 + \cdots + j_m$ and $x^j = x_1^{j_1} \cdot x_2^{j_2} \cdot \ldots \cdot x_m^{j_m}$. A homogeneous polynomial of degree k has $\psi_m(k)$ coefficients, where

$$\psi_m(k) = \sum_{j=0}^{k} \psi_{m-1}(j) = \binom{k+m-1}{m-1}.$$

The working space for a homogeneous polynomial of degree k and m variables consists of an array of $\psi_m(k)$ objects of type `sf`. The coefficients of this array can be identified by their position on the array or by the exponents of the variables for which the coefficient is to be multiplied. There are two functions that act as a translator. These functions are named `llex` and `exll` in [Jor99]. Given $j \in \{0, \ldots, \psi_m(k)-1\}$, `llex(j)` returns an array $(j_1, \ldots j_m) \in \mathbb{Z}^m$ with $|j| = k$, the function `exll` is the inverse function. All the repeated values concerning exponents and locations are computed in advanced and stored in global tables that can be accessed at any moment by the program.

The program to compute normal forms needs to perform three basic operations between homogeneous polynomials: sum, product and the Poisson bracket. The sum is straightforward to implement, summing the coefficients positions by position. In this case we do not have to care about producing coefficients to be located in other places of the array. The product is different, here we have to compute the products corresponding to all the possible combinations between the coefficients of the input polynomials and accumulate them in the corresponding output array. The Poisson bracket function, handling two homogeneous polynomials, x and y, in variables $(P, Q) \in \mathbb{C}^{2n}$, is based on the following identity

$$\left\{ \sum_{k,l} x_{k,l} Q^k P^l, \sum_{k',l'} y_{k',l'} Q^{k'} P^{l'} \right\} = \sum_{k,l,k',l'} x_{k,l} y_{k',l'} \left(\sum_{j=1}^{n} (k_j l'_j - k'_j l_j) \frac{Q^{k+k'} P^{l+l'}}{P_j Q_j} \right).$$

This formula can be implemented using the same ideas discussed for the product. Let us recall that the term $-\omega_H \frac{\partial}{\partial \Theta} y$ needs to be introduced to get the non-autonomous version of the Poisson bracket.

1.4.2 On the implementation of the Floquet Change

Let us discuss some details on the implementation of the Floquet Change. The computations in this part of the program are performed in extended accuracy. This is done for several

reasons that shall be pointed out during the discussion. We use the `mpfr` [FHL+07] arithmetic and the library `mpreal` [Hol18] to overload the arithmetic. The language `C++` is used for that purpose. The computation of the Floquet Change works as follows:

First of all, we read some approximated periodic orbit and refine it up to the desired accuracy. The eigenvalues and the eigenvectors of the monodromy matrix are computed and, with these, we are able to construct the real reduced Floquet matrix B (see Section 1.2). On the other, we construct the change R that casts B into real Jordan normal form J_B and compute it by evaluating $R^{-1}BR$. Notice that there is no need to compute J_B after computing the diagonal normalized logarithm as we know the entries of J_B. However, doing it in this way permits to test the change R. We also perform other test during the computation such as the symplecticity of the matrices involved. If any of these tests is not passed, the program stops with a suitable message. All these extra checks are done because the outputs of the function that computes the eigenvalues sorts them according to their modulus. In principle we do not know in advance if there will be real eigenvalues or not, therefore, at each run of the program, we have to select an order for the eigenvalues to perform the subsequent computations.

Once the change R and the Jordan normal form J_B are obtained, we proceed to integrate equation (1.2) and the variational equation together. These integrations are done together so we can produce coherent meshes of the periodic orbit and the periodic change at the same time, without the necessity to recompute the input. Obviously this can be done separately but, as the problem invites to play with the parameters, we think that doing it together is a safer option. In some cases, the dynamics around the periodic orbit will be largely unstable and the accumulation of errors will be severe. This is, again, overcame by the high accuracy we use for the integrations. The integrations are carried out by means of a Taylor method, see [JZ05a] and Chapter 2, where some considerations on multiple accuracy integrations are discussed.

By this stage of the process, we have computed a tabulation of the periodic orbit and the change of variables. We do an extra computation: We perform a Fast Fourier Transform (using our own implementation) and check the leading harmonics of each entry of the change of variables, this is printed together with the output. If the produced change is not close enough to constant coefficients, we rerun the program using another choice for the normalized logarithms of the eigenvalues.

There are several parts of this program that could be implemented in a more efficient manner. For instance, the multiple accuracy could be avoided by using a multiple shooting strategy. However, as a few integrations (taking into account the refinement of the initial data) are required, the loss of efficiency is not critical in terms of computing time. We think that, simply, it does not pay off to try other strategies with a more involved development process. After a successful run of this program, we end up with a tabulation of the periodic

orbit and the Floquet change with more than 16 correct digits. Multiple accuracy shall not be used in the subsequent computations.

1.4.3 The Main Algorithm

Here we give some remarks on the implementation of the main algorithm. In particular we discuss how the r-th step of the normal form process is performed. Let us fix $r \geq 3$ and assume that $H = H_2 + H_3 + \cdots + H_{r-1} + H_r + \ldots$ is already in normal form up to degree $r-1$. First we compute the order r of the generating function, i.e. G_r according to Proposition 1.3.7. The transformed Hamiltonian shall be denoted by $\bar{H} = \bar{H}_2 + \cdots + \bar{H}_r + \ldots$. After the arrangement produced by G_r, $\bar{H}$ verifies the following:

- $\bar{H}_l = H_l$ for $l = 2, \ldots, r-1$.
- $\bar{H} = H_r + \{H_2, G_2\}$.
- $\bar{H}_{r+1} = H_{r+1} + \{H_3, G_r\} + \ldots$.

  $\vdots$

Notice that, to implement this scheme, we only need to save space for the expansion (that is constantly being modified) and some working space for a homogeneous polynomial of degree r. Obviously we also need to store the corresponding monomial of the generating function which is acting at each step. After $\bar{H}$ is arranged, we write (in a file) the monomial G_r.

1.4.4 Testing the software

Together with the programs to compute the normal form and the change of variables, we have developed a test to check the correctness of them. The test is based in the behaviour of the remainder. Let us explain the main idea in a simplified setting. Let $\mathcal{U}$ be an open set of $\mathbb{R}^m$ containing the origin and $F \in \mathcal{C}^\infty(\mathcal{U}, \mathbb{R})$. Assume, to simplify the exposition that $F(0) = 0$ and $x \in \mathcal{U}$ with $\|x\| = h$ with h small enough. Let F_r be an approximation of order r i.e. its Taylor polynomial of order r around the origin. Then,

$$\|F(x) - F_r(x)\| = A\|x\|^{r+1} + H.O.T.$$

Let us select $\tilde{x}$ such that $\|\tilde{x}\| = 2h$. Then, we can compare the errors on the approximations on the evaluations of x and $\tilde{x}$ as

$$q_r(x, \tilde{x}) = \frac{\|F(\tilde{x}) - F_r(\tilde{x})\|}{\|F(x) - F_r(x)\|} = \frac{A(2h)^{r+1}}{Ah^{r+1}} + H.O.T.$$

It follows that $q_r(x,\tilde{x}) = 2^{r+1} + \nabla_r(x,\tilde{x})$, where ∇_r is some residue due to the contribution of higher order terms. To check the correctness of the approximation F_r, we have to compute the quantity q_r and see if it is reasonably close to 2^{r+1}. Obviously, we have to take into account that the higher order terms play their role. We have also to take care on not choosing a point x with a extremely low norm, as, for moderately high values of r, the expression h^{r+1} lies below the accuracy of the machine (in standard double precision, 10^{-16}).

Let us discuss how to apply these ideas to the actual computations this chapter is concerned with. Let us assume first that the normal form is autonomized, i.e. the final output does not depend on time. The non-autonomous case can be handled similarly. The problem we undertake here is the computation of a canonical change of variables (up to some order r) of some Hamiltonian function H, as well as the transformation of the last. Let us call $\bar{H}$ the transformed Hamiltonian and T_G^r the change of variables casting the normal form coordinates to the original ones. Let us name

$$\vec{X}_H = \left(\frac{\partial H}{\partial p}, -\frac{\partial H}{\partial q}\right),$$
$$\vec{X}_{\bar{H}} = \left(\frac{\partial \bar{H}}{\partial P}, -\frac{\partial \bar{H}}{\partial Q}\right),$$

the vector-fields associated to each Hamiltonian function. We have to check that the following diagram

$$\begin{array}{ccc} H & \xrightarrow{T_{-G}^r} & \bar{H}_r \\ \downarrow & & \downarrow \\ \vec{X}_H & \xrightarrow{T_G^r} & \vec{X}_{\bar{H}_r} \end{array}$$

commutes up to order r. To do so, we produce a table of points containing a mesh of a trajectory in the normal form. The orbit is computed from an initial condition v_{nf} with $\|v_{nf}\| = \lambda$ small. The rest of the trajectory is obtained integrating numerically the vectorfield. This integration is carried out by means of a Runge-Kutta-Fehlberg method. The trajectory on the normal form is sent, through the change T_G^r, to the original coordinates. Then the transformed table is vindicated in the following way. Each point of the transformed mesh is associated with a time. Notice that, as the Hamiltonian on normal form coordinates does not depend on time and the original does, the choice of the time is free but, obviously, it has to be done coherently. Then we integrate each point of the transformed table from its associated time to the time corresponding to the next point. Summarizing, we produce two tables of points on original coordinates. If the approximation of the Hamiltonian is of order

r, the agreement between the points of these two tables must be of order $r-1$ in λ, as the test is performed on the vectorfield. Obviously, one must take care on not choosing an initial condition outside the radius of convergence of the normal form to have a successful test.

High hyperbolicity can affect severely the results of this test. That is, if the original periodic orbits has a large unstable eigenvalue, the integrations carried out in the original vectorfield shall propagate small errors in a dramatic way. This impossibilities to estimate sufficiently well how the contributions of the tails of the approximations are transported through the flow. Therefore, the evaluation of the quantity q_{r-1} shall be far from what is expected. There are two ways to deal with this problem. First, we can reduce the integration time as one classically does. A smaller piece of the trajectory is to be computed and this will provide a sufficient validation test for the program. One can also use a parallel shooting for the integrations in the original system pursing also the goal of shorting the integration time. The second approach is based in brute force and it consists on using high accuracy arithmetic during the whole computation: for the normal and for the integrations on the original vectorfield. The accuracy is to be chosen to overcome the propagation of error produced by the largest unstable eigenvalue. We have not implemented the second option.

We do not need to integrate the whole grid to estimate the quantity q_{r-1}, two points are enough. However this test, integrating the whole of the mesh, gives insight on the accuracy of the centre manifold.

Estimation of the radius of convergence

A rough upper bound for the distance of the origin at which the normal form is valid is the radius of convergence of the series itself. Let us define the following quantities:

$$r_n^1 = \frac{\|H_n\|_1}{\|H_{n-1}\|_1}, \quad r_n^2 = \sqrt[n]{\|H_n\|_1}, \quad \|H_n\|_1 = \sum_{|k|=n} |h_k|, \quad 3 \leq n \leq N.$$

These are estimations are based in the well known ratio and root tests for power series.

1.5 The Centre Manifold of L_1 in the BCP

In this section we illustrate the methodology presented along the previous pages. To do so, we have chosen a model which is a periodic perturbation of the Restricted Three Body Problem (RTBP): the Bicircular Problem (BCP). The BCP will be used as a test model for the numerical methods presented in the first part of the thesis. For this reason we give an brief introduction of the BCP here.

The BCP is a restricted version of the Four Body Problem. It is build assuming Earth and Moon to behave as in the RTBP, that is, they move following circular orbits centred in

their common barycentre. At the same time, this barycentre and Sun move following another circular orbit, with Sun, around the barycentre of Earth-Moon and Sun. Notice that is this model can be seen as two coupled RTBP's. We take the units and the system of coordinates as in the Earth-Moon RTBP. With all this considerations the model, a three and a half degrees of freedom perturbation of the RTBP, has a Hamiltonian function that writes as

$$\begin{aligned} H_{BCP} = &\frac{1}{2}(p_x^2 + p_y^2 + p_z^2) + yp_x - xp_y - \frac{1-\mu}{r_{PE}} - \frac{\mu}{r_{PM}} \\ &- \frac{\varepsilon m_S}{r_{PS}} - \frac{\varepsilon m_S}{a_S^2}(y\sin\theta - x\cos\theta). \end{aligned}$$

Here the units and coordinates are taken as in the Earth-Moon RTBP, m_S is the mass of Sun, a_S the semimajor axis of Sun, $r_{PE}^2 = (x-\mu)^2 + y^2 + z^2$, $r_{PM}^2 = (x-\mu+1)^2 + y^2 + z^2$, $r_{PS}^2 = (x-x_S)^2 + (y-y_S)^2 + z^2$, $x_S = a_S\cos\theta$, $y_S = -a_S\sin\theta$, $\theta = \omega_S t$ and ω_S is the mean angular velocity of Sun in these synodic coordinates. Notice that we have introduced an additional parameter ε establishing an homotopy between the RTBP ($\varepsilon = 0$) and the BCP ($\varepsilon = 1$). Due to the periodic perturbation due to Sun, the Lagrangian points are no longer equilibria, they are replaced by periodic orbits with the same period as Sun's ($T_S = 2\pi/\omega_S$). We name these replacements as **dynamical equivalents** of the Lagrangian points.

Let us focus on L_1. If we continue L_1 as a periodic orbit of period T_S we find that the replacement is a small unstable periodic orbit with the same normal behaviour as L_1 (four elliptic directions and two hyperbolic ones). The size of the orbit is around 10^{-3} and it revolves L_1 twice in T_S units of time. An important feature to be noticed about this orbit is its high instability. The unstable eigenvalue of the monodromy matrix is large, around 10^8. For this reason we are interested in decoupling the hyperbolic and the elliptic part. This can be achieved by means of a semi normal form known as the Centre Manifold Reduction (CMR for short).

1.5.1 Expansion of the Hamiltonian

We can split the Hamiltonian in two parts: The monomials of degree less or equal than two and the higher order ones. Instead of computing the expansion directly, we rather perform some changes of variables to put the Hamiltonian in a suitable way to succeed in having an efficient implementation and avoid pathological behaviour of propagation of error. Let $t \mapsto g(t) \in \mathbb{R}^6$ be a T_S-periodic orbit of the system. We Name g_i for $i = 1, \dots 6$ its components. And let $\bar{\gamma}_i = \frac{1}{T_S}\int_0^{T_S} g_i(s)ds$ be the corresponding averages and $\gamma = d(\bar{\gamma}, M_c)$ be the distance between Moon and the average of the periodic orbits. We apply the three following changes:

1. A scaling by γ. This is done to get a new units such that the (averaged) distance between the periodic orbit and the Moon is equal to one. With this we assure the expansion of the Hamiltonian expanded around the periodic orbit to have radius of convergence close to one.

2. A translation by g, to put the periodic orbits at the origin. This leads to a Hamiltonian with no order one monomials as discussed in the previous section, see Lemma 1.1.8.

3. A Floquet symplectic change. This puts the second order of the Hamiltonian in diagonal form.

With these changes, the Hamiltonian gets the simpler form

$$\begin{aligned} H = &\frac{1}{2}\omega_1 x p_x + \frac{\omega_2}{2}(y^2+p_y^2) + \frac{\omega_3}{2}(z^2+p_z^2) \\ &- \left(\frac{1-\mu}{r_{PE}} + \frac{\mu}{r_{PM}} + \frac{m_S}{r_{PS}}\right)^{[\geq 3]}. \end{aligned}$$

Notice that the names of the variables have been kept. This is to avoid heavy notation and we hope this will cause no confusion to the reader. The main issue is, therefore, to expand the gravitational potentials of the Earth, the Moon and the Sun in these new variables. To produce the Taylor expansion of a gravitational potential is a well known problem and there are several approaches to do so. We focus on the following one: A gravitational potential can be expressed in the basis of Legendre polynomials as

$$\begin{aligned} \frac{1}{r_{pb}} &:= \frac{1}{\sqrt{(x-A(\theta))^2+(y-B(\theta))^2+(z-C(\theta))^2}} \\ &= \frac{1}{D(\theta)} \sum_{k\geq 0} \left(\frac{\rho}{D(\theta)}\right)^k P_k\left(\frac{A(\theta)x+B(\theta)y+C(\theta)z}{D(\theta)\rho}\right). \end{aligned}$$

Where P_k is the k-th Legendre polynomial, $\rho^2 = x^2+y^2+z^2$, $D(\theta)^2 = A(\theta)^2 + B(\theta)^2 + C(\theta)^2$. Using the well known recurrences for the Legendre polynomials one can compute the expansion $1/r_{pb} = \sum_k T_k(x,y,z,\theta)$ by using the recurrence

$$T_{k+1} = \frac{1}{D(\theta)}\left[\frac{2n+1}{n+1}(A(\theta)x+B(\theta)y+C(\theta)zT_k - \frac{n}{n+1}\rho^2 T_{k-1}\right].$$

with

$$T_0 = \frac{1}{D(\theta)}, \text{ and } T_1 = \frac{A(\theta)x+B(\theta)y+C(\theta)z}{D(\theta)^3}.$$

This approach is used in the autonomous case for a number of works [Ric80, JM99a] and adapted to the periodic case in [GJMS01, GJ01, And98].

1.5.2 Results

In Table 1.1 we display (a part of) the output of the program, i.e., the expansion, up to order 5 of a Hamiltonian function describing the motion in the centre manifold near L_1 in the BCP. Notice that this is a power expansion depending on four variables. Indeed, the hyperbolic variables have been eliminated setting them to zero as explained in Section 1.3.1. From now on, we name q_1, p_1, q_2 and p_2 the coordinates in the normal form. Notice that the second order is in Floquet normal form and the Hamiltonian is positive definite. In fact, the frequencies has been chosen to be close to the ones of the equilibrium point L_1 in the RTBP. To do so it has been required to select a suitable value for the complex logarithm of the monodromy matrix as explained in Remark 1.2.6.

With this procedure we have reduced a phase-space of seven dimensions (six in phase space and one in time) to a phase-space of four dimensions. To kill time dependence, we have to pay the price of dealing with small divisors, something that does not happen in the autonomous case. Notice that each periodic orbit with the same period as Sun in the BCP is seen in the centre manifold coordinates as a equilibrium point.

k	h_k	k	h_k
2 0 0 0	1.1649098180164408e+00	0 0 0 4	-1.0348782998835562e-01
0 2 0 0	1.1649098180164408e+00	5 0 0 0	1.0264782557981226e-02
0 0 2 0	1.1334757457923905e+00	4 1 0 0	3.7619428205357514e-10
0 0 0 2	1.1334757457923905e+00	3 2 0 0	-2.0054752043567642e-01
3 0 0 0	2.5693578279580818e-02	2 3 0 0	3.8876501349683572e-10
2 1 0 0	3.1702117420693472e-12	1 4 0 0	1.4559576772383684e-01
1 2 0 0	-4.9448428550932333e-01	0 5 0 0	-2.5423357823370180e-09
0 3 0 0	-1.7544012476322530e-12	3 0 2 0	2.0888453131734916e-02
1 0 2 0	-1.3766966842132522e-05	2 1 2 0	5.9597785080495011e-10
0 1 1 1	2.4889345211309699e-04	1 2 2 0	-1.2896984231151304e-01
1 0 0 2	-4.2633398428144847e-01	0 3 2 0	-3.2492259262120318e-10
0 1 0 2	-1.4922351924828205e-12	1 0 4 0	1.0175778627823241e-02
4 0 0 0	-1.5577863823260266e-02	0 1 4 0	4.2809850666393616e-10
3 1 0 0	-6.1616971706903765e-10	3 0 1 1	-1.0877606231885910e-10
2 2 0 0	2.8564148192576455e-01	2 1 1 1	-9.6120205208013051e-02
1 3 0 0	-2.8143619007744429e-09	1 2 1 1	-1.4890100416718836e-09
0 4 0 0	-1.4095686241715544e-01	0 3 1 1	7.4319820910869139e-02
2 0 2 0	-1.5182786740122127e-02	1 0 3 1	-3.9856569722432594e-10
1 1 2 0	-9.0811627840660254e-10	0 1 3 1	-1.6587385255867039e-02
0 2 2 0	9.8084945140029522e-02	3 0 0 2	-1.1007274890710875e-01
0 0 4 0	2.7349354108086033e-06	2 1 0 2	3.9233900939123978e-10
2 0 1 1	2.8699060120477501e-11	1 2 0 2	1.6954634125760315e-01
1 1 1 1	3.1360886696206763e-02	1 2 0 2	1.6954634125760315e-01
0 2 1 1	1.2488835674665644e-10	0 3 0 2	-4.7756409515958644e-09
0 0 3 1	4.6759744179628845e-11	1 0 2 2	-1.2491759136180372e-01
2 0 0 2	2.1511497160209828e-01	0 1 2 2	-3.8369989294752567e-10
1 1 0 2	-2.5269581613867271e-09	1 0 1 3	-1.2021379445008337e-09
0 2 0 2	-2.4159925248364317e-01	0 1 1 3	6.3802839325266036e-02
0 0 2 2	8.4829974514227080e-02	1 0 0 4	3.8098893935709088e-02
0 0 1 3	1.1863049638841200e-10	0 1 0 4	-2.2253462228317867e-09

Table 1.1: Expansion, up to order 5 of the centre manifold of L_1. The four integers in the first and third column are the exponents k_1, k_2, k_3 and k_4 that identify each monomial. The order of each monomial is given by $k_1 + k_2 + k_3 + k_4$. The first non-zero order is two.

We are dealing now with a two degrees of freedom Hamiltonian system. A standard strategy to visualize the dynamics of this kind of systems is to select a Poincaré spatial section and fix a level of energy to reduce the system to a family of Area Preserving Maps parametrized by the energy. We have considered, in fact, two different sections.

The first one is $\Sigma_h = \{q_2 = 0\}$, this corresponds, at linear order, to fix $z = 0$ in the synodical coordinates. We will name this section as the *horizontal* one. See, in Figure 1.1, a representation of the phase space in the horizontal section for the values of the normalized energy fixed at $h = 0.2, 0.5, 0.7$ and 0.9. The second section is $\Sigma_v = \{q_1 = 0\}$ and will be named *vertical* section. See in Figure 1.2, a representation of the phase space in the vertical section for the values of the normalized energy fixed at $h = 0.2, 0.5, 0.7$ and 0.9.

Let us explain Figures 1.1 and 1.2. As the Hamiltonian restricted to the centre manifold is positive definite at the origin, each level of energy defines a three dimensional compact set of the phase space. When these compact sets are intersected by Σ_h and Σ_v, we obtain a two dimensional section. The periodic orbit replacing L_1 is at the origin in the centre manifold coordinates, it is totally elliptic, and has zero energy. The fixed points of both figures correspond to periodic orbits and the invariant curves to two dimensional invariant tori. In particular, the process this two Figures capture is the pitchfork bifurcation (of periodic orbits) that lead to Halo orbits. Note that, in synodical coordinates, this corresponds to a pitchfork bifurcation of two dimensional invariant tori, giving rise to quasi-periodic Halo orbits.

In Figure 1.1 the regions of bounded motion are determined by the image through the change of planar Lyapunov tori (the dynamical replacement of the planar family of Lyapunov periodic orbits). The elliptic structure near the origin, fixed on the p_1 axis, corresponds to (the image of) the vertical family of invariant tori that replace the vertical family of Lyapunov periodic orbits. Figure 1.1 is a representation of a bifurcation of a family of two dimensional invariant tori. Of course, as the change of variables removes time dependence, this is seen in Figure 1.1 as a bifurcation of periodic orbits.

The translation of what we see, in Figure 1.1, (b), to synodic coordinates is a new bifurcating family of elliptic tori appearing from the boundary of the phase-space. These tori are the dynamical replacements of the Halo orbits. This Poincaré section, permits us to observe the three families of vertical invariant tori (periodic orbits in the plot) near the L_1 periodic orbit. However, to observe the bifurcation from the boundary of the plot can be a little bit misleading. In Figure 1.2, the phase space the centre manifold intersected with Σ_v the bifurcation can be seen much better. Here the roles of the vertical and horizontal families are switched. That is, at each plot of Figure 1.2, the boundary is determined by a vertical Lyapunov torus while the invariant structure at the origin of the plots is the planar Lyapunov family of tori. As we have said, is this manifold the one that undergoes into a pitchfork bifurcation leading to the family of Halo tori. In Figure 1.2 we can see the classical

figure eight associated to the Hamiltonian Pitchfork bifurcation.

Most of the motion occurring in both pictures is quasi-periodic. There is however, small gaps of chaotic motion that increase in size with the energy. This gaps are produced by the homoclinic trajectories associated to the planar family once it is turned into hyperbolic. These homoclinic trajectories do not coincide, they split in a very small angle. We will be concerned about the precision and accuracy of this representation in a moment, but let us first say some words on the comparison with the autonomous case. The centre manifold of L_1 in the RTBP shows a very similar picture, however, there the bifurcating one is a family of periodic orbits while here it is a family of two-dimensional quasi-periodic tori.

We also remind that killing time introduces small divisors in the centre manifold, that means that the divergence of the change is not as mild as in the autonomous case, see [LJ]. However not killing time would have the consequence of dealing with four dimensional symplectic maps and therefore, the representation appearing in Figures 1.1 and 1.2 would not be possible.

On performance and accuracy

In this section we are concerned with the accuracy of the obtained results. We give also some words on the performance of the software. Table 1.2 shows several computation times for the centre manifold. Let us point out that these benchmarks are performed with a large discretization, with 64 coefficients for each Fourier series. To compute the manifold up to order 8 takes less than a second. The computations of order 12, the ones we use to work with, take around 18 seconds.

Table 1.3 shows the estimation of the quantity q_N as explained in Section 1.4.4. We have picked up two points x_1, x_2, with $\|x_1\| = h$ and $\|x_2\| = h/2$. The value h is the distance at the origin and it is the left value, ranging from 0.2 to 0.9, at each column. Notice the good results of the test even if the distance to the origin is close to one unit. To perform this test we have kept the integration time at 0.1 units.

Figure 1.3 shows the accuracy of the centre manifold with respect to the distance to the origin (a) and with respect to the energy (b). The vertical axis, shows the $\log_{10}$ of the error. As it is to be expected, as the order of the expansion increases, the accuracy of of the representation is better. At distance one of the origin, all the discretizations seem, more or less, equally bad. Notice, however, that the error is still less that 10^{-4}. Panel (b) shows the same tendency.

Finally, Table 1.4 shows the estimation of the radius of convergence of the expansion with respect to the order. The estimations are done by means of the quantities r_1^n and r_2^n defined in Section 1.4.4. Notice that the data seem to show a mild divergence, as is to be expected.

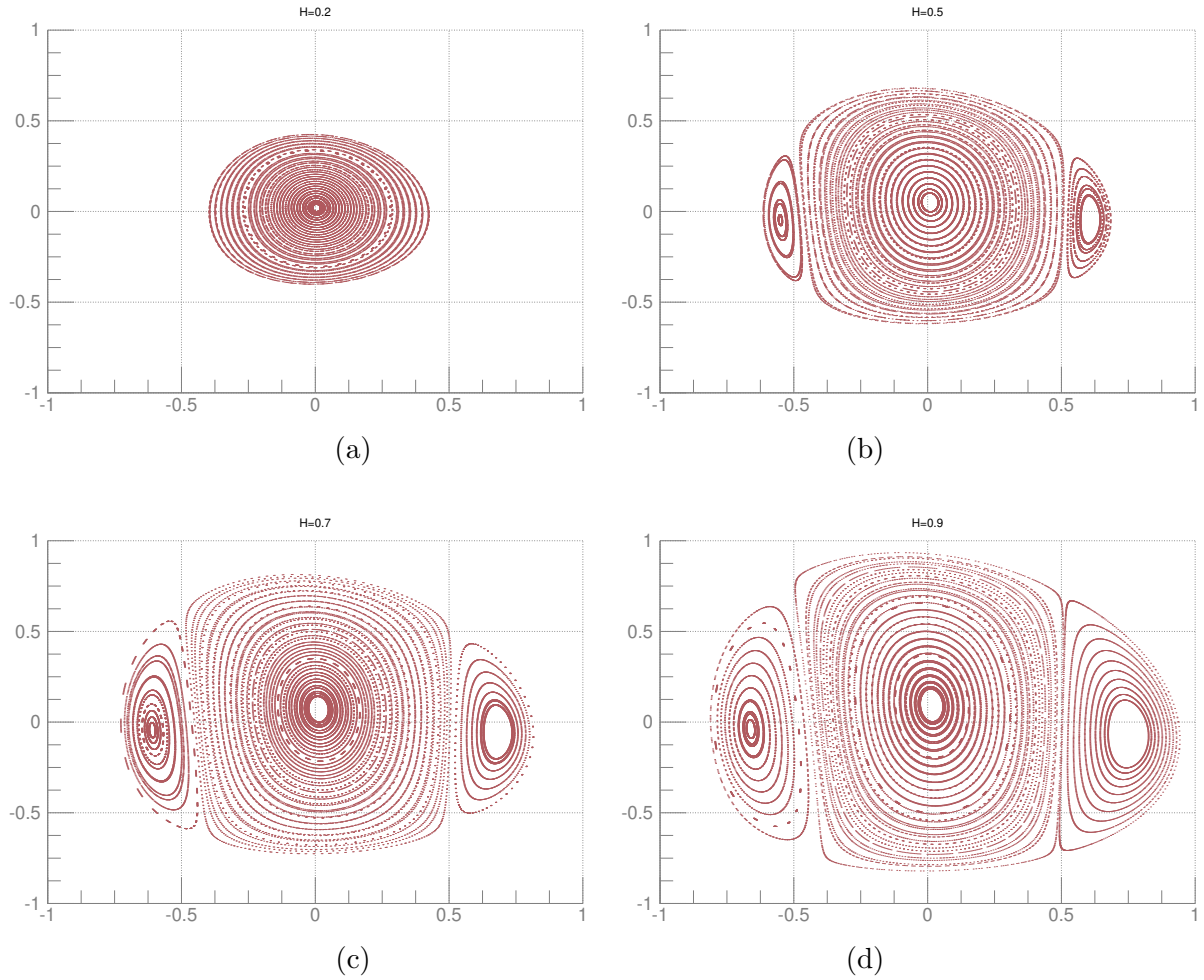

Figure 1.1: Horizontal section for the Centre Manifold of L_1. The expansion used for the Hamiltonian is of order 12. The planar plots are obtained fixing the energy h at 0.2, 0.5, 0.7 and 0.9. Horizontal axis: q_1. Verical axis: q_3. See text for more details.

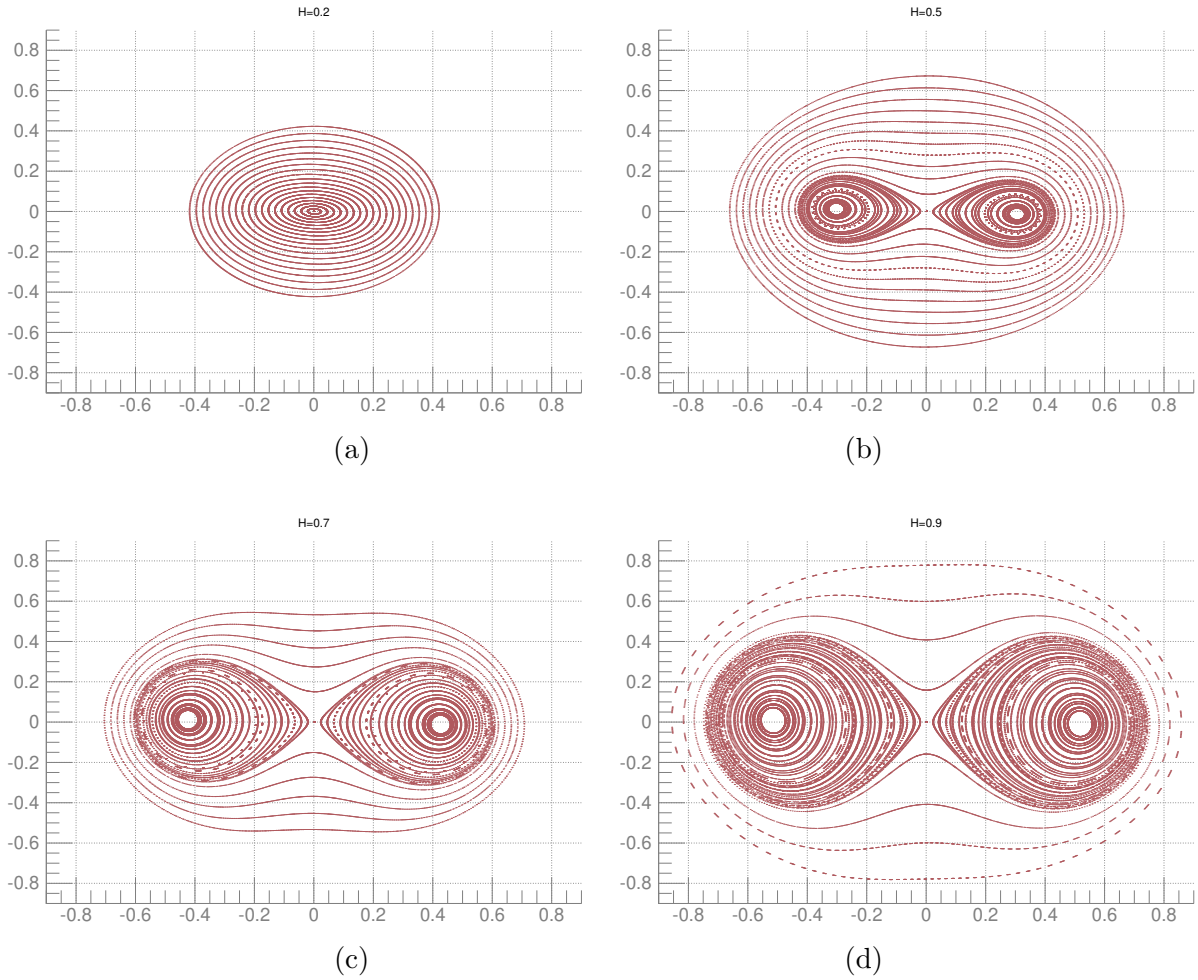

Figure 1.2: Vertical section for the Centre Manifold of L_1. The expansion used for the Hamiltonian is of order 12. The planar plots are obtained fixing the energy h at 0.2, 0.5, 0.7 and 0.9. Horizontal axis: q_2. Verical axis: q_4. See text for more details.

COMPUTATIONS WITH 64 FOURIER COEFFICIENTS.

ORDER CENTRE MANIFOLD	TIME
8	0m0.996s
10	0m4.574s
12	0m17.807s
16	2m51.168s
20	19m42.121s

Table 1.2: Computation time of the centre manifold for a periodic orbit discretized using 64 Fourier coefficients.

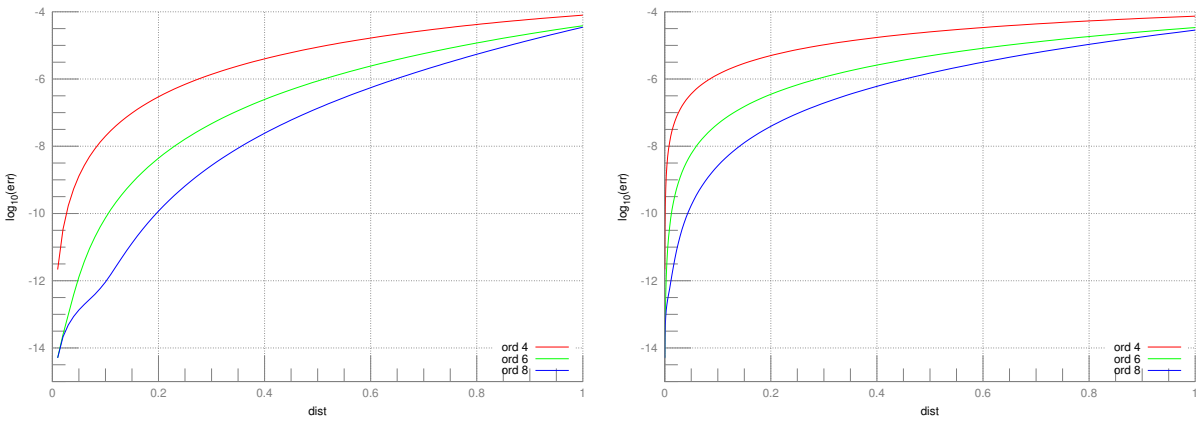

(a) (b)

Figure 1.3: Accuracy of the centre manifold of with respect the distance to the origin (a) and the energy (b). The vertical axis is the $\log_{10}$ of the error. The red curve stands for the expansion of order 4, the green for order 6 and the blue for order 8.

$N=4$		$N=6$		$N=8$	
0.200	3.83342	0.200	5.85911	0.200	7.71452
0.300	3.73735	0.300	5.78999	0.300	7.68591
0.400	3.62864	0.400	5.71815	0.400	7.66042
0.500	3.50490	0.500	5.64343	0.500	7.69628
0.600	3.3640	0.600	5.56486	0.600	7.80194
0.700	3.20490	0.700	5.48108	0.700	7.96387
0.800	3.02969	0.800	5.39039	0.800	8.15330
0.900	2.84785	0.900	5.29066	0.900	8.34003

Table 1.3: Test on the order of the expansion for orders $N = 4$, $N = 6$ and $N = 8$. From each column, the number on the left gives the distance to the origin and the one on the right, the result of the test. Notice that, in the first column, the results are close to 4, in the second close to 6 and, in the third, to 8.

N	r_1	r_2
5	8.001798275249360e-01	1.108223672025772e+00
6	8.953896643057171e-01	1.069526455563068e+00
7	8.949700211137991e-01	1.042645831174083e+00
8	1.024209844746597e+00	1.040323306083407e+00
9	1.085810670652100e+00	1.045281861705680e+00
10	9.256892069122457e-01	1.032658187980448e+00
11	1.021040232136258e+00	1.031596570022462e+00
12	1.321852391298590e+00	1.053131602771703e+00

Table 1.4: Radius of convergence of the centre manifold. The first column indicates the order of the expansion. The second and the third give the estimation of the radius of convergence by the quantities r_1^n and r_2^n.

"Never let your sense of morals prevent you from doing what is right."

Salvor Hardin

2

The parameterization method on Poincaré maps

Since the time of Poincaré, it has been known that invariant objects organize the long time behavior of dynamical systems. They are the skeleton of the dynamics and, hence, for a correct understanding of a concrete dynamical system it is required first to study its invariant objects. The research in dynamical systems concerns mostly with the existence and the properties of invariant manifolds. In order to have a complete picture, both theoretical and numerical approaches must be undertaken.

A standard tool to study continuous dynamical systems is the use of suitable Poincaré sections. They allow to decrease the dimension of the invariant objects (and of the phase space) by one which usually simplifies the use of analytical and numerical tools. One of the main difficulties when working with Poincaré maps is the lack of a closed expression for such a map, so that all the explicit computations have to be done by means of numerical integration of Ordinary Differential Equations.

The parametrization method is based on finding a suitable parametric form for the desired invariant object. For instance, for stable and unstable manifolds of a fixed point the manifold is usually represented as a (high order) Taylor expansion w.r.t. some parameter. The coefficients of this Taylor expansion are found by solving, order by order, a sequence of linear equations coming from the invariance equation satisfied by the manifold.

As the parametrization method deals with high order derivatives of the dynamical system

at hand, there is an extra difficulty in applying it to Poincaré maps. In this Chapter we focus on the effective computation of high order power expansions of stroboscopic maps (a special kind of Poincaré maps) with the final goal of computing high order approximation of stable/unstable manifolds of fixed points of the map (which corresponds to periodic orbits of the flow). We also require the process to be efficient enough so that extended precision arithmetic can be used if necessary.

This Chapter is structured as follows: First, in Section 2.1, we review a basic computational tool to produce high order expansions of flows: The *jet transport*. This technique is based in applying the so-called *automatic differentiation* technique to compute the solutions of high order variational equations of Ordinary Differential Equations. To address this, we review some basic facts on Automatic Differentiation and then we discuss jet transport. We also take our time to summarize the Taylor method, as it will be the integrator used in our implementation. The Taylor method stands out among other integrators when high accuracy is required.

In Section 2.2 we enumerate a number of known facts on stroboscopic maps of periodic time dependent Hamiltonians. This section is useful to provide a theoretical context for the rest of the Chapter, and several notions shall be used along the rest of this manuscript. We also discuss briefly several applications of high order expansions of stroboscopic maps to give some insight of the potential that the technology presented in this Chapter has.

Section 2.3 is devoted to the application of the parametrization method to the stable and unstable manifolds of fixed points. The discussion is adapted to our particular context. The analysis is oriented to the algorithmic point of view. This permits us to provide some remarks on the implementation.

In Section 2.4, we test our methodology in three specific examples. In the first one, we compute a high order parametrization of the unstable manifold related to the dynamical equivalent of the collinear point L_3 in the Bicircular Problem (recall that this model has already appeared in Chapter 1 and it is developed in Chapter 5). Notice that this computation has its own interest as it is a first step to understand how the centre-unstable manifold of L_3 drives the motion near the triangular points determining regions of effective stability near them. The second example deals with a periodically forced pendulum that can be regarded as a perturbation of the integrable pendulum. Because of the perturbing term, the system is no longer integrable so the separatrices intersect transversely. The angle between the manifolds determines *the splitting*. We set the values of the parameters so that the splitting is exponentially small. Then we use a high order approximation of the manifolds to compute the splitting. Notice that, as the splitting is exponentially small, the use of high accuracy arithmetic is essential. We also highlight the advantages of using high order approximations instead of the usual linear approximations to grow the manifold. The third example deals with the motion of an electron around an atomic core. The model is a soft Coulomb potential

perturbed with a (periodic) lased field. We avoid giving details on the model in this Chapter as it will be developed in Chapter 8 . This example is selected because requires multiple precision but not for the same reason as the perturbed pendulum. Indeed, we deal with a fixed point that have two unstable eigenvalues with modulus of different size. This situation is numerically challenging as the strong unstable direction attracts the dynamics leading to huge propagation of errors when computing the weak unstable manifold. This effect is softed at some distance of the fixed point, therefore, it is mandatory to compute high order approximations of the weak unstable manifold. We also compute the parametrization of the two dimensional unstable manifold, that is, the manifold which is tangent to the subspace spanned by the weak and strong unstable eigenvectors.

This is a joint work with N. Miguel and J. Gimeno.

2.1 Automatic differentiation and jet transport

Automatic differentiation is a computational tool to obtain (high order) derivatives of the output of an algorithm with respect to initial data and/or parameters [GC91, Gri00, Nau12]. Here we summarize the main ideas behind automatic differentiation.

2.1.1 A first example

Let us introduce automatic differentiation by means of a simple example: Assume we want to obtain the power expansion, up to a degree n, of

$$f(x_1, x_2) = \frac{x_1 x_2}{x_1 + x_2}, \tag{2.1}$$

at the point $(x_1, x_2) = (1, 2)$. Let us write $x_1 = 1 + s_1$, $x_2 = 2 + s_2$, where s_1 and s_2 are "symbols" (this means that they will be treated symbolically during the operations). Now, we evaluate $f(1 + s_1, 2 + s_2)$. Obviously, $x_1 x_2 = (1 + s_1)(2 + s_2) = 2 + 2s_1 + s_2 + s_1 s_2$ and $x_1 + x_2 = 3 + s_1 + s_2$. To obtain an expression for the quotient, we write

$$\frac{p_0 + p_1 + \cdots + p_n}{q_0 + q_1 + \cdots + q_n} = r_0 + r_1 + \cdots + r_n,$$

where p_i, q_i and r_i denote the terms of degree i. Then,

$$\sum_{i=0}^{n} p_i = \sum_{k=0}^{n} \left[\sum_{j=0}^{k} q_j r_{k-j} \right].$$

Note that this allows to express p_i as

$$p_i = q_0 r_i + \sum_{j=1}^{i} q_j r_{i-j},$$

and, therefore,

$$r_i = \frac{1}{q_0}\left[p_i - \sum_{j=1}^{i} q_j r_{i-j}\right]. \tag{2.2}$$

This is a recursive formula that allows to compute r_i in terms of p_i, q_0, ..., q_i, and r_0, ..., r_{i-1}. This recurrence is easily started noting that $r_0 = p_0/q_0$.

Applying this formula to example (2.1) up to degree 2, we obtain

$$f(1+s_1, 2+s_2) = \frac{2}{3} + \frac{4}{9}s_1 + \frac{1}{9}s_2 - \frac{4}{27}s_1^2 + \frac{4}{27}s_1 s_2 - \frac{1}{27}s_2^2 + O_3,$$

which is the power expansion, up to second degree, of f at the point $(1, 2)$. These ideas can be extended to the usual operations and functions done on the computations (square root, trigonometry, etc).

2.1.2 The arithmetic of formal series

The manipulation of formal power series goes back to L. Euler, a modern reference is, for instance, the book by D. Knuth [Knu98]. This means that, given an algorithm (defined by a sequence of mathematical formulas), we can replace its arithmetic of real numbers by a power series arithmetic and then, the same algorithm will produce not only the result but also its derivatives. In other words, given a computer program that outputs some results from some initial data, we can replace the floating point operations by operations with power series (truncated to a given degree and with floating point coefficients) to produce the power series of the result w.r.t. initial data and/or parameters. The arithmetic of power series has already been discussed in Chapter 1, there we focus on products and Poisson brackets. To make this Chapter self contained and fix some basic notation we recall the following definition.

Definition 2.1.1 (Formal series)**.** *A formal series in the variables $x = (x_1, \ldots, x_n)$ is an expression of the form:*

$$F(x) = \sum_{m=0}^{\infty} F_m, \qquad F_m = \sum_{|k|=m} F_{m,k} x^k,$$

where $F_{m,k} \in \mathbb{K}$ ($\mathbb{K}$ stands for $\mathbb{R}$ or $\mathbb{C}$). Here $k = (k_1, \ldots, k_n) \in (\mathbb{N} \cup \{0\})^n$, $|k| = k_1 + \cdots + k_n$ and $x^k = x_1^{k_1} \cdot \ldots \cdot x_n^{k_n}$.

The arithmetic of formal series is defined in the usual way. For instance, the product of two formal series is defined by means of the standard formula

$$F(x) \cdot G(x) = \sum_{m=0}^{\infty} \sum_{l=0}^{m} F_l G_{k-l}.$$

We note that the products $F_l G_{k-l}$ are products of homogeneous polynomials. This is the operation that has been discussed in Chapter 1.

The rest of usual elementary operations have similar formulae as the product and the sum. To implement all these recurrences we have to perform multiplications between homogeneous polynomials, therefore the efficiency of the arithmetic of formal series is based in the product to compute homogeneous polynomials.

There are several standard applications of automatic differentiation. Here we discuss a couple of them. First we summarize briefly the Taylor method for the computation of solutions of Ordinary Differential Equations and, after that, we concern on the so-called jet transport technique. There are, however, other context in which this technology can be applied as well. For instance, automatic differentiation can be used to obtain high order expansions Hamiltonian functions avoiding to implement recursive formulas as we have explained in Chapter 1.

2.1.3 Jet transport

In this Chapter we apply these ideas to the computation of the Poincaré map of a flow. As the numerical integration can be seen as the iteration of a sequence of mathematical expressions, we can replace the computer arithmetic by a truncated power series arithmetic. This can be done regardless of the numerical integrator used (Runge-Kutta, Taylor, etc). The use of automatic differentiation w.r.t. initial data (and/or parameters) of a ODE is what we called jet transport. Note that this can be viewed as an extension of the phase space to propagate, in addition to points, the derivatives of the flow. As the set of derivatives of a function on a point is sometimes called the jet of derivatives of the function at this point, we refer to this technique as "jet transport" ([AFJ+08, JPN10]).

The Taylor method

Consider the initial value problem

$$\left\{ \begin{array}{rcl} x'(t) & = & f(t, x(t)), \\ x(a) & = & x_0, \end{array} \right. \tag{2.3}$$

where f is assumed to be analytic on its domain of definition, and that $x(t)$ is assumed to be defined for $t \in [a, b]$. We are interested in approximating the function $x(t)$ on $[a, b]$. The idea of the Taylor method is very simple: given the initial condition $x(t_0) = x_0$ ($t_0 = a$), the value $x(t_0 + h_0)$ is approximated from the Taylor series of the solution $x(t)$ at $t = t_0$,

$$\begin{aligned} x_0 &= x(t = 0), \\ x_{m+1} &= x_m + x'(t_m)h_m + \frac{x''(t_m)}{2!}h_m^2 + \cdots + \frac{x^{(p)}(t_m)}{p!}h_m^p, \quad m = 0, \ldots, M-1, \end{aligned} \tag{2.4}$$

where $t_{m+1} = t_m + h_m$, $h_m > 0$ and $t_M = b$.

For a practical implementation one needs an effective method to compute the values of the derivatives $x^{(j)}(t_m)$. A first procedure to obtain them is to differentiate the first equation in (2.3) w.r.t. t, at the point $t = t_m$. Hence,

$$x'(t_m) = f(t_m, x(t_m)), \quad x''(t_m) = f_t(t_m, x(t_m)) + f_x(t_m, x(t_m))x'(t_m),$$

and so on. Therefore, the first step to apply this method is, for a given f, to compute these derivatives up to a suitable order. Then, for each step of the integration (see (2.4)), we have to evaluate these expressions to obtain the coefficients of the power series of $x(t)$ at $t = t_m$. Usually, these expressions will be very cumbersome, so it will take a significant amount of time to evaluate them numerically. This, jointly with the initial effort to compute the derivatives of f, is the main drawback of this approach for the Taylor method.

This difficulty can be overcome by means of the so-called *automatic differentiation* (see [BKSF59], [Wen64], [Moo66], [Ral81], [GC91], [BCCG92], [BBCG96], [Gri00]). This is a procedure that allows for a fast evaluation of the derivatives of a given function, up to arbitrarily high orders. As far as we know, these ideas were first used in Celestial Mechanics problems ([Ste56], [Ste57]; see also [Bro71]).

We note that the algorithm to compute these derivatives by automatic differentiation has to be coded separately for different systems. This coding can be either done by a human (see, for instance, [Bro71] for an example with the N-body problem) or by another program (see [BKSF59, Gib60, CC94, JZ05b] for general-purpose computer programs). An alternative procedure to apply the Taylor method can be found in [SV87] and [IS90]. We can also find some public domain software to generate numerical integrators of ODEs using Taylor methods:

- `ATOMFT`, `http://www.eng.mu.edu/corlissg/FtpStuff/Atom3_11/`. ATOMFT is written in Fortran 77 and it reads Fortran-like statements of the system of ODEs and writes a Fortran 77 program that is run to solve numerically the system using Taylor series.

- `taylor`. It can be obtained from `http://www.maia.ub.es/~angel/taylor/`. It reads a file with a system of ODEs and it outputs a time-stepper for it (in C/C++), with

automatic selection of order and step size. Several extended precision arithmetics are supported.

There is also a public domain package for automatic differentiation, ADOL-C, included as an option in many Linux distributions (home page: `http://www.math.tu-dresden.de/~adol-c/`). It facilitates the evaluation of first and higher derivatives of vector functions that are defined by computer programs written in C or C++.

There are several papers that focus on computer implementations of the Taylor method in different contexts; see, for instance, [BWZ70], [CC82], [CC94] and [Hoe01]. A good survey is [NJC99] (see also [Cor95]).

Elementary operations for the one-dimensional case

As it has been mentioned before, automatic differentiation is a recursive procedure to compute the value of the derivatives of certain functions at a given point (relevant references are [Moo66, Ral81, Gri00]). The functions considered are those that can be obtained by sum, product, quotient, and composition of elementary functions (elementary functions include polynomials, trigonometric functions, real powers, exponentials and logarithms). We note that the vector fields used in Celestial Mechanics and Astrodynamics belong to this category. Other functions can be considered as elementary if they are defined as the solution of some differential equation whose coefficients are previously known to be elementary functions. A notorious case of a non-elementary function is $\Gamma(x)$. A celebrated theorem of Hölder states that Γ does not satisfy any algebraic differential equation whose coefficients are rational functions.

Assume that a is a real function of a real variable t.

Definition 2.1.2. *The normalized j-th derivative of a at the point t is*

$$a^{[j]}(t) = \frac{1}{j!} a^{(j)}(t).$$

Assume now that $a(t) = F(b(t), c(t))$ and that we know the values $b^{[j]}(t)$ and $c^{[j]}(t)$, $j = 0, \ldots, n$, for a given t. The next proposition gives the n-th derivative of a at t for some functions F.

Proposition 2.1.3. *If the functions b and c are of class C^n, and $\alpha \in \mathbb{R} \setminus \{0\}$, we have*

1. *If $a(t) = b(t) \pm c(t)$, then $a^{[n]}(t) = b^{[n]}(t) \pm c^{[n]}(t)$.*
2. *If $a(t) = b(t)c(t)$, then $a^{[n]}(t) = \sum_{j=0}^{n} b^{[n-j]}(t) c^{[j]}(t)$.*

3. *If* $a(t) = \dfrac{b(t)}{c(t)}$, *then* $a^{[n]}(t) = \dfrac{1}{c^{[0]}(t)}\left[b^{[n]}(t) - \displaystyle\sum_{j=1}^{n} c^{[j]}(t)a^{[n-j]}(t)\right]$.

4. *If* $a(t) = b(t)^{\alpha}$, *then* $a^{[n]}(t) = \dfrac{1}{nb^{[0]}(t)} \displaystyle\sum_{j=0}^{n-1} ((n-j)\alpha - j)\, b^{[n-j]}(t)a^{[j]}(t)$.

5. *If* $a(t) = e^{b(t)}$, *then* $a^{[n]}(t) = \dfrac{1}{n} \displaystyle\sum_{j=0}^{n-1} (n-j)\, a^{[j]}(t)b^{[n-j]}(t)$.

6. *If* $a(t) = \ln b(t)$, *then* $a^{[n]}(t) = \dfrac{1}{b^{[0]}(t)}\left[b^{[n]}(t) - \dfrac{1}{n}\displaystyle\sum_{j=1}^{n-1}(n-j)b^{[j]}(t)a^{[n-j]}(t)\right]$.

7. *If* $a(t) = \cos c(t)$ *and* $b(t) = \sin c(t)$, *then*

$$a^{[n]}(t) = -\frac{1}{n}\sum_{j=1}^{n} jb^{[n-j]}(t)c^{[j]}(t), \quad b^{[n]}(t) = \frac{1}{n}\sum_{j=1}^{n} ja^{[n-j]}(t)c^{[j]}(t).$$

It is possible to derive similar formulas for other functions, like inverse trigonometric functions.

We note that the number of arithmetic operations to evaluate the normalized derivatives of a function up to order n is $O(n^2)$. We will come back to this point later on.

Estimation of order and step size

There are several possibilities to estimate an order and step size for the Taylor method. When Taylor is used in a non-validated way, these estimates come from the asymptotic behaviour of the error. The following result can be found in [Sim01].

Proposition 2.1.4. *Assume that the function* $z \mapsto x(t_m + z)$ *is analytic on a disk of radius* ρ_m. *Let* A_m *be a positive constant such that*

$$|x_m^{[j]}| \leq \frac{A_m}{\rho_m^j}, \qquad \forall\, j \in \mathbb{N}, \tag{2.5}$$

and assume that the dominant part in the computational cost is proportional to the square of the order up to which the Taylor series is computed. Then, if the required accuracy ε *tends to 0, the values of* h_m *(local step) and* p_m *(local order) that give the required accuracy and minimize the global number of operations tend to*

$$h_m = \frac{\rho_m}{e^2} \quad \text{and} \quad p_m = -\frac{1}{2}\ln\left(\frac{\varepsilon}{A_m}\right) - 1. \tag{2.6}$$

Note that the optimal step size does not depend on the level of accuracy. The optimal order is, in fact, the order that guarantees the required precision once the step size has been selected.

It is important to note that the values (2.6) are optimal only when the bound (2.5) cannot be improved. If the value A_m can be reduced –or if the function $x(t)$ is entire– the previous values are not optimal in the sense that a larger h_m and/or a smaller p_m could still deliver the required accuracy.

Extended precision

In some situations, extended precision for the coefficients is needed. The are several floating point arithmetics with extended precision. Among them, we have chosen MPRF. Note that changing the basic arithmetic of a numerical integrator can lead you to a very intensive computational problem: As example, assume that you are using a Runge-Kutta with an error of h^8 (h denotes the stepsize), which means that to achieve an accuracy of 10^{-16} you need an stepsize of $h = 10^{-2}$. If we use an arithmetic of 64 digits, and we want an error of 10^{-64}, the step size has to be $h = 10^{-8}$. This means that the number of steps of Runge-Kutta is increased by a factor 10^6. For this reason we prefer to use the Taylor method. If a Taylor method of order n has an error of h^n, to go from an error of 10^{-16} to 10^{-64} we can change the order of the method, from order 8 to order 32. The number of operations of a step of Taylor method is $O(n^2)$. So, going from order 8 to 32 increase the number of operations by a factor of 16. Due to this behaviour, Taylor method is the best option to integrate an ODE with extended accuracy. The Taylor method has to be modified so that its basic arithmetic is not numbers but polynomials (jets). To this end, we have used an experimental version of the Taylor package by M. Zou and A. Jorba (not yet in the public domain). The arithmetic of polynomials with MPFR coefficients has been coded specifically to maximize efficiency. Whith these tools, is not difficult to produce highly accurate power expansions of Poincaré maps.

2.2 Stroboscopic maps of Periodic Hamiltonians

This thesis concerns with periodic time dependent Hamiltonian systems. These systems are the simplest examples of non-autonomous system, as the time can be regarded as an additional angular coordinate. This is why periodic Hamiltonians of n degrees of freedom are usually refereed as systems of n and a half degrees of freedom. A standard tool to tackle periodic time-dependent systems is the so-called Stroboscopic map:

Definition 2.2.1 (Stroboscopic map)**.** *Let $A \subset \mathbb{R}^n$ be an open set and $f : \mathbb{R} \times A \mapsto \mathbb{R}^n$, a differentiable function such that $f(t + T, x) = f(t, x)$ for all $x \in A$ for some minimal $T > 0$.*

Consider the following Cauchy Problem:

$$\begin{cases} \dot{x} = f(t, x), \\ x(t_0) = x_0. \end{cases} \tag{2.7}$$

Name $\varphi(t; t_0, x_0)$ the solution that, at time t_0 passes through x_0 evaluated at time t. We define the ***stroboscopic map*** *$P : A \mapsto \mathbb{R}^n$ as $P(x) = \varphi(T; 0, x)$.*

Stroboscopic maps are the simplest kind of Poincaré maps, as the section is temporal, fixed and can be used to reduce the dimension of the whole phase-space by one. In periodic systems, there are no equilibrium points, the simplest invariant objects are the periodic orbits with the same period as the vector-field. Moreover, if γ is a periodic orbit of (2.7) with period T', then $T' = mT$ for $m \in \mathbb{N} \setminus \{0\}$. Let us name minimal periodic orbits the orbits with period T. Minimal periodic orbits are fixed points of the stroboscopic map P, orbits whose period is a m-multiple of T are periodic points of period m.

The notion of stroboscopic map can be extended for vectorfields that depend on time in a quasi-periodic way. In this case, the dynamics of the map has two components: A part of the dynamics is an irrational rigid rotation taking place on a torus (the basis), the other part takes place on A (the bundle). These systems are called **quasi-periodic skew-products** and will be considered later in this Thesis.

If the vector-field is induced by a Hamiltonian function of m and a half degrees of freedom ($2m = n$), then the stroboscopic map is a **symplectic map**, i.e. for each $z \in A$, the linearization of the map around z, $Df(z)$, verifies the following $Df(z)^t J Df(z) = J$, where

$$J = \begin{bmatrix} -I_m & 0 \\ 0 & I_m \end{bmatrix}$$

and I_m is the identity matrix of $\mathbb{R}^m$. This condition implies a number of interesting properties: symplectic mappings are volume preserving, i.e. $\det(Df(z)) = 1$. The converse is only true if $m = 1$. The spectrum of a symplectic matrix is also tied by certain constrictions. In first place, if λ belongs to the spectrum of a symplectic matrix, then λ^{-1} also does it. Moreover, each generic pair (λ, λ^{-1}) can be classified in the following stability types:

1. If λ has modulus different than one and it is real, the pair is said to be of hyperbolic (saddle) type.

2. If $\lambda = e^{2i\rho}$, the pair is said to be of elliptic type.

3. If λ is complex and its modulus is different from one, it is part of a **Krein quartet** $(\lambda, \lambda^{-1}, \bar{\lambda}, \bar{\lambda}^{-1})$. The quartet is said to be of complex saddle type.

If the matrix $Df(z_0)^{j_0} - I_n$ is not invertible, for some $j_0 \in \mathbb{N}$, we say that z_0 is a bifurcating point. These points are not generic but appear when the system depends on parameters. The bifurcating points represent transitions between different stability types. Let us think that the eigenvalues are moving with respect some parameter. In absence of degeneracies in higher order terms we have the following description:

1. **Saddle-Centre bifurcation:** A pair of elliptic eigenvalues meet at $\lambda = \lambda^{-1} = 1$, then, they abandon the unit circle along the real line. One of the eigenvalues starts being less than one and the other larger, both positive. In this case, the pair goes from elliptic type to hyperbolic. The opposite situation can happen as well, that is, two eigenvalues abandoning the real line and entering the unit circle through 1.

2. **Period Doubling bifurcation:** A pair of elliptic eigenvalues meet at $\lambda = \lambda^{-1} = -1$, then, they abandon the unit circle along the real line. One of the eigenvalues starts being less than minus one and the other larger, both negative. In this case, the pair goes from elliptic type to hyperbolic and two families of two-periodic elliptic points emerge from the collision. The opposite situation in which two families of doubled period merge with a family of fixed points and the last gains elliptic character is named period halving bifurcation.

3. **Krein Collision:** Two pair of elliptic eigenvalues meet at $\lambda = \lambda^{-1} = \bar{\lambda} = \bar{\lambda}^{-1} = e^{i\alpha}$, then all the eigenvalues get expelled from the unit circle. This has more complicated consequences. In the first place, the fixed point, after the bifurcation has 2D complex unstable and stable manifold. Then, depending on arithmetical properties of ρ it grows a family of q-period points (if $\alpha = \frac{p}{q} \in \mathbb{Q}$) or a family of invariant curves (if $\alpha \notin \mathbb{Q}$). There are several aspects of this bifurcation that depend on higher order terms.

Some aspects of the dynamics around the fixed points can be infered from its linear character. Under generic conditions, from the fixed point and along each plane associated to an elliptic pair, it grows a Cantorian family of invariant curves whose frequency tends to the (linear) frequency ρ of the pair. This result can be regarded as the discrete version of the Lyapunov Theorem for elliptic equilibria for autonomous Hamiltonian systems. In fact, more can be said: The nonlinear coupling of two different elliptic direction results in a Cantorian family of $2D$ invariant tori. If the point is totally elliptic, the nonlinear coupling of all the elliptic directions produces a set of maximal dimension of KAM tori that is what is expected around a totally elliptic fixed point.

This Chapter is concerned with the hyperbolic directions of fixed points. Under generic conditions, from the fixed point and along each hyperbolic direction it grows an unstable (along the eigendirection related with the eigenvalue with modulus larger than one) and a stable (along the eigendirection related with the eigenvalue with modulus smaller than one)

invariant manifolds. This case will be considered in the next section. The same ideas can be used to deal with fixed points of type complex saddle. We have performed no computations for this last case but the same tools can be applied to achieve high order expansions of these objects[1].

2.2.1 High order expansions of stroboscopic maps

As we have mentioned before, jet transport allows to compute high order expansions of Poincaré maps (in particular, stroboscopic maps). The idea is to replace the standard floating point arithmetic of the computer for an arithmetic of polynomials. One of the most useful applications of this technique is the computation of the variational flow. Indeed, to obtain the variational equations for some systems can be tedious in some cases. By means of jet transport we can use an arithemtic of polynomials of degree 1 to obtain the partial derivatives of the stroboscopic map at a given point. In the same way, given some concrete values for the parameters, we can also obtain the derivatives of the stroboscopic map with respect to the parameters. This technique has been used widely in this thesis when computing continuations curves of fixed points.

Let us give some words on other type of computations that could be performed using these ideas. Bifurcation analysis on stroboscopic maps can be approached from this point of view as well. Normal forms around periodic orbits, to with it is concerned Chapter 1, can be performed as well directly in the stroboscopic map. Notice that, in this case, there is no need to compute the Floquet Change of variables as, in this case, the map is already autonomous. The advantages of using jet transport for this kind of computations will be clear in the following subsection.

Remark 2.2.2. *To compute (high order) derivatives of a Poincaré map defined by a spatial section is much more involved since the time needed to return to the section depends on the initial point.*

2.2.2 On the composition of power series

One option to work with Poincaré maps around a given fixed point could be to compute the power expansion of the map at the fixed point and then to work with this expansion. The main inconvenient of this approach appears if we need to compose this expansion with another power expansion, since this requires a very large number of operations.

A more efficient alternative is the following: Let P denote the Poincaré map, and assume we want to compute $P(x(s))$, where $x(s)$ is a (truncated) power series w.r.t. some parameters

[1] We expect to follow this direction in the near future

s. Then, it is not difficult to see that the power expansion of $P(x(s))$ can be obtained with the same numerical integration used to expand P but using as initial data $x(s)$ (recall that to expand P we used $x_0 + s$ as initial data).

2.3 The parametrization method

This method was already used for numerical computations in the 80's by C. Simó (see also [FR81]), but it is remarkable that is also an excellent tool to prove the existence of invariant manifolds, as shown by X. Cabré, E. Fontich and R. de la Llave [CFdlL05b]. Here we simply summarize the method from an algorithmic point of view. A very good exposition of the method can be found in the book [HCL+16]. In order to fix ideas and notations, we remind the following well known result:

Theorem 2.3.1 (Stable and unstable manifolds)**.** *Let $A \subset \mathbb{R}^{2n}$ be an open set and $P \in \mathcal{C}^\omega(A, P(A))$ a symplectic diffeomorphism. Assume the following hypotheses to be fulfilled:*

1. *There exists a fixed point $z_0 \in A$, that is $P(z_0) = z_0$,*
2. *there exist a decomposition $\mathbb{R}^n = \Lambda_u \bigoplus \Lambda_c \bigoplus \Lambda_s$, where $dim(\Lambda_u) = dim(\Lambda_s) = d$, and a linear change of variables for which the linear system induced by $DP(z_0)$ reads as*

$$\begin{pmatrix} u \\ c \\ s \end{pmatrix} \longmapsto \begin{pmatrix} Uu \\ Cc \\ Ss \end{pmatrix},$$

   where $u \in \Lambda_u$, $c \in \Lambda_c$, $s \in \Lambda_s$, $U, S \in \mathrm{GL}_d(\mathbb{R})$ are diagonal matrices such that $[\rho(U)]^{-1}$, $\rho(S) < 1$ and $\mathrm{Spec}(C) \subset \mathbb{S}^1 := \{\zeta \in \mathbb{C} \mid |z| = 1\}$,
3. *defining $\mathrm{diag}(U) = (\lambda_1^u, \ldots, \lambda_d^u) =: \lambda_u$, $\mathrm{diag}(S) = (\lambda_1^s, \ldots, \lambda_d^s) =: \lambda_s$, the relations $\lambda_u^{k_1} - 1 = 0$ and $\lambda_s^{k_2} - 1 = 0$, $k_1,\ k_2 \in \mathbb{Z}^d$, hold only for $k_1 = k_2 = 0$.*

Then, there exit $\mathcal{C}^\omega$ maps $K_u : \bar{\Lambda}_u \mapsto \mathbb{R}^n$, $K_s : \bar{\Lambda}_s \mapsto \mathbb{R}^n$, $\bar{\Lambda}_u \subset \Lambda_u$, $\bar{\Lambda}_s \subset \Lambda_s$, such that:

1. *$K_u(z_0) = K_s(z_0) = z_0$,*
2. *K_u and K_s satisfy the following invariance equations:*

$$P \circ K_u = K_u \circ U,$$
$$P \circ K_s = K_s \circ S.$$

In particular $K_u(\bar{\Lambda}_u)$ and $K_s(\bar{\Lambda}_u)$ are invariant under the dynamics of P and tangent to U and S (respectively) at z_0.

Remark 2.3.2. *The case of the centre manifold is not considered in this Chapter. We provide an alternative approach in Chapter 1.*

Remark 2.3.3. *Notice that the manifolds henerits the smoothness of the map P. We assumed P to be analytic but the same hold for infinite or finite differentiability. For general maps, the smoothness hypothesis can be relaxed to Lipzchizd conditions. However we require analyticiy because it is necessary in the further discussion.*

Remark 2.3.4. *The third assumption is called non-resonance condition, see also Chapter 1. If it is not satisfied, the regularity of the manifold is affected. In fact, the order of the resonance determines the number of derivatives the invariant manifold has at the fixed point.*

2.3.1 Discussion of the method

Let us discuss how to compute the parametrization of the unstable invariant manifold (from now on K) by means of the parametrization method. The stable manifold can be computed similarly replacing P by P^{-1}, as we are dealing with stroboscopic maps, the inverse mapping cap be obtained integrating the differential equation backwards. The main idea of the method is to set a formal series for the manifold, plug it into the in variance equation and solve it order by order. Notice that, if we find a series converging to the parametrization K, this will be unique up to scaling. Let us assume, formally, that the parametrization is given by

$$K(u) = \sum_{k=0}^{\infty} A_k.$$

We recall that $u = (u_1, \dots, u_d) \in \bar{\Lambda}_u$, $k \in \mathbb{Z}^d$, $|k| = k_1 + \cdots + k_d$ and $u^j = u_1^{k_1} \cdot \ldots \cdot u_d^{k_d}$. Note also that

$$A_k = \sum_{|j|=k} a_j \; u^j$$

and $a_j \; u^j$ are the different monomials of degree $|j| = k$. The invariance equation is

$$P \circ K = K \circ U.$$

It is to be solved, order by order, recursively. The order 0 is fixed by the coordinates of the fixed point z_0. The first order has the form $A_1 = a_1^1 u_1 + \cdots + a_d^1 u_d$. Let $\{e_j^u\}_{j \le d}$ be a basis of Λ_d, then we can select $a_j^1 \in \text{span}(e_j^u)$. In this case,

$$\begin{aligned} P \circ A_1 u &= DP(z_0) a_1^1 u_1 + \cdots + DP(z_0) a_d^1 u_d + \mathcal{R}_{\ge 2} \\ &= U A_1 u + \mathcal{R}_{\ge 2}, \end{aligned}$$

were $\mathcal{R}_{\geq 2}$ is some reminder of higher order. This choice, therefore, verifies the invariance equation at first order. It follows that we have some freedom to choose the first order of the parametrization. This freedom can be used to find well behaving truncated series from the numerical point of view. This shall be discussed with more detail later. Now we proceed to solve the invariance equation recursively, order by order. Assume we have computed the coefficients of A_j up to order k. Then, for l such that $|l| = k+1$ is given by

$$\big(DP(z_0) - \lambda_u^l I_n\big) a_l = -b_l,$$

where

$$A_{k+1} = \sum_{|l|=k+1} a_l \; u^l$$

is a the homogeneous polynomial of degree $k+1$ that provides we are looking for. The polynomial B_{k+1} is the term of order $k+1$ in the evaluation of the parametrization up to order k (already known) by the stroboscopic map:

$$P_{\leq k+1}\big(K_{\leq k}(u)\big) = \sum_{|j|=0}^{k} B_j u^j + \sum_{|j|=k+1} b_j u^j.$$

The jet transport technique is applied to perform this last operation, as we discussed in Section 2.2.2. From the computational point of view, this is, by far, the most expensive operation.

Remark 2.3.5. *After the last discussion it is straightforward to draw a sketch of the proof of Theorem 2.3.1. Indeed, the hypotheses on the eigenvalues of $Df(z_0)$ assure the matrix $DP(z_0) - \lambda_u^{k+1} I_n$ to be invertible for each k. The analyticity of P provides a suitable decay of the coefficients of B_{k+1} and this is transferred to A_k. The convergence of the series gives the parametrization of the manifold.*

2.3.2 Further discussion for the one dimensional case

Let us face some numerical aspects on the implementation of the parametrization method. To do so, we focus in the case in which we want to compute one dimensional invariant manifolds. Let us name $\lambda \in \operatorname{Spec} Df(z_0)$, with $|\lambda| > 1$. The parametrization is given by

$$K(u) = \sum_{k=0}^{\infty} a_k u^k,$$

where $a_k \in \mathbb{R}^n$ is given by the recursive formula

$$\big(DP(z_0) - \lambda_u^{k+1} I_n\big) a_k = -b_{k+1}.$$

The non-uniqueness of the expansion is due to the freedom we have in choosing the linear part. In this case, any eigenvector of eigenvalue λ can be selected for a_1. Let us define a new expansion

$$\tilde{K}(u) = \sum_{k=0}^{\infty} \tilde{a}_{k+1} u^k,$$

where $\tilde{a}_k = \alpha^k a_k$ for some $\alpha > 0$. Then,

$$P_{\leq k+1}\big(\tilde{K}_{\leq k}(u)\big) = \sum_{j=0}^{k+1} b_j (\alpha u)^j = \sum_{j=0}^{k+1} \tilde{b}_j u^j.$$

The new set of coefficients verify the recurrent formula

$$\big(DP(z_0) - \lambda_u^{k+1} I_n\big)\tilde{a}_k = -\tilde{b}_{k+1}$$

and, therefore, provide another solution of the invariance equation. The expansion of the parametrization K is unique up to the choice of the linear term. The value α provides an scaling of the series. Notice that this can be used to obtain series with better decay and, consequently, a larger radius of convergence.

Parallel shooting

There is another obstacle that can appear when dealing with stroboscopic maps: if the orbit is very unstable, the hyperbolic direction may lead to a huge error propagation. As we already mentioned, we can handle large errors with high precision arithmetics. However, there is another tool that can be used to avoid this problem: the parallel shooting. The idea behind parallel shooting is to enlarge the dimension of the system in order to decrease the time of integration. Let us denote by $\varphi_{t_0}^{t_f}(x) := \varphi(t_f; t_0, x)$ the solution of the differential equation with initial condition (t_0, x) evaluated at time t_f. Fix $k \in \mathbb{N}$, the number of sections, and set $h = T/k$. For $i = 0, \dots k$, we define $\tau_i = ih$. If $m = nk$, we define the function $F : \mathcal{V} \mapsto \mathbb{R}^m$

$$F : \begin{pmatrix} x_1 \\ x_2 \\ \vdots \\ x_k \end{pmatrix} \mapsto \begin{pmatrix} f_k(x_k) \\ f_1(x_1) \\ \vdots \\ f_{k-1}(x_{k-1}) \end{pmatrix}.$$

Here $\mathcal{V} = \mathcal{A}^k$ is an open set of $\mathbb{R}^m$, and, for $x \in A$, $f_j(x) = \varphi_{\tau_{j-1}}^{\tau_j}(x)$. The differential map DF is given by

$$DF = \begin{pmatrix} 0 & \dots & \dots & Df_k \\ Df_1 & \dots & \dots & \vdots \\ \vdots & \dots & \dots & \vdots \\ 0 & \dots & Df_{k-1} & 0 \end{pmatrix}.$$

For $\bar{x} \in \mathcal{U}$, name $y = (x_1, \dots, x_k)$ where $x_1 = \bar{x}$ and $x_j = f_j(x_{j-1})$ if $1 < j \leq k$. Then:

1. y is a fixed point of F if and only if $\bar{x}$ is a fixed point of f.
2. The duple $(\zeta, v = (v_1, \dots, v_k))$, $\zeta \in \mathbb{C}$ and $v_k \in \mathbb{C}^n$ is a pair eigenvalue/eigenvector of $DF(y)$ if and only if (ζ^k, v_1) is a pair eigenvalue/eigenvector of $Df(\bar{x})$.
3. The projection to the first coordinate of the invariant manifold of F related to ζ coincides with the invariant manifold of f related to $\zeta^k = \lambda$.

Numerical extension of invariant manifolds

Let us suppose that we have an approximation $K : U \mapsto \mathbb{R}^{2n}$, $K(z_0) = z_0$ of some one dimensional invariant manifold related to an unstable eigenvalue λ of a fixed point z_0. This parametrization has a local validity. Obviously, the range of validity depends on the degree of the approximation. Generally, we are interested in the global properties of the manifolds. Let us explain how to expand numerically the approximation so our goal of global knowledge can be fulfilled. The following method is explained in more deeply in [Sim90].

- In first place, we have to seek for an interval $\mathcal{I}$ for which we trust our parametrization. Let us set $s_i = i * m^{-1}$. Here m is some (not too large) integer number. Then, select

  $$s_0 = \max_i \{\|P(K(s_i) - K(\lambda s_i)\| < \tau\},$$

  for a suitable norm $\|\cdot\|$ and a certain tolerance τ. Stress that one does not has to be very restrictive with the tolerance. The compression due to the stable eigenvalue will fix the errors. The **fundamental domain** is defined as $\mathcal{I} = (s_0\lambda^{-1}, s_0)$.

- Now we are interested in computing a sequence of points of the manifold. In principle, the iterates of any point given by a value of the parameter selected in the fundamental domain will lie on the invariant manifold. This does not mean that iterate a random (or equispaced) mesh of points is a promising strategy. It is probable that, this way, we end up with a large number of point near the fixed points and a few away.

- To solve this problem we have to require some control on the distance between successive points and the angles between tangent vectors.
  Let us suppose that we have a sequence

$$\left\{z_i\right\}_{i=1,\dots,m}$$

  of points on the manifold. These points correspond to certain values of parameters

$$\left\{s_i\right\}_{i=1,\dots,m},$$

  i.e., $z_i = K(s_i)$ for $i = 1, \dots, m$. Let us name:

$$\begin{aligned}\Delta\delta_m &= d(z_m, z_{m-1}),\\ \Delta\alpha_m &= (z_m - z_{m-1}) \wedge (z_{m-1} - z_{m-2}).\end{aligned}$$

  Let us suppose that, form the beginning, we fix the control quantities $\Delta\delta$ and $\Delta\alpha$. Then, the choice for the new value of the parameter s_{m+1} is given by

$$\begin{aligned}\Delta s_{m+1} &= \min\left(\frac{\Delta\delta}{\Delta\delta_m}, \frac{\Delta\alpha}{\Delta\alpha_m}\right)\Delta\delta_m 0.8,\\ s_{m+1} &= s_m + \Delta s_{m+1}.\end{aligned}$$

  Here, 0.8 can be considered as a security factor. Two different cases may happen:

  1. The new parameter is contained in the fundamental domain. Then, we iterate $K(s_{m+1})$ k times (k is the number of iterated used to compute z_m) and we get z_{m+1}.
  2. The new parameter is not contained in the fundamental domain. Then, we divide by λ both s_{m+1} and Δs_{m+1} and iterate $k+1$ times.

2.3.3 Testing the software

The computations presented in this Chapter rely on several computations with truncated series. As explained in Section 2.1, the main idea is to replace the standard floating point arithmetic with an arithmetic of truncated series (with floating point coefficients). We have coded several libraries to handle expressions with several dimensions. That is, we have coded an arithmetic to operate with polynomials with one variable, with two variables, etc. Treating those cases separately permits us to write more efficient codes. Let us explain a method that can be used to test the validity of any expansion, from the elementary operations to high order expansions of stroboscopic maps. We discuss it here for the stroboscopic map:

We have implemented, both, a regular standard floating point arithmetic integrator and a polynomial arithmetic. If everything is done correctly, the propagation of jets should give us the expansion of the stroboscopic map around a point. Let z_0 be a fixed point of P, that is $P(z_0) = z_0$. Where P denotes a stroboscopic map. The transport of the initial conditions of the variational equations along a period should produce the (truncated) Taylor series around the point. Let us suppose that the jet is truncated at order $m-1$ (so the error is of order m) and denote the polynomial by P_m. Choose now an arbitrary (unitary) direction v and a small $h > 0$. Then.

$$\|P(\bar{x} + hv) - P_m(\bar{x} - hv)\| = r(h)$$

where $r(h) = ah^m$, for some real number a. Then, $r(h)/r(h/2) = 2^m$.

2.4 Examples

This section concerns with some examples in which we apply the technology described in this Chapter. We have selected three of them, being, each of them, suited to illustrate several difficulties encountered during the computations.

In the first example we discuss the computation of the unstable manifold of a periodic orbit near the Earth-Moon L_3 collinear point in the Bicircular Problem. This model is discussed with a little extent here as it is used also in Chapters 1 and 3 to illustrate numerical methods. Moreover, it is analyzed in detail in Chapter 5 and used in Chapters 6 and 7.

In the second example we show how to use high order approximations of unstable manifolds to compute the splitting of separatrices of a periodically forced pendulum. Due to the exponentially small character of the splitting, extended precision has been used.

The third example deals with the motion of an electron near an atomic core. It shall not be developed in detail here as Chapter 8 is concerned about it. We use this example to illustrate the computation of a two-dimensional unstable manifold. Moreover, the unstable eigenvalue are quite different in modulus, therefore we have to use extended accuracy as well to avoid huge propagation of errors.

2.4.1 The unstable manifold of L_3 in the Bicircular Problem

The (Earth-Moon) Bicircular Problem (BCP) is a restricted version of the Four Body Problem. This model assumes that (while Earth and Moon move as in the RTBP) Sun and the Earth-Moon barycentre move along a circular orbit around the centre of mass of the Sun-Earth-Moon system, everything in the same plane. The first thing to point out is that the BCP is not coherent, that is, the motion of the primaries does not verify Newton's laws. This aspect is worrying to a certain extent. In fact, our main concern is the qualitative dynamics,

which is accurate enough for our purposes. The BCP can be regarded as a (periodic) time dependent perturbation of the RTBP. The associated Hamiltonian function can be written as

$$H_{BCP} = \frac{1}{2}(p_x^2 + p_y^2 + p_z^2) + yp_x - xp_y - \frac{1-\mu}{r_{PE}} - \frac{\mu}{r_{PM}} - \frac{m_S}{r_{PS}} - \frac{m_S}{a_S^2}(y\sin\theta - x\cos\theta). \quad (2.8)$$

where the units are taken as in the Earth-Moon RTBP, m_S is the mass of Sun, a_S the semimajor axis of Sun, $r_{PE}^2 = (x-\mu)^2 + y^2 + z^2$, $r_{PM}^2 = (x-\mu+1)^2 + y^2 + z^2$, $r_{PS}^2 = (x-x_S)^2 + (y-y_S)^2 + z^2$, $x_S = a_S\cos\theta$, $y_S = -a_S\sin\theta$, $\theta = \omega_S t$ and ω_S is the mean angular velocity of Sun in these synodic coordinates.

We can split the Hamiltonian in two parts, the one corresponding to the RTBP and the one that contains the contribution of Sun's gravity: Notice that we have introduced an additional parameter ε so that, when $\varepsilon = 0$, the system reduces to the RTBP and, when $\varepsilon = 1$, the system reduces to the BCP. Due to the periodic perturbation of Sun the Lagrangian points are no longer equilibria. A simple application of the Implicit Function Theorem shows that, under suitable non-degeneracy hypotheses, they are replaced by periodic orbits with the same period as the Sun ($T_S = 2\pi/\omega_S$).

This section shall be concerned with the periodic orbit that replaces L_3. According to the discussion of the present Chapter, we use the stroboscopic map obtained from evaluating the flow of (2.8) at time T_S, denote it by P. The dynamical equivalent of L_3 appears as a fixed point of P. It can be computed by means of a continuation scheme: we start from the coordinates of L_3 in the Restricted Three Body Problem and continue it, as a T_S periodic orbit, with respect to ε until the homotopy level $\{\varepsilon = 1\}$. The characteristic curve show no special feature nor properties. The resulting orbit is small and slightly unstable. The orbit revolves twice around the coordinates of L_3 in one period. The linear character of the periodic orbit at L_3 is of type saddle×centre×centre. We name the unstable eigenvalue as $\lambda \approx 3.372815778644077$ and focus on the unstable manifold which emanates from L_3 and, in particular, the branch that starts at the upper semiplane $\{y > 0\}$. We have computed the expansions in standard double precision up to several orders. We also have tried several scalings to check how the coefficients of the manifold behave. In Table 2.1 we show the expansion, up to order 32, of the manifold choosing the linear term as the eigenvector related to $\lambda =$ with Eucledian norm equal to one.

In Figure 2.1 we display validated pieces of the manifold. These pieces are obtained evaluating the error of the invariance equation as explained in Section . In particular we show pieces corresponding to expansions of order 32 (red) and order 64 (green). For the expansion of order 64 we have used the scaling $\alpha = \lambda$. As it is to be expected, the expansion of order 64 provides a larger portion of the manifold. It is remarkable that this semianalytical approximation of the manifold has the length in the phase space of a quarter of the Earth-Moon

0	9.9718669389179371e-01	3.8389519208446525e-15	4.2979033728022076e-16	1.8600909637452853e-02
1	-1.1226258676127698e-01	9.7955262533840792e-01	-1.4335303142736063e-02	1.6633780355080233e-01
2	-4.7566726078384963e-01	-3.7307055233740782e-02	-1.7242540319767924e-01	-2.8340374895230901e-02
3	-1.4167268964851968e-02	-1.8244885047620843e-01	1.0562174694694387e-03	-9.2619864346972031e-02
4	6.1486489593889297e-02	-1.6085194058369084e-02	4.2158012952443168e-02	-3.9881619025362034e-03
5	1.0114400092095828e-02	1.8955557518925421e-02	4.5596240765657129e-03	1.5530127793476425e-02
6	-5.1373826012643458e-03	4.6290875180280862e-03	-5.0963740028579273e-03	2.3767294211194641e-03
7	-1.8175647884452817e-03	-1.2354039395735840e-03	-9.7561189205184378e-04	-1.4657982480960738e-03
8	2.4781066436786048e-04	-6.2986795476325261e-04	4.0872563347303919e-04	-2.8254959046055723e-04
9	2.0298313609914322e-04	3.8699940902897075e-05	5.8194224476160206e-05	1.2614196511952995e-04
10	-2.2859970664102100e-06	6.1908061070045076e-05	-4.8806498890439207e-05	-5.4275177977844409e-08
11	-1.8499749167637963e-05	8.8628224866440160e-07	6.3671291056522488e-06	-2.3426226880655971e-05
12	-3.9537780651975706e-07	-5.6670598000424450e-06	1.1623967061253092e-05	3.6857119098536839e-06
13	1.8428935797322241e-06	-5.3041163141238404e-08	-1.3537295858203407e-06	5.5851974808889243e-06
14	-1.5323205452268415e-08	6.5113523029254136e-07	-2.4978501288417354e-06	-3.3641391176920135e-07
15	-2.4314272761645669e-07	-1.2325393227525048e-08	2.8061789602778807e-08	-1.0577691968416155e-06
16	3.6369582018585852e-09	-9.3696085593696905e-08	4.2779953550213427e-07	-3.1185174737087217e-08
17	3.6071229714735483e-08	-9.5229345651437775e-11	2.5807604202281266e-08	1.6898586620971063e-07
18	7.7928324358539108e-10	1.3782711622394862e-08	-6.6205597368808003e-08	1.4352890197315709e-08
19	-5.2047496913511424e-09	5.9834520492589687e-10	-6.8711562746470178e-09	-2.6085841786738980e-08
20	-3.2835089483384848e-10	-1.9566243905209568e-09	1.0397503900809982e-08	-3.1656616902305215e-09
21	7.3620311287695795e-10	-1.5954705224469813e-10	1.4406640456182209e-09	4.1836194526926242e-09
22	7.2364528318411776e-11	2.7869762982690079e-10	-1.6918068824679466e-09	6.6455629863779958e-10
23	-1.0632442211316929e-10	3.2254459617926258e-11	-3.0673281736795387e-10	-6.8213345269463490e-10
24	-1.4226726494892822e-11	-4.0783553257338095e-11	2.7352150625991000e-10	-1.4149680491277764e-10
25	1.5690395707708227e-11	-6.2955903503242201e-12	6.4361337272694242e-11	1.0862894071855290e-10
26	2.7697796168399203e-12	6.0262573899930762e-12	-4.2848650551614680e-11	2.8912048461061549e-11
27	-2.3085790980101849e-12	1.2134692514214643e-12	-1.2781160408344972e-11	-1.6768610437810758e-11
28	-5.2549280102879944e-13	-8.7975323047380834e-13	6.5411464910561575e-12	-5.5905847078034612e-12
29	3.3417010672758926e-13	-2.2554521730265839e-13	2.4212669352684045e-12	2.5386244827973341e-12
30	9.5747594940620048e-14	1.2635017361451631e-13	-9.8360554306971416e-13	1.0431316213352663e-12
31	-4.7691638960564778e-14	4.0367253027779868e-14	-4.4721924654101336e-13	-3.7883984778847648e-13
32	-1.6903434234807335e-14	-1.7932793835468102e-14	1.4533892480216184e-13	-1.9119114217965851e-13

Table 2.1: Expansion of the unstable manifold of L_3 with no scaling. The first column indicates the order of the coefficient. The other four columns stand for x, y, $\dot{x}$ and $\dot{y}$ respectively

distance. To end this example, we grow numerically the unstable manifold. This is achieved by iterating the points shown in Figure 2.1 (we have selected the points corresponding to the manifold expanded up to order 64. In Figure 2.2 we show 5 iterates (red) of a mesh (green) of points obtained by evaluating the Taylor expansion of order 64 of the unstable manifold. The manifold does a long excursion around the Earth-Moon system. Notice that, in this phase portrait, the unit of length is the Earth-Moon distance and the manifold achieves horizontal values of 10 units. It is also remarkable that the manifold passes close to the triangular points.

2.4.2 Splitting of sepratrices of a pendulum

In this section we consider the well-known model for the rapidly forced pendulum [DS92],

$$\begin{aligned} \dot{x} &= y, \\ \dot{y} &= -\sin x + \mu \sin \frac{t}{\varepsilon}, \end{aligned}$$

where $0 < \varepsilon < 1$ and μ are small parameters. Let us take x defined mod 2π so the phase space is a cylinder. The dynamics of the unperturbed ($\mu = 0$) system is very simple. It has two equilibrium points, an elliptic one at $(0, 0)$ and a hyperbolic one at $(-\pi, 0)$. The rest of the trajectories of the system are integral curves. These curves can be divided in three types. The rotational curves (homotopically non-trivial), the librational curves (homotopically trivial) and the separatrices, the curves that separate the libration and rotational curves. The separatrices are given by the invariant manifolds associated to the hyperbolic point, which is homoclinic i. e. the stable and unstable manifold coincide (see Figure 2.3, left). The two

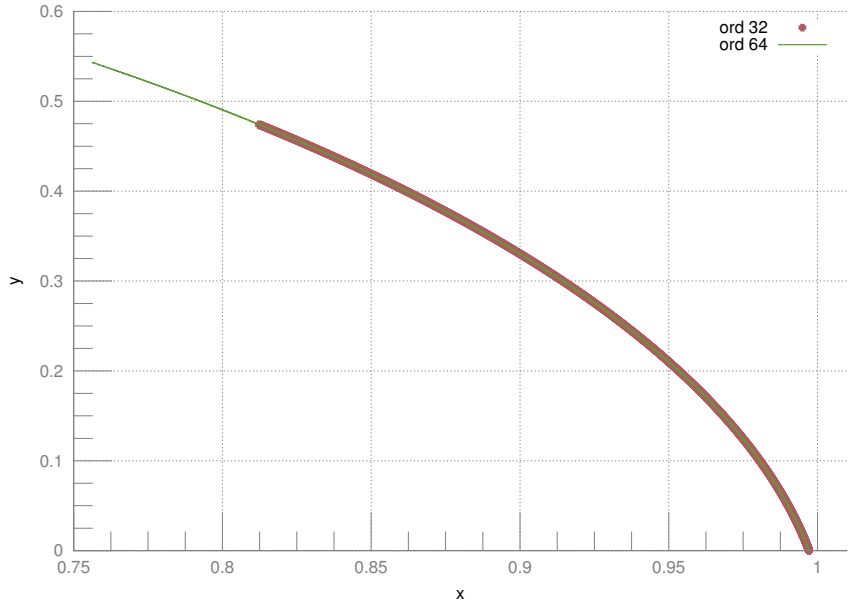

Figure 2.1: Unstable manifolds of order 32 (red) and 64 (green) attached to the periodic orbit replacing L_3. The horizontal axis stands for the x coordinate and the vertical axis for the y. The manifolds intersect the horizontal axis as the coordinates of the periodic orbit as a fixed point.

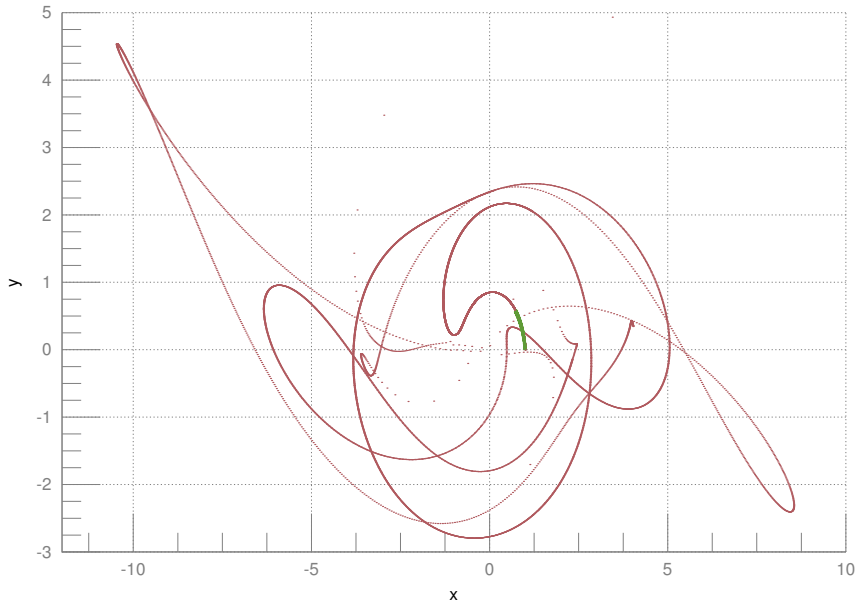

Figure 2.2: Numerically grown unstable manifold of L_3. The red points are obtained by iterating 5 times the green ones under the stroboscopic map. The horizontal axis stands for the x coordinate and the vertical axis for the y.

homoclinic orbits can be parametrized by

$$\begin{aligned} \Gamma_{\pm} &= \{(x_0(t), \pm y_0(t))\}, \\ x_0(t) &= 2\arctan(\sinh t), \\ y_0(t) &= \dot{x}_0(t) = \frac{2}{\cosh t}. \end{aligned}$$

The picture changes when we set $\mu \neq 0$. In first place, the dimension of the system increases by one. The equilibrium points no longer exist. It is an elementary application of the Implicit Function Theorem that they are replaced, for sufficiently small values of μ, by periodic orbits with the same period as the perturbation ($T = \varepsilon 2\pi$). Since the system is no longer autonomous it is suitable to study it by means of a Poincaré map with temporal section at the period. That is, $P(x, y) = \varphi(0, T, x, y)$ and φ stands for the flow of the Ordinary Differential Equation. Periodic orbits of period T appear as fixed points of P. As the original system is Hamiltonian, P is symplectic. If the values of μ are sufficiently small, the linear behaviour of the equilibria corresponding the the unperturbed case is preserved. Therefore, there exist a hyperbolic fixed point of P and it has two invariant manifolds associated to it.

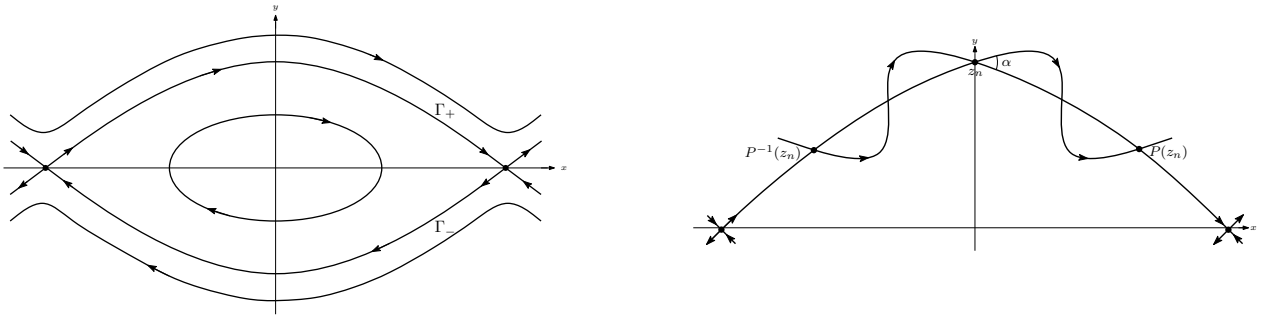

Figure 2.3: Phase space of the pendulum. Left: unperturbed pendulum, the stable and unstable manifolds coincide. Right: perturbed pendulum, the invariant manifolds intersect transversely.

Due to the symmetries of the system, they must intersect at the vertical axis (this is shown in Figure 2.3, right). It is of special interest the angle α between the manifolds. If α is different from zero, the invariant curve intersect transversely. That leads to regions of chaotic motion near the separatrices. There is an asymptotic formula for the angle between the manifolds.

Theorem 2.4.1 ([DS92])**.** *For $\varepsilon \to 0$ and $\mu \to 0$, the splitting angle for the rapidly forced pendulum is given by the following asymptotic formula:*

$$\alpha = \frac{\pi}{2\varepsilon} \frac{\mu}{\cosh \frac{\pi}{2\varepsilon}} \left[1 + O(\mu, \varepsilon^2)\right]. \tag{2.9}$$

We use the methodology presented in this work to compute a parametrization of the stable/unstable manifolds up to high order. This is used then, to compute the splitting angle with a few integrations. Indeed, high order expansions allow us to start integrations far away from the fixed point. As the splitting angle is exponentially small with the size of the perturbation, we have implemented the above-mentioned computation with an extended precision arithmetic. To show the efficiency of the high order invariant manifold computation, we have computed the splitting angle with and without using this manifold. Let us first discuss some details of the computation.

Let us choose the values $\varepsilon = 1/1024$ and $\mu = 1/32$. We will perform the computation for the Poincaré map P. For the numerical integration we use a Taylor method (see Section 2.1.3) with a MPFR arithmetic with mantissa of 320 bits, which is about 96 decimal digits (when extended precision is required, the Taylor method is the best choice for the numerical integration, see the discussion in Section 2.1.3). In this example, the equations are invariant by the symmetry $x \mapsto -x$, $t \mapsto -t$, which sends the unstable manifold on the stable one (and viceversa), so it is enough to compute one of them. We choose to compute the unstable manifold of the periodic orbit near the point $(-\pi, 0)$.

x =-3.14159265358979323846264338327950288419716939937510582097494 5
y =-0.00003048780487804878348741641977273061910125692778654579395 0
λ =1.21695220550761317997660218588773509916027624940673711060844 7
v_x =0.70710678118658760124047248750533567611697820126936749788789 2
v_y =0.70710678118650744756121623443291894113642980629050741284498 0

Table 2.2: Coordinates of the hyperbolic fixed point (x, y), the unstable eigenvalue λ, and the corresponding eigenvector $v = (v_x, v_y)$, with 60 digits.

The first step is to obtain the hyperbolic fixed point of P. As usual, this is done by means of a Newton method applied to the equation $P(x, y) - (x, y) = 0$, where the Jacobian of P is obtained by using jet transport of order 1. As initial guess we have used the coordinates of the hyperbolic point of the unperturbed pendulum, $(-\pi, 0)$. Once the fixed point is computed, the differential of P at this point gives the linear approximation to the stable/unstable manifolds. Here we compute the splitting angle α using first the linear approximation to the unstable manifold to start growing the manifold, and then a high order power expansion of the same manifold. This allows the see the difference in efficiency.

Using the linear approximation for the unstable manifold

The idea is to look for a point on the linear approximation to the stable manifold such that: a) it is close enough to the point such that the linear approximation is accurate enough; and b) after some iterates of the map, this point lans on the axis $x = 0$. To achive condition a) we chosee a point at a distance of about the square root of the precision of the used arithmetic, so that the accuracy of the manifold will be of the same order as the arithmetic. Se also note that, near this fixed point, this manifold is attracting so the iterations will stick to it. As we stop te iterations near $x = 0$, we will not feel the repulsion that appear when we come back to the point (and close to the stable manifold). To attain condition b), we use a secant method to find a point on the linear approximation of the manifold that lands on $x = 0$ after some iterates.

To estimate the intersection angle, we use the symmetry of the phase space of the map through the axis $x = 0$. This means that it is enough to compute the intersection angle of the manifold with the line $x = 0$. There are several methods to approximate this angle. The one we have used is to tabulate the intersection point of the manifold not only at $x = 0$ but also at $x = \pm h$ and $x = \pm 2h$ (we have used $h = 10^{-5}$) and then to approximate the derivative of the manifold at $x = 0$ by means of centered differences with extrapolation (with an accuracy of the order of h^4). Another approach could be to simply compute the intersection at $x = 0$ (which means that we have obtained a point on the linear approximation of the manifold

that arrives to $x = 0$ after several iterations), and then to propagate the tangent vector to the linear manifold from this initial point to the intersection. This propagation is done using the differential of the map. The value for the slope of the intersecion of the manifold with $x = 0$ is $-7.260194191847831 \times 10^{-24}$, while that the same value predicted by (2.9) is $-7.26019419361023 \times 10^{-24}$ (we stress that this is the slope, not the angle). The number of iterates needed to reach $x = 0$ is of 573, and the total computational time is of 2m 43s.

Using a high order approximation for the unstable manifold

Here we use the parametrization method to compute an approximation of order 32 to the unstable manifold. The program is very similar to the previous one but, as we use the higher order approximation to the manifold, we can start at a much larger distance distance of the fixed point, and this implies that the number of iterates needed to reach $x = 0$ will be much smaller. To approximate the manifold up to order 32 (working with numbers with a mantissa of 320 bits) requires 1m of cpu time, and to reach $x = 0$ now only requires about 18 iterates of the map. The results obtained are essentially the same, but now the computing time for the intersection is of about 3s, which means that the total computime time is 1m 3s.

2.4.3 A chemistry problem

As a first example, we will discuss the computation of the unstable invariant manifold of a periodic orbit of the following Hamiltonian system,

$$H = \frac{1}{2}(p_x^2 + p_y^2) - \frac{1}{\sqrt{x^2 + y^2 + a^2}} + E_c x \cos \omega t + E_s y \sin \omega t,$$

with $a = 1$, $\omega = 0.0584$, $E_c = 0.1$ and $E_s = 0$, which has an hyperbolic periodic orbit (of period $\frac{2\pi}{\omega}$) near $x = 30.5$, $y = p_x = p_y = 0$. This orbit is easily found by means of a Newton method on the map defined by the time-period ($\frac{2\pi}{\omega}$) map. The eigenvalues of the monodromy matrix are

```
1.0598923797401292e+03
2.1924563502992269e+00
4.5610942259513210e-01
9.4349201788190840e-04
```

so it has a 2D unstable manifold and a 2D stable manifold.

1D manifold

Let us first focus on the computation of the 1D manifold related to the "weakly" unstable eigenvalue $\lambda = 2.1924563502992269$. We will give some computing times on a desktop computer to give a hint of the efficiency of the method.

Computing this manifold using the standard double precision of the computer up to order 8 takes 0.1s. The size of the coefficients of order 8 is 5×10^{-13}, which gives an estimate of the radius of convergence of about 35. Next, we use MPFR with mantissa of 128 bits (39 decimal digits) up to order 8, and the computation time is of 17.4s. Computing up to order 16 takes 1m 22s. Finally, computing with mantissa of 192 bits (57 decimal digits), up to order 30 takes 17m 15s. The comparisons between these computations show a very important error propagation, due to the strongly unstable direction.

Next, we grow the manifold by using the dynamics. Here we have to pay attention to the fact that this manifold is not attracting (recall that there is another eigenvalue at the point close to 1059.89). To deal with this error amplification, at each iteration of the Poincaré map we compute (and accumulate) the norm of the differential so that we have an estimate of the growth of the error at each step.

As example, we select an initial point on this manifold at 1 unit of distance from the fixed point. We estimate the error on the manifold (we can use, for instance, the last terms of its power expansion). Then, we can monitor the growth of the (estimated) error during the iterations:

```
iter:  0  err: 0.000000e+00
iter:  1  err: 8.466197e-43  dist: 2.199796e+00
iter:  2  err: 8.928646e-40  dist: 4.848533e+00
iter:  3  err: 9.240140e-37  dist: 1.081419e+01
iter:  4  err: 8.411957e-34  dist: 2.553592e+01
iter:  5  err: 2.083436e-32  dist: 1.745048e+01
iter:  6  err: 1.966030e-29  dist: 1.976583e+01
iter:  7  err: 1.310301e-27  dist: 7.533221e+01
iter:  8  err: 1.615796e-27  dist: 1.267686e+02
iter:  9  err: 1.771004e-27  dist: 1.773365e+02
iter: 10  err: 1.873796e-27  dist: 2.275002e+02
```

The first column is the iterate of a point obtained from the parametrization of the manifold, the second column is the accumulated product of the norms of the differential of the Poincaré map at each point, and the third is the distance to the fixed point. As it happens in many situatitions, the unstability of this weakly unstable manifold decreases as the move away from the fixed point. This simplifies the approximation of the manifold up to long distances.

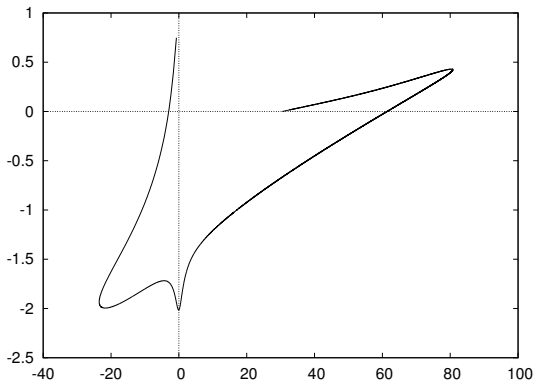

Figure 2.4: The 1D weakly unstable manifold.

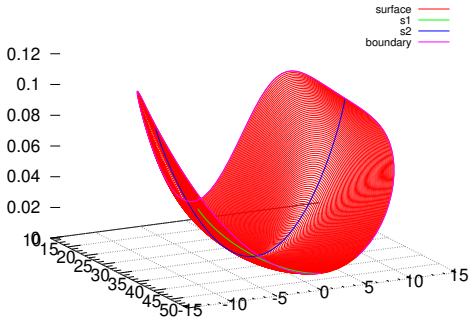

Figure 2.5: The 2D manifold drawn from the expansion obtained in the parametrization method.

2D manifold

The unstable eigenvalues are $\lambda_1 \approx 2.1924563502992269$ and $\lambda_2 \approx 1059.8923797401292$. Computing this 2D manifold (double precision) up to order 8 takes 0.5s. Using MPFR with mantissa of 128 bits (39 decimal digits) it takes 1m 19s. Computing up to order 16 requires 15m 26s. Finally, to compute it up to order 30 using extended precision arithmetic (MPFR with 192 bits mantissa $\approx$ 57 decimal digits) takes 8h 50m. As in the 1D case, we use these different approximations to estimate the error on the coefficients of the expansion. Figure 2.5 shows a representation of this manifold.

"Whether or not what you do has the effect you want, it will have at least three you never expected, and one of those usually unpleasant."

Siuan Sanche

3 Computation of invariant curves

In this thesis we have emphasized the importance of invariant structures in dynamical systems. In Hamiltonian dynamics, the invariant tori have especial importance. We have discussed briefly the importance of invariant tori in KAM theory. In autonomous systems, KAM tori have the same dimension as the number of degrees of freedom of the Hamiltonian and there are no invariant tori with larger dimension. In periodic time dependent Hamiltonians the dimension of KAM tori increases by one. As we have mentioned, KAM tori can enclose the motion (in two degrees of freedom) and are crucial to show the stability of certain regions of the phase space.

Lower dimension invariant tori play, as well, an important role. These have some normal behaviour and, in particular, can have stable and unstable manifolds attached to it, the so-called whiskers. Several dynamical mechanisms can be driven by low dimension invariant tori together with their whiskers (an example of this can be found in Chapter 8). It is reasonable to study the invariant objects in order of simplicity: First we have to understand fixed points and periodic orbits, the next step to be taken is the study of invariant curves.

This chapter is devoted to the computation of invariant curves of quasi-periodic skew-products and autonomous maps[1]. The method explained here has been developed in a number of previous works [CJ00, JO04, Jor01, GM01]. The present chapter fulfills two main goals: First, it is added to this dissertation for completeness. The method is used widely in

[1] Although the method is discussed for both autonomous and non-autonomous case, all the applications appearing in this thesis involve autonomous maps.

Chapters 5, 6 and 8. Moreover, due to the complicated nature of this kind of computations (compared, for instance, with the computation of periodic orbits), one is usually forced to come up with tricks that, because they are simple or tangential, are not explained deeply in the literature. The author of this thesis feels that this is a good place to agglutinate all these artifices. A place to come back eventually if these type of problems are to be faced in future research problems. The second goal of this chapter is to introduce the concept of **reducibility of invariant curves**. That is, the quasi-periodic Floquet Theory. This problem arises naturally when computing the stability of invariant curves ant it is studied in a very simple setting in Chapter 4.

The method presented here is not the only one nor the most efficient method for the computation of invariant tori, however, it requires nothing from the invariant curve besides regularity and a simple inner dynamics. Other methods rely on the reducibility of the invariant curve or other conditions. See, for instance [JO09, FH12, HL05a, HL05b] and also [Sim98] for an alternative approach that does not need extra assumptions. We refer to [HLS09] to a vast summary of efficient methods and to [BOS18] for the particular context of astrodynamics. Let us note that we discuss the algorithm for the particular case of invariant curves. This method can be extended to higher dimensional tori. This extension has not been used in this thesis.

This chapter is structured as follows: In Section 3.1 we introduce the discrete systems known as **quasi-periodic skew-products**. These systems arise naturally when considering quasi-periodic perturbations of autonomous systems. In Section 3.2 we discuss the implementation of a Newton scheme to compute invariant curves of quasi-periodic skew-products. The method is based on a discretization, by means of Fourier series, of a suitable operator defined in a Banach space. We focus, essentially, in the discretization of the operator, the error analysis and explain how to deal with some complications appearing in the autonomous case. Section 3.3 we explain how the normal behaviour of invariant curves is computed in the reducible case. This section is a summary of [Jor01]. The discussion of the computation is done in terms of the spectrum of a suitable operator. The method for the computation of the normal behaviour of an invariant curve is independent from the Newton scheme presented in Section 3.2. Moreover, as it is explained in [Jor01], it seems to detect numerically the non-reducibility. In Section 3.3 we also discuss the computation of linear approximations of stable and unstable invariant manifolds related to normally hyperbolic invariant curves. In Section 3.4 we discuss a prediction-correction scheme adapted to the vicissitudes of the computation of invariant curves emerging along some elliptic direction related to a fixed point of a symplectic map. We provide, in Section 3.5 some details on the implementation. As the method presented in this chapter is well-known, this section is way shorter than its analogous in previous chapters. Finally, in Section 3.6 we illustrate the method by means of an example. As usual, we choose the Bicircular Problem as a test model and compute a

family of invariant curves related to some dynamical equivalent of the triangular point L_4.

3.1 Quasi-periodic skew-products

Let $\mathcal{U} \subset \mathbb{R}^n$ be open sets, $f \in \mathcal{C}^r(\mathbb{T} \times \mathcal{U}, \mathcal{U})$, $r \geq 1$, a diffeomorphisim, and $\omega \in \mathbb{T} \setminus \mathbb{Q} \cap \mathbb{T}$. A discrete dynamical system of the form

$$\begin{cases} \bar{x} = f(x, \theta), \\ \bar{\theta} = \omega + \theta, \end{cases} \tag{3.1}$$

is known, in the literature, as **quasi-periodic skew-product**. The dynamics on the basis, a rigid rotation, is independent from the dynamics on the bundle, given by f. The dynamics on the bundle may depend on the basis (as in the case of system (3.1)). In that case, the system is said to be **non-autonomous**. Otherwise, if the dynamics on the bundle is independent from the basis, the system is said to be **autonomous**.

Let us introduce an example.

Example 3.1.1 (Typical case)**.** *Consider the following Ordinary Differential Equation:*

$$\begin{cases} \dot{x} = F(x) + \varepsilon G(x, \theta_1, \theta_2), \\ \dot{\theta}_1 = \omega_1, \\ \dot{\theta}_2 = \omega_2. \end{cases}$$

Here, ω_1 and ω_2 are rationally independent frequencies, $\varepsilon > 0$ is a small parameter. An associated skew-product is:

$$\begin{cases} \bar{x} = \varphi_T(x, \theta), \\ \bar{\theta} = \theta + \omega. \end{cases}$$

where φ_T is the flow at time $T = 2\pi/\omega_1$ and $\omega = 2\pi\frac{\omega_2}{\omega_1}$.

This is a common way to produce a non-autonomous skew-product: From a quasi-periodic differential equation, depending on two frequencies, one takes the stroboscopic map with respect to one of the periods of the vectorfield. If the original system is periodic, to take the stroboscopic map defines an autonomous system. In this case, the dynamics on the basis becomes trivial.

Let us explain the context in which skew-products have a relevant role in Part II of this dissertation. Consider a periodic time dependent Hamiltonian system which is a perturbation of some autonomous system. Generically, the periodic orbits whose frequency is not resonant

to the one of the perturbation are replaced by invariant tori with two frequencies. From these two frequencies one corresponds to the frequency of the temporal variable of the Hamiltonian and the other is close to the one of the periodic orbit, see [JV97b]. This result appears frequently in this dissertation. Sometimes we say that the periodic orbit gains the frequency of the perturbation to summarize this statement. In this case, taking the stroboscopic map we obtain an autonomous map. Notice that, in principle we have no structure of skew-product. However we do know in advance that:

- The tori with two frequencies that replace the periodic orbits of the autonomous system appear as invariant curves of the stroboscopic map.
- The inner dynamics of the invariant curves is conjugate to an irrational rigid rotation.

3.2 Computation of invariant curves

An invariant curve with frequency ω is the graph of a smooth map $K \in \mathcal{C}^s(\mathbb{T},\mathcal{U})$, $s \leq r$, which verifies the so-called **invariance equation**:

$$f \circ K = T_\omega \circ K. \tag{3.2}$$

Consider $E_s = (\mathcal{C}^s(\mathbb{T}, \mathbb{R}^n), \|\cdot\|_s)$ the Banach space of s-regular periodic functions and define

$$\begin{aligned} F : E_r &\longmapsto E_r, \\ \varphi &\mapsto f \circ \varphi - T_\omega \circ \varphi. \end{aligned}$$

For $K \in E_s$ fixed, we define the differential map (around K) as

$$\begin{aligned} DF_K : E_r &\longmapsto E_r, \\ \varphi &\mapsto D_x f \circ K \circ \varphi - T_\omega \circ \varphi. \end{aligned}$$

An invariant curve K of system (3.1) is a zero of the operator F. If some approximation of the curve $\tilde{K}$ is sufficiently close to a real zero, i.e. $\|F(\tilde{K})\|_r < \varepsilon$, with ε positive and small, a Newton method shall converge quadratically (provided that the differential map DF_K is bounded, compact and has bounded inverse) to that zero.

Technically, to find an invariant curve is an infinite dimensional problem. Obviously, we cannot store an infinite amount of information on the computer, so we have to come out with a strategy to encode good approximations of invariant curves with a finite set of data. We take advantage on the fact that invariant curves can be expanded in Fourier series. Moreover,

the regularity of the invariant curve is translated into the decay of its Fourier coefficients. For most of applications coming from physical problems, and certainly the ones encountered in this thesis, the invariant curves are analytic. The decay of the Fourier coefficients of an analytic curve is exponential, therefore, just a few of them shall be required to describe the curve with good accuracy[2].

We can also save invariant curves as a mesh of points in the phase space. One can pass from points to coefficients (or viceversa) by means of a Fast Fourier Transform (FFT). Depending on the situation, it is suitable to work with coefficients or with points. We use both ways of encoding invariant curves.

The first step is to build discrete versions of the space E_s, the operator F and the differential map DF_K. Consider the following set:

$$E_s^N := \{P \in E \ \mid P \text{ is a trigonometric polynomial of degree } N\}.$$

The integer N is the order of truncation we work with. This number must be large enough so the coefficients of the curve we are neglecting have norm below some tolerance. Besides from that, the number N should be as small as possible. Let us derive a discrete version of the operator F, to do so, we select an element $K \in E_r^N$. This element can be written as $K(\theta) = \sum_{|j|\leq N} K_j \exp(\mathrm{i}j\theta)$. The operator F_N, acting on E_r^N, is defined by means of the following diagram:

$$F_N : \begin{bmatrix} K_1 \\ \vdots \\ K_M \end{bmatrix} \underset{\text{(a)}}{\longrightarrow} \begin{bmatrix} p_1 \\ \vdots \\ p_M \end{bmatrix} \underset{\text{(b)}}{\longrightarrow} \begin{bmatrix} f(p_1, \theta_1) \\ \vdots \\ f(p_m, \theta_M) \end{bmatrix} - \begin{bmatrix} K(\theta_1 + \omega) \\ \vdots \\ K(\theta_M + \omega) \end{bmatrix} \underset{\text{(c)}}{\longrightarrow} \begin{bmatrix} \bar{K}_1 \\ \vdots \\ \bar{K}_M \end{bmatrix}.$$

Here $M = 2N + 1$. Notice that each Fourier coefficient (and point of the phase space) is n dimensional. Therefore, the dimension of the vectors in the diagram is Mn. The letters, from (a) to (c) denote different steps to build the operator. Step (a) stands for the evaluation of the Fourier series at the mesh $\{\theta_j := \frac{j2\pi}{M} \ \mid \ j \in \{0, \ldots, M\}\}$. The points p_j are named after this evaluation, i.e. $p_j := K(\theta_j)$. Step (b) is the evaluation of the invariance equation, the core of the operator. The last step, (c), is a Fourier transform to recover the Fourier coefficients of the evaluation. The Fourier transform is a linear operator (we will discuss its associated matrix later), therefore, it sends zero to zero. Since we are looking for zeros of F, we can obviate the last step in practical computations. From now on we will be a little bit more precise. First of all we start to work with real Fourier coefficients series, which can be

[2]Indeed, Fourier expansions are very suited to represent smooth invariant sets. There are other bases which are suited for less regular invariant sets, see [LN02, AMR17].

tedious here but more practical from the coding point of view.

$$K(\theta) = a_0 + \sum_{k=1}^{N} a_k \cos k\theta + \sum_{k=1}^{N} b_k \sin k\theta. \tag{3.3}$$

We rewrite the diagram with this new notation.

$$F_N : \begin{bmatrix} a_0 \\ \vdots \\ b_N \end{bmatrix} \underset{\text{(a)}}{\longrightarrow} \begin{bmatrix} K(\theta_0) \\ \vdots \\ K(\theta_{2N}) \end{bmatrix} \underset{\text{(b)}}{\longrightarrow} \begin{bmatrix} f(K(\theta_0),\theta_1) \\ \vdots \\ f(K(\theta_{2N}),\theta_{2N}) \end{bmatrix} - \begin{bmatrix} K(\theta_0+\omega) \\ \vdots \\ K(\theta_{2N}+\omega) \end{bmatrix} \underset{\text{(c)}}{\longrightarrow} \begin{bmatrix} \bar{a}_0 \\ \vdots \\ \bar{b}_N \end{bmatrix}.$$

Remark 3.2.1. *Notice the order of the vector of Fourier coefficients:* $(a_0, a_1, b_1, \ldots, a_N, b_N)$. *There is a reason behind this arrangement. A periodic function* φ *can be determined by its Fourier coefficients* $\{a_0, a_k, b_k\}_{k\in\mathbb{N}}$. *Define now,* $\psi(\theta) = \varphi(\theta+\omega)$, *which has Fourier coefficients,* $\{\bar{a}_0, \bar{a}_k, \bar{b}_k\}_{k\in\mathbb{N}}$. *It is easy, by using basic trigonometrical identities, to find the relation between the coefficients*

$$\begin{bmatrix} \bar{a}_k \\ \bar{b}_k \end{bmatrix} = \begin{bmatrix} \cos k\omega & \sin k\omega \\ -\sin k\omega & \cos k\omega \end{bmatrix} \begin{bmatrix} a_k \\ b_k \end{bmatrix}.$$

We name the matrix of rotation of angle $k\omega$ *as* $R_{k\omega}$. *With the arrangement we have chosen a vector of coefficients representing* K *can be transformed to a one representing* $T_\omega \circ K$ *by means of the matrix* $\operatorname{diag}(1, R_{1\omega}, \ldots, R_{N\omega})$.

To discretize the differential map and obtain DF_N, we take the derivative of F_N with respect to the Fourier coefficients. To do so, it is suitable to apply the chain rule:

$$\begin{aligned} \frac{\partial F_N}{\partial a_k} &= D_x f(x(\theta_j),\theta_j)\frac{\partial K}{\partial a_k}(\theta_j) - \frac{\partial K}{\partial a_k}(\theta_j+\omega) \quad j = 0,\ldots,N, \\ \frac{\partial F_N}{\partial b_k} &= D_x f(x(\theta_j),\theta_j)\frac{\partial K}{\partial b_k}(\theta_j) - \frac{\partial K}{\partial b_k}(\theta_j+\omega) \quad j = 0,\ldots,N. \end{aligned}$$

Notice that

$$\begin{aligned}
\frac{\partial K}{\partial a_k}(\theta_j) &= I_n \cos k\theta_j, \\
\frac{\partial K}{\partial a_k}(\theta_j + \omega) &= I_n \cos k(\theta_j + \omega), \\
\frac{\partial K}{\partial b_k}(\theta_j) &= I_n \sin k\theta_j, \\
\frac{\partial K}{\partial b_k}(\theta_j + \omega) &= I_n \sin k(\theta_j + \omega).
\end{aligned}$$

The implementation of the discretized differential map is critical for the performance of the program: This is a large matrix ($Mn \times Mn$) arranged according the order of the Fourier coefficients. Because of the curse of dimensionality, the method slows down as the degree of truncation increases, so the construction of the matrix has to be implemented in a very efficient way.

3.2.1 On the lack of uniqueness for the autonomous case

In the autonomous case, the Fourier coefficients do not give a unique representation of invariant curves: If φ denotes a periodic function, then $\psi(\theta) := \varphi(\theta + \rho)$, $\rho \in \mathbb{T}$, has a different Fourier series but the same graph. In other words, there are infinitely many Fourier series representing each invariant curve. This implies that, in the autonomous case, the differential matrix has, generically, a kernel of dimension 1 which leads to numerical difficulties. However, this eventuality can be overcome by imposing some condition on the curve. This condition depends on the problem and it may fulfill distinct purposes. This new condition is added as an extra equation when solving the linear system in the Newton method. To add an extra equation means to add an extra row in the differential matrix. The system we have to cope with is non-squared. There are several strategies to follow. A QR decomposition can be used to obtain the least squares solution. A Gaussian elimination with maximal pivoting works as well: The redundant equation is sent to the last row by the pivoting. As this equation reads like '$0 = 0$', it can be removed harmlessly to obtain a squared system.

3.2.2 Estimation of the error

Assume we have found an approximation K of an invariant curve. Then, the discretized invariance equation is satisfied with good accuracy by the mesh of points,

$$\|f(K(\theta_j), \theta_j) - K(\theta_j + \omega)\| \leq \varepsilon.$$

However, we do not have control on the error when discretizing the invariance equation, therefore the last bound does not assure us we have computed the invariant curve K with accuracy less than ε. Consider the value:

$$E(K,\theta) = \max_{\theta\in\mathbb{T}} \big\| f(K(\theta),\theta) - K(\theta+\omega) \big\|.$$

If K is an invariant curve of rotation number ω, then $E(K,\omega) = 0$. Now, given an approximation K, we can tabulate its value on a mesh of points of $\mathbb{T}$. This mesh has to be finer than the one used to solve the equation. If this estimate is bigger than a prescribed threshold we need to increase the truncation order and recompute the invariant curve starting from the last approximation. This process has to be repeated until the estimated error E is below some tolerance.

Remark 3.2.2. *In the context in which we know that the invariant curves are analytic, we can estimate the order of truncation required for a trigonometric polynomial to represent a periodic orbit with good accuracy provided that we know in advance some of the first coefficients. Indeed*

$$\|a_k\| \sim Me^{-\rho|k|}, \qquad \|b_k\| \sim Me^{-\rho|k|}.$$

The constants M and ρ can be estimated by means of a regression. This strategy can be used when the truncation order needs to be increased. We can estimate the minimal increment on the truncation order for a better performance.

3.3 On the normal behaviour of invariant curves

In dynamical systems, to know the stability of an invariant object may be as important as knowing the object itself. Indeed, most of the times, the dynamics around invariant objects is organized, locally, by their linear approximations. In this section we are concerned about the normal linear behaviour around invariant curves carrying quasi-periodic motions. To put ourselves in context, we give some words on the periodic case first. Recall that the linear stability of a periodic orbit is a problem solved satisfactorily by Floquet theorem (see [Arn74] for a classical reference and Theorem 1.2.1 where the statement is adapted to the symplectic case). Stability properties of periodic orbits are given by the eigenvalues and eigenvectors of the Monodromy matrix. The main result in Floquet theory states that, for each linear Ordinary Differential Equation with periodic time dependence, there is a (maybe complex) linear periodic change of variables that casts the system to a new one with constant coefficients. The case of quasi-periodic linear systems is much harder. There are some cases in which reducibility of invariant tori can be established. As two remarkable examples we can take the maximal KAM tori for Hamiltonian systems [dlLGJV05] and systems which are close

to constant coefficients [JS92]. If an invariant curve is reducible, the task of computing its stability can be accomplished by finding the reduced matrix and computing the corresponding spectrum (as in the case of periodic orbits). Even the works we refereed to deal with ordinary differential equations, we keep our mindset in the context of discrete systems.

3.3.1 Linear quasi-periodic skew-products

Let us suppose that we know some invariant curve K satisfying the invariance equation (3.2) for some known ω. Let h represent any small displacement with respect to an arbitrary point $K(\theta)$, $\theta \in \mathbb{T}$, on the invariant curve. Then

$$f(K(\theta)+h) = f(K(\theta),\theta) + D_x f(K(\theta),\theta)h + \mathcal{O}(\|h\|^2),$$

where $\|\cdot\|$ is some suitable norm. The linear normal behaviour is described by the following system.

$$\begin{cases} \bar{x} = A(\theta)x, \\ \bar{\theta} = \theta + \omega, \end{cases} \tag{3.4}$$

where $A(\theta) = D_x f(K(\theta),\theta)$.

Definition 3.3.1. *System (3.4) is said to be reducible if and only if there exists a (maybe complex) continuous change of variables $x = C(\theta)y$ such that casts (3.4) to*

$$\begin{cases} \bar{y} = By, \\ \bar{\theta} = \theta + \omega, \end{cases} \tag{3.5}$$

where the matrix $B := C^{-1}(\theta+\omega)A(\theta)C(\theta)$ does not depend on θ.

Our goal is, for a given invariant curve K, to compute the matrix B as well as its spectrum. This is possible only if the curve is reducible. Hence, to accomplish our purposes, we should be aware of whether a curve is reducible or not. In other words, we should be able to detect non-reducibility. Let us face the non-reduced problem first.

Let us consider the following generalized eigenvalue problem:

$$A \circ \psi = \lambda T_\omega \circ K. \tag{3.6}$$

We have named $A = D_x f \circ K$ for shortness. The operator $\mathcal{T} : \varphi(\theta) \in \mathcal{C}^r(\mathbb{T},\mathbb{R}^n) \mapsto A(\theta-\omega)\varphi(\theta-\omega)$, $r \leq 1$, is called **transfer operator**.

In [Jor01] À. Jorba shows how this eigenvalue problem can be used to study the spectrum of the reduced matrix B whenever (3.4) can be reduced to (3.5). Let us present the main

result in [Jor01] concerning this issue. We state it slightly differently and we highlight some relevant points of the proof as, like in most of the results in Floquet theory, it is constructive and easily transferable to numerical algorithms. It also provides a good perspective to give a proper interpretation of the results.

Theorem 3.3.2. *Consider the generalized eigenvalue problem (3.6). The spectrum of (3.6) consists on the union of n concentric circles centered at the origin of the complex plane if and only if system (3.4) can be reduced to (3.5).*

Some comments on the proof : Let us denote by σ the spectrum of (3.6) and by σ_{eig} the subset of eigenvalues:

- It is easy to see that the eigenvalues of (3.6) fill densely circles. Indeed, if $\lambda \in \sigma_{eig}$, then, for any $k \in \mathbb{Z}$, $\lambda \exp(\mathrm{i}k\omega) \in \sigma_{eig}$. If ψ is the eigenfunction related to λ, then $\psi(\theta) := \exp(-\mathrm{i}k\theta)\psi(\theta)$ is also an eigenfunction whose corresponding eigenvalue is $\lambda \exp(\mathrm{i}k\omega)$. Notice that two eigenvalues in the same circle can be obtained, one from the another, by rotating them by a multiple of ω. Given two eigenfunctions ψ_1 and ψ_2, we say these functions to be ω-related if there exist $k \in \mathbb{Z}$ such that $\psi_1(\theta) = \exp(\mathrm{i}k\theta)\psi_2$. Otherwise they are ω-unrelated.

- If (3.4) is reducible to (3.5), then $\mathrm{spec}(B) \subset \sigma_{eig}$. Moreover, if $\lambda \in \sigma_{eig}$, there exist $k \in \mathbb{Z}$ such that $\lambda \exp(\mathrm{i}k\omega) \in \mathrm{spec}(B)$.

- The eigenfunctions associated to a two ω-unrelated eigenvalues are linearly independent for each θ.

- Suppose there are n unrelated eigenvalues of (3.6). Consider the $n \times n$ matrix constructed by setting as columns n eigenfunctions of (3.6). As there are n unrelated eigenvalues, we can select the columns to be linearly independent. This matrix provides the change of variables that casts (3.4) to (3.5).

These are the main points of the proof. From these it follows that the eigenvalue problem (3.6) is to be solved to obtain a spectrum consisting of circles. From these circles we can get the actual eigenvalues of the reduced system if the number of circles is maximal.

Remark 3.3.3. *For the sake of simplicity, we have excluded the cases where the reduced matrix has multiple eigenvalues. This is reflected on the spectrum of (3.6) where the circle related to the multiple eigenvalue has also the corresponding multiplicity.*

3.3.2 Numerical computation of the normal modes

Assume we are given an approximation K of an invariant curve and we aim to compute an approximation of its normal modes. From Theorem 3.3.2, it is clear that we have to compute the spectrum of the operator $T_{-\omega}A$ (we recall that $A = D_x f \circ K$). To compute numerically this spectrum, we have to discretize the operator in a very similar way as in the previous section, when computing the approximation of the curve. Les us write a diagram:

$$F_N : \begin{bmatrix} a_0 \\ \vdots \\ b_N \end{bmatrix} \underset{\text{(a)}}{\longrightarrow} \begin{bmatrix} K(\theta_0) \\ \vdots \\ K(\theta_{2N}) \end{bmatrix} \underset{\text{(b)}}{\longrightarrow} \begin{bmatrix} \frac{\partial F}{\partial a_0}(\theta_0) & \dots & \frac{\partial F}{\partial b_N}(\theta_0) \\ \vdots & \dots & \vdots \\ \frac{\partial F}{\partial a_0}(\theta_M) & \dots & \frac{\partial F}{\partial b_N}(\theta_M) \end{bmatrix} \begin{bmatrix} K(\theta_0 + \omega) \\ \vdots \\ K(\theta_{2N} + \omega) \end{bmatrix} \underset{\text{(c)}}{\longrightarrow} \begin{bmatrix} \bar{a}_0 \\ \vdots \\ \bar{b}_N \end{bmatrix}.$$

Again the step (c) is given by the Fourier transform and (a) by the inverse Fourier transform. As the Fourier transform is linear, there exist matrices $\mathcal{F}_N$ and $\mathcal{F}_N^{-1}$ that take care of steps (c) and (a). These steps appear in the computation of the invariant curve itself but the final one can be avoided (as we already pointed out) and the first is completed computing the inverse transformation. There is no need to build the matrices $\mathcal{F}_N$ and $\mathcal{F}_N^{-1}$ in order to get the curve but they are essential to compute the stability. The matrix whose spectrum is to be studied is:

$$M = T_{-\omega}\mathcal{F}^{-1}A\mathcal{F}.$$

Here we dropped the subindices to avoid heavy notation. We have already explained how to ensemble matrix T_ω, see Remark 3.2.1. Moreover, $T_{-\omega} = T_\omega^t$. The entries of matrix $\mathcal{F}$ can be read directly from (3.3):

$$\mathcal{F} = \begin{bmatrix} I & \cos(\theta_0)I & \sin(\theta_0)I & \dots & \cos(N\theta_0)I & \sin(N\theta_0)I \\ \vdots & \vdots & \vdots & \vdots & \vdots & \vdots \\ I & \cos(\theta_M)I & \sin(\theta_M)I & \dots & \cos(N\theta_M)I & \sin(N\theta_M)I \end{bmatrix}$$

where I is the identity matrix of dimension n. With this, we have all the components to ensemble matrix M. Notice that $A\mathcal{F}$ is already computed during the Newton method. We have, hence, to build the matrices $T_{-\omega}$ and $\mathcal{F}^{-1}$ and compose them to get M. Then we apply a method to compute the eigenvalues and eigenvectors of matrix M.

3.3.3 On the accuracy of the eigenvalues

In this section we discuss the accuracy of the eigenvalues we get from M. To simplify the analysis, assume system (3.4) to be reducible and that we have solved the generalized eigenvalue problem (3.6) with a discretization of order N. At this point we have $(2N + 1)n$

pairs eigenvalue-eigenvector while B has n eigenvalues. Each one of the eigenvalues of B is bestly approximated (hopefully goodly enough) by one of the $(2N+1)n$ eigenvalues of (3.6). The question is which one. We already mentioned that, by rotating an eigenfunction by an angle $k\theta$, we obtain a new eigenfunction. However this can be dangerous in terms of the error. Let us explain how rotating series may increase the error: The advantage of approximating periodic functions by Fourier series lies on the fast decay of the coefficients. However, we work with discretizations and we need to be sure the order of truncation is large enough so we do not skip the terms with larger norm. One has to care about the dominant harmonics and to be sure the tail of the discretized series consists of sufficiently small terms. In an idealistic situation, the average of the Fourier series is the dominant harmonic and the decay of the coefficients is event with respect to negative and positive indices (in the complex expansion). To understand better what do we mean think of a periodic function expanded in the complex basis up to a certain order $K(\theta) = \sum_{|j|\leq N} K_j \exp(\mathrm{i}j\theta)$. If the dominant term is the average, any discretization contains it and therefore we always take into account the most important harmonic of the series. Now, we look at what happens when we rotate such optimal truncated series by $j_0\theta$. This is equivalent to multiply the series by $\exp(\mathrm{i}j_0\theta)$ i.e.

$$\exp(\mathrm{i}j_0\theta)K(\theta) = \sum_{|j|\leq N} K_j \exp\big(\mathrm{i}((j+j_0)\theta)\big).$$

Now, the dominant term is the j_0-th one. Moreover, the average is shifted up from the coefficients with negative j which is probably small. Therefore if j_0 is large, the resulting series has small average and a high order dominant harmonic which leads to high errors. In fact, if $j_0 > N$, the dominant term is taken out of the discretization. Let us address now the question on how to choose the correct pair of eigenvalue-eigenvector. Each circle in the solution of problem (3.6) is an equivalence class and we have to choose the representant which provides a better approximation of the corresponding eigenvalue of B (which belongs to the equivalence class). According to the previous argument, the best approximation to the eigenvalue of B is the representant whose corresponding eigenfunction has the best decay behavior in the terms explained before. The norm $\|\cdot\|^{(p)}$, defined as

$$\|\psi\|^{(p)} = \sum_{j\in\mathbb{Z}} |\psi_j||j|^p,$$

captures these decay behaviour. We can select our representant of each equivalence class minimizing the norm $\|\cdot\|^{(p)}$ (selecting $p=1$ seems to be enough) over the eigenfunctions of this class.

Some extra comments: In principle we can choose any eigenvalue we have computed with sufficient accuracy, but sometimes it is convenient to find some eigenvalue satisfying

specific conditions. That depends on the problem. Moreover, in the case of symplectic skew-products, the structure of the eigenvalues gives us information in advance. For instance, we know that hyperbolic eigenvalues only can be complex if there are, at least, other three hyperbolic directions. Otherwise, the eigenvalue must be real. If we know in advance that the eigenvalue is real, we have to chose the eigenvalue with smaller (in absolute value) imaginary part.

3.3.4 Stable and unstable manifolds

As any other invariant object with a hyperbolic linear direction, under suitable conditions, hyperbolic invariant curves have stable and unstable manifolds attached to. In this context a stable/unstable manifold of an invariant curve K related to a certain real eigenvalue $|\lambda| \neq 1$ is the graph of a function $m \in \mathcal{C}^r(\mathbb{T} \times \mathbb{R}, \mathcal{U})$ that verifies the invariance equation:

$$f \circ m(\theta, s) = T_\omega \circ m(\theta, \lambda s). \tag{3.7}$$

A linear approximation of the manifold is given by the eigenfunction ψ related to λ. Indeed, let us define $m^{[1]}(\theta, s) = K(\theta) + s\psi(\theta)$. Then:

$$\begin{aligned} f \circ m^{[1]}(\theta, s) &= f \circ K + sA \circ \psi + \mathcal{O}(s^2) \\ &= T_\omega \circ K + \lambda s T_\omega \circ \psi + \mathcal{O}(s^2) \\ &= T_\omega(K + \lambda s \psi) + \mathcal{O}(s^2). \end{aligned}$$

An estimate of the error of this linear approximation, for a fixed value of the parameter s, is given by the operator

$$\mathrm{Err}(s) = \max_{\theta \in \mathbb{T}} \left\| f \circ m^{[1]}(\theta, s) - T_\omega \circ (\theta, \lambda s) \right\|.$$

Here, $\|\cdot\|$ is some suitable vector norm. By using Err we can compute an interval $\mathcal{I} = [0, s_{max}]$ for which $m^{[1]}$ is a good enough approximation of the manifold according to some prescribed threshold. From this we can produce a fundamental domain, i.e. a sub-interval $[a, b] \subset \mathcal{I}$ from which select a set of curves $\{C_1, C_2, \dots C_m\}$ where $C_j = m^{[1]}(\cdot, s_j)$, $s_j \in [a, b]$ that can be iterated (backwards or forwards, depending if we are dealing with the stable or the unstable manifold) to produce a dense grid of the manifold i.e. $C_j^l = \tilde{f}(C_j^{l-1})$ (here $\tilde{f} = f$ if $|\lambda| > 1$ and $\tilde{f} = f^{-1}$ if $|\lambda| < 1$). At each iterate, the dynamics may spread the points of the mesh approximating the curve C_j^l. This can lead to misleading plots as the mesh of points representing the curve C_j^l in the phase space can be far from equidistant. We can use the matrix $\mathcal{F}$ (or, even better, a Fast Fourier Transform) to produce, at each step, the Fourier coefficients of the curve C_j^l. With the coefficients we are able to re-mesh the curve C_j^l in the seek of a better representation. This process, nevertheless, slows down the program an it is only worth in very specific cases.

3.4 Continuation of invariant curves: A paradigmatic example

In this section we explain a continuation method for invariant curves in a very specific context: The family of invariant curves attached to a fixed point with some elliptic direction. This is, in fact, the only context for which we compute invariant curves in this thesis. The (local) existence of these kind of families follows from the results in [JV97a] by considering a suitable stroboscopic map, at least in the cases we explored here. The general setting is the following: Let us assume that we are provided with a symplectic autonomous skew-product defined from a periodic time dependent Hamiltonian by means of the stroboscopic map. Assume also that there is a fixed point x^* with some elliptic subspace attached to and given by the eigenvalues $\lambda_{1,2} = \exp(\pm \mathrm{i}\nu)$. The values $\pm\nu$ are the normal frequencies associated to x^*. Then, under generic conditions, there exist a Cantor family of invariant curves, parametrized by the frequency such that it tends to the fixed point as the frequency value gets close to the argument ν. In principle we do not know if the frequency of the family tends to the argument from below or from above, we shall comment on a small trick to avoid this eventuality later. The continuation parameter can be chosen to be the pseudo arc length or the frequency of the family. The method follows the classical prediction-correction scheme:

Algorithm 3.4.1. *Let h be a step-size, N be a truncation order and let* deg *denote the degree of a trigonometric polynomial. Assume that l invariant curves ((K_1, ω_1), (K_2, ω_2), $\ldots$, (K_l, ω_l) have been already computed and* $\deg(K_1) \leq \deg(K_2) \leq \cdots \leq \deg(K_l) \leq N$.

1. *Create a prediction by extrapolating a new pair $(\tilde{K}_{l+1}, \omega_{l+1})$. To do so, interpolate the previous pairs, meaning that the both the coefficients and the frequencies are interpolated. The prediction is chosen to be h-close to the pair (K_l, ω_l), therefore, it is an approximation of a new invariant curve.*

2. *Given an approximation, refine it by means of the Newton scheme explained in Section 3.2. We can refine or not the frequency as, in most of the cases, the extrapolated ones are good enough. This will be qualified later: When computing the first invariant curves, the frequency is always refined.*

3. *Control the step-size of the continuation by looking at the number of iterates the Newton method takes to converge. As the differential matrix of the curve is numerically expensive to evaluate, keep the step-size small enough so the Newton method only requires between 2 or 3 iterates to converge.*

4. *Verify if the refined curve has sufficient harmonics (see Section 3.2.2). If this is not the case, increase N and restart step (2).*

On the extra condition: As we explained in Section 3.2.1, if the skew-product is autonomous, the Fourier coefficients do not determine uniquely the invariant curve. To overcome this problem we have to add an extra condition. In the present context we force the invariant curve to cross a suitable linear subspace of codimension 1 for $\theta = 0$. This subspace is usually given by some coordinate of the fixed point. The crossing subspace will be precised at each case.

Remark 3.4.2. *Notice that, as the method assumes the frequency ω to be known, we interpolate the frequencies of the previous invariant tori in the family to get the new frequency. Usually, the interpolation is good enough. However, the frequency can be set free, incrementing the size of the system by one. Another extra condition on the curve is to be imposed also. We can fix another coordinate of the curve and this condition must be compatible with the problem. In the next section we give details on extra conditions which are suited for the first invariant curves.*

3.4.1 The initial guess and the first invariant curves

Let us discuss how to select the initial guess and how to produce the first invariant curves. We already commented that we do not know in advance whether the frequency of the family increases or decreases close to the argument of the fixed point. Of course, there are only two possibilities. We could try both and see which one works but we prefer to set the frequency free in the first steps of the method. To to so, we have to add another extra condition. The one we use is related with the shape of the first initial guess. Being said that, we explain how to select the first pair to be refined. Recall that we are coping with a fixed point with elliptic eigenvalues $\lambda_{1,2} = \exp(\pm \mathrm{i}\nu)$. Let us give a name to the corresponding eigenvectors $v_{1,2} = v_r \pm \mathrm{i} v_i$. The initial guess is given by

$$\tilde{K}_0(\theta) = x^* + h(\tilde{v}_r \cos\theta + \tilde{v}_i \sin\theta), \quad \tilde{\omega}_0 = \nu + h,$$

where h is a small and positive parameter. Notice that $\tilde{K}_0$ and $\tilde{\omega}_0$ verify the invariance equation at linear order:

$$\begin{aligned} f \circ \tilde{K}_0 &= f(x^*) + hA(\tilde{v}_r \cos\theta + \tilde{v}_i \sin\theta) + \mathcal{O}(h^2) \\ &= x^* + h\big(\tilde{v}_r \cos(\theta+\nu) + \tilde{v}_i \sin(\theta+\nu)\big) + \mathcal{O}(h^2), \end{aligned}$$

We have not assumed nothing about the norm of v_r and v_i. When computing the eigenvectors $\lambda_{1,2}$ our method normalize them to have norm one. Therefore we do not have control on the norms of v_r and v_i. The relation between their norms gives us insight on the eccentricity of the family of invariant curves close to the fixed point. We can take advantage on that by

normalizing v_r and v_i using the larger norm. That is, if $s = \max\{\|v_r\|, \|v_i\|\}$, then we select $\tilde{v}_r = v_r/s$ and $\tilde{v}_i = v_i/s$. Finally we comment on how to select the extra condition we need to set the frequency free. The extra condition is given by

$$A\|a_1\|^2 + B\|b_1\|_2^2 = h^2. \tag{3.8}$$

Here, $A = 1$ if $s = \|v_r\|$ and $A = 0$ otherwise and we select $B = 1$ if $A = 0$ and $B = 0$ otherwise. This extra condition allow us to regard ω as a variable and has an extra benefit: This condition, assuming $h \neq 0$, is not satisfied by the fixed point. This is of capital importance if we want the program to start automatically as the basin of attraction of the fixed point is usually larger than the ones of the invariant curves. As a consequence, without the extra condition, the Newton method may converge to the fixed point if the step-size is too small.

Subsequent invariant curves We also compute the subsequent invariant curves using a modified version of (3.8). The number of curves produced using this extra condition is the initial size of the interpolation that is, just a few ones. We modify the condition so the method is not stacked at the first curve. Therefore, if we increment the parameter of continuation by h', (recall that the step-size may be changed due to the step-size control), then we select the second curve to satisfy

$$A\|a_1\|^2 + B\|b_1\|_2^2 = \delta^2,$$

where $\delta = h + h'$. Notice that this extra condition should only be used near the fixed point. Indeed, near a turning point of the continuation curve, it would be problematic as the conditiou would not be satisfied. These few curves at the beginning are computed this way also to prevent the continuation to go back to the fixed point.

3.5 Details on the implementation

A practical problem we face when implementing this program in a computer is the fact that the order of truncation changes as the method goes on. To avoid spending much time allocating and freeing space in memory, we save all the required memory at the beginning of the program. We select a maximal truncation order and save space for a curve, its image and the differential matrix corresponding to this maximal size. The operations on Fourier series are performed only up to the suitable order: The order up to we operate is a global variable that changes according the criterion explained in step (4) of Algorithm 3.4.1. If this global variable exceeds the maximal truncation order, the program stops with a suitable message. At each step we have to repeat operations involving the same evaluations of trigonometric series (namely $\cos\theta_j$, $\sin\theta_j$,$\cos 2\theta_j$, ...), we compute all these quantities and save it in a vector. This vector is also allocated at the beginning of the program and admits the values corresponding to the maximal truncation order. Every time the order of truncation is changed, this vector must be recomputed. This strategy to avoid operations is sometimes known in the literature as "plan" [FJ97]. Once the invariant curve is refined, it is written on a file (together with the differential matrix). To compute the extrapolation, we need the coefficients of the previous curves which are read from the file. The stability of the invariant curve could be computed once step (4) of Algorithm 3.4.1 is completed successfully. However, we do it in a separate program. Again this is done to increase the speed of the continuation. Moreover, the method of continuation may compute a lot of invariant curves (that depends on the step-size) and we may not be interested in computing the stability of all of them. This other program reads the file with the Fourier coefficients of the invariant curves (and their differential) and compute its stability. If a suitable flag is up, this second program performs a Newton method to the curve before computing the stability. This procedure can be adjusted to compute the stability for a selected subset of curves (e.g. one in five).

A dirty trick: To avoid ending up with a very small step-size (and keeping the number of Newton's iterates small) we may select a poor accuracy for the curves (say 10^{-6}). This is low precision is usually good enough for plots but not for other specific purposes. In that cases we refine the curve applying an extra Newton iteration. This is the situation in which we activate the mentioned flag in the program to compute the stability.

3.6 A working example

Let us illustrate the algorithms discussed in the present chapter by means of an example. We compute a continuation of invariant curves of a stroboscopic map obtained from a periodic

Hamiltonian system, the Bicircular Problem (BCP). This example has been presented in Chapters 1 and 2 and deeply discussed in Chapter 5.

We summarize some basic facts to facilitate the reading but we refer to Chapter 5 for details and context. The BCP is a (periodically time dependent) perturbation of the Restricted Three Body Problem. As a consequence of the periodicity of the perturbation, the quasi-periodic invariant structures gain, generically, the frequency of the perturbation. In this example, we focus on the Lagrangian point L_4 and a family of Lyapunov periodic orbits related to one of the elliptic direction to this triangular point. As the perturbation is considered, the Lagrangian point is replaced by a periodic orbit with the same period as the perturbation. In a similar manner, the Lyapunov orbits are replaced by two dimensional invariant tori.

If we consider the stroboscopic map given by the evaluation of the flow at the period of the perturbation, we see the periodic orbit as a fixed point and the family of two dimensional invariant tori as a family of invariant curves. This family emerges from the fixed point and occupies some region of the phase space. In this thesis we discuss the BCP for the Earth-Moon-Sun parameters, being the gravitational potential of Sun the periodic perturbation. In this case, due to the uniformly large effect of Sun's gravity near the triangular points, the Lagrangian point is replaced by three different periodic orbits, due to a broken pitchfork bifurcation. Again, we refer to Chapter 5 for a deeper explanation. These orbits are named by the labels $PO1$, $PO2$ and $PO3$ and their linear character is saddle×centre×centre, centre×centre×centre and centre×centre×centre respectively.

We focus on $PO3$ which is, as said, totally elliptic, therefore has three families of invariant curves growing along each of the elliptic directions: FH3F1, FH3F2, and FV3. This notation is coherent with the one of Chapter 5 and each label is put in context there. Let us point out, for the moment being, that FH3F1 and FH3F2 are horizontal families, the ones enclosed in the planar problem and FV3 is a vertical family.

In Figure 3.1 we display the result of continuing the family FH3F2 with respect the frequency. At the left panel, (a), we show the projection of the family on the (x, y) plane. At the right panel, (b), we present a characteristic curve, the y-value of the invariant curve at $\theta = 0$ versus the frequency of the family. The x component of the invariant curve is fixed, also at $\theta = 0$, to coincide with the one of the fixed point.

The invariant curves in panel (a) are close to ellipses near the fixed point and start to wrinkle as their frequency changes. Notice the loops in the last invariant curves, a consequence of them is that the number of harmonics needed to describe the curve increases significantly. We have stopped the computation at $N = 200$ which corresponds to a system of dimension 1604 harmonics. Moreover, the truncation order has to be increased very rapidly in the last curves. This can be considered as a numerical evidence of a possible ending of the family FHF2. However, we stress that the method presented in this chapter is not suited to

studies near the end of the family, as the numerical cost increases rapidly with the size of the discretization of the operator.

The characteristic curve shown in panel (b) shows how the frequency of the family is changed from the fixed point. At the top right corner of the plot the frequency of the family is close to the natural frequency of the fixed point $PO3$ (approximately 2.18). As the family grows away from the fixed point, the frequency decreases, the last tori in the family has a frequency close to 2.14. We have detected a change of stability near 2.15 at the first turning point. There, the family FH3F2, which is totally elliptic near $PO3$, losses one of his elliptic directions and becomes hyperbolic. At the second turning point, near the vertical value 2.145, the order of truncation of the invariant curves is not enough to produce a trustful approximation of the normal modes. The family seems to loose the remaining elliptic direction, however the accuracy of the eigenfunctions and the eigenvalues is much lower than the one we would be pleased with. We have not investigated further in this direction since, as we have mentioned, this method is not suited neither to study of ending of families, destruction of invariant curves nor loss of smoothness.

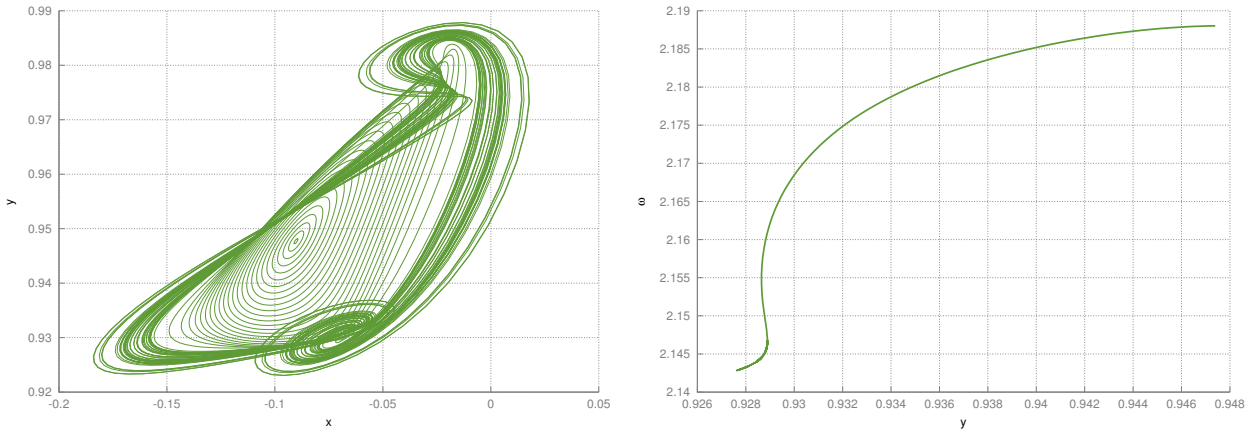

(a) (b)

Figure 3.1: **(a):** Family FH3F2 of invariant curves emerging from the fixed point. **(b):** Characteristic curve related to the family FH3F2. The vertical axis corresponds to the frequency. The horizontal one to y value of the curve at $\theta = 0$.

"Per cada problema que no sabem resoldre, n'hi ha un de més fàcil que tampoc sabem resoldre."

Àngel Jorba

4

Linear skew-products of the complex plane and an affine route of fractalization

Quasi-periodically forced systems are relevant to describe a number of situations in physical problems. We have already mentioned examples in celestial mechanics. The context in which we have worked, up to now, is the symplectic setting but there is a fruitful and vast literature concerning dissipative systems. A large portion of the studies of quasi-periodically forced dissipative systems take care about the mechanisms of destruction of quasi-periodic attractors when some parameter of the system is changed. These mechanisms are, typically, related to a failure[1] of the Implicit Function Theorem (IFT). This is not new: The bifurcation theory of fixed points and periodic orbits (well understood from the early days of development of dynamics as a field of research) also takes care about systems, depending on some parameters, displaying failures of the IFT.

The systematic study of dissipative quasi-periodically forced systems, which generically contain robust quasi-periodic invariant structures, revealed that this is the natural context for non-common phenomena to occur. These phenomena are usually related to the mechanism of destruction we have refereed to above. Of special interest are the mechanisms that lead to the apparition of Strange Nonchaotic Attractors (SNA), see [GOPY84, PNR01a, Kel96, AC09]. These are attracting, non-smooth, invariant objects with non-positive Lyapunov exponents

[1] By a failure of the IFT, we mean that the hypotheses of the theorem, especially the non-degeneracy one, cannot be applied.

and appear frequently in quasi-periodically forced systems after the destruction of some quasi-periodic invariant object. The mechanisms of destruction of invariant curves, are commonly attached to studies of those systems. It is essential to understand the processes in which regular invariant sets become strange, how they breakdown, and identify the key ingredients taking part on it. The correct understanding of this kind of vicissitudes is indispensable to avoid misinterpretations of numerical experiments [HS06, JT08].

Summing up: We are far from having a complete bifurcation theory of quasi-periodic invariant objects. In Chapter 3 we have already mentioned a key ingredient that makes bifurcation of quasi-periodic objects a hard business: The **non-reducibility**. Indeed, reducible quasi-periodic objects can be approached, more or less with success, similarly as periodic ones. Once the linear character is reduced to constant coefficients, classic bifurcation analysis can be carried out and the classical saddle-node, period-doubling, pitchfork, etc. find their counterpart in the quasi-periodic setting. However, not even reducible quasi-periodic invariant sets lack of strange phenomena, see [JMAT18]. Non-reducible invariant sets are much more complicated to understand. In the analysis carried out in Section 3.3 for the linear behaviour of invariant curves we can observe the main difficulty: eigenvalue problems of invariant curves are infinite dimensional. The meaning of reducibility is that only a finite amount of eigenvalues are relevant for the dynamics, while in the non-reducible case the problem stays infinite-dimensional. As a matter of fact, the tools used to study non-reducible dynamics are more complicated and hard to master.

The goal of this chapter is to contribute to the understanding of non-reducible dynamics. To do so, we have to restrict ourselves to the simpler context of low dimensionality as most of the works concerning these issues do. In fact, the bulk of the literature deal with one-dimensional systems. In a perspective to tackle the two-dimensional case we stay in a intermediate step: the complex setting. Indeed, the complex plane, regarded as a real two-dimensional space, has room for some phenomena not allowed to exist in the real line. On the other hand, it does not stop being a one-dimensional space. In this chapter, non-reducibility is induced by a topological obstruction. This kind is known in the literature as **essential non-reducibility**. We would like to stress that essential non-reducibility can not occur in discrete dynamical systems induced by Poincaré maps of Ordinary Differential Equations. Moreover, we also preponderate the dissipative setting and the approach is based on rigorous proofs rather than numerical computations, although some interesting remarks on numerics are given. The system is chosen to be dissipative to force the hyperbolicity of invariant objects as these kind of objects persist under perturbation. We recall that the rest of this thesis is devoted to symplectic systems. Therefore, in terms of applicability, this chapter certainly seems unrelated to the rest of the thesis. However, it is indispensable to simplify the setting when seeking for rigorous proofs in this topic. Indeed, here we are facing fundamental questions and it is mandatory to separate the wheat from the chaff. Let us stress, however, that

these questions arise in the wider context of the rest of the thesis and this chapter should not bee seen as completely isolated, but a small step in the road to understand non-reducible dynamics as a feature that much more complicated systems exhibit.

This chapter is structured as follows: First we devote Section 4.1 to put in context the study and mention relevant results that precede the ones here. In Section 4.2 we review some definitions and results that we will use during the rest of the chapter. We introduce the concept of essential non-reducibility and explain the main feature that distinguish it. The main framework of the rest of the chapter, complex skew-products, is also set. Section 4.3 is devoted to complex linear invertible skew-products. There, essential reducibility is characterized and a linear and topological classification is provided. In section 4.4 we study the behaviour of the Lyapunov exponent with respect to a parameter, in particular we study the regularity of this dynamical indicator in a reducibility loss. Section 4.5 concerns with a particular route of destruction of non-reducible smooth invariant curves. The study is performed on a very simple system. Both numerical and analytical approaches are undertaken.

This is a joint work with Núria Fagella and Joan Carles Tatjer.

4.1 To be or not to be

Let $\mathcal{U} \subset \mathbb{R}^n$ be an open set and $f \in \mathcal{C}^r(\mathcal{U} \times \mathbb{T}, \mathcal{U})$, $r \geq 1$. A diffeomorphisim on its image. Fix $\omega \in \mathbb{T} \setminus (\mathbb{T} \cap \mathbb{Q})$) an irrational number and consider the dynamical system induced by the iteration of the map f:

$$\begin{cases} \bar{x} = f(x, \theta), \\ \bar{\theta} = \theta + \omega. \end{cases}$$

Recall that this kind of systems has been named in Chapter 3 as **quasi-periodic skew-products**. Let us recall some basic facts. The phase space is the product of a basis ($\mathbb{T}$) and a bundle ($\mathcal{U}$). The dynamics on the basis is an irrational rigid rotation with rotation number ω. The dynamics on the bundle depends on the dynamics on $\mathbb{T}$. It is well known that rigid rotations with irrational rotational number do not have fixed points nor periodic orbits. Therefore, skew-products do not have them neither. The simplest invariant objects in this context are **invariant curves**, that is, the graph of a (at least continuous) function $K \in \mathcal{C}^s(\mathbb{T}, \mathcal{U})$, $s \leq r$, which verifies the so-called **invariance equation**:

$$f \circ K = T_\omega \circ K. \tag{4.1}$$

The existence of this kind of invariant objects can be proved rigorously under quite general conditions, by means of a Fixed Point Theorem, when the dynamics on the bundle is contractive. Moreover, the invariant curve K inherits the regularity properties of f, see [Sta97]. See also [Gra74, Eli88, Pös89, JLZ99, Bou97] for results in the symplectic case.

More exotic invariant sets appear in quasi-periodically forced systems. In [GOPY84] it is introduced the concept of SNA. As we already pointed out, these are invariant sets whose associated Lyapunov exponent is non-positive and their geometry is not regular, i.e. the set is not given by the graph of a piecewise continuous function. In that paper, it is studied the following map (named after the authors, Grebogi; Ott; Pelikan; and Yorke, as GOPY map):

Example 4.1.1 (The GOPY map)**.** *Let* $\mathcal{U} = \mathbb{R}$*,*

$$\begin{cases} \bar{x} = 2\lambda \tanh(x)\cos(\theta), \\ \bar{\theta} = \theta + \omega. \end{cases}$$

Here, λ *is a real parameter and* $\omega = \pi(\sqrt{5} - 1)$*.*

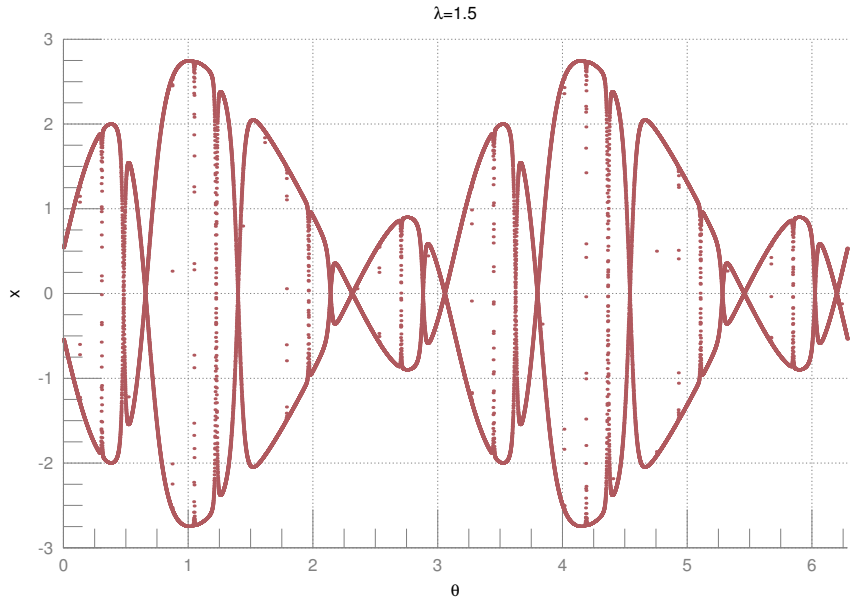

Figure 4.1: SNA for the GOPY map. The horizontal axis corresponds to θ, the vertical to x. It is fixed $\lambda = 1.5$.

The authors are able to prove that, for $|\lambda| > 1$, that there is an attractor that cannot be regular. Moreover, its Lyapunov exponent is non-positive. Numerical computations illustrate, for specific values of the parameters, these assertions. These first ideas were generalized by Keller [Kel96]. He tackles a slightly different setting:

$$\begin{cases} \bar{x} = f(x)g(\theta), \\ \bar{\theta} = \theta + \omega. \end{cases} \tag{4.2}$$

Here f it is required to be differentiable with continuity, non-negative, increasing, strictly concave and to vanish at the origin. The function g must be non-negative and continuous. Notice that the GOPY map does not verify these hypotheses, as $g(\theta) = \cos(\theta)$ takes negative values. Anyhow, the same kind of ideas play around in both cases. In [PF95], it is considered also the case $g(\theta) = \cos(\theta)$ and rational approximations are discussed. It follows, from Keller's work, that the skew-product (4.2) displays a SNA if g has a zero. In particular, the presence of the zero is essential to show the strangeness of the attractor. Notice that, g having a zero means that the linearized dynamics around an invariant set is non-invertible. In [JT08] Jorba and Tatjer characterize (smooth) non-reducible one-dimensional real cocycles as the ones that are non-invertible. Putting together the last results one concludes that there is a relation between strangeness and non-reducibility. As a matter of fact, in the one dimensional case, with suitable regularity hypotheses, non-reducibility and non-invertibility are the same thing. That, as we shall see, is not the case in higher dimensions. In [GOPY84] Grebogy et al. also study the two dimensional map:

Example 4.1.2 (The $2D$ GOPY map)**.** *Let* $\mathcal{U} = \mathbb{R}^2$,

$$\begin{cases} \begin{pmatrix} \bar{x} \\ \bar{y} \end{pmatrix} = \dfrac{\lambda}{1+x^2+y^2} \begin{pmatrix} 1 & 0 \\ 0 & \gamma \end{pmatrix} \begin{pmatrix} \cos\theta & -\sin\theta \\ \sin\theta & \cos\theta \end{pmatrix} \begin{pmatrix} x \\ y \end{pmatrix}, \\ \bar{\theta} = \theta + \omega. \end{cases}$$

Here, λ *and* γ *are real parameters and* $\omega = \pi(\sqrt{5}-1)$.

In [GOPY84], numerical evidences of the existence of an SNA are provided (see Figure 4.2), however, no rigorous proof is presented. As we will see in the next section, non-reducibility also plays a role here. One can observe from the simulations that, as the attractor approaches to the line $\{x = 0, y = 0\}$, it gets increasingly wrinkled, displaying a rare behaviour. This attractor is shown in Figure 4.2.

In the subsequent years to the publication of [GOPY84], a number of works [HH94, NK96, HdlL06, FH12, FH15, FH16, JMAT18] analyze the mechanisms of destruction of quasi-periodic attractors that seem to lead to SNA. Several of them were identified. In [PNR01a] we find a summary of the earliest results. Among all of these mechanisms of breakdown, we pay especial attention to the one named **fractalization mechanism**. This process is described as an attracting invariant curve depending on a parameter that, as this parameter is tuned, the curve gets increasingly wrinkled until it stops being smooth. These mechanism leads, usually, to a chaotic attractor. In the transition between regular curve and chaotic attractor there is some range of the parameters in which the attractor is strange but the Lyapunov exponent is still non-positive. In [NK96] it is introduced the following example

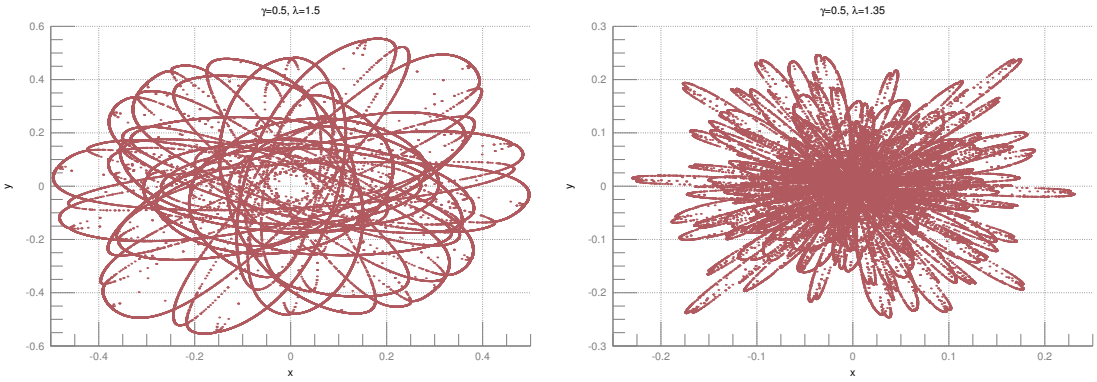

(a) (b)

Figure 4.2: Attractor for the 2D GOPY map. The horizontal axis corresponds to x, the vertical to y. Right: Attractor for $\lambda = 1.5$. Left: Attractor for $\lambda = 1.35$. For all the plots it is fixed $\gamma = 0.5$.

Example 4.1.3 (The quasi-periodically forced logistic map)**.** *Let* $\mathcal{U} = \mathbb{R}$*,*

$$\begin{cases} \bar{x} = bx(1-x) + \varepsilon \sin(\theta), \\ \bar{\theta} = \theta + \omega. \end{cases}$$

Here, b *and* ε *are real parameters and* $\omega = \pi(\sqrt{5} - 1)$*.*

Example 4.1.3 is a quasi-periodic perturbation of the well known logistic map. The parameter ε is to be regarded as the size of the perturbation. For $\varepsilon = 0$, there is an invariant curve which is a straight line given by $\mathbb{T} \times \{1 - 1/b\}$. As the parameter ε is set to be larger than zero this invariant line is deformed into a more sophisticated curve. In Figure 4.3 we show the (attracting) invariant curve for $\varepsilon = 0.1$ (a), $\varepsilon = 0.15$ (b), $\varepsilon = 0.156$ (c) and $\varepsilon = 0.18$ (d). We fix $b = 3$ for all the plots. Notice that, as the value of the perturbing parameter grows, the curve gets increasingly wrinkled until, at first look, the invariant curve stops being a smooth curve. Moreover, the Lyapunov exponent in (c) is non-positive. The authors of [NK96], Nishikawa and Kaneko, suggest that the invariant object seen in (c) is a SNA. In [HS06] Haro and Simó[2] discuss how misleading this kind of computations can be. Using higher accuracy, they show that the attractor shown in (c) is, in fact, a smooth curve. The fractal structure is lost in a closer scale. To explain the odd geometry of the attractor in (c), one has to look at the slope of the invariant curve and notice that it becomes enormous. Indeed,

[2]The title of this section, very similar to the one of [HS06], is an acknowledge to the authors.

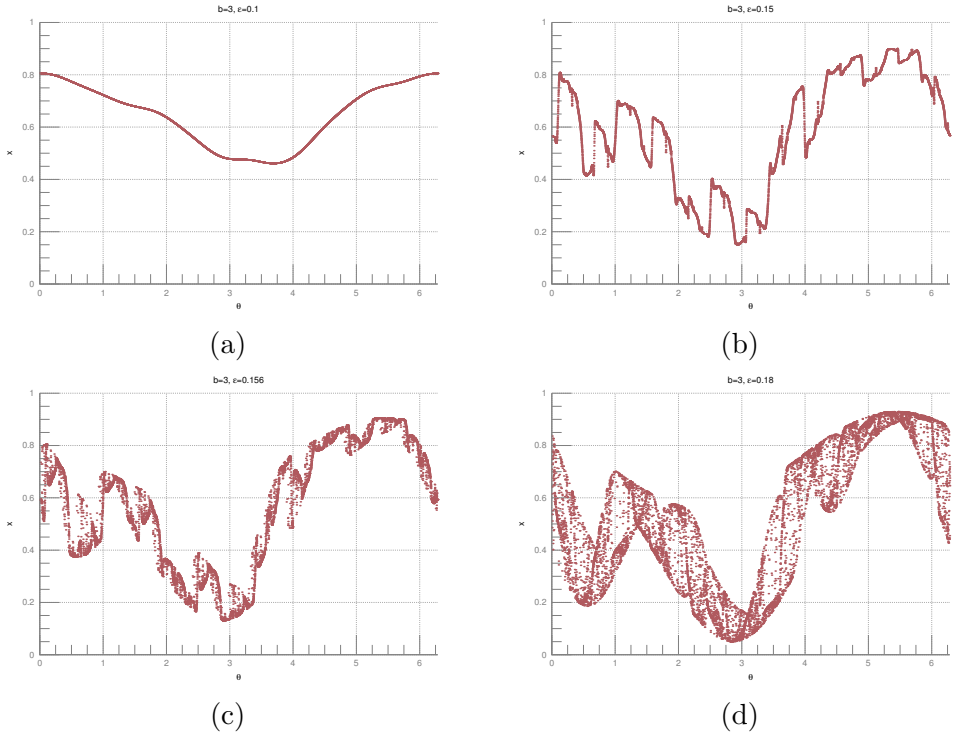

Figure 4.3: Attractor for the quasi-periodically forced logistic map. The horizontal axis corresponds to θ, the vertical to x. Top right: Attractor for $\varepsilon = 0.1$. Top left: Attractor for $\varepsilon = 0.15$. Bottom right: Attractor for $\varepsilon = 0.156$. Bottom left: Attractor for $\varepsilon = 0.18$. For all the plots it is fixed $b = 3$..

a property that captures this odd behaviour is the fact that the derivative of the invariant curve grows much faster than the curve itself. In [HS06] it is also proposed a theoretical explanation for the phenomenon. This is given in terms of the **transfer operator**[3] and its spectrum. We will retrieve this ideas in the following pages. In [JT08], the authors give an alternative approach to this problem. In particular a rigorous definition of fractalization is provided and it is related, in the case of affine systems, to the non-reducibility of the invariant curve. Although these rigorous results cannot be applied to Example 4.1.3, the numerical results are in agreement with the theoretical scenario proposed in [JT08]. It is clear, from all these results that non-reducibility allows some phenomena to occur that cannot happen in reducible cases. One may ask itself whether it is a good idea to take a purely numerical

[3]The transfer operator is introduced in Chapter 3.

approach to this kind of problems. In any case, a critical examination of the numerical results and also of the reports of physical SNA [DDDW97, UMH+13, LKK+15] should always be applied.

4.2 Technical preliminaries

This section is a compendium of definitions and results that shall be used during the rest of the chapter. This is intended to introduce notations and facilitate the reading. From now on, we move to the complex setting, context in which we shall remain until the end of this chapter. Let $a \in \mathcal{C}^0(\mathbb{T}, \mathbb{C}^n)$, consider the system

$$\begin{cases} \tilde{x} = a(\theta)z \\ \tilde{\theta} = \theta + \omega, \end{cases} \tag{4.3}$$

where, ω, as usual is an irrational number. The use of the tilde to denote the iteration of a map is used in the complex case to avoid possible confusions with the complex conjugation.

Let us recall the notion of reducibility adapted in the present context.

Definition 4.2.1 (Reducibility)**.** *A linear skew-product*

$$\begin{cases} \tilde{z} = a(\theta)z, \\ \tilde{\theta} = \theta + \omega, \end{cases}$$

is said to be reducible *iff there exists a linear change of variables, $z = e(\theta)u$ such that the transformed system becomes uncoupled. That is, the transformed system takes the form*

$$\begin{cases} \tilde{u} = b\, u, \\ \tilde{\theta} = \theta + \omega, \end{cases}$$

where $b = e(\theta + \omega)^{-1}a(\theta)e(\theta)$ does not depend on θ.

Definition 4.2.2 (Transfer operator)**.** *Given $a \in \mathcal{C}^0(\mathbb{T}, \mathbb{C}^n)$ and ω irrational, we define the transfer operator $\mathcal{T}$, acting on $\mathcal{T} : \mathcal{C}^0(\mathbb{T}, \mathbb{C}^n) \mapsto \mathcal{C}^0(\mathbb{T}, \mathbb{C}^n)$, as $\mathcal{T}(\psi) = A(\theta - \omega)\psi(\theta - \omega)$.*

The set

$$\Sigma = \mathrm{spec}(\mathcal{T}) = \{z \in \mathbb{C} \mid \mathcal{T} - z \text{ is not invertible}\}$$

is known as the **Mather spectrum** of the transfer operator. As we have seen in Chapter 3, see also [HL07], the spectrum Σ related to a reducible cocycle consists of a finite set of circles.

Moreover, it can be recovered by rotating the eigenvalues of the reduced matrix and the set of eigenvalues is dense in Σ. The spectrum can have more sophisticated properties in the non-reducible case. Let us move back to the real setting for a moment, the reason why we do this will be clear later. In [Her83], Herman introduces the cocycle induced by:

$$M_\lambda = \begin{bmatrix} \cos\theta & -\sin\theta \\ \sin\theta & \cos\theta \end{bmatrix} \begin{bmatrix} \lambda & 0 \\ 0 & \lambda^{-1}. \end{bmatrix}$$

There it is shown that this cocycle is non-reducible. The spectrum of the transfer operator associated to M_λ consists on an anuli for $\lambda > 1$ that collapse into the unit circle at $\lambda = 1$. The non-reducibility, in this case, comes from a topological obstruction. Assuming some arithmetic property on ω, one can prove that M_λ is non-uniformly hyperbolic. By identifying the real and the complex plane, we preserve the same notion of topological obstruction to the reducibility but, due to the rigidity of the last, we loose the space for the non-uniformly hyperbolic linear character to occur.

To understand better this kind of non-reducibility, we restrict ourselves to the one dimensional case. That is, from now on, until the rest of the chapter, we consider cocycles induced by $a \in \mathcal{C}^r(\mathbb{T}, \mathbb{C})$ with $r \geq 0$. A remarkable tool we will use during this chapter is the winding number.

Definition 4.2.3 (Winding number)**.** *Let $a \in \mathcal{C}^0(\mathbb{T}, \mathbb{C} \setminus \{z_0\})$. The **winding number** of a about z_0 is the unique integer* $\operatorname{wind}(a, z_0)$ *such that $\tilde{a}(2\pi) - \tilde{a}(0) = 2\pi\mathrm{i} \operatorname{wind}(a, z_0)$ for all $\tilde{a}$ verifying* $\exp(\tilde{a}(\theta)) = a(\theta) - z_0$.

Remark 4.2.4. *In the case $a \in \mathcal{C}^1(\mathbb{T}, \mathbb{C} \setminus \{z_0\})$, it holds:*

$$\operatorname{wind}(a, z_0) = \frac{1}{2\pi\mathrm{i}} \oint_a \frac{dz}{z - z_0}.$$

In basic courses of complex analysis, it is shown that the curve $\tilde{a}$ exist and that $\operatorname{wind}(a, z_0)$ depends only on a and z_0 (and not on the lifting $\tilde{a}$). For a fixed a, the function $g : \mathbb{C} \setminus [a] \mapsto \mathbb{Z}$ (where $[a]$ denotes the trace of a) defined by $g(z) := \operatorname{wind}(a, z)$ is constant in each connected component of $\mathbb{C} \setminus [a]$. Let us enumerate some relevant properties for fixed $z_0 \in \mathbb{C}$ and $a \in \mathcal{C}^0(\mathbb{T}, \mathbb{C} \setminus \{z_0\})$

1. If $b(\theta) := a(-\theta)$, then $\operatorname{wind}(b, z_0) = -\operatorname{wind}(a, z_0)$.
2. If $\gamma \in \mathbb{C}$, then $\operatorname{wind}(\gamma a, 0) = \operatorname{wind}(a, 0)$.
3. If $\omega \in \mathbb{T}$ and $b(\theta) = a(\theta + \omega)$, then $\operatorname{wind}(b, z_0) = \operatorname{wind}(a, z_0)$.
4. If $\gamma \in \mathbb{C}$, then $\operatorname{wind}(\gamma, z_0) = 0$.

5. If $b \in \mathcal{C}^0(\mathbb{T}, \mathbb{C} \setminus \{z_0\})$, then $\text{wind}(a \cdot b, z_0) = \text{wind}(a, z_0) + \text{wind}(b, z_0)$.

The winding number with respect to 0 is preserved by homotopy in $\mathbb{C}^*$. In particular, reducible cocycles must have winding number about the origin equal to zero. As we will see, if a cocycle has non vanishing winding number around zero, it must be non-reducible. This motivates the following definition.

Definition 4.2.5. *Let $a \in \mathcal{C}^0(\mathbb{T}, \mathbb{C})$. The associated cocycle is said to be* ***essentially non-reducible*** *if* $\text{wind}(a, 0) \neq 0$.

Lemma 4.2.6. *Let $a \in \mathcal{C}^0(\mathbb{T}, \mathbb{C})$ and $\omega \in \mathbb{T}$. If* $\text{wind}(a, 0) \neq 0$*, the transfer operator associated to a has no eigenvalues.*

Proof. We proceed by contradiction. Let $\lambda \in \mathbb{C}$ be an eigenvalue and $\psi \in \mathcal{C}^0(\mathbb{T}, \mathbb{C})$ its associated eigenfunction. Then

$$a(\theta)\psi(\theta) = \lambda\psi(\theta + \omega).$$

Taking winding numbers at both sides of last equation, we have:

$$\text{wind}(a, 0) + \text{wind}(\psi, 0) = \text{wind}(\psi, 0).$$

It follows that $\text{wind}(a, 0) = 0$ which is a contradiction. The result follows. □

Therefore, in the case of essential non-reducibility, the Mather spectrum Σ consists only on spectral values.

Remark 4.2.7. *The concept of winding number can be extended to the case of two dimensional real cocycles. The winding number of a matrix is defined as the winding number of the curve obtained by multiplying the matrix by a constant vector. It is easy to see that the winding number defined in this manner does not depend on the choice of the vector. Therefore it is straightforward to generalize the notion of essential non-reducibility in the case of 2-dimensional cocycles. Moreover, exponential matrices are never essentially non-reducible, see [MH92]. The kind of non-reducibility considered in this chapter does not occur in skew-products that are Poincaré maps of quasi-periodic Ordinary Differential Equations.*

We remind now two standard arithmetic properties of the frequency ω (see e.g. [Lan95, Khi97]). The set of Diophantine numbers defined as follows.

Definition 4.2.8 (Diophantine numbers)**.** *A number ω is called Diophantine of type (γ, τ) for $\gamma > 0$ and $\tau \geq 1$ if*

$$\left|\omega - \frac{p}{q}\right| > \frac{\gamma}{|q|^\tau} \tag{4.4}$$

for all $\frac{p}{q} \in \mathbb{Q}$. We denote by $\mathcal{D}_{\gamma,\tau}$ the set of numbers that satisfy (4.4) for fixed $\gamma > 0$ and $\tau \geq 1$.

We define, as well, the set of numbers of constant type.

Definition 4.2.9 (Number of constant type)**.** *A number ω is said to be of constant type if the coefficients of its continued fraction are bounded.*

The numbers of constant type are Diophantine of type $(\gamma, 1)$. The Diophantine condition shall be used widely during Section 4.3. We require ω to be of constant type in Theorem 4.5.4 and related results.

An important dynamical observable is the Lyapunov exponent. We shall deal with this concept during the whole chapter (see e.g. [KH95]).

Definition 4.2.10. *Fixed $\theta \in \mathbb{T}$, we define the Lyapunov exponent at θ of the skew-product as*

$$\lambda(\theta) = \limsup_{n\to\infty} \frac{1}{n} \log\left|\prod_{j=0}^{n-1} a(\theta + j\omega)\right|. \tag{4.5}$$

We define, as well, the quantity

$$\Lambda = \frac{1}{2\pi} \int_{\mathbb{T}} \log|a(\theta)| d\theta. \tag{4.6}$$

If Λ happens to be finite, then the Birkhoff ergodic Theorem tells us that, for Lebesgue-a.e. $\theta \in \mathbb{T}$, the lim sup (4.5) is in fact a limit and $\lambda(\theta) = \Lambda$. If $a(\theta)$ never vanishes, lim sup is again a lim and coincides with Λ for all $\theta \in \mathbb{T}$. In this last case (4.5) converges uniformly. This follows from the fact that irrational rotations on $\mathbb{T}$ are uniquely ergodic.

The Argument principle is a standard result in complex analysis, see, for instance, [Ahl66]. This result, shall be used In Sections 4.4 and 4.5.

Theorem 4.2.11 (Argument principle)**.** *Let U be a bounded domain of $\mathbb{C}$ with piecewise regular positively oriented boundary. Let V be an open set $\bar{U} \subset V$, and f a meromorphic function on V. Let n be the number of zeros of f in V (counted with multiplicity). Suppose that there are neither zeros nor poles of f on ∂U. Then*

$$\frac{1}{2\pi i} \int_{\partial U} \frac{f'(z)}{f(z)} dz = n.$$

The last result we want to mention is the generalization on complex-valued functions of the Malgrange collocation Theorem, see [Nir71].

Theorem 4.2.12 (Malgrange-Nirenberg)**.** *Let $\mathcal{U} \subset \mathbb{R}^{n+1}$ an open set containing the origin. Consider $f : (t, x) \in \mathcal{U} \mapsto f(t, x) \in \mathbb{C}$ of $\mathcal{C}^\infty$ class. Let $p > 0$ be the first integer such that*

$$\frac{\partial^p}{\partial t^p} f(0, 0) \neq 0.$$

Then, in an neighbourhood of the origin, one has the factorization

$$f(t,x) = Q(t,x)P(t,x),$$

where

$$P(t,x) = t^p + \sum_{j=1}^{p} \lambda_j(x) t^{p-j},$$

and Q and λ_j are $\mathcal{C}^\infty$ complex-valued functions with $Q(0,0) \neq 0$. If f is real, Q and P can be chosen to be real.

When classifying linear skew-products, we will use the following concept.

Definition 4.2.13. *A homeomorphism $g : \mathbb{C} \to \mathbb{C}$ is isotopic to the identity if there exists a continuous map*

$$\begin{array}{rccc} G: & [0,1] \times \mathbb{C} & \longrightarrow & \mathbb{C} \\ & (t,z) & \longmapsto & G(t,z) = G_t(z) \end{array}$$

such that

1. *G_t is a homeomorphism of $\mathbb{C}$ for all $t \in [0,1]$,*
2. *$G_0 = g$ and G_1 is the identity map.*

4.3 Linear invertible skew-products

In this section we focus on linear skew-products on the complex plane,

$$\begin{array}{rccc} F_a: & \mathbb{T} \times \mathbb{C} & \longrightarrow & \mathbb{T} \times \mathbb{C} \\ & (\theta, z) & \longmapsto & (\theta + \omega, a(\theta) z), \end{array} \tag{4.7}$$

where $a(\theta) \in \mathbb{C} \setminus \{0\}$ for all $\theta \in \mathbb{T}$. This means that (4.7) is an invertible map. Moreover, we assume that the map $\theta \mapsto a(\theta)$ is of class C^r ($r \geq 1$) and that $\omega \in \mathcal{D}_{\gamma,\tau}$.

We are interested in classifying these linear skew-products and, to this end, we consider two different types of conjugacies.

Definition 4.3.1 (Topological and linear conjugacy as skew-products)**.** *Two linear skew-products F_a and F_b are* topologically conjugate as skew-products *if there exists a change of coordinates of the form*

$$\mathcal{H}(\theta, z) = (\theta + \nu, H(\theta, z))$$

where $\nu \in \mathbb{T}$ and, for each θ, $H(\theta, \cdot)$ is a homeomorphism of the plane verifying $H(\theta, 0) = 0$ and such that

$$\mathcal{H}^{-1} \circ F_a \circ \mathcal{H} = F_b.$$

When H can be chosen to be linear w.r.t. z, i.e. $H(\theta, z) = c(\theta)z$, with c continuous and $c(\theta)$ different from zero for all θ, then F_a and F_b are said to be linearly conjugate as skew-products up to an angle translation. *If $\nu = 0$ we simply say that F_a and F_b are linearly conjugate as skew-products. Note that this is equivalent to*

$$\frac{a(\theta)}{b(\theta)} = \frac{c(\theta + \omega)}{c(\theta)}, \qquad \text{for all } \theta \in \mathbb{T}.$$

In what follows, we will refer to "conjugacies as skew-products" simply as "conjugacies".

Definition 4.3.2 (Isotopic to the identity as skew-product)**.** *A topological conjugacy as above is isotopic to the identity if $H(\theta, \cdot)$ is isotopic to the identity for each $\theta \in \mathbb{T}$ (see Definition 4.2.13).*

Note that linear conjugacies, in the sense described above, are always isotopic to the identity.

Remark 4.3.3. *The condition of being isotopic to the identity implies that we are asking $H(\theta, \cdot)$ to be a positively oriented embedding of $\mathbb{T}$ on $\mathbb{C}$.*

4.3.1 Linear conjugacy classes

Next, we give necessary and sufficient conditions for two systems to be linearly conjugate. Recall that $\mathrm{wind}(a, 0)$ denotes the winding number of the closed curve $a(\theta)$[4] with respect to the origin.

Proposition 4.3.4 (Linear conjugacy classes)**.** *Let $\omega \in \mathcal{D}_{\gamma,\tau}$. Then there exists $r = r(\tau) > 0$ such that if a and b are of class C^r then F_a and F_b are linearly conjugate if and only if the following two conditions are satisfied:*

(a) $\mathrm{wind}(a, 0) = \mathrm{wind}(b, 0)$.

(b) There exists $m \in \mathbb{Z}$ and a branch of the logarithm such that

$$\int_{\mathbb{T}} \log\left(e^{-im\omega} \frac{a(\theta)}{b(\theta)}\right) d\theta = 0.$$

[4]When it is clear from the context, we use this notation to denote the trace of the function a.

Moreover, if such m exists, it is unique and the linear change of coordinates $H_\theta(z) = c(\theta)z$ satisfies that $\mathrm{wind}(c, 0) = m$.

It is easy to check that (a) and (b) are independent conditions.

Proof. ($\Longleftarrow$) Because of (a), the curve $\frac{a(\theta)}{b(\theta)}$ has winding number 0 and so does $e^{-im\omega}\frac{a(\theta)}{b(\theta)}$. Hence the curve defined by $l(\theta) = \log\left(e^{-im\omega}\frac{a(\theta)}{b(\theta)}\right)$ is also a closed C^r curve. Let us consider its Fourier series

$$l(\theta) = \log e^{-im\omega}\frac{a(\theta)}{b(\theta)} = \sum_{k\in\mathbb{Z}} \alpha_k e^{ik\theta},$$

where $\alpha_0 = 0$ because of (b). As $l(\theta) \in C^r$ we know that $|\alpha_k| = O(1/|k|^r)$. We now define for any $k \neq 0$

$$\widetilde{c_k} = \frac{\alpha_k}{\exp(ik\omega) - 1},$$

and set for example $\widetilde{c_0} = 0$. Note that the Diophantine condition on ω implies that $|\widetilde{c_k}| = \mathcal{O}(|k|^{\tau-r})$. So, if $r > \tau + 1$, the series $\sum_k \widetilde{c_k}e^{ik\theta}$ is absolutely and uniformly convergent and defines a $2\pi-$periodic function L,

$$L(\theta) = \sum_{k\in\mathbb{Z}} \widetilde{c_k}e^{ik\theta}.$$

Moreover, $L \in \mathcal{C}^s$, with $s \geq s(\tau)$, where $s(\tau)$ is the integer part of $-1 + r - \tau$ if $r - \tau \notin \mathbb{N}$ or $s(\tau) = -2 + r - \tau$ if $-1 + r - \tau \in \mathbb{N}$. It is easy to check by comparing the coefficients in the Fourier series that, by construction,

$$l(\theta) = \log e^{-im\omega}\frac{a(\theta)}{b(\theta)} = L(\theta + \omega) - L(\theta).$$

Let $\widetilde{c}(\theta) = \exp(L(\theta))$ which has winding number zero with respect to $z = 0$ because $L(\theta)$ is a closed curve. It follows that

$$\exp\left(L(\theta + \omega) - L(\theta)\right) = \frac{\widetilde{c}(\theta + \omega)}{\widetilde{c}(\theta)},$$

and therefore

$$e^{-im\omega}\frac{a(\theta)}{b(\theta)} = \frac{\widetilde{c}(\theta + \omega)}{\widetilde{c}(\theta)}.$$

Finally, if we define $c(\theta) = e^{im\theta}\widetilde{c}(\theta)$, we have

$$\frac{a(\theta)}{b(\theta)} = \frac{c(\theta + \omega)}{c(\theta)}.$$

Hence, c provides the linear change and $\mathrm{wind}(c,0) = m$.

($\Longrightarrow$) Suppose F_a and F_b are linearly conjugate by a change c and let m be the winding number of $c(\theta)$ with respect to 0. Then

$$\frac{a(\theta)}{b(\theta)} = \frac{c(\theta+\omega)}{c(\theta)}.$$

which already implies (a). Define $\tilde{c}(\theta) = e^{-im\theta}c(\theta)$ which makes $\mathrm{wind}(\tilde{c},0) = 0$ and also

$$e^{-im\omega}\frac{a(\theta)}{b(\theta)} = \frac{\widetilde{c}(\theta+\omega)}{\widetilde{c}(\theta)}.$$

Since $\tilde{c}$ has zero winding number, there exists a branch of the logarithm $\log(\tilde{c}(\theta))$. Then define

$$l(\theta) = \log(\tilde{c}(\theta+\omega)) - \log(\tilde{c}(\theta))$$

which is a branch of the logarithm of $\frac{\widetilde{c}(\theta+\omega)}{\widetilde{c}(\theta)}$, and hence it is a branch of $\log e^{-im\omega}\frac{a(\theta)}{b(\theta)}$. Moreover,

$$\int_{\mathbb{T}} l(\theta)d\theta = \int_{\mathbb{T}} \log(\tilde{c}(\theta+\omega)) - \log(\tilde{c}(\theta))d\theta = 0,$$

and (b) follows. □

Remark 4.3.5. *The value of $r(\tau)$ given in the proof is not optimal, but in any case $r(\tau) > 0$ (see [Rüs76]).*

Remark 4.3.6. *If a and b are C^∞, then $c(\theta)$ is also C^∞.*

From now on, we will denote by $r(\tau) \in \mathbb{N}$ a value of r for which the previous proposition holds. We shall use the previous proposition to find canonical forms for these linear skew-products. We need to differentiate cases depending on the winding number of the curve $\theta \mapsto a(\theta)$.

Proposition 4.3.7 (Linear normal form)**.** *Assume $\omega \in \mathcal{D}_{\gamma,\tau}$, a is $C^{r(\tau)}$ and $\mathrm{wind}(a,0) = n$. Then, for any $m \in \mathbb{Z}$, there exists a linear change, of winding number $-m$, which conjugates F_a to*

$$F_{b(m,\theta)}(\theta, z) = (\theta+\omega, be^{im\omega}e^{in\theta}z)$$

where $b = |b|e^{i\rho} \in \mathbb{C}$ satisfies

$$|b| = \exp\left(\frac{1}{2\pi}\int_{\mathbb{T}} \log|a(\theta)|\, d\theta\right)$$

and

$$\rho = \frac{1}{2\pi}\Im \int_{\mathbb{T}} \log(a(\theta)e^{-in\theta})\, d\theta, \tag{4.8}$$

for any determination of the logarithm. Moreover, two such systems $(\theta+\omega, b_1 e^{in\theta}z)$ *and* $(\theta+\omega, b_2 e^{in\theta}z)$*, with* $b_1, b_2 \in \mathbb{C}$ *are linearly conjugate if and only if* $b_1 = b_2 e^{im\omega}$ *for some* $m \in \mathbb{Z}$*.*

Proof. Consider $m \in \mathbb{Z}$ fixed and choose a branch l of $\log(a(\theta)e^{-in\theta})$ which exists since this expression has winding number 0. We want to find $b = |b|e^{i\rho}$ such that condition (b) in Proposition 4.3.4 is satisfied (observe that condition (a) is already fulfilled). That is, we want that

$$\int_{\mathbb{T}} \log e^{im\omega} e^{i(-m\omega-\rho)} \frac{a(\theta)}{|b|e^{in\theta}} d\theta = 0,$$

for some branch of the logarithm. Given that $l(\theta) = -\log|b| - i\rho$ is such a branch, we obtain

$$\int_{\mathbb{T}} l(\theta) d\theta = 2\pi \log|b| + 2\pi i\rho.$$

Separating real and imaginary part,

$$\int_{\mathbb{T}} \log|a(\theta)| = 2\pi \log|b| \quad \text{and} \quad \Im \int_{\mathbb{T}} l(\theta) d\theta = 2\pi\rho,$$

and the expressions follow. To finish the proof, observe that the systems are conjugate if and only if there exists $p \in \mathbb{Z}$ such that

$$\int_{\mathbb{T}} \log e^{-ip\omega} \frac{b_1}{b_2} d\theta = 0,$$

for some branch of the logarithm. But this is equivalent to requiring $e^{-ip\omega}\frac{b_1}{b_2} = 1$ for some $p \in \mathbb{Z}$. □

From the Proposition above we obtain a trivial corollary about the reducibility of these systems, in the case of winding number 0.

Corollary 4.3.8 (Zero index and reducibility)**.** *Assume* $\omega \in \mathcal{D}_{\gamma,\tau}$*,* $a(\theta)$ *is* $C^{r(\tau)}$*. If* $\operatorname{wind}(a, 0) = 0$*, then the system is reducible. Moreover, the system is reducible to a system of the form* $(\theta+\omega, bz)$ *with* $b \in \mathbb{R}$*, if and only if there exists* $m \in \mathbb{Z}$ *and a branch of the argument such that*

$$\int_{\mathbb{T}} \arg(a(\theta)) d\theta - m\omega = 0.$$

In such case, the change has winding number equal to $-m$*.*

In the nonzero winding number case, it turns out that we can always reduce to the case of $b \in \mathbb{R}$ by changing the phase. More precisely we have the following statement.

Proposition 4.3.9 (Nonzero index)**.** *Assume $\omega \in \mathcal{D}_{\gamma,\tau}$, $a(\theta)$ is $C^r(\tau)$ and $\mathrm{wind}(a,0) = n \neq 0$. Then, there exists a unique $b \in \mathbb{R}$ such that F_a is linearly conjugate (up to angle translation) to*

$$F_b(\theta, z) = (\theta + \omega, be^{in\theta}z).$$

Similarly as before, the precise value of b is

$$b = \exp\left(\frac{1}{2\pi}\int_{\mathbb{T}} \log|a(\theta)|\, d\theta\right).$$

Proof. We apply Proposition 4.3.7 to conjugate F_a to a system $(\theta+\omega, |b|e^{i\rho}e^{in\theta}z)$ by considering $m = 0$. We now change the angle by $H(\theta, z) = (\theta + \rho/n, z)$. If we denote $\psi = \theta + \rho/n$, the transformed system becomes $(\psi + \omega, |b|e^{in\psi}z)$. □

4.3.2 Topological conjugacy classes

We now proceed to classify linear invertible skew-products of class $C^{r(\tau)}$ from a topological point of view. We recall from Definition 4.3.1 that if two linear skew-products F_a and F_b are topologically conjugate then there exist a constant $\nu \in \mathbb{T}$ and a continuous map $H : \mathbb{T} \times \mathbb{C} \to \mathbb{C}$ with $H(\theta, 0) = 0$, such that

$$H(\theta + \omega, a(\theta)z) = b(\theta + \nu)H(\theta, z), \quad \forall \theta \in \mathbb{T},\ \forall z \in \mathbb{C}.$$

In the case H is isotopic to the identity we say that F_a and F_b are topologically conjugate by means of a change isotopic to the identity.

Lemma 4.3.10 (Winding numbers)**.** *Consider $f \in C^0(\mathbb{T}\times\mathbb{T}, \mathbb{C}\setminus\{0\})$ such that, $\forall \rho \in \mathbb{T}$, $\mathrm{wind}_\theta(f(\theta,\rho),0) = p$ and, $\forall \theta \in \mathbb{T}$, $\mathrm{wind}_\rho(f(\theta,\rho),0) = q$, where wind_θ and wind_ρ denote the winding numbers with respect to θ and ρ respectively. Then, $\mathrm{wind}_\theta(f(\theta,\theta),0) = p + q$. In particular*

$$\mathrm{wind}(x(\theta)y(\theta),0) = \mathrm{wind}(x(\theta),0) + \mathrm{wind}(y(\theta),0)$$

for all $x, y : \mathbb{T} \to \mathbb{C}\setminus\{0\}$ continuous.

Proof. First of all notice that, since $f(\theta,\rho) \neq 0$ for each $(\theta,\rho) \in \mathbb{T}\times\mathbb{T}$, we can assume that $|f(\theta,\rho)| = 1\ \forall(\theta,\rho) \in \mathbb{T}\times\mathbb{T}$. As the winding number of f w.r.t. a closed path on the torus remains constant under continuous deformations of this path, we can write the path (θ,θ) $(0 \leq \theta \leq 2\pi)$ as the composition of the paths $(\theta, 0)$ and $(0,\theta)$ and the result follows. □

Proposition 4.3.11 (Winding number and topological conjugacy)**.** *If two linear skew-products F_a and F_b are topologically conjugate, by means of change isotopic to the identity, then* $\mathrm{wind}(a,0) = \mathrm{wind}(b,0)$.

Proof. Since F_a and F_b are topologically conjugate we have the relation

$$H(\theta+\omega, a(\theta)z) = b(\theta+\nu)H(\theta,z) \tag{4.9}$$

that holds for all $\theta \in \mathbb{T}$, $z \in \mathbb{C}$ and some $\nu \in \mathbb{T}$. Let us name $n = \mathrm{wind}(a,0)$ and $m = \mathrm{wind}(b,0)$. Now let us fix the value of z, say $z = 1$. Taking winding numbers at both sides of equation (4.9), and, applying Lemma 4.3.10, it follows:

$$\mathrm{wind}(H(\theta+\omega, a(\theta)), 0) = m + \mathrm{wind}(H(\theta,1),0).$$

Note that $\ell = \mathrm{wind}(H(\theta,1),0)$ is well-defined as $H(\theta,\cdot)$ is a homeomorphism with $H(\theta,0) = 0$ for all θ.

$$\mathrm{wind}(H(\theta+\omega, a(\theta)), 0) = \mathrm{wind}_\rho(H(\rho, a(\theta)), 0) + \mathrm{wind}_\theta(H(\rho, a(\theta)), 0).$$

We have that $\mathrm{wind}_\rho(H(\rho, a(\theta)), 0) = \ell$ and $\mathrm{wind}_\theta(H(\rho, a(\theta)), 0) = n$. The result follows. □

Next, in Theorems 4.3.12 and 4.3.13 we give a topological classification of linear skew-products, depending on the winding number and the Lyapunov exponent defined in Definition 4.2.10.

Theorem 4.3.12 (Topological conjugacy classes)**.** *Assume that $\omega \in \mathcal{D}_{\gamma,\tau}$, and a is a $C^{r(\tau)}$ function which never vanishes. Then the linear skew-product (4.7), namely $(\theta,z) \mapsto (\theta+\omega, a(\theta)z)$ is topologically conjugate to one of the following:*

(a) *If* $\mathrm{wind}(a,0) = 0$ *and the Lyapunov exponent is negative,*

$$\begin{cases} \tilde{z} = \frac{1}{2}z, \\ \tilde{\theta} = \theta + \omega, \end{cases} \tag{4.10}$$

(b) *If* $\mathrm{wind}(a(,0) = 0$ *and the Lyapunov exponent is positive,*

$$\begin{cases} \tilde{z} = 2z, \\ \tilde{\theta} = \theta + \omega, \end{cases} \tag{4.11}$$

(c) *If* $\mathrm{wind}(a,0)=0$*, the Lyapunov exponent is zero,*

$$\begin{cases}\tilde{z}=e^{i\rho}z,\\ \tilde{\theta}=\theta+\omega,\end{cases} \tag{4.12}$$

where ρ *is given by (4.8).*

(d) *If* $\mathrm{wind}(a,0)=n\neq 0$ *and the Lyapunov exponent is negative,*

$$\begin{cases}\tilde{z}=\frac{1}{2}e^{in\theta}z,\\ \tilde{\theta}=\theta+\omega,\end{cases} \tag{4.13}$$

(e) *If* $\mathrm{wind}(a(,0)=n\neq 0$ *and the Lyapunov exponent is positive,*

$$\begin{cases}\tilde{z}=2e^{in\theta}z,\\ \tilde{\theta}=\theta+\omega,\end{cases} \tag{4.14}$$

(f) *If* $\mathrm{wind}(a,0)=n\neq 0$ *and the Lyapunov exponent is zero,*

$$\begin{cases}\tilde{z}=e^{in\theta}z,\\ \tilde{\theta}=\theta+\omega,\end{cases} \tag{4.15}$$

Proof. Items (a) and (b) are an immediate consequence of Corollary 4.3.8 and the fact that in $\mathbb{R}^2$ two attracting (respectively repelling) linear focus are topologically conjugate.

To show (d) observe that Proposition 4.3.9 gives that F_a is linearly conjugate (up to an angle translation) to

$$F_{be^{in\theta}}(\theta,z)=(\theta+\omega,be^{in\theta}z).$$

It is then easy to see that, if the Lyapunov exponent is negative, the following change of variables

$$w=|z|^{\alpha}z,\qquad \alpha=\frac{\log 2}{\log b}-1,$$

produces the desired result. Case (e) is analogous. Items (c) and (f) follow from Propositions 4.3.7 and 4.3.9. □

Theorem 4.3.13. *Assume that* $\omega\in\mathcal{D}_{\gamma,\tau}$*. Then, the skew-products (4.10), (4.11), (4.12), (4.13), (4.14) and (4.15) belong to different topological conjugacy classes. Moreover,*

a) Assume that ρ, ω and 2π are linearly independent over $\mathbb{Z}$. Then, two linear skew-products of the type (4.12) are topologically conjugate by means of a change isotopic to the identity iff they are linearly conjugate.

b) Two linear skew-products of the types (4.13), (4.14) or (4.15) with two different values of n are not topologically conjugate by means of an isotopic change.

Proof. The first claim is obvious. To prove item a), we assume that

$$\begin{cases} \tilde{z} = e^{i\rho_1} z, \\ \tilde{\theta} = \theta + \omega, \end{cases} \qquad \begin{cases} \tilde{z} = e^{i\rho_2} z, \\ \tilde{\theta} = \theta + \omega, \end{cases}$$

are topologically conjugate and that, for instance, ρ_1, ω and 2π are linearly independent over $\mathbb{Z}$. As they are topologically conjugate, by definition, there exists a continuous map H such that

$$H(\theta + \omega, e^{i\rho_1} r e^{i\varphi}) = e^{i\rho_2} H(\theta, r e^{i\varphi}),$$

where $z = re^{i\varphi}$. Let us fix the value of r (for instance, $r = 1$) and let us look at H as a continuous function of two angles. Expanding both sides of the last equality in Fourier series w.r.t. φ, we obtain

$$\sum_k h_k(\theta + \omega) e^{ik\rho_1} e^{ik\varphi} = e^{i\rho_2} \sum_k h_k(\theta) e^{ik\varphi}.$$

As H cannot be the zero function, there exists k such that h_k does not vanish. Hence,

$$h_k(\theta + \omega) = e^{i(\rho_2 - k\rho_1)} h_k(\theta).$$

Expanding h_k in a Fourier series w.r.t. θ, and selecting a non-zero Fourier coefficient h_{kj}, we have that

$$h_{kj} e^{ij\omega} = e^{i(\rho_2 - k\rho_1)} h_{kj},$$

which implies that $j\omega = \rho_2 - k\rho_1 \mod 2\pi$. Applying the same calculation for the inverse conjugation, we have that there exist integer values $\hat{j}$ and $\hat{k}$ such that $\hat{j}\omega = \rho_1 - \hat{k}\rho_2 \mod 2\pi$. Using this last two equations we obtain that

$$(\hat{j} + j\hat{k})\omega = (1 - k\hat{k})\rho_1 + 2\pi m,$$

for some $m \in \mathbb{Z}$. As ρ_1, ω and 2π are linearly independent over $\mathbb{Z}$ we have that $1 - k\hat{k} = 0$, $\hat{j} + j\hat{k} = 0$ and $m = 0$. The solutions of these equations are: $k = \hat{k} = 1$, $\hat{j} = -j$ and $k = \hat{k} = -1$, $\hat{j} = j$, which implies that H has to be of the form $H(\theta, e^{i\varphi}) = h_{-1}(\theta) e^{-i\varphi} + h_1(\theta) e^{i\varphi}$.

Notice that the last conditions cannot hold at the same time. Indeed, if such is the case, there exist j_1 and j_2 verifying the following:

$$j_1\omega = \rho_1 - \rho_2 + 2\pi m_1,$$
$$j_2\omega = \rho_2 + \rho_1 + 2\pi m_2.$$

Adding these equations, it follows $(j_1 + j_2)\omega = 2\rho_1 + 2\pi(m_1 + m_2)$. This case is out of the study as this condition also imply that ρ_1, ω and 2π are linearly dependent over $\mathbb{Z}$ which leads to a contradiction with the hypothesis assumed in (a). Then, if $k = \hat{k} = -1$, as $H(\theta, \cdot)$ restricted to $z = e^{i\varphi}$ is $h_{-1}(\theta)e^{-i\varphi}$, it cannot be isotopic to the identity as it is reversing the orientation of the unit circle. Therefore, the only remaining possibility is $k = \hat{k} = 1$ and then, it is immediate to check that $(\theta, z) \mapsto (\theta, h_1(\theta)z)$ is a linear conjugacy between the two skew-products.

Item b) follows from Proposition 4.3.11 and from the fact that the attracting or repelling character of the origin is preserved by a topological conjugacy. □

Remark 4.3.14. *The dynamics of the maps (4.10), (4.11), (4.13) and (4.14) are locally robust in a neighbourhood of the origin under generic perturbations, because the origin is attracting or repelling. This is not the case for (4.12) and (4.15).*

If we write $(\mathbb{R}/\mathbb{Z}) \times \mathbb{C} = \{0\} \bigcup \left(\bigcup_{r>0} \mathbb{T}^2_r\right)$, where $\mathbb{T}^2_r = \{(\theta, z) \,|\, z = re^{i\varphi}\}$, then $\mathbb{T}^2_r$ is an invariant torus for the maps (4.12) and (4.15). These invariant foliations could be destroyed by a generic perturbation of the map. Moreover, if we consider coordinates (θ, φ) in the torus, the map (4.12) restricted to $\mathbb{T}^2_r$ satisfies $(\theta, \varphi) \mapsto (\theta + \omega, \varphi + \rho)$ which is a translation in the torus and the map (4.15) restricted to $\mathbb{T}^2_r$ satisfies $(\theta, \varphi) \mapsto (\theta + \omega, n\theta + \varphi)$, which is sometimes called a skew shift. The second map is uniquely ergodic if $\frac{\omega}{2\pi}$ is irrational, with the Lebesgue measure as the unique invariant measure and the first map is uniquely ergodic if ω, ρ and 2π are rationally independent.

4.4 Normal forms and Lyapunov exponents

Let us consider a linear quasi-periodic skew-product as defined in (4.7), given by $a \in \mathcal{C}^r(\mathbb{T}, \mathbb{C})$, $r \geq 1$. We have shown that the winding number of a is preserved by linear changes of variables (see Proposition 4.3.4) so that it can be seen as an invariant of the cocycle. In this section we shall study how the Lyapunov exponent varies when introducing a (real) new parameter μ. In particular we are interested about the regularity with respect to the Lyapunov exponent as μ crosses a critical value for which the skew-product is not invertible. Notice that, up to now, all the skew-products have been invertible. To carry out this study, we use Λ_μ as in Definition 4.2.10. Recall that, if Λ_μ is finite, it coincides with the Lyapunov exponent.

Roughly speaking, the next result shows that Λ_μ depends smoothly on μ except when a changes its winding number.

Theorem 4.4.1 (Regularity of Λ)**.** *Let us consider a one-parametric family of quasi-periodic cocycles*

$$\begin{cases} \tilde{z} = a(\theta, \mu)z, \\ \tilde{\theta} = \theta + \omega, \end{cases} \tag{4.16}$$

where ω is Diophantine, μ belongs to an open nonempty interval $I \subset \mathbb{R}$ and $a \in \mathcal{C}^\infty(\mathbb{T} \times I, \mathbb{C})$. We assume that

1. *There exists a unique pair (θ_0, μ_0) such that $a(\theta_0, \mu_0) = 0$.*
2. *$\dfrac{\partial a}{\partial \theta}(\theta_0, \mu_0)$ and $\dfrac{\partial a}{\partial \mu}(\theta_0, \mu_0)$ are linearly independent as vectors of $\mathbb{R}^2$.*

Then, the Lyapunov exponent $\Lambda(\mu)$ is a continuous function of μ such that

1. *Λ is $\mathcal{C}^\infty$ at any $\mu \neq \mu_0$.*
2. *Λ is $\mathcal{C}^0$ at $\mu = \mu_0$ and there exist constants A^+ and A^-, such that, when $\mu \to \mu_0$, the following expression holds:*

$$\Lambda(\mu) = \Lambda(\mu_0) + A^{\pm}(\mu - \mu_0) + \mathcal{O}(|\mu - \mu_0|^2) \tag{4.17}$$

where A^+ is used when $\mu > \mu_0$ and A^- when $\mu < \mu_0$. The values A^+ and A^- never coincide.

A particular situation is when the system is reducible for $\mu < \mu_0$, and non-reducible for $\mu > \mu_0$. In the real 1D case, it is known that the dependence of the Lyapunov exponent w.r.t. the parameter μ is continuous but never differentiable at μ_0, see [JT08]. In the real 2D case, there is numerical evidence of the same phenomenon [HdlL06, FH15]. As a matter of fact, the recent preprint [FT18] contains a rigorous proof of this phenomenon for a class of 2D cocycles arising from the study of the spectrum of some discrete Schrödinger operators. Nevertheless, in our case, the behaviour of the side derivatives of the Lyapunov exponent when μ goes to μ_0 (described in Theorem 4.4.1) is essentially different from the ones described in this paragraph.

The proof of Theorem 4.4.1 is based on finding a suitable normal form in a small neighbourhood of (θ_0, μ_0). To this end, we shall need the following three auxiliary lemmas.

Lemma 4.4.2. *Let $I \subset \mathbb{R}$ be a nonempty open interval and let $a \in \mathcal{C}^r(\mathbb{T} \times I, \mathbb{C})$, $r \geq 2$, such that*

1. *There exists a unique pair* (θ_0, μ_0) *for which* $a(\theta_0, \mu_0) = 0$,

2. $\dfrac{\partial a}{\partial \theta}(\theta_0, \mu_0)$ *and* $\dfrac{\partial a}{\partial \mu}(\theta_0, \mu_0)$ *are linearly independent as vectors of* $\mathbb{R}^2$.

Then

1. $\operatorname{wind}(a(\cdot, \mu), 0)$ *is constant for* $\mu < \mu_0$,

2. $\operatorname{wind}(a(\cdot, \mu), 0)$ *is constant for* $\mu > \mu_0$,

3. $|\operatorname{wind}(a(\cdot, \mu_1), 0) - \operatorname{wind}(a(\cdot, \mu_2), 0)| = 1$ *for* $\mu_1 < \mu_0 < \mu_2$.

Proof. First note that, for $\mu < \mu_0$, condition 1 implies that the curves $a(\cdot, \mu)$ are homotopic on $\mathbb{C} \setminus \{0\}$ (the homotopy is given by $a(\theta, \mu)$ itself) and this shows that $\operatorname{wind}(a(\cdot, \mu), 0)$ is constant for $\mu < \mu_0$. As the same reasoning applies for $\mu > \mu_0$ we can also conclude that $\operatorname{wind}(a(\cdot, \mu), 0)$ is constant for $\mu > \mu_0$. Note that, if $|\theta - \theta_0|$ and $|\mu - \mu_0|$ are small enough,

$$a(\theta, \mu) = \frac{\partial a}{\partial \theta}(\theta_0, \mu_0)(\theta - \theta_0) + \frac{\partial a}{\partial \mu}(\theta_0, \mu_0)(\mu - \mu_0) + \mathcal{O}_2,$$

where $\mathcal{O}_2$ is a term of order 2 in $(\theta - \theta_0)$ and $(\mu - \mu_0)$ For θ near θ_0, $a(\theta, \mu_0)$ is close to a straight line passing through the origin at $\theta = \theta_0$, and hence, dividing a conveniently small disk centered at the origin into two almost equal components. Moreover by condition 2, if $\mu_1 < \mu_0$ the curve $a(\cdot, \mu_1)$ lies in one of these components and, if $\mu_2 > \mu_0$, the curve $a(\cdot, \mu_2)$ lies in the other component. In the situation described, the winding number changes by 1 when μ crosses μ_0, this can be seen, for instance, by applying the Argument principle to the function $f(z) = z$. □

Lemma 4.4.3. *Consider the skew-product defined by* $a \in \mathcal{C}^\infty(\mathbb{T}, I, \mathbb{C})$, *where* I *is a nonempty open interval of* $\mathbb{R}$. *Let us assume that*

1. *There exists a unique pair* (θ_0, μ_0) *such that* $a(\theta_0, \mu_0) = 0$,

2. $\dfrac{\partial a}{\partial \theta}(\theta_0, \mu_0)$ *and* $\dfrac{\partial a}{\partial \mu}(\theta_0, \mu_0)$ *are linearly independent as vectors of* $\mathbb{R}^2$,

3. $\operatorname{wind}(a(\cdot, \mu), 0) = n$ *if* $\mu < \mu_0$,

4. $\operatorname{wind}(a(\cdot, \mu), 0) = n + 1$ *if* $\mu > \mu_0$,

Then, if $|\mu - \mu_0|$ is small enough, there exists a change of coordinates of the form

$$\begin{cases} z = c(\varphi, \mu)\zeta, \\ \theta = \varphi + \theta_0 - \pi, \end{cases}$$

such that the skew-product takes the form

$$\begin{cases} \tilde{\zeta} = h(\mu)e^{in\varphi}(e^{i\varphi} + \nu(\mu))\zeta, \\ \tilde{\varphi} = \varphi + \omega, \end{cases} \tag{4.18}$$

where h is a $\mathcal{C}^\infty$ zero-free function and $\nu(\mu) = 1 + \mu - \mu_0$.

Remark 4.4.4. *The assumptions on the winding number are done in order to assure the winding number to increase when μ crosses μ_0. The fact that changes by 1 follows from Lemma 4.4.2.*

Proof. Note that we can assume that $\theta_0 = \pi$ by simply redefining θ. We call φ to this new angle and, for simplicity, we keep the same notation for the function a (that is, $a = a(\varphi, \mu)$). Note that, as we have $a(\pi, \mu_0) = 0$ and $\frac{\partial a}{\partial \varphi}(\pi, \mu_0) \neq 0$, we can apply the Malgrange Theorem to the function a, which says that a can be factorized as

$$a(\varphi, \mu) = q(\varphi, \mu)(\varphi - \lambda_1(\mu))$$

where q and λ_1 are smooth functions, $|\mu - \mu_0|$ and $|\varphi - \pi|$ are small enough, $\pi - \lambda_1(\mu_0) = 0$ and q is different from zero for all values of φ and μ. Indeed, the function $\varphi - \lambda_1(\mu)$ is complex valued and it has no zeros apart from (π, μ_0). Note that the expression

$$q(\varphi, \mu) = \frac{a(\varphi, \mu)}{\varphi - \lambda_1(\mu)},$$

allows to define q as a $\mathcal{C}^\infty$ function for all values of φ. Then, the equation

$$a(\varphi, \mu) = \frac{q(\varphi, \mu)(\varphi - \lambda_1(\mu))}{e^{in\varphi}(e^{i\varphi} + \nu(\mu))} e^{in\varphi}(e^{i\varphi} + \nu(\mu))$$

is valid for all φ. Let us define

$$b(\varphi, \mu) = \frac{q(\varphi, \mu)(\varphi - \lambda_1(\mu))}{e^{in\varphi}(e^{i\varphi} + \nu(\mu))}.$$

The function b is periodic (and, therefore, continuous) with respect to φ (because a and $e^{in\varphi}(e^{i\varphi} + \nu(\mu))$ are periodic) and has no zeros (notice that the zero of the denominator and the zero of the numerator is the same one). As $a(\varphi, \mu) = b(\varphi, \mu)e^{in\varphi}(e^{i\varphi} + \nu(\mu))$, taking into account that $\mathrm{wind}(a(\varphi, \mu), 0) = \mathrm{wind}(e^{in\varphi}(e^{i\varphi} + \nu(\mu)), 0)$ we obtain that $\mathrm{wind}(b(\varphi, \mu), 0) = 0$. Corollary 4.3.8 gives the existence of the change of coordinates of the form $z = c(\varphi, \mu)\zeta$ in the statement. Hence, the original system is linearly conjugate to (4.18). The result follows. □

Remark 4.4.5. *It is possible to add an extra change of parameters so that (4.18) becomes even simpler, namely*

$$\begin{cases} \tilde{\zeta} = h(\nu)e^{in\varphi}(e^{i\varphi} - \nu)\zeta, \\ \tilde{\varphi} = \varphi + \omega, \end{cases}$$

where h is C^∞ function without zeros.

Lemma 4.4.6. *Consider the linear skew-product associated to*

$$a(\theta, \mu) = h(\mu)e^{in\theta}(e^{i\theta} + \nu(\mu)),$$

where, as usual, μ belongs to a nonempty open interval $I \subset \mathbb{R}$. Let us assume:

1. *h is $\mathcal{C}^\infty$ and has no zeros,*
2. *$\nu \in \mathcal{C}^\infty(I, \mathbb{R})$, $\nu(\mu_0) = 1$ and $\frac{d\nu}{d\mu}(\mu_0) \neq 0$ for some $\mu_0 \in I$.*

Then, the Lyapunov exponent Λ is a continuous function of μ and

1. *Λ is $\mathcal{C}^\infty$ at any $\mu \neq \mu_0$.*
2. *Λ is $\mathcal{C}^0$ at $\mu = \mu_0$ and, there exist constants A^+ and A^- for which, when $\mu \to \mu_0$, the following expression holds:*

$$\Lambda(\mu) = \Lambda(\mu_0) + A^{\pm}(\mu - \mu_0) + \mathcal{O}(|\mu - \mu_0|^2) \tag{4.19}$$

where A^+ is used when $\mu > \mu_0$ and A^- when $\mu < \mu_0$. The values A^+ and A^- are always different.

Proof. We take (4.6) as the definition of the Lyapunov exponent, then

$$\Lambda(\mu) = \log|h(\mu)| + \frac{1}{2\pi}\int_{\mathbb{T}} \log|e^{i\theta} + \nu(\mu)|d\theta.$$

Since h is zero-free and smooth the term $\log|h(\mu)|$ depends smoothly on μ. If something compromises the smoothness of the Lyapunov exponent with respect to μ, it must be located at the second term. Recall that ν is real for all μ. It is easy to see that

$$\frac{1}{2\pi}\int_{\mathbb{T}} \log|e^{i\theta} + \nu(\mu)|d\theta = \frac{1}{2\pi}\int_{\mathbb{T}} \frac{1}{2}\log\left|2\nu(\mu)\left(\frac{\nu^2(\mu)+1}{2\nu(\mu)} + \cos\theta\right)\right|d\theta.$$

After some algebraic manipulation, one can show that, for a given τ

$$\frac{1}{4\pi}\int_{\mathbb{T}} \log\left|2\tau\left(\frac{\tau^2+1}{2\tau} + \cos\theta\right)\right|d\theta = \begin{cases} 0 & \text{if } |\tau| \leq 1, \\ \log\tau & \text{if } |\tau| \geq 1. \end{cases} \tag{4.20}$$

Since $\nu(\mu)$ crosses the value 1 when μ goes through μ_0, (4.20) implies that Λ is only continuous at μ_0. The asymptotic expression (4.19) follows from (4.20). □

Proof of Theorem 4.4.1. Using Lemma 4.4.2 we conclude that the winding number of $a(\cdot,\mu)$ around the origin changes by 1 when μ crosses μ_0. Suppose that $\text{wind}(a(\cdot,\mu),0) = n$ if $\mu < \mu_0$ and $\text{wind}(a(\cdot,\mu),0) = n+1$ if $\mu > \mu_0$ (the inverse situation can be reduced to this one by reversing the parameter μ w.r.t. μ_0). We use Lemma 4.4.3 to put $a(\theta,\mu)$ in normal form with a linear change. The system is transformed to

$$\begin{cases} \tilde{\zeta} = h(\mu)e^{in\varphi}(e^{i\varphi} + \nu(\mu))\zeta, \\ \tilde{\varphi} = \varphi + \omega, \end{cases} \tag{4.21}$$

Recall that the Lyapunov exponent is preserved by linear changes. We finally use Lemma 4.4.6 where the value of the Lyapunov exponent is computed for the normal form. □

4.5 A fractalization mechanism

This section shall be concerned about a breakdown mechanism a certain invariant curve undergoes after an Implicit Function Theorem failure. In this context, an invariant curve is always the graph of a continuous function. In particular, we are concerned with the dynamics of affine skew products of the complex plane. These are maps $F_{\mu,\omega} : \mathbb{T}\times\mathbb{C} \to \mathbb{T}\times\mathbb{C}$ of the form

$$\begin{cases} \tilde{z} = a(\theta,\mu)z + c, \\ \tilde{\theta} = \theta + \omega, \end{cases}$$

where $\omega, \mu \in \mathbb{R}$ and $c \in \mathbb{C}$ are parameters and $\theta \mapsto a(\theta,\mu) \in \mathbb{C}$ is a smooth and invertible map for each μ. The special case of linear skew-products on the complex plane ($c = 0$) appear in a natural way when linearizing the dynamics around an invariant curve of a quasi-periodically forced complex map [Pon07]. Despite its simplicity, we shall see that affine skew-products may exhibit an invariant curve which experiences a fractalization process (see Section 4.5 for a precise definition) as the parameter varies, a phenomenon which is well-known to be found in maps with a non-linear coefficient [GOPY84]. Generally speaking, quasi-periodically forced systems have been considered by several authors (see, for instance, [Sta97, Jor01, Gle02]), and very often specifically to study the fractalization phenomenon and the existence of Strange Non-chaotic Attractors (SNAs) [PMR98, PNR01b, Jäg03, HS06, Jäg07, JNOT07, JT08, Bje09].

As a paradigmatic example, let us consider the map

$$\begin{array}{rccc} F: & \mathbb{T}\times\mathbb{C} & \longrightarrow & \mathbb{T}\times\mathbb{C} \\ & (\theta,z) & \longmapsto & (\theta+\omega, \mu e^{i\theta}z + c), \end{array} \tag{4.22}$$

where ω is the golden mean. The parameter μ is used to control the Lyapunov exponent and to display the fractalization process. As we will see, this system has an attracting invariant

curve z_μ for $|\mu| < 1$. Before undertaking a rigorous approach to study this simple example, let us perform some numerical computations. We display in Figure 4.4, for $c = 1$ and several values of μ, the invariant curve of system (4.22). The behaviour of the curves seems pathological as the parameter μ gets close to one. In particular, the invariant curve wrinkles on itself and winds wildly as grows to infinity. As indicators of the behaviour of this curve when μ approaches 1 from below, we compute its norm, the norm of its derivative, its length and its winding number w.r.t. the origin. It is remarkable that their respective asymptotic behaviour seems very well adjusted by quite simple functions, as shown in Figure 4.5. In Figure 4.6 we also display the following quantity:

$$\Lambda_\mu = \frac{1}{2\pi} \int_{\mathbb{T}} \log |z_\mu(\theta)| d\theta.$$

In this case, we fix $c = \sqrt{1-\mu}$ as scaling factor to prevent the curve to explode to infinity. Here, Λ_μ gives no information about the original system, but it is the Lyapunov exponent of the cocycle

$$\begin{cases} \tilde{\zeta} = z_\mu(\theta)\zeta \\ \tilde{\theta} = \theta + \omega. \end{cases}$$

This quantity, however, provides some insight on the odd behaviour of z_μ. Let us see why. Notice that the curve representing the Lyapunov exponent seems to be continuous but, as the parameter μ gets close to 1, there is an increasing number of peaks. Theorem 4.4.1 gives a theoretical explanation of the situation. As the curve gets close to the bifurcation at zero Lyapunov exponent, its winding number around zero changes dramatically. Every time the curve changes its winding number, it appears a peak in the curve displayed in Figure 4.6. The panel (d) of Figure 4.5 shows that the winding number around zero is going to infinity with as $\mathcal{O}(1-\mu)^{-1}$. It is important to note that the linearization of the dynamics at the invariant curve of this example (which in this case is just the linear part of the system) is not reducible.

At this point, we need a rigorous definition for the word "fractalization". We use the same definition as in [JT08].

Definition 4.5.1 (Fractalization process)**.** *Consider a family curves $z_\mu \in \mathcal{C}^r(\mathbb{T}, \mathbb{C})$, $r \geq 1$, depending continuously on a real parameter μ. A curve undergoes a fractalization process iff there exists some critical value $\mu^\star$ such that for any nontrivial closed interval I.*

$$\limsup_{\mu \to \mu^\star} \frac{\|z'_\mu\|_{I,\infty}}{\|z_\mu\|_\infty} = \infty,$$

where $\|\cdot\|_{I,\infty}$ denotes the sup *norm on I.*

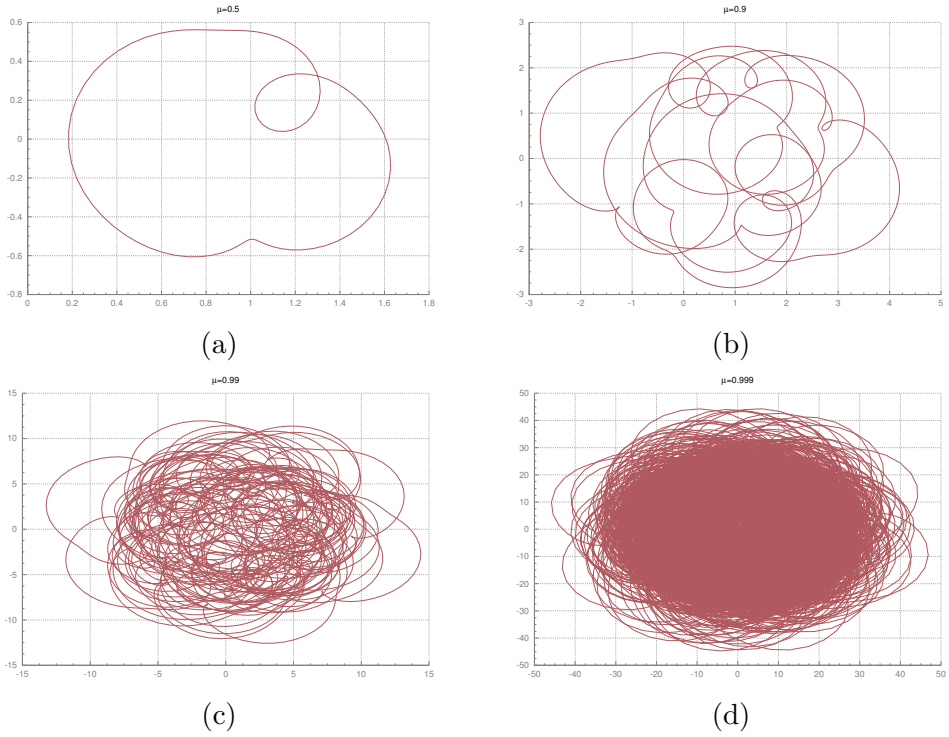

(a) (b) (c) (d)

Figure 4.4: The Attractor of the map (4.22). The horizontal axis corresponds to the real part, the vertical to the imaginary part. Top right: Attractor for $\mu = 0.5$. Top left: Attractor for $\mu = 0.9$. Bottom right: Attractor for $\mu = 0.99$. Bottom left: Attractor for $\varepsilon = 0.999$. For all the plots it is fixed $c = 1$..

Different definitions of fractalization process can be found in the literature. Based numerical evidences appearing in [FH15], Figueras and Haro propose in [FH16] an alternative definition of Fractalization that excludes some cases that fractalize in the sense of Definition 4.5.1. In this chapter, we use Definition 4.5.1 because it gives a straightforward interpretation of the numerical computations shown in Figure 4.22.

Another alternative to characterize the complicated patterns of the invariant curves shown in Figure 4.4 could be the winding number of the curve w.r.t. a given point (for instance, the origin). If this number grows to infinity, that also indicates a kind of irregular behaviour. Let us introduce a rigorous definition.

Definition 4.5.2 (Wild winding process)**.** *Let $z_\mu \in \mathcal{C}^r(\mathbb{T}, \mathbb{C})$, $r \geq 1$ be a family of curves and S a (nonempty) subset of $\mathbb{C}$. If for any $s \in S$ there exists a monotonically increasing sequence $\{\mu_j\}_{j\in\mathbb{N}}$ such that*

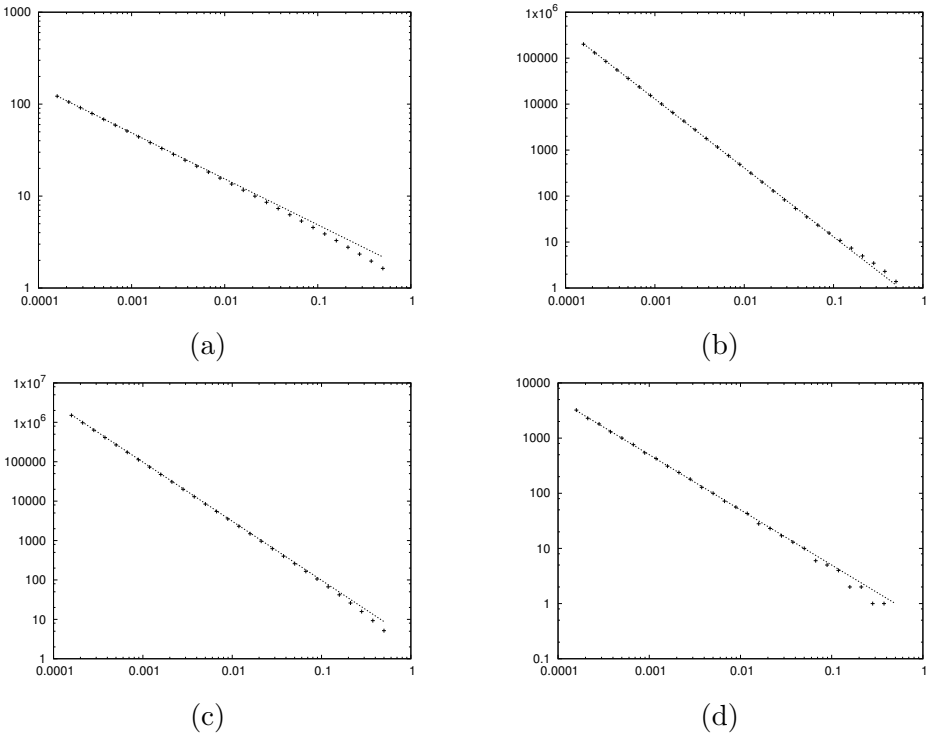

Figure 4.5: Asymptotic growth of the invariant curve of (4.22) w.r.t. μ when $\mu \nearrow 1$, for $c = 1$. The horizontal axis shows $1 - \mu$ and the symbols "+" denote the computed values. The dotted line is the fitting function. **Top:** On the left, fitting $\|z_\mu\|_\infty$ by $1.54(1-\mu)^{-1/2}$. On the right, fitting of $\|z'_\mu\|_\infty$ by $0.41(1-\mu)^{-3/2}$. **Bottom:** On the left, fitting of the length of z_μ by $3.1(1-\mu)^{-3/2}$. On the right, fitting of $\mathrm{wind}(z_\mu, 0)$ by $0.5(1-\mu)^{-1}$.

1. $\lim_{j\to\infty} \mu_j = \mu^\star$,

2. *for each* j, $z_{\mu_j}(\theta) \neq s$ *for all* $\theta \in \mathbb{T}$,

3. $\lim_{j\to\infty} |\,\mathrm{wind}(z_{\mu_j}, s)| = \infty$,

then z_μ *is undergoing a wild winding process on* S *from below when* $\mu \to \mu^\star$.

The following result shows that a curve undergoing a wild winding process fills a certain region of the plane.

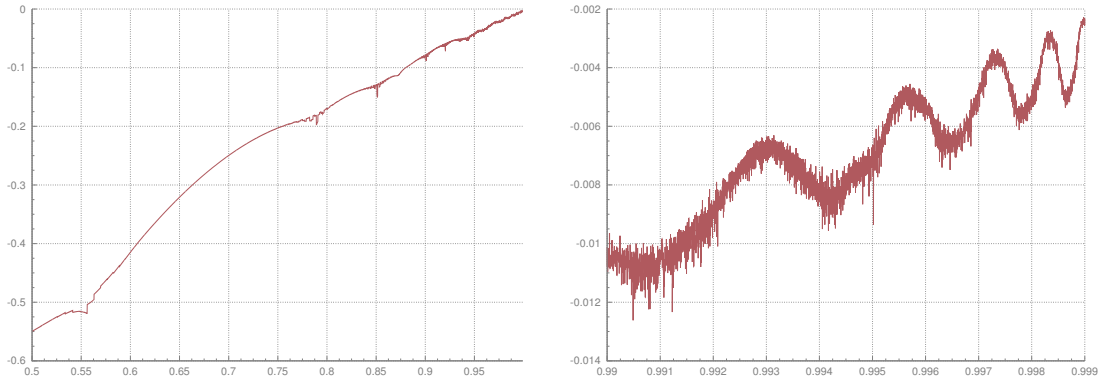

(a) (b)

Figure 4.6: Lyapunov exponent of the attractor of the map (4.22). The horizontal axis correspond to μ. The vertical is the Lyapunov exponent in the bundle direction. It is fixed $c = \sqrt{1-\mu}$

Lemma 4.5.3. *Let $z_\mu \in \mathcal{C}^r(\mathbb{T}, \mathbb{C})$, $r \geq 1$ be a family of curves and S be any subset of $\mathbb{C}$. Assume that z_μ undergoes a winding process on S from below when $\mu \to \mu^\star$. Then,*

$$S \subset \bigcup_{\mu \in (\mu^\dagger, \mu^\star)} \operatorname{graph} z_\mu \qquad \forall \mu^\dagger < \mu^\star.$$

Proof. Let us select a value $\mu^\dagger < \mu^\star$, and let $\{\mu_j\}_{j\in\mathbb{N}}$ be the sequence associated to the process as in Definition 4.5.2. Then, since the sequence is increasing, there exists $\ell > 0$ such that $\mu_j \in (\mu^\dagger, \mu^\star)$ for all $j \geq \ell$. We need to show that, for each $s \in S$, there exists $\mu \in (\mu^\dagger, \mu^\star)$ and $\theta_0 \in \mathbb{T}$ such that $z_\mu(\theta_0) = s$. Let $k \geq \ell$ be such that $\operatorname{wind}(z_{\mu_k}, s) < \operatorname{wind}(z_{\mu_{k+1}}, s)$. Notice that such k exists because of the third condition of Definition 4.5.2. Since there is a change of winding number, there exists a value $\mu \in (\mu_k, \mu_{k+1})$ such that $z_\mu(\theta_0) = s$ for some $\theta_0 \in \mathbb{T}$. The result follows from applying the same argument for each $s \in S$. □

4.5.1 Asymptotic behaviour

Here we focus on the asymptotic behaviour of the invariant curve of the initial example (4.22), as shown in Figures 4.4 and 4.5. In this section we will add the hypothesis that the frequency ω is not only Diophantine, but it is also a number of constant type, that is a Diophantine number with $\tau = 1$ (see Definitions 4.2.8 and 4.2.9) or equivalently an irrational number whose continued fraction expansion has bounded coefficients [Lan95, Khi97].

Theorem 4.5.4 (Fractalization of the invariant curve)**.** *Assume that ω is of constant type. Consider the following affine skew-product*

$$\begin{cases} \tilde{z} = \mu e^{i\theta} z + c, \\ \tilde{\theta} = \theta + \omega, \end{cases} \tag{4.23}$$

where $z \in \mathbb{C}$, $\theta \in \mathbb{T}$, $c \in \mathbb{C} \setminus \{0\}$ and $\mu \in \mathbb{R}$ is a parameter. Then:

1. *This map has a unique invariant curve z_μ for each $\mu \neq 1$. The invariant curve is attracting if $\mu < 1$ and repelling if $\mu > 1$.*

2. *The invariant curve undergoes a fractalization process when $\mu \to 1$. More precisely,*

$$\frac{\|z'_\mu\|_{I,\infty}}{\|z_\mu\|_\infty} = \mathcal{O}(1-\mu)^{-1}$$

   for any nontrivial I.

3. *The invariant curve undergoes a wild winding process on $\mathbb{C}$ when $\mu \to 1$. More concretely,*

$$\mathrm{wind}(z_\mu, s) = \mathcal{O}(1-\mu)^{-1} \qquad \text{for each } s \in \mathbb{C}.$$

Using Lemma 4.5.3, we obtain the following immediate corollary.

Corollary 4.5.5. *For any $\mu_0 \in [0,1)$ we have that*

$$\bigcup_{\mu_0 < \mu < 1} \{z_\mu(\theta) | \text{ for } \theta \in \mathbb{T}^1\} = \mathbb{C}$$

The first step in the proof of Theorem 4.5.4 is to note that the invariant curve can be obtained explicitly as stated by the next lemma.

Lemma 4.5.6. *Assume that $0 < |\mu| < 1$. Then, (4.23) has a unique invariant curve given by*

$$z_\mu(\theta) = c \sum_{k=0}^{\infty} \mu^k e^{-i\frac{k(k+1)}{2}\omega} e^{ik\theta}. \tag{4.24}$$

Proof. Any continuous closed curve can be written as a (convergent) Fourier series,

$$z_\mu(\theta) = \sum_{k \in \mathbb{Z}} z_k^\mu e^{ik\theta},$$

and the invariance equation $z_\mu(\theta+\omega) = \mu e^{i\theta} z_\mu(\theta) + c$ determines the Fourier coefficients of z_μ:

$$\begin{aligned}
&\vdots \\
e^{-i2\omega} z_{-2}^\mu &= \mu z_{-3}^\mu \\
e^{-i\omega} z_{-1}^\mu &= \mu z_{-2}^\mu \\
z_0^\mu &= \mu z_{-1}^\mu + c \\
e^{i\omega} z_1^\mu &= \mu z_0^\mu \\
e^{i2\omega} z_2^\mu &= \mu z_1^\mu \\
&\vdots
\end{aligned}$$

Note that, as the Fourier series converges, the condition $|\mu| < 1$ implies that $z_k^\mu = 0$ if $k < 0$. Then, it is straightforward to derive an expression for coefficients with $k \geq 0$:

$$z_k^\mu = c\mu^k e^{-i\frac{k(k+1)}{2}\omega}, \qquad k = 0, 1, 2, \ldots. \qquad \square$$

Remark 4.5.7. *Note that, if $|\mu| < 1$, the series converges to an analytic function. When $|\mu| > 1$ the situation is similar, but now Fourier coefficients corresponding to positive indices are zero, and the series also converges to an analytic function. When $|\mu| = 1$, the map (4.23) does not have invariant curves.*

Taking derivatives w.r.t. θ, the invariance equation $z_\mu(\theta+\omega) = \mu e^{i\theta} z_\mu(\theta) + c$ becomes

$$z'_\mu(\theta+\omega) = \mu e^{i\theta} z'_\mu(\theta) + i\mu e^{i\theta} z_\mu(\theta),$$

and this suggests that the sup norm of z'_μ grows faster (w.r.t. μ) than the sup norm of z_μ. It is remarkable that the study of the Fourier series of this invariant curve was already considered by Hardy and Littlewood in 1914. More concretely, if ω is of constant type, in [HL14] it is shown that

$$z_\mu(\theta) = \mathcal{O}(1-\mu)^{-1/2}, \tag{4.25}$$
$$z'_\mu(\theta) = \mathcal{O}(1-\mu)^{-3/2}, \tag{4.26}$$

both uniformly in θ. As a consequence, the growth of the corresponding sup norm obey corresponding asymptotic laws. This explains Figure 4.22 We are now ready to give the proof of Theorem 4.5.4.

Proof of Theorem 4.5.4. The existence and uniqueness of the invariant curves are given by Lemma 4.5.6. Notice that the Lyapunov exponent of the curve is $\Lambda_\mu = \log \mu$. Therefore, the curve is attracting if $\mu < 1$ and repelling if $\mu > 1$. The fractalization of the invariant curve when $\mu \to 1$ is given directly by (4.25) and (4.26).

Let us prove now that the curve undergoes a wild winding process when $\mu \to 1$. The winding number of z_μ around a point s is given by

$$\operatorname{wind}(z_\mu, s) = \frac{1}{2\pi i} \int_{\mathbb{T}} \frac{z'_\mu(\theta)}{z_\mu(\theta) - s} d\theta \tag{4.27}$$

and can be defined whenever $z_\mu(\theta) \neq s$ for all $\theta \in \mathbb{T}$. If $\mu < 1$, by the Argument principle , the winding number of z_μ around s is the number of zeros of the power series

$$f(z) = \sum_{k=0}^{\infty} e^{-i\frac{k(k+1)}{2}\omega} z^k - s$$

inside the region with boundary given by the curve $\gamma(\theta) := \mu e^{i\theta}$ (i.e. the disk of radius μ). It follows that (4.27) increases with μ. Let $\epsilon > 0$ be small enough so that f is analytic on the closed disk $D_{\mu+\epsilon}(0)$ (i.e. $\mu + \epsilon < 1$). Since the zeros of f are discrete, it has a finite number of zeros in $D_{\mu+\epsilon}(0)$. This implies that the winding number of z_μ around s can be defined for almost every $\mu \in (0, 1)$, exactly those for which γ does not have any zero of f. Therefore, there exists an increasing sequence $\{\mu_j\}_{j\in\mathbb{N}} \subset (0, 1)$ such that $\lim_{j\to\infty} \mu_j = 1$ and $z_{\mu_j}(\theta) \neq s$ for each $\theta \in \mathbb{T}$. Hence, the winding number of z_{μ_j} around s can be defined for each $j \in \mathbb{N}$. To find the asymptotic behaviour of $\operatorname{wind}(z_\mu, s)$ we can use (4.25) and (4.26) on the expression (4.27). □

Corollary 4.5.8. *Theorem 4.5.4 also holds for the map*

$$\begin{cases} \tilde{z} = \mu e^{in\theta} z + c, \\ \tilde{\theta} = \theta + \omega, \end{cases} \tag{4.28}$$

for any $n \in \mathbb{Z} \setminus \{0\}$, but with asymptotic behaviour:

$$\frac{\|z'_\mu\|_{I,\infty}}{\|z_\mu\|_\infty} = \mathcal{O}((1 - \hat{\mu})^{-1})$$

and

$$\operatorname{wind}(z_\mu, s) = \mathcal{O}((1 - \hat{\mu})^{-1}) \qquad \text{for each } s \in \mathbb{C},$$

where $\hat{\mu} = \sqrt[n]{\mu}$.

Proof. Using a similar argument as in Lemma 4.5.6 one can show that the invariant curve of this new skew-product is

$$z_\mu(\theta) = c\sum_{k=0}^{\infty} \mu^k e^{-i\frac{nk(nk+1)}{2}\omega} e^{ink\theta}.$$

Finally, renaming $j = nk$, $\hat{\mu} = \sqrt[n]{\mu}$, we reduce this series to the invariant curve of Theorem 4.5.4.

□

Remark 4.5.9. *Note that, for $n = 0$, (4.28) is reducible, the invariant curve for $\mu \neq 1$ is $z_\mu(\theta) = c/(1-\mu)$ and, obviously, it does not fractalize when μ goes to 1.*

On the reducible case

There is a more general context in which we can show that no fractalization exist in the reducible case. Let us see how reducibility to real coefficients is, under suitable hypotheses, an obstruction to fractalization. Suppose that we deal with an affine skew-product such as

$$\begin{cases} \tilde{z} = \mu a(\theta) z + b(\theta), \\ \tilde{\theta} = \theta + \omega, \end{cases} \tag{4.29}$$

with a and b C^∞ functions not depending on μ and $\mathrm{wind}(a, 0) = 0$. Then it can be reduced to constant coefficients. Assume, in order to simplify the discussion, that there exists $m \in \mathbb{Z}$ and branch of the argument such that

$$\int_{\mathbb{T}} \arg(a(\theta))d\theta - m\omega = 0.$$

Then, by Corollary 4.3.8, system (4.29) is linearly conjugate to a system with real linear part:

$$\begin{cases} \tilde{\zeta} = \mu\zeta + b(\theta), \\ \tilde{\theta} = \theta + \omega. \end{cases} \tag{4.30}$$

In order to avoid heavy notation, we have recovered the symbols μ, and b keeping in mind that are not the same ones as in the beginning. Let us expand the invariant curve in Fourier series and apply the invariance condition, this yields an (diagonal) infinite system of equations for the coefficients. One has,

$$z_k^\mu = \frac{b_k}{e^{ik\omega} - \mu}.$$

As b is of class C^∞ and ω is Diophantine. The decay of the Fourier coefficients overcomes the small divisors if b is average free (i.e. $b_0 = 0$). Moreover, in any case, the $\mathcal{C}^0$ norm of

the derivative is always bounded, therefore the invariant curve does not undergo neither a fractalization nor a winding process. Indeed,

- If b is average free, there is no loss of smoothness when μ passes through the critical value $\mu = 1$.
- If b has average different from zero, the curve stops being bounded when μ crosses $\mu = 1$ and blows up as $(1 - \mu)^{-1}$.

Part II

Applications

"The Sun is a wondrous body. Like a magnificent father! If only I could be so grossly incandescent!"

Solaire of Astora

5

The effect of Sun's gravity on a small particle in the Earth-Moon system

During the last years, the scientific community has increased its interest in the natural motion occurring in the Earth-Moon system. The list of possible applications is vast, for instance: the study of the far side of Moon and the relation with the translunar point; the aim to exploit the cis-lunar space and the convenience of using the invariant structures related to L_1.

We have mentioned a couple or applications which are specifically related to the Lagrangian points but, obviously, the list goes on covering a wide range of interests. Efficient mission designs depend ultimately on the understanding of the natural dynamics. To fulfill this goal, it is advisable to use simplified models. Simple models allow us to understand the underlying mechanisms that lead to interesting phenomena. From the dynamical systems point of view, the comprehension of the invariant structures and its stability of simple models has helped to shed light on difficult problems such as the motion of asteroids through the solar system, station keeping of spacecrafts and taking advantage on the natural dynamics to design spacecraft mission. Perhaps the most illustrative example for the purpose of this chapter is the existence of the Trojan asteroids that can be predicted using the effective stability around the triangular points of the Sun-Jupiter Restricted Three Body Problem. This example is convenient for the purposes of this chapter because the existence of objects in the triangular points may have a counterpart in the Earth-Moon system: the Kordylewsky

clouds[1]. We shall come back to this example during this chapter but, for the moment being, we want to stress that the existence of these clouds cannot be established by using the same theoretical mechanisms as the Trojan asteroids. In fact, the literature related to the Kordylewsky clouds has been stumbling around the existence or nonexistence of objects in the Earth-Moon triangular points, mostly because of the lack of observations. Therefore it is convenient to analyze whether a simple model is suitable for the problem we want to study.

The Earth-Moon Restricted Three Body Problem (RTBP) is the most used simple model for the motion of a small body in the Earth-Moon system. There is, however, a remarkable number of works that take into account the presence of Sun's gravitation (see, for instance, [GJMS91b, GJMS91a, GJMS93, GLMS01, GLMS85]). Indeed, the most relevant effect ignored by the Earth-Moon RTBP is the gravitational attraction of Sun. In this respect, a simple model to study the dynamics near the Earth-Moon system needs to take into account Solar gravity. The problem, has a natural non-autonomous periodic time dependence formulation. An advantage of the periodic models is that they can be handled by means of a stroboscopic map i.e. the map defined by the evaluation of the flow at the period of the vectorfield. This is crucial because, while the complexity of the system increases, the study of maps (even if they are numerically defined) is, in some aspects, more comfortable than the study of flow. In periodic time dependent systems, the simplest invariant objects, the ones the dynamics is organized from, are the periodic orbits with the same period as the vectorfield. These periodic orbits appear as fixed points of the stroboscopic maps and their robustness is assured by the classical Implicit Function Theorem. We would like to remark that, in quasi-periodic models the simplest invariant objects are invariant tori. The computation and study of these objects is more difficult. The discussion in this paragraph vindicates a closer look to periodic models for the Earth-Moon system. We have selected two among the literature, the Bicircular Problem and the Quasi-Bicircular Problem. Both models include Sun's gravity and can be written as periodic perturbations of the RTBP.

The Bicircular Problem is a periodic perturbation of the RTBP that takes into account the direct gravitational effect of a third primary (in our case, Sun) on the particle. This model captures the non-stable character of the triangular points. Henceforth, is is suitable to use it when studying problems related with these locations (see, for instance, [CJ00, Jor00]). A remarkable shortcoming of the BCP is its lack of coherence i e. the motion assumed for the primaries does not verify Newton's laws. Moreover, the BCP has no translunar dynamical structure. This justifies the seek for a more complicated model for the study of, at least, the L_2 point.

The Quasi-Bicircular Problem is a coherent version of the BCP. It takes into account, not only the effect of Sun on the test particle, but also the effect on Earth and Moon. As a consequence, the distance between the two smallest primaries, Earth and Moon, is

[1]See Chapter 7

non constant. Moreover, unlike the BCP, the QBCP has a dynamical equivalent of the L_2 equilibrium point. Hence, the QBCP is suitable for the study of the collinear points, especially L_1 and L_2. This model was introduced by C. Simó, and it has been used in several works, see [And98, AS00, And02] and, more recently, [BMGLD17].

With this chapter, we aim to provide a general insight about the dynamics of these models for a particle in the Earth-Moon system. We care about (practical) stable motion near the triangular points and, to do so, we use the BCP. We also study invariant manifolds related to the collinear points in the QBCP. We believe that the value of this chapter is, precisely, giving a wide perspective and help the interested reader to choose a suitable simple model to face a first exploration related to a problem concerning the Earth-Moon system.

The chapter is organized as follows: Section 5.1 is devoted to a brief description of the RTBP. We explain how the phase space near the Lagrangian points is organized referencing some remarkable works and mentioning the techniques used to study the problem. Section 5.2 describes how the BCP can be used to study the motion near the triangular points. The advantage of this model with respect to the RTBP is that it captures the unstable character of the triangular points in the real system. The results presented are mainly devoted to stable motion in an extended vicinity of the triangular points. In Section 5.3 we describe results concerning the QBCP. We focus on the unstable manifolds related to the periodic orbits that replace the collinear points. Finally, Section 5.4 is devoted to conclusions and Section 5.5 to technical details.

5.1 Restricted Three Body Problem

The (Circular) Restricted Three Body Problem (RTBP) is a simplified model for the motion of a massless particle under the gravitational attraction of two massive bodies, the so-called primaries [Sze67]. The primaries are assumed to revolve along circular orbits around their common centre of masses. It is usual to take units of masses so the sum of the masses of the primaries is equal to one. The units of length are taken so the distance between the primaries is equal to one and the units of time are taken so the period of the revolution of the primaries is equal to 2π. It is also standard to take a rotating frame of reference that fixes the primaries at the horizontal axis. The RTBP is an autonomous Hamiltonian system with three degrees of freedom. The Hamiltonian function writes as:

$$H_{RTBP} = \frac{1}{2}(p_x^2 + p_y^2 + p_z^2) - xp_y + yp_x - \frac{1-\mu}{r_{PE}} + \frac{\mu}{r_{PM}}, \tag{5.1}$$

where $r_{PE}^2 = (x-\mu)^2+y^2+z^2$, $r_{PM}^2 = (x-\mu+1)^2+y^2+z^2$ and $\dot{x} = p_x+y$, $\dot{y} = p_y-x$, $\dot{z} = p_z$. The parameter μ is called the mass parameter and is the mass of the smallest primary. In

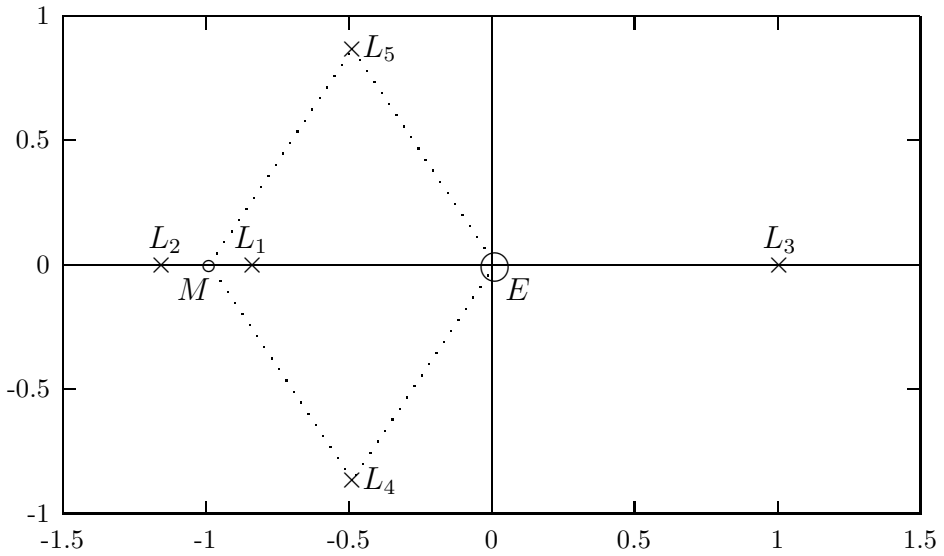

Figure 5.1: The Restricted Three Body Problem: Location of Earth, Moon and the Lagrangian points.

the case of the Earth-Moon system $\mu \approx 0.012$. It is well known that the RTBP has five equilibrium points. Three of them, the collinear points, are located in the horizontal axis. The other two, the triangular points, are located at the third vertex of an equilateral triangle whose other two vertices are the position of the primaries.

The Hamiltonian of the RTBP is an integral of motion and no other independent integral exists in the problem. In many texts, this integral of motion is presented under a slightly different form as the Jacobi integral. Each surface level of this integral is a five dimensional manifold. If the velocities are set to zero, this defines the so-called Zero Velocity Surface. These surfaces separate the configuration space in different regions. The trajectories of the system cannot cross the boundary between two of these regions. The shape of these regions change with the value of the Jacobi integral. As the Lagrangian equilibrium points are critical points of the Jacobi integral, the topology of these regions change when the energy value crosses the value associated to one of the Lagrangian points (for more details, see [Sze67]).

5.1.1 Motion near the collinear points

The three collinear points are of type saddle×centre×centre. This means that, under generic conditions, a 4-dimensional centre manifold emerges from each of these points. These man-

ifolds are tangent to the elliptic eigendirections at the points. There exist, as well, one dimensional stable and unstable invariant manifolds emerging tangentially to the hyperbolic eigendirections. Moreover:

- By the Lyapunov Centre Theorem [MH92], two families of periodic orbits, the Lyapunov families, emanate from the equilibria. One of the families is born tangent to the (z, p_z) plane so it is called vertical family. The other family is contained in the (x, y, p_x, p_y) plane and it is called horizontal family. One can parametrize each families by the amplitude of the orbits. The horizontal families related to L_1 and L_3 can be continued up to trajectories which collide with Earth. The horizontal family related to L_2 can be followed up to collisions with Moon. The vertical families end up in bifurcating planar orbits [Mon01, GJMS91c].

- The Lyapunov families can be regarded as the non-linear continuation of the harmonic oscillator given by each elliptic direction of the linearization around the equilibria. When the amplitude tends to zero, the frequency of the family tends to the normal modes of the equilibria.

- As the frequency varies, the horizontal family undergo a $1:1$ resonance and the Halo family [FK73a, BB79, GJMS91c] are originated (by means of a pitchfork bifurcation). Secondary families of Halo-type orbits appear by duplication and triplication of the main family [GM01, Bro68].

The centre manifold can be computed by means of normal form techniques [Jor99, JM99b, JM99a], with the parametrization method [HL05a, HL05b, FJ10b, FJ10c] and also numerically [GM01]. The dynamics restricted to the centre manifold can be described by a Hamiltonian with two degrees of freedom. By fixing a level of energy and taking a Poincaré section, one can reduce the problem to the study of a family of area preserving maps. This methodology suffices to observe the phase space during the bifurcation that give rise to the Halo families. We have explained in Chapter 1 how to generalize the computation, by means of normal form techniques, of the centre manifold related to periodic orbits.

5.1.2 Motion near the triangular points

The Earth-Moon triangular points of the RTBP are linearly stable [Sze67]. KAM theory can be used to establish the existence of a dense set of Lagrangian invariant tori close enough to the equilibria [MS86]. This has important consequences on the nonlinear stability of the triangular points. If we restrict ourselves to the planar case, these KAM tori (of dimension two) act as barriers for the dynamics in a fixed level of energy. Therefore, KAM tori enclose

stable motion for initial conditions which are close enough to the triangular points. This argument based on KAM theory falls apart in the spatial case. Indeed, Lagrangian tori have, in that case, dimension three and the phase space, for a fixed level of energy, is five dimensional. There is, in general, no way to avoid Arnold diffusion [Arn64] . However, using normal form techniques, it is possible to derive bounds on the diffusion time [GDF$^+$89]. These, make us think about regions of practical stability i. e. regions in which the motion is non-stable but initial conditions take a long time, maybe longer than the expected age of the solar system, to escape. These theoretical results are valid for a small region near the triangular points and numerical simulations provide evidences of large regions of practical stability [SSST13].

It is natural to look for other invariant structures that play a remarkable role to define the shape of the (numerically computed) region. In this regard, [SSST13] provides numerical evidence on the role of the centre-unstable and centre-stable manifolds of the collinear point L_3. These manifolds are of dimension five and act as barriers of the dynamics. Obviously, the motion driven by these manifolds escape from the vicinity of the triangular points at some moment, but, again, the required time to do so can be large.

5.2 The Bicircular Problem and the triangular points

The Bicircular Problem (BCP) is a restricted four body problem [Hua60, CRR64]. There are three primaries and a fourth, massless, test particle. In our case, the three primaries are Earth, Moon and Sun. However, this model has been utilized in other cases [BGMO16]. It is assumed that Earth and Moon move as in the RTBP, that is, along a circular orbit around its common centre of masses. Let us name C_{EM} this barycentre. Name C_{SEM} the centre of masses of the Sun-C_{EM} system. As Moon and Earth move, it is assumed that Sun and C_{EM} move in another circular orbit around C_{SEM}. It is usual to take the units and the synodic coordinates of the Earth-Moon RTBP (see Figure 5.2). We refer to [GJMS91c] for a detailed derivation of the equations of motion. The BCP is not coherent, that is, the trajectories followed by the primaries do not obey Newton's laws. This is not an inconvenient since the model has been shown to be useful to describe the dynamics near the triangular points [SGJM95]. As a dynamical system, the BCP is a Hamiltonian system with three and a half degrees of freedom, i.e., a non-autonomous periodically time dependent with three degrees of freedom. The Hamiltonian function, written in the RTBP coordinates and units, is given by

$$H = \frac{1}{2}(p_x^2 + p_y^2 + p_z^2) - xp_y + yp_x - \frac{1-\mu}{r_{PE}} - \frac{\mu}{r_{PM}} - \frac{m_S}{a_S^2}(y\sin\theta - x\cos\theta) - \frac{m_S}{r_{PS}}. \qquad (5.2)$$

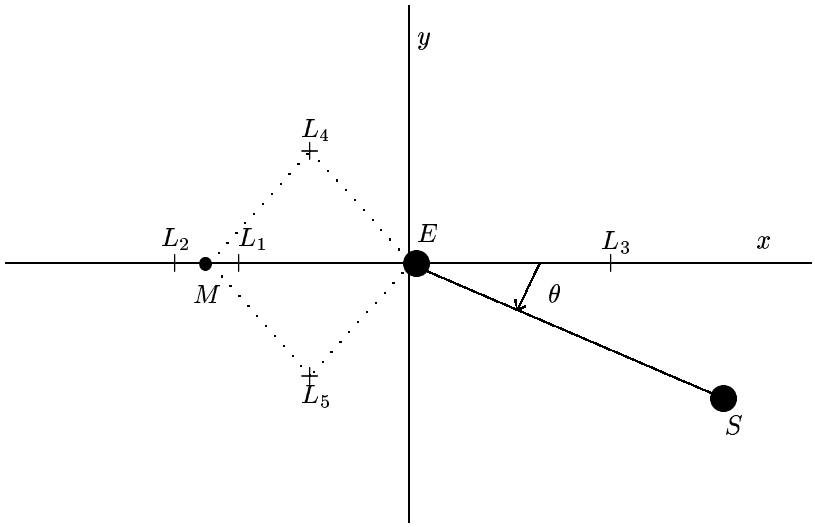

Figure 5.2: The Bicircular model: Location of Earth, Moon, Sun and the Lagrangian points.

Here μ, r_{PE} and r_{PM} denote the same quantities as in (5.1). Moreover, m_S denotes the mass of Sun, a_S the averaged semi-major axis of Sun, $\theta = \omega_S t$, ω_S is the frequency of Sun in this system of reference, $T_S = \frac{2\pi}{\omega_S}$ is its period and finally, $r_{PS}^2 = (x - a_S\cos\theta)^2 + (y - a_S\sin\theta)^2 + z^2$. Notice that this Hamiltonian can be splitted in two parts:

$$H_{BCP} = H_{RTBP}(X) + H_S(X, \theta),$$

where X is used to denote (x, y, z, p_x, p_y, p_z). The time dependent part contains two terms, a Coriolis effect due to the rotating frame of coordinates and Sun's gravitational potential. The Taylor expansion of the potential starts with

$$\frac{1}{a_S}\left(1 + \frac{x\cos\theta - y\sin\theta}{a_S}\right).$$

Therefore, the Hamiltonian, if we truncate the Sun's potential at linear order is written as

$$H_{BCP}^{<2} = H_{RTBP} - \frac{m_S}{a_S}.$$

So, the Coriolis term and the truncated Sun's potential cancel out and the dynamics is the one of the RTBP. This is to say that the contribution due to Sun's potential starts at order two, that is, the BCP is a periodic time dependent perturbation with size $\mathcal{O}(\frac{m_S}{a_S^3}) \approx 0.0056$.

Anyhow, it is large enough to produce remarkable changes on the dynamics, especially near the triangular points.

In Figures 5.3 (a) and 5.6 (a) we display continuations of L_4 and L_2 (respectively) from the RTBP to the BCP. The vertical axis in these plots represent an artificial parameter ε which multiplies the mass of Sun. Therefore, when $\varepsilon = 0$, the model corresponds to the RTBP and, when $\varepsilon = 1$, the model corresponds to the BCP. The points of the characteristic curves are the periodic orbits replacing each equilibrium point but regarded as a fixed point of the stroboscopic map. We shall comment these figures in more detail in the next sections.

5.2.1 Dynamical equivalents of the triangular points

First of all let us mention that, due to a symmetry, the dynamics near L_4 is the same as the dynamics near L_5 (in fact, this symmetry maps orbits in the region $y > 0$ to orbits in the region $y < 0$). A feature of the BCP to be stressed is that the region around the geometrically defined triangular points is unstable. The influence of Sun's potential is enough to produce a bifurcation in the periodic orbit that replaces L_4 (i.e., L_5). It is well known [SGJM95] that each triangular point is replaced by three periodic orbits with the same period as Sun. One small and unstable (the actual replacement of L_4) and two larger orbits which are stable. We have named these orbits $PO1$, $PO2$ and $PO3$. See Figure 5.3 (a) for a continuation diagram from the RTBP to the BCP. The two additional periodic orbits are produced by an imperfect pitchfork bifurcation (i.e. a pitchfork bifurcation broken due to a loss of symmetry).

One may ask which is the model that displays the perfect bifurcation and which is the broken symmetry. To address this question we take a look at the order two of the Taylor expansion of Sun's gravitational potential. We have

$$H_S^2(\theta, x, y) = \frac{1}{a_S^3}\left(\frac{3}{2}T(x, y, \theta)^2 - \frac{1}{2}(x^2 + y^2)\right).$$

We have named $T(x, y, \theta) = -x\cos\theta + y\sin\theta$. We would like to stress again that H_S^2 is the first contributing non-autonomous term in the model due to the cancellation produced by the Coriolis acceleration. This term is invariant under the symmetry $(x, y, z, \theta) \mapsto (x, -y, z, -\theta)$. The order three of the expansion is given by:

$$H_S^3 = \frac{1}{a_S}\left(\left(\frac{\rho}{a_S}\right)^3 \frac{\frac{5}{2}T(x, y, \theta)^3 - \frac{3}{2}T(x, y, \theta)}{a_S\rho}\right).$$

Here $\rho^2 = x^2 + y^2$. The polynomial in T is no longer even. This breaks the symmetry and, hence, the pitchfork bifurcation. The non-autonomous model that displays the perfect bifurcation is:

$$H_{BCP}^{\leq 2} = H_{RTBP}(X) + H_S^2(X, \theta).$$

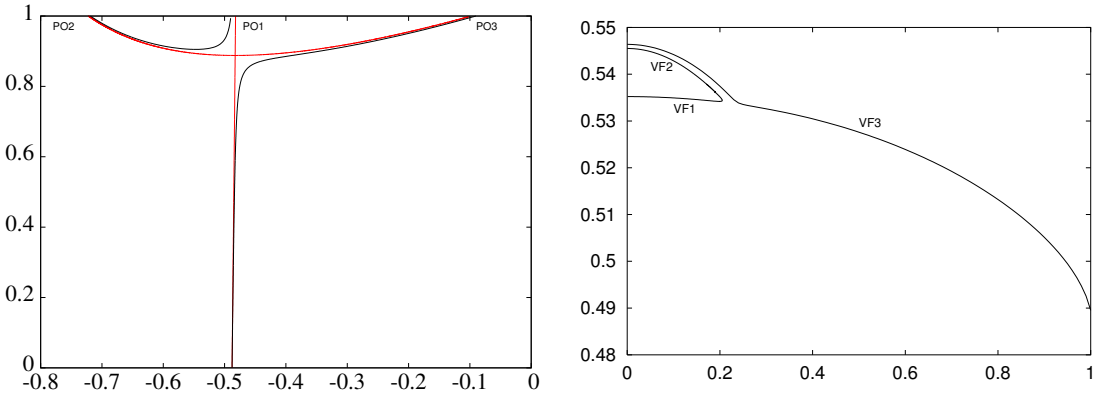

(a) (b)

Figure 5.3: **(a):** Continuation of L_4 as a periodic orbit with respect to the mass of Sun. Horizontal axis: x. Vertical axis: ε. The black curve stands for the continuation to the BCP. The red curve for the truncated version of the BCP. **(b):** Vertical families of $2D$ tori for the BCP. The horizontal axis is the p_z coordinate and the vertical axis displays the frequency. See text for more details.

The perfect (non broken) pitchfork bifurcation in Figure 5.3 (a, curve in red) shows the continuation diagram from the RTBP to this simplified version of the BCP. Due to the symmetry, periodic orbits $PO2$ and $PO3$ only differ on the phase on the orbit.

5.2.2 Phase space of the stroboscopic map near the triangular points

The three periodic orbits appear as fixed points of the stroboscopic map. We recall that their linear normal behaviour is of type saddle×centre×centre for $PO1$ and totally elliptic for $PO2$ and $PO3$. From the elliptic directions of each fixed point, there is a family of invariant curves whose frequency tends to the normal modes of the fixed points [JV97b, JV97a].

Therefore, we have a family of invariant curves for each elliptic direction, that is, two for $PO1$ ($HF1$ in the horizontal plane and $VF1$ in the vertical direction), three for $PO2$ ($HF2F1$ and $HF2F2$ are horizontal, and $VF2$ is vertical) and three for $PO3$ ($HF3F1$ and $HF3F2$ horizontal, and $VF3$ vertical). As the remaining eigendirections of $PO1$ are a saddle, there exist stable and unstable one-dimensional invariant manifolds associated to this hyperbolic direction. Initial conditions near the triangular points shadow the unstable manifold which wonder some time around the periodic orbits $PO2$ and $PO3$ and finally abandon the vicinity

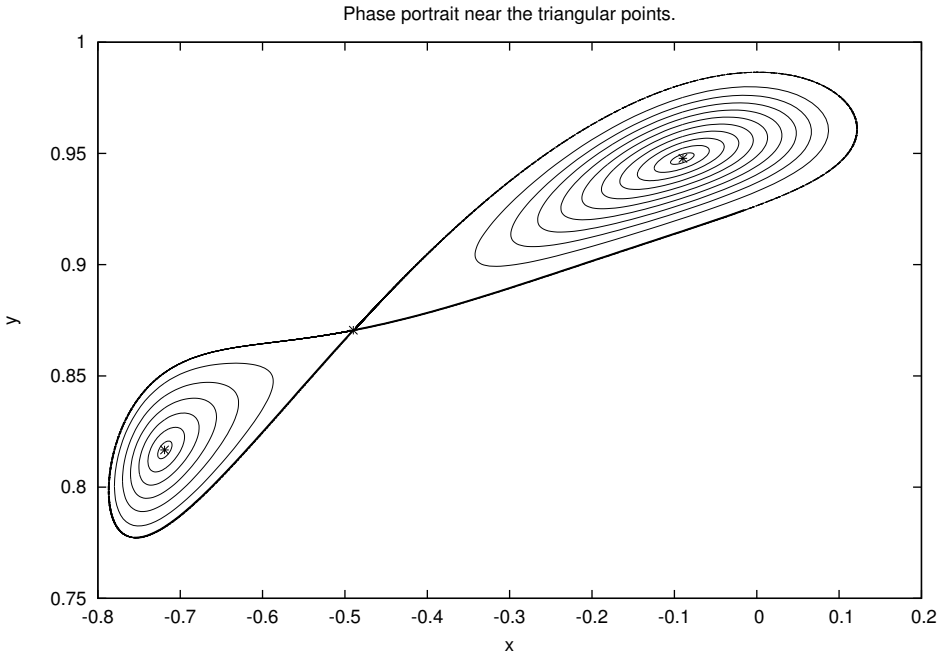

Figure 5.4: Stroboscopic map near the triangular points in the BCP: Horizontal axis x. Vertical axis y. See text for more details.

of the triangular points. These manifolds are of special interest if one plans to put or take out objects near L_4 and L_5. The stable and unstable manifolds related to $PO1$ can be computed up to high order directly on the stroboscopic map (Chapter 2 and [FGJ$^+$18]). In Figure 5.4 we observe a projection of the phase portrait of the map. The three points displayed with crosses correspond to $PO1$ (in the middle), $PO2$ and $PO3$. It is displayed as well, semi-analytical approximations of the stable and unstable invariant manifolds. We have used an approximation of order 64. The thick curve are the pieces given by the parameterization. The thin curve correspond to some iterations of these pieces. It can be observed, also, some invariant curves growing from $PO2$ and $PO3$. These invariant curves are totally elliptic near the fixed points.

5.2.3 Regions of effective stability near the triangular points

As we have observed, the triangular points are replaced by three periodic orbits, one of them unstable. This is the reason why the BCP is an interesting model [GJMS91c]. Indeed, the unstable manifold of the triangular periodic orbit takes initial conditions away from the

vicinity of the triangular points. However, we can pursue on seeking for regions of (effective) stability out of the plane of motion of the primaries. The mechanism that suggest the existence of regions of effective stability is the stickiness of normally elliptic low dimensional invariant tori, see [JV98, JV97a]. As we discussed before, there are families of invariant tori emanating from the periodic orbits $PO2$ and $PO3$. These families are elliptic close enough to the periodic orbits. This results on two small regions of effective stability in the plane of motion of the primaries related to the totally elliptic orbits.

Let us put our attention on the vertical families (one for each orbit) of invariant tori. We label these families $VF1$, $VF2$ and $VF3$ after the corresponding periodic orbits. The families $VF1$ and $VF2$ are connected, as it happens with $PO1$ and $PO2$. On the other hand, $VF3$ reaches high amplitudes in the (z, p_z) plane. It is known that, skipping resonances, the three families have the same stability as the corresponding periodic orbits (close enough to them). Therefore the tori of $VF1$ have hyperbolic directions while the ones of $VF2$ and $VF3$ are normally elliptic (except for small intervals of instability produced by resonances involving internal and normal frequencies) close enough to $PO2$ and $PO3$.

In Figure 5.3, (b), we show how these families vary when they grow out of the plane of motion of the primaries. We observe that the three families display a broken pitchfork bifurcation, analogous to the one of the periodic orbits. The linear normal behaviour of the tori is the same as the periodic orbit, at least near the plane. As a consequence of the pitchfork bifurcation, at some distance of the plane, the surviving family is totally elliptic. Therefore, after the bifurcation occurs, the tori are sticky and regions of effective stability are to be expected. The tori of $VF3$ are normally elliptic up to very high values (again, except for resonances).

Normally elliptic lower dimensional tori induce regions of effective stability. Numerical estimations of the shape and the size of these regions show that, in the case of $VF2$, the regions are small and narrow while, in the case, of $VF3$ large regions exist for sufficiently high values of the vertical amplitude. In Figure 5.5 we show two stability regions out of the horizontal plane. These regions seem to persist in the real model for time spans of 1000 years (see [Jor00] and also [HXSW15] for similar computations).

Let us explain how Figure 5.5 is obtained. Each torus of the vertical family of invariant tori can be identified by the value of the coordinate p_z when $z = 0$ and $p_z > 0$. Denote by $a(p_z) \in \mathbb{R}^6$ the coordinates of the point that identifies a torus. We have to select a set of initial conditions near $a(p_z)$ and integrate them for a long time span. Let us be more precise on how to select the initial conditions. We use a two dimensional grid in x, y, where the coordinates z, p_x, p_y and p_z are to be fixed at the corresponding values of $a(p_z)$. To adapt to the shape of the regions, we use a polar-like grid, centered at Earth:

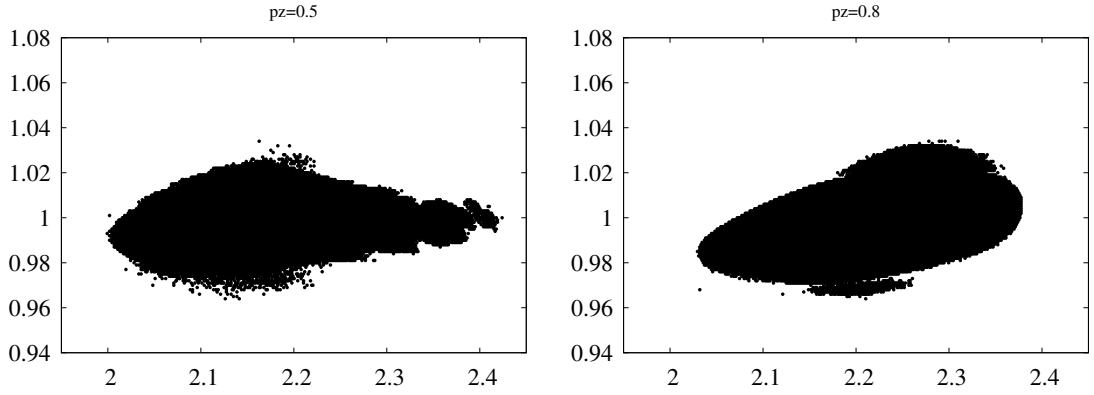

(a) (b)

Figure 5.5: Stability regions with initial conditions on the tori of the $VF3$ identified by $p_z = 0.5$ and $p_z = 0.8$. Horizontal axis: α. Vertical axis r. See text for more details.

$$\begin{cases} x_{ij} = r_i \cos\alpha_j + \mu, & r_i = 1 + ih_r, \\ y_{ij} = r_i \sin\alpha_j, & \alpha_j = 2\pi j h_\alpha, \end{cases}$$

where h_r (selected such that ih_r ranges form 0.5 to 1.) and h_α (selected such that jh_α ranges -0.5 to 0.5) are used to control the density of the grid. The computation goes as follows: Fixed a torus identified by some coordinates $a(p_z)$, take a point of the grid and integrate the vector field 15000 Moon revolutions. At each integration step, we test if there is a collision with Earth or Moon. If there is a collision, or the coordinate y becomes negative, we stop the integration (Recall that we are interested in the points that remain close to L_4). We have used $h_r = 0.001$ and $h_\alpha = 0.0002$. The difference on the sizes of these small quantities is aimed to produce a nearly squared grid.

5.2.4 A weakness of the BCP

The translunar point is one of the most interesting locations of the Earth-Moon system. The reason is that L_2 seems suitable to observe the far side at Moon. Taking into account that, a natural criticism to the BCP is that it does not have a dynamical replacement of L_2. In Figure 5.6 it is displayed a continuation of L_2 as a periodic orbit from the RTBP to the BCP. Again, the vertical axis is an additional parameter multiplying the mass of Sun. The point L_2 is the middle crossing of the characteristic curve with the homotopy level corresponding to the RTBP, at the bottom. The other two points of the RTBP correspond to the same

$1:2$ resonant planar Lyapunov orbit. We observe that the continuation of L_2 undergoes a turning point and it never reaches the homotopy level of the BCP. The result is that the translunar dynamical structure is lost in the BCP. This suggest that a more complex model needs to be used in order to analyze the natural behaviour near the translunar point.

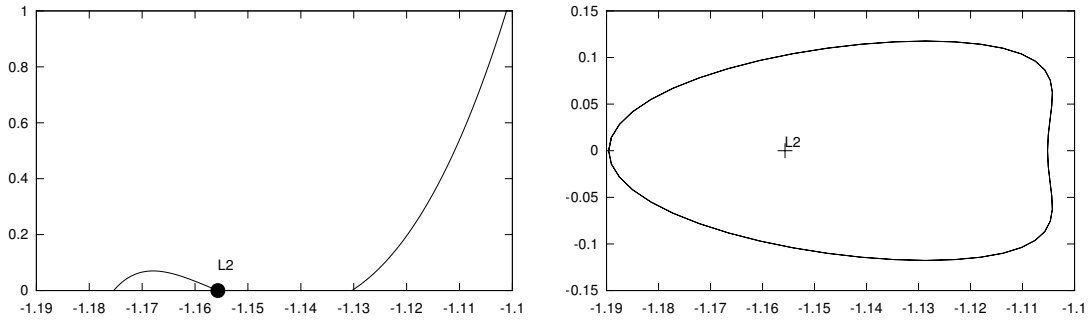

(a) (b)

Figure 5.6: **(a):** Continuation of L_2 as a periodic orbit with respect to the mass of he Sun. Horizontal axis: x. Vertical axis: ε. See text for more details. **(b):** Periodic orbit near L_2 in the BCP. Horizontal axis: x. Vertical axis: y.

5.3 The Quasi-Bicircular Problem and the collinear points

The Quasi-Bicircular Problem (QBCP) is a version of the four body problem. It is conceived to be a coherent counterpart of the BCP. A characteristic of the BCP is the lack of coherence of the bicircular solution assumed for the primaries. However, there exist solutions of the three body problem which are close to bicircular. To build the QBCP it is necessary to compute a quasi-bicircular solution of the three body problem, in this case, for the Earth-Moon-Sun case. There are several ways to do such a thing. In [And98, AS00, And02] the authors build a specific algebraic manipulator and compute directly the Fourier coefficients of the quasi-bicircular solution. In [Gab03, GJ01, GJR04] the authors use a continuation scheme to compute the desired solution starting from a solution of the two body problem. After that, a Fourier transform is applied to get the Fourier coefficients of the solution.

The quasi-bicircular solution of the Earth-Moon-Sun system is planar i.e. the three bodies move in the same plane. After the quasi-bicircular solution is computed one can write the equations of motion of the test particle, prescribing the quasi-bicircular solution as motion for the primaries. It is usual to compute the quasi-bicircular solution in the Jacobi frame,

however, if one has the purpose of describing the dynamics in the Earth-Moon vicinity, it is suitable to use the frame of coordinates corresponding to the Earth-Moon RTBP. To do so, one has to perform three different transformations. First, one has to use a translation to move the origin from the global barycentre to Earth's and Moon's centre of masses. Second, one has to use a rotating (synodic) frame to keep Earth and Moon fixed on the horizontal axis. Third, the unit of length is scaled so the distance between Earth and Moon is equal to one. The units of mass and time which are usually selected in the Earth-Moon RTBP can be imposed already in the *Jacobi formulation* of the Three Body Problem (see [Mar90]).

The resulting model is a Hamiltonian system with three and a half degrees of freedom. The Hamiltonian function can be written as

$$\begin{aligned} H = \frac{1}{2}\alpha_1(p_x^2 + p_y^2 + p_z^2) + \alpha_2(p_x x + p_y y + p_z z) + \alpha_3(p_x y - p_y x) \\ +\alpha_4 x + \alpha_5 y - \alpha_6\left(\frac{1-\mu}{r_{pe}} + \frac{\mu}{r_{pm}} + \frac{m_S}{r_{ps}}\right), \end{aligned} \tag{5.3}$$

where, $r_{pe}^2 = (x-\mu)^2 + y^2 + z^2$, $r_{pm}^2 = (x-\mu+1)^2 + y^2 + z^2$, $r_{ps}^2 = (x-\alpha_7)^2 + (y-\alpha_8)^2 + z^2$, and for $i = 1, \ldots, 8$ $\alpha_i : \mathbb{T} \mapsto \mathbb{R}$ are periodic functions. That is,

$$\alpha_i(\theta) = a_0^i + \sum_{k\geq 0} a_k^i \cos k\theta + \sum_{k\geq 0} b_k^i \sin k\theta. \tag{5.4}$$

Here, $\theta = \omega_S t$ and ω_S is the frequency of Sun. Moreover, α_i is odd for $i = 1, 3, 4, 6, 7$ and even for $i = 2, 5, 8$. Obviously one can only have a numerical approximation of these functions. In this case, we take advantage on the computations done in [And98] and take the same values for the Fourier coefficients of the periodic functions α_i's. To end, and taking into account the properties of the functions α_i's, it is easy to see that the Hamiltonian function (5.3) has the symmetry $(\theta, x, y, z, \dot{x}, \dot{y}, \dot{z}) \mapsto (-\theta, x, -y, z, -\dot{x}, \dot{y}, -\dot{z})$.

The meaning of these periodic functions is the following:

1. $(\alpha_7, \alpha_8, 0)$ is the position of Sun in the plane of motion of the primaries.
2. α_1, α_2, α_3 and α_6 capture the fact that the distance between Earth and Moon is not constant.
3. α_4 and α_5 take into account the Coriolis effect due to the rotating frame of reference.

5.3.1 Dynamical equivalents of the collinear points

In this section we give some words about the minimal periodic orbits that replace the collinear points in the QBCP. In Figure 5.7 we display the dynamical equivalents of L_1 (a), L_2 (b) and

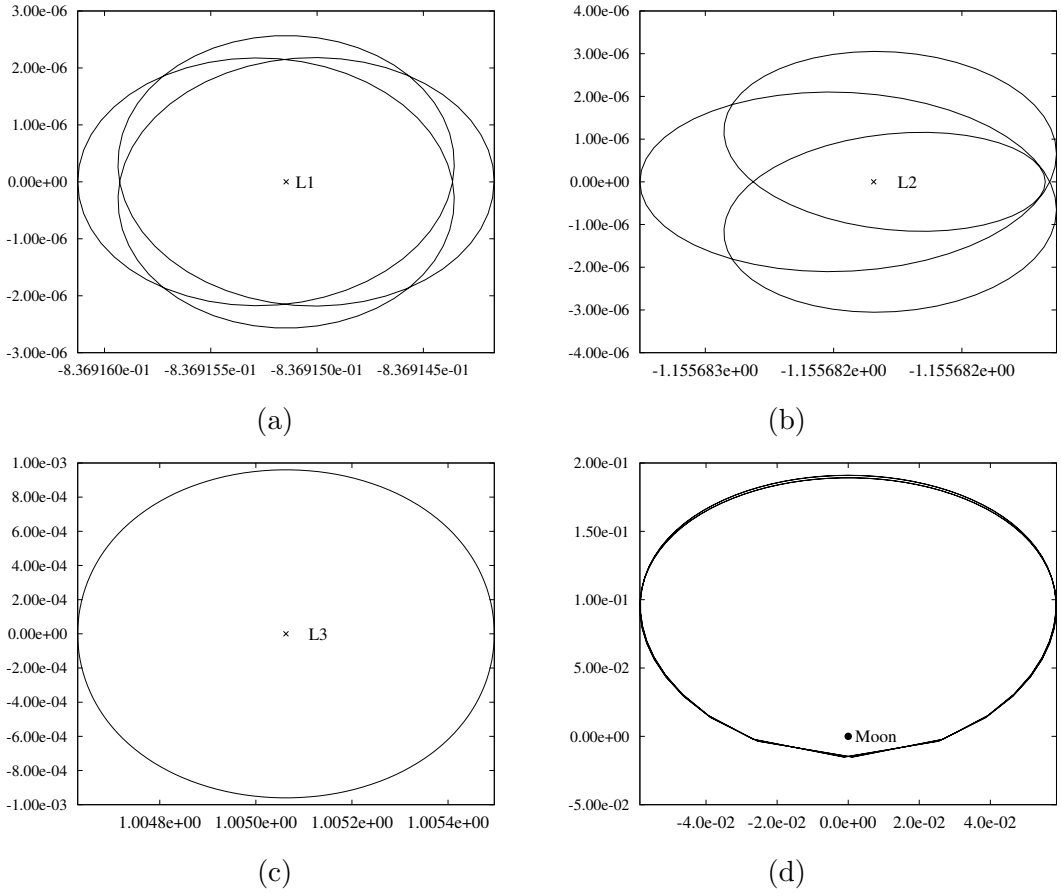

Figure 5.7: Dynamical equivalents of the collinear points. **(a):** L_1. **(b):** L_2. **(c):** L_3. **(d):** $2G$. For panels (a), (b), (c): Horizontal axis: x. Vertical axis: y. For panel (d): Horizontal axis: y. Vertical axis z. See text for more details.

L_3 (c). We observe that the orbits replacing L_1 and L_2 are small, its maximal distance to the corresponding equilibrium point is of order $\mathcal{O}(10^{-6})$. As the original equilibrium points, the linear normal behaviour of these orbits is of type saddle×centre×centre. In Table 5.1 we display the eigenvalues of each orbit. We notice that the unstable direction of L_1 (of order 10^8) and the unstable direction of L_2 (of order 10^6) are large and this implies huge propagation of errors near these orbits. On the other hand, the dynamical equivalent of L_3 has a very weak unstable direction, at least compared to the other two.

	L_1	(real)	(imag)	L_2	(real)	(imag)	L_3	(real)	(imag)
1		460182151.57	0		2397196.84	0		3.370855	0
2		−0.987151	0.159784		0.995818	0.0913562		0.863840	−0.503764
3		−0.963639	0.267205		0.917527	0.3976716		0.841148	0.5408042

Table 5.1: Eigenvalues of the three dynamical equivalents of L_1, L_2 and L_3. We only put three for each orbit. The rest are given by their inverses due to the symplectic character of the stroboscopic map.

5.3.2 Resonant orbits of low order

As the QBCP is a T_S-periodic system, the simplest invariant objects are T_S-periodic orbits. We have already mentioned that the equilibrium points are replaced by these periodic orbits of minimal period. Periodic orbits of the RTBP whose frequency is resonant with the one of Sun also persist as T_S-periodic orbits in the QBCP. The Lyapunov and Halo families of periodic orbits related to the equilibrium points L_1 and L_2, are a source for these kind of resonant orbits. In contrast with the families related with L_3, the families of the two first libration points are nourished with low order resonant orbits. A relation of low order resonant periodic orbits of the RTBP can be found in [And98]. In [GM01] the authors show the ranges for the admissible periods for each family. The families related to L_3 are of relatively large period and there are not many periodic orbits whose frequency are in low order rational relation with the frequency of Sun. There is, however, a $1:1$ resonant periodic orbit near the end of the vertical family. This orbit is enormous in size and cannot be considered in the vicinity of L_3. In Table 5.2 details of the continuations of low order resonant orbits from the RTBP to the QBCP are given: The first column corresponds to resonant periodic orbits of the RTBP. The label in this first column consist in three numbers that encode each orbit. The first is a zero and indicates that the orbit belongs to the RTBP (this is intended to distinguish them from the orbits in the last column corresponding to the QBCP). The second number refers to the libration point related to each orbit (all of them belong to Lyapunov and Halo families related to L_1 and L_2). The third number is just an enumeration. The second column indicates the order of the resonance. We stress that the influence of Sun is relevant enough to produce bifurcating orbits in each of the continuations. The third column shows how many orbits bifurcate from the original ones when they are continued to the QBCP. Finally the last column contains the labels of the resulting orbits in the QBCP. Table 5.2 can be found originally in [And98]. We have added the order of the resonance and the color code to indicate the linear normal behaviour of each orbit. Labels in red stand for orbits of type saddle×centre×centre. Labels in green denote linear character of the kind saddle×saddle×centre. Names in cyan denote totally hyperbolic orbits. The color black

denotes totally elliptic orbits.

RTBP	RES	BIF	QBCP
012	1 : 2	2	12, 13
014	1 : 1	4	14, 15, 16, 17
018	1 : 1	4	18, 19, $1A^{\pm}$, $1B^{\pm}$
01C	1 : 3	2	$1C^{\pm}$, $1D^{\pm}$, $1N^{\pm}$
01E	1 : 3	2	$1E^{\pm}$, $1F^{\pm}$
022	1 : 2	4	22, 23, 24, 25
026	1 : 6	4	26, 27, 28, 29
02A	1 : 2	4	$2A^{\pm}$, $2B^{\pm}$, $2C^{\pm}$, $2D^{\pm}$
02E	1 : 3	2	$2E^{\pm}$, $2F^{\pm}$
026	1 : 4	2	$2G^{\pm}$, $2H^{\pm}$

Table 5.2: Continuation of the low order resonant orbits from the RTBP to the QBCP. The first column contains the label of the orbits corresponding to the RTBP. The second column contains the order of the resonance. The third columns contains number of bifurcating orbits. The fourth column contains the label of the orbits corresponding to the QBCP. See [And98] for more details. See text for the color code.

5.3.3 High order approximation of the unstable manifolds of the collinear periodic orbits

This section is devoted to the results of applying the algorithm (explained in Chapter 2) for the computation of high order stable/unstable manifolds to the dynamical equivalents of the collinear points. Figure 5.8 shows pieces of the stable (dashed) and unstable (solid) manifolds related to the three collinear periodic orbits (the other branches can be obtained by symmetry). The one related to L_1 is displayed in panel (a), the one related to L_2 in (b) and the one related to L_3 in (c). We would like to remark that these pieces are obtained directly from the evaluation of the approximation (of order 64) of the manifolds. They are not grown numerically as usual. We can observe that these approximations already give large excursions far away from the collinear points. Especially in the case of L_3, where the piece of the manifold passes very close to the triangular points. The axes of Figure 5.8 show the x and y values. These pieces can be mapped through the stroboscopic map to obtain larger pieces of the manifolds if it is necessary. The point of giving high order approximations of the manifold is that, just a fewer number of iterates are necessary. For the computation of the manifold related to L_3, a simple shooting method has been used. Indeed, the instability associated to this libration orbit is very weak. For the computation of the manifold related

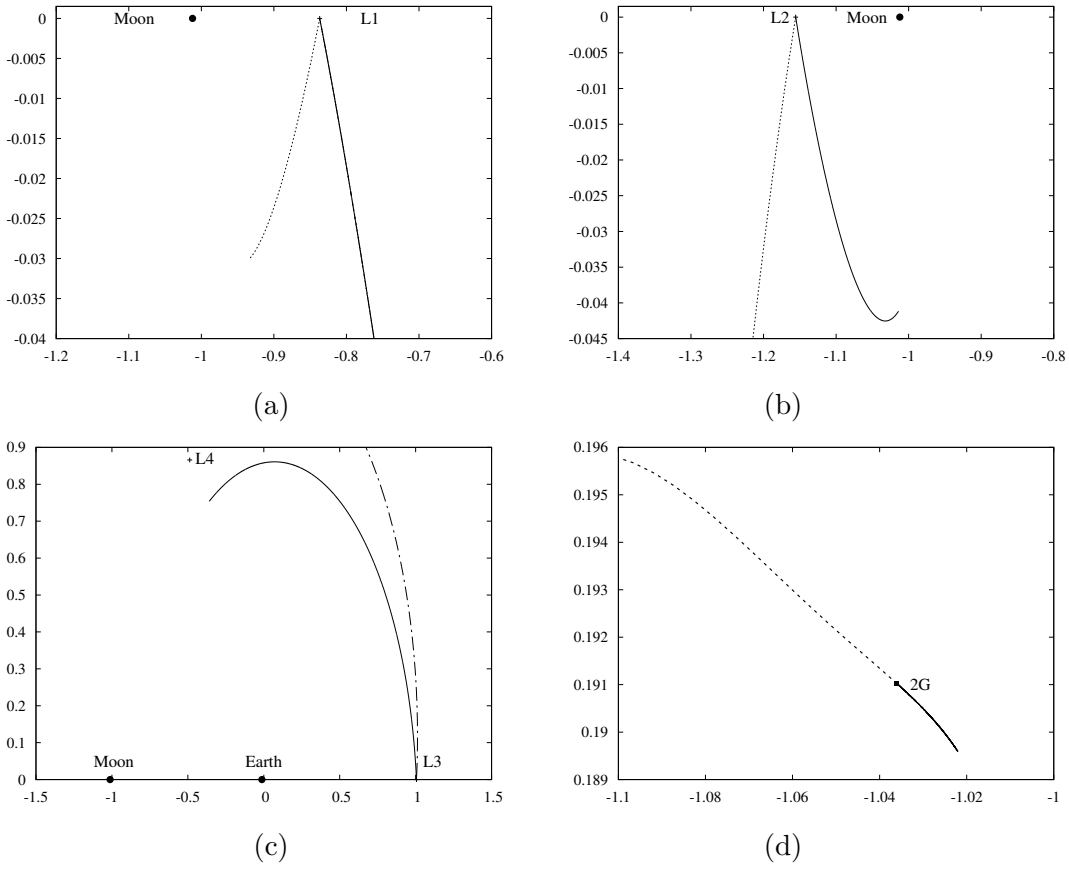

Figure 5.8: Approximation of order 64 of the stable (dashed) unstable (solid) manifolds related to several fixed points. **(a):** L_1, **(b):** L_2, **(c):** L_3, **(d):** $2G$. Horizontal axis: x. Vertical axis: y.

to L_2, multiple shooting is required, we have used two sections. For the computation of the manifold related to L_1, the most unstable one, we have used a single shooting strategy but with an extended precision arithmetic of 128 bits. This last approach makes the program far slower but very simple to code. In Figure 5.7 (d), we show the resonant orbit $2G$ of Table 5.2. We display also in Figure 5.8 (d) the stable (dashed) and unstable (manifolds).

5.4 Some concluding remarks

We have presented two alternatives to the RTBP for the study of the motion of a test particle in the Earth-Moon system. Both models, the BCP and the QBCP, depend periodically on the time. We use the so-called stroboscopic map to study the minimal periodic orbits of the systems and the invariant manifolds related to them.

The BCP is as useful model for the study of the triangular points. The simplicity of the vectorfield is a strong point, especially in problems related to effective stability where massive integrations are mandatory. We have also stressed its weakness: it is not suitable to understand the dynamics around the collinear points. The BCP is useless to describe the vicinity of the translunar point.

We have used the parametrization method to obtain high order approximations of the unstable manifolds related to the minimal periodic orbits that replace the collinear points in the QBCP. This is helpful to design long excursions between the two primaries and the collinear points. The main novelty is that we have computed the manifolds directly on the stroboscopic map. The QBCP is a complicated model with a numerically computed vectorfield. This makes it a bad candidate (in front of the BCP) to be the model used to face the problems involving massive simulations around to the triangular points.

We would like to stress that the BCP should be used to face problems related to the triangular points. Especially if this problems involve large time integrations to seek for regions of practical stability. The QBCP should be used when dealing with problems involving the collinear points.

5.5 Technical details

The integrations for the RTBP, the BCP and the QBCP have used a Taylor method with variable order and stepsize. The demanded accuracy for the standard double precision has been 10^{-16}. The computations in multiple accuracy have been done using the library MPFR. The LAPACK library has also been used for some computations related to linear algebra. The rest of the programs have been written by the authors in C and C++ languages from the scratch. Table 5.3 contains the values of the parameters used for the computations. Table 5.4 contains the numerical values of the Fourier coefficients that determine the functions α_i, $i = 1, \ldots, 8$.

μ	a_S	m_S	ω_S
0.012150581623433623	388.81114302335106	328900.54999999906	0.92519598551829646

Table 5.3: Values of the parameters used in this thesis.

α_1		α_2		α_3		α_4	
k	a_k	k	b_k	k	a_k	k	a_k
0	1.001841608924835e+00	0	0.e0	0	9.999999999999983e-01	0	-9.755242327484885e-04
1	5.767517726198399e-04	1	-2.644376028499938e-04	1	5.634125997553694e-04	1	2.154764362707107e+00
2	1.438777025507630e-02	2	-1.328686903400173e-02	2	1.889687440172882e-02	2	3.657484468968697e-04
3	-2.630362974972015e-06	3	9.386093208089751e-06	3	-9.911758802567132e-06	3	3.295673376166588e-03
4	1.176278356118933e-04	4	-1.218509057517414e-04	4	1.568708136031134e-04	4	3.301031400812427e-07
5	-8.068581391005552e-08	5	1.522127598557008e-07	5	-1.707762576173484e-07	5	1.278840687376320e-05
6	9.843249766501285e-07	6	-1.072102664277996e-06	6	1.319613679707437e-06	6	-2.623797952127926e-09
7	-1.172054394418197e-09	7	1.889371261374048e-09	7	-2.136550041985646e-09	7	6.533805514561511e-08
8	8.311905970879588e-09	8	-9.324985038927486e-09	8	1.117168916673893e-08	8	-3.891720707783511e-11
9	-1.408584238695393e-11	9	2.114490981280258e-11	9	-2.387253631031108e-11	9	3.812275838944432e-10
10	7.050713786466840e-11	10	-8.071111743144353e-11	10	9.490879622095902e-11	10	-3.907906049834876e-13
11	-1.494259634910463e-13	11	2.218118050420168e-13	11	-2.462732581558427e-13	11	2.407471187576443e-12
12	5.982418979451232e-13	12	-7.036155161882012e-13	12	8.101067708009743e-13		

α_5		α_6		α_7		α_8	
k	b_k	k	a_k	k	a_k	k	b_k
0	0.e0	0	1.000907457708158e+00	0	-6.314069568006227e-02	0	0.e0
1	-2.192570751040067e+00	1	2.870921750053134e-04	1	3.885638623098048e+02	1	-3.897437256237654e+02
2	-3.337210485472868e-04	2	7.187177998612875e-03	2	1.736910203345558e-01	2	-1.734279166322518e-01
3	-3.295001430200974e-03	3	-2.351183147213254e-06	3	3.382908071669699e+00	3	-3.385696486642120e+00
4	-3.100635053052634e-07	4	4.585758971122060e-05	4	1.574837565380491e-04	4	-1.555886632413398e-04
5	-1.277777336854128e-05	5	-3.848683620107037e-08	5	2.936360489004438e-02	5	-2.937582671967532e-02
6	2.652806405498111e-09	6	3.270677504935666e-07	6	-1.224434550116014e-05	6	1.225851213107933e-05
7	-6.528479245085066e-08	7	-4.406966481041876e-10	7	2.538935434262443e-04	7	-2.539596887692642e-04
8	3.891720707783511e-11	8	2.452600662570259e-09	8	-2.278929040007574e-07	8	2.280029220202363e-07
9	-3.812275838944432e-10	9	-4.542938800673444e-12	9	2.190432706181655e-06	9	-2.190834624429040e-06
10	3.907906049834876e-13	10	1.892348855112616e-11	10	-3.033311961234353e-09	10	3.036109035120856e-09
11	-2.407471187576443e-12	11	-4.178420101480123e-14	11	1.886971545290216e-08	11	-1.887457647579322e-08
		12	1.480048946961583e-13	12	-3.432375106898453e-11	12	3.432375106898453e-11
				13	1.611513703999101e-10	13	-1.631723641506449e-10

Table 5.4: Coefficients of the functions α_j, $j = 1, \ldots, 8$, in (5.4). Due to the symmetries of the model, each α_j only contains either sin or cos terms, so we only list either the a_k or b_k coefficients.

"Choose the best player for every position, and you'll end up not with a strong XI, but with 11 strong 1's."

Johan Cruyff

6

Solar Sailing in the Earth-Moon system

In Chapter 5 we discussed the dynamics in the Earth-Moon system. As we point out there, a number of missions that will take place in the vicinity of Earth and Moon are being planned, see [VKCG10, SBA+11, Sun18]. Of special importance is the translunar point i.e. the geometrically defined L_2 Lagrangian point. The mentioned location is flawless for either Moon scientific observation or to establish permanent communication with the Earth from a hypothetical station in the far side of Moon. To this purpose a special type of trajectories, the Halo orbits [Far70, FK73b, GMS97] have been the classic basis for mission design. This is because a spacecraft following a Halo orbit can, typically, communicate with Earth avoiding the obstruction of Moon's body. There are, nevertheless, other approaches to follow. Solar sailing is among the most promising ones.

The idea behind solar sailing is to endow a spacecraft with a large and highly reflecting surface, the sail. When photons impact upon the sail, some momentum is transferred and the spacecraft receives a certain acceleration. Despite the variation of velocity due to the sail is much smaller than the ones achieved by a traditional propeller, it is continuous and only limited by the lifespan of the sail. Mathematically, to put a sail in a spacecraft means to modify a classical restricted model by including the effect of Solar Radiation Pressure (SRP), see [McI93, OGH09, HTL09, SM10b, SM10a, SM09b, WH11a, WH11b, HHNC14, HMP16a, HHNM15b, JCFJ16a, SH16] for works concerning the Earth-Moon system and [MMSM94, FJ08a, FJ08b, FJ10a, FJ10b, FJ10c] for the Sun-Earth. SRP modifies the natural dynamics of the model, the invariant structures change their shape, their linear normal

behaviour and move around the phase space. Playing with the parameters of the sail, its effectivity and orientation, one can find out different dynamical conditions that can be used for, otherwise inconceivable, mission concepts.

A model for the dynamics of a solar sail is constructed in the following way: First, one decides the relevant forces, besides SRP, that are to be considered. Usually, some primaries are to be taken into account and a corresponding restricted model is build after prescribing some motion for these primaries. After that, the restricted model is modified to include SRP. In the case of the Earth-Moon system, the most commonly repeated approach is to extend the Earth-Moon Restricted Three Body Problem (RTBP) to include the effect of SRP upon the sail.

Thought, in the view of the conclusions from Chapter 5, a study of the dynamics on the Earth-Moon system must include Sun's gravity. There is, moreover, another good reason to include Sun's gravity when studding the motion of a solar sail in the Earth-Moon system: It does not increase the dynamical complexity of the model. Indeed, SRP depends periodically on time with the same period as Sun's gravitational potential.

Recall that in Chapter 5 we discuss two different ways to introduce Sun's gravity in the Earth-Moon system: The Bicircular Problem (BCP) and the Quasi-Bicircular Problem (QBCP) (see also a model based in the Hill Problem in [Sch98]). These two models are the ones that shall be modified to include the effect of SRP. Recall that the BCP is suitable to study the motion near the triangular points while the QBCP is convenient for the motion near the collinear points.

This chapter is organized as follows: In Section 6.1 we provide a historical introduction to solar sailing and a state of the art of solar sailing in the Earth-Moon system. Section 6.2 is devoted to the construction of the dynamical models used to face the problem. Essentially it is explained how to modify the QBCP and the BCP to include SRP. Section 6.3 is devoted to preliminaries: Most of the content of this section can be found in Chapter 5. We include it here to facilitate the reading of the present chapter. Section 6.4 and Section 6.5 are devoted to the study of the motion near the collinear points L_1 and L_2. To do so, we use the QBCP as a basis model. In Section 6.6 we pay attention on the stabilizing effect SRP has on some orbits of the QBCP. Section 6.7 is concerned with the motion near the triangular points and L_3 [1], here we use the BCP as the basis model. Finally, in Section 6.8 we explain the consequences of including Sun's gravity. A comparison with the most used model (for the dynamics of a solar sail in the Earth-Moon system) in the literature is provided.

[1]Notice L_3 is a collinear point and we use the BCP, not the QCBP.

6.1 Historical overview

The conquest of space undertaken by humankind started in the mid-twentieth century and it was strongly stimulated by the geopolitical conflict between the Soviet Union and the United States. Soviets were the firsts to lunch an artificial satellite (Sputnik 1, 1957) and to put a human being orbiting Earth (Yuri Gagarin, 1961). From these early years to the present time, spacecraft science has evolved enormously, taking its own place among the most useful and applicable areas of knowledge: from monitoring climate, to facilitate navigation within Earth. Space science makes possible this new age of people connected worldwide and possibly it will give mankind a chance to survive when Earth is no longer habitable. All this evolution has its fundamental pillar on the rocket and modern evolutions which rely on powerful thrusters obtained from some kind of propellant. This approach seems to be inappropriate for advanced and long-term missions as these type of spacecraft is able to carry a ephemeral source of energy. While efficient design can help to manage long-term mission using the propellant at very specific times and taking advantage of the natural dynamics in the solar system, novel approaches have irrupted to become an alternative to traditional ways of spacecraft propelling.

If one thinks about an alternative source of energy to move spacecrafts, Sun is, perhaps, the most brutal and endless one that easily pops up in mind. However, how can we take advantage on all this energy? The answer is that we are already doing it. Indeed, life is sustained by sunlight which consists of photons. The nature of photons is among the most exciting debates the scientific community has held. Since the works of Maxwell it is widely accepted that photons act as a particle and transport momentum. A satisfactory theoretical formulation of photon's nature had to wait until Einstein stated that photons exhibit properties of both waves and particles, the well-known wave-particle duality. This momentum, the one carried by photons, can be transferred. The acceleration induced upon a body, located at an astronomical unit of Sun, is called **characteristic acceleration**. The force induced by the photons, proportional to the characteristic acceleration, is called Solar Radiation Pressure. The key to get benefit of the immense amount of photons emitted by Sun is to understand the interaction between light and matter.

Now we feel free to give some words on the interaction between light and matter. Any surface that is hit by photons undergoes a gain of momentum. However, there is a stark difference on the resulting acceleration acquired by reflecting and non-reflecting surfaces. Indeed, non-reflecting surfaces (think of an object painted in black) absorb most of the light while the reflecting ones (a mirror), well, reflects it. The main point is that, as the photons have their acceleration changed some force is acting on them and, by the action-reaction law, on the reflecting surface. A perfectly reflecting and flat surface doubles the amount of acceleration received by the impact of photons upon it. These basic principles lead to the

concept of a solar sail: a highly reflecting surface. To get the maximal amount of photons from the solar photon flow, the sail must have a large area and, to get the maximal amount of momentum, the sail must be have a low mass. Adding up, a solar sail is a highly reflecting surface with a high area-to-mass ratio.

Before continuing the discussion, let us tackle one of the most common misconceptions about solar sailing. Sun emits photons which are massless particles and it also emits massive particles: protons, electrons and α-particles (among others). This stream of charged particles is known as solar wind. By analogy with the sea sailing, some people thinks that solar wind is used to move solar sails and it is not. In fact, solar wind tends to deteriorate the sail.

It is surprising how early in history of space-science the idea of propelling spacecraft with light came out. In the early 20's the pioneer of Soviet's rocket-science K. E. Tsiolkovsky and his coworker F.A. Tsander wrote about the basic principles of light-propelled spacecraft. The first technical paper about solar sailing appeared in 1958. The author, R. Garwin coined the term 'Solar Sail' and was specially optimistic about the potential of this way of propelling spacecrafts:

"*It is difficult to exaggerate the importance of solar radiation pressure for the propulsion of satellites or space ships within the solar system; but since I have never seen any allusion to this powerful method, while less practical and more difficult schemes are frequently cited, I feel it desirable to publish this paper.*"

Clearly, Garwin was aware of the advantages of solar sailing with respect to traditional propellers, but, what are these advantages? We have been mentioning some of them in a rather subtle way, let us summarize. As the solar photon flow is always present, a sail-craft is provided by a continuous thrust that reaches any location. This is of capital importance to undertake a study of the dynamics of a spacecraft endowed with a solar sail as it will be discussed later. There is no need for propellant and, therefore, the sail-craft is accelerated constantly during the lifespan of the sail. Solar sails could, in principle, be designed to be reusable which is an advantage on itself and it is worth to mention that reusability of space-crafts is a way to fight the growing problem of space debris. However, the current technology capabilities are far from producing a reusable solar sail. Even if the sail is not reusable a deployed sail subjected to the atmospheric drag seems an obvious and cheap end-of-life strategy for spacecraft. The way a sail-craft navigates is unique: a change on the orientation of the sail is translated to a change on the force acting upon the craft. Solar sailing permits to design missions that are inconceivable with traditional propellers. Obviously, sail-craft technology also has cons with respect to traditional propellers. In the first place, the acceleration provided by a solar sail is much smaller than the one offered by traditional thrusters. Moreover, the engineering necessary to deploy a large sail is extraordinarily complicated. Not in vain, this technology is not established at all.

Other authors continued the work of Garwin during the beginning of the nineteen-sixties.

Tsu (1959) and London (1960) investigated exact solutions of the Keplerian model extended to include the force of Solar Radiation Pressure upon a sail. These exact solutions were logarithmic spirals. The term "non-Keplerian orbit" was coined in reference to this kind of trajectories that cannot be found in the classical version of Kepler's problem. During these days also tentative mission designs to trip to Mars and Venus appeared. Key aspects like the optimal orientation of the sail and an estimation of the time of travel were also investigated. The research of these early days has inspired a countless number of papers. It is out of the scope of this brief introduction to reference them all. We refer to [McI93] for a complete list of references up to the year 1999 and to [Mac11] for a more recent one.

6.1.1 Solar sails in space

From the early optimism of the pioneers to the current days, solar sailing has evolved from theoretical speculations to a new reality in the field of astrodynamics. Up to this day three sail-crafts have been launched to the space and many other programs involving solar sails are being planned.

The first sail-craft to be deployed successfully in history was IKAROS (Kite-craft Accelerated by Radiation of the Sun) by the Japan Aerospace Agency (May, 2010). The purpose of this mission was to test technology. The sail, a square 14m^2 membrane made of polymide, was successfully deployed and controlled. The effect of Solar Radiation Pressure to the orbit was monitored by AKATSUKI probe. IKAROS traveled to Venus and after the first experiments were completed, it continued traveling towards the far side of Sun. The project team was dissolved in 2013. IKAROS shifted to hibernation on May 2015.

The second sail-craft in space was Nanosail-D2 by NASA (November, 2010). This was the second version of a solar sail project named Nanosail-D. The first probe was lost at launch on August 2008. Nanosail-D2 was a $30 \times 10 \times 10$ three-unit Cube-Sat with a mass of 4kg, and sail area of 10m^2 when deployed. It was launched abroad Minotaur IV/HARS rocked inside the FASTSAT satellite. Nanosail-D2 was ejected and separated from FASTSAT, after some problems, on January, 2011. In September, 2011 the sail-craft re-entered the atmosphere after 240 days sailing in a low-Earth orbit.

The LightSail project, by Planetary Society, is an ongoing enterprise to test solar sail technology in a Cube-Sat satellite. The first craft launched in the context of this project was LightSail 1 on March, 2015. The project, as we mentioned, is still alive and currently the launch of LightSail 2 is being planned.

6.1.2 Solar sails in the Earth-Moon system

The first paper on solar sails in the Earth-Moon system we are aware of is due to C. McInnes, [McI93]. In this work, the author focuses on the translunar point. An out-of-plane orbit near L_2 is refined for a pitched sail. The author insists in the advantages this kind of orbit can provide in a hypothetical mission to observe the far side of Moon.

We had to wait until 2009 for a new paper on Solar Sails in the Earth-Moon system to appear. Hou et. al, [HTL09], focus on the triangular points. In this paper, the authors use station keeping strategies, based on solar sailing, to control a slightly unstable quasi-periodic motion near the Earth-Moon L_4 point in the whole solar system. This work is justified with the interesting features the location of triangular points have for deep space exploration. Also in 2009, Ozimek, Grebow and Howell, [OGH09], explore the facilities of a spacecraft endowed with a solar sail have to cover the lunar south pole. The authors remark the fact that, when it is propelled by a solar sail, a single spacecraft is able to undertake this task. The model used is based on the Restricted Three Body Problem, modified to take under consideration the Solar Radiation Pressure upon the sail (it is, in fact, the same model used by McInnes in 1993). Some interesting orbits are refined to the real solar system by means of the JPL ephemerides. Some orbits covering the south pole of Moon have also continuous communication with Earth. Howell and collaborators pursued in the problem of coverage of the lunar south pole. In the year 2011 three more publications, [WH11a, WH11b, WH11c], appeared completing the study: better methods and further calculations are presented in these new works.

The work by Simo and McInnes, [SM09a, SM10b, SM10a], appeared between 2009 and 2010. The authors control orbits (obtained from the linearized vector-field) near L_1, L_2 and L_4. The last publication ([SM10a]) includes a discussion on hybrid propulsion (sail and electric). The model used is, again, the modified Restricted Three Body Problem.

Heiligers' (together with a number of collaborators) work is a further step in the understanding the natural dynamics of a solar sail in the Earth-Moon Restricted Three Body Problem. The works we are about to mention have been inspiring for the realization of this thesis, as their approach is much closer to the one we used in this thesis than others. In [HHNC14, HHNM15a] continuations with respect to the effectivity of the sail of resonant Halo and Lyapunov orbits are presented. These periodic orbits are computed by means of an ODE with boundary conditions imposing the periodicity. This study has been expanded in the subsequent years, [HMP16b, HMP16b, HMP18], improving the method and dealing with other resonant orbits. In [HC17] the role of an oscillating sail is explored. The period of the sail is taken to be commensurable with the period of Sun. We think that oscillating solar sails have a huge potential to change the natural dynamics in a rather significant way. See also [LHC18] for computations regarding hybrid propulsion.

Finally, we mention the works related to this thesis [JCFJ16b, FJJC15a, JCFJ18]. The results shall be exposed in the present chapter. However, we would like to stress that previous works mentioned in this section use the same simplified model which does not take under consideration Sun's gravity. Certainly, some of the works refine orbits to the whole solar system but the deep explorations of the phase space needs to be done in simplified models.

6.2 The Model

In the present section, we discuss the model to describe the motion of a solar sail in the Earth-Moon System. The recipe to construct such a model is, first, to select a convenient basic model for the motion of the primaries: Earth, Moon and Sun. Once this is accomplished, the selected model has to be completed including the effect of SRP on the sail. We refer to the resulting model to be the **augmented** version of the former. This nomenclature has already used in the literature. In Chapter 5 we analyzed the role of Sun's gravity in the Earth-Moon system. In summary, we explored two different models, the BCP and the QBCP. According to our conclusions, the QBCP is the suitable model to study the motion around the collinear points, specially the translunar point. The BCP is suitable to undertake explorations near the triangular points. We build our models for the motion of a solar sail according to the conclusions of Chapter 5. We use the Augmented Quasi-Bicircular Problem (AQBCP) to study the dynamics near the Lagrangian points L_1 and L_2. The Augmented Bicircular Problem (ABCP) is used to study the motion of the triangular points and L_3. The reason we study the collinear point L_3 together with the triangular ones will be clear during the exposition of the results. These three (geometrically defined) points are related in a very specific way when the sail is added.

Stress again that, in the literature concerning to solar sails, most of the works do not take under consideration Sun's gravity. In fact, the only publications we are aware of are the ones related with this dissertation. Henceforth, to complete our exposition, we end up this chapter providing a comparison with the Augmented Restricted Three Body Problem (ARTBP).

Remark 6.2.1. *The following discussion involves the periodic functions α_i's presented in Chapter 5 (see Table 5.4). These functions are used to define the Hamiltonian of the QBCP. However, if we set,*

$$\begin{aligned} \alpha_1 &= \alpha_3 = \alpha_6 = 1, & \alpha_2 &= 0, \\ \alpha_4 &= \frac{m_S}{a_S^2}\cos\theta, & \alpha_5 &= -\frac{m_S}{a_S^2}\sin\theta, \\ \alpha_7 &= a_S\cos\theta, & \alpha_8 &= -a_S\sin\theta, \end{aligned}$$

these values define the Hamiltonian of the BCP and, setting also $m_S = 0$, we obtain the RTBP. Therefore, the next derivation of the acceleration due to the SRP can be applied to the three models but using the corresponding values of the functions α_i's. Notice that the mass of Sun m_S should not be taken zero when it multiplies the solar sail acceleration in the case of the ARTBP. We also point out that one of the angles defining the orientation of the sail is named α. This is rather an unfortunate notation that could be problematic only in the present section. We prefer to keep this notation, as it is used in previous works, and hope this will not confuse the interested reader.

6.2.1 Modeling SRP

SRP is the pressure exerted by the impact of photons upon a body. While the incidence of this effect is negligible in our everyday experience, SRP has a remarkable impact in the Solar System and some phenomena cannot be explained without it. Perhaps two of the most relevant ones are the existence of comet tails and the motion of interstellar dust. In both cases SRP acts together with the solar wind.

Recall that the idea behind solar sailing is to take advantage of this effect to move a spacecraft. The concept of this type of propulsion is radically different from the traditional ones, hence solar sails have to be used in different contexts. The main advantage of solar sailing is that the propellant is unlimited. The main inconvenient is that the acceleration given by SRP is much smaller than the one achieved by a traditional thruster.

The force exerted by SRP can be derived from any theory consistent with the fact that light (as a particle) can push matter. In [McI99] the author describes how the action of SRP is derived from both quantum mechanics and electromagnetic point of view. It holds that, as a first approximation, the pressure on some point at distance r to the Sun is given by

$$\mathcal{P} = \frac{W_E}{c}\left(\frac{R_E}{r}\right)^2, \qquad W_E = \frac{L_S}{4\pi R_E^2},$$

where, R_E is the Earth-Sun distance, L_S is the solar luminosity and c is the speed of light. Notice that this is an inverse square law, fact that eases to compare SRP and Solar gravitation. This formulation assumes Sun to be a punctual mass, if one takes into account the angular size of the solar disk, the expression for $\mathcal{P}$ becomes more sophisticated [McI99]. Stress that, if the photons impact on a perfectly reflecting surface, the observed pressure is twice this value of $\mathcal{P}$ (due to the action-reaction law). Consider now a solar sail with area A and mass m. Suppose also that the sail is **perfectly reflecting** [2]. The force exerted upon the spacecraft by SRP is given by

$$F_{SS} = 2\mathcal{P}A\langle \vec{r}, \vec{n}\rangle^2 \vec{n},$$

[2] In this chapter, solar sails are perfectly reflecting.

where $\vec{r}$ is the Sun-sail vector and $\vec{n}$ is a unitary normal vector to the surface of the sail. We will be more precise in how to chose the normal vector n in a moment. As we already have pointed out, the solar sail acceleration can be written in terms of Sun's gravitational acceleration

$$a_{\vec{SS}} = \beta \frac{Gm_S}{r_{PS}^2} \langle \vec{r}, \vec{n} \rangle^2 \vec{n}, \tag{6.1}$$

where m_S is the mass of the Sun, G is the universal gravitational constant and β is the so-called lightness number of the Sail, see [McI99].

Let us take a look again to expression (6.1). The term Gm_S/r_{PS}^2, depends on the position of the sail in the Earth-Moon system. However, this dependence is negligible compared to the dependence on the position of Sun. Hence, it is usual [SM09b, FJJC15b, HHNM15b, HMP16a, JCFJ16a] to perform the following simplification:

$$\frac{m_S}{r_{PS}^2} \approx \frac{m_S}{x_S^2 + y_S^2}.$$

Here, the vector $(x_S, y_S, 0)$ gives the position of Sun in the plane of motion of the primaries. Therefore, it is assumed that the sail can be regarded as frozen at the centre of masses of the Earth-Moon system. This is done to keep the Hamiltonian character of the model for all the orientations of the sail.

Now we can adjust SRP acceleration to the features provided by the functions α_i. This has only an impact when these functions are the ones corresponding to the QBCP, see Remark 6.2.1 for more details. In the first place, the solar sail acceleration is modified to take into account the non-constant distance between Earth and Moon.

$$a_c = \alpha_6 \frac{m_S}{\alpha_7^2 + \alpha_8^2} =: \alpha_6 \frac{m_S}{D^2}.$$

Now we only have to determine the orientation of the sail. The unitary vector $\vec{r}$ is taken as the unitary Sun Earth-Moon barycentre direction, that is

$$\vec{r} = (\tilde{\alpha}_7, \tilde{\alpha}_8, 0) = \frac{(\alpha_7, \alpha_8, 0)}{D}$$

Let us choose γ orthogonal to r i.e. $\vec{\gamma} = (-\tilde{\alpha}_8, \tilde{\alpha}_7, 0)$. Finally, $\vec{n} = \mathcal{R}_\alpha^x \mathcal{R}_\delta^{\vec{\gamma}} \vec{r}$, where $\mathcal{R}_\delta^{\vec{\gamma}}$ stands for the rotation matrix of angle δ along the axis γ and $\mathcal{R}_\alpha^x$ denotes the rotation of angle α about the x axis i. e.

$$\mathcal{R}_\delta^{\vec{\gamma}} \vec{r} = \begin{pmatrix} \cos\delta + \tilde{\alpha}_8^2(1-\cos\delta) & -\tilde{\alpha}_8\tilde{\alpha}_7(1-\cos\delta) & \tilde{\alpha}_7 \sin\delta \\ -\tilde{\alpha}_8\tilde{\alpha}_7(1-\cos\delta) & \cos\delta + \tilde{\alpha}_7^2(1-\cos\delta) & -\tilde{\alpha}_8 \sin\delta \\ -\tilde{\alpha}_7 \sin\delta & -\tilde{\alpha}_8 \sin\delta & \cos\delta \end{pmatrix} \begin{pmatrix} \tilde{\alpha}_7 \\ \tilde{\alpha}_8 \\ 0 \end{pmatrix} = \begin{pmatrix} \tilde{\alpha}_7 \cos\delta \\ \tilde{\alpha}_8 \cos\delta \\ \sin\delta \end{pmatrix}.$$

Finally, after the composition with the matrix $\mathcal{R}_\alpha^x$, the direction of the acceleration due to SRP, denoted by the vector $\vec{ss}$, is given by:

$$\begin{aligned} ss^x &= \cos^3\delta\cos^2\alpha(\cos\alpha\tilde{\alpha}_7 + \sin\alpha\tilde{\alpha}_8),\\ ss^y &= \cos^3\delta\cos^2\alpha(\sin\alpha\tilde{\alpha}_7 + \cos\alpha\tilde{\alpha}_8),\\ ss^z &= \cos^2\delta\cos^2 2\alpha\sin\delta. \end{aligned}$$

Here, $\delta, \alpha \in (-\pi/2, \pi/2)$ are angles relative to the Sun line and ω_S is Sun frequency. Once we have an expression for SRP acceleration we can add it to the equations of the our restricted model, to complete it. The system is given by the periodic time dependent (with the same period as Sun, $T_S = 2\pi/\omega_S$) Hamiltonian function:

$$\begin{aligned} H = &\frac{1}{2}\alpha_1(p_x^2 + p_y^2 + p_z^2) + \alpha_2(p_x x + p_y y + p_z z)\\ &+ \alpha_3(p_x y - p_y x) + \alpha_4 x + \alpha_5 y - \alpha_6\left(\frac{1-\mu}{r_{pe}} + \frac{\mu}{r_{pm}} + \frac{m_S}{r_{ps}}\right) - \frac{\beta m_S}{a_S^2}\langle\vec{ss}, \vec{e}\rangle. \end{aligned} \tag{6.2}$$

Here, the vector $\vec{e}$ is given by $\vec{e} = (x, y, z)^T$. It is easy to see that the Hamiltonian function (6.2) has the symmetries

$$(\theta, x, y, z, \dot{x}, \dot{y}, \dot{z}, \beta, \alpha, \delta) \mapsto (-\theta, x, y, -z, \dot{x}, \dot{y}, -\dot{z}, \beta, \alpha, -\delta), \tag{6.3}$$

and

$$(\theta, x, y, z, \dot{x}, \dot{y}, \dot{z}, \beta, \alpha, \delta) \mapsto (-\theta, x, -y, z, \dot{x}, -\dot{y}, \dot{z}, \beta, \alpha, \delta), \tag{6.4}$$

where $\dot{x} = p_x + y$, $\dot{y} = p_y - x$, $\dot{z} = p_z$.

6.2.2 Values of the parameters used in this work

Parameter β: The lightness number is the ratio between SRP and Sun's gravitational acceleration. It is used to quantify the effectivity of the sail. Real solar sails in space have achieved the following values: $\beta = 0.001$ (IKAROS), $\beta = 0.008$ (Nanosail) and $\beta = 0.011$ (LightSail-1). When $\beta = 1$ the magnitude of SRP acceleration (if the sail is perpendicular to the Sun) is the same as Sun's gravitational acceleration but in the opposite direction. Indeed,

$$\beta = \frac{\sigma^*}{\sigma}, \qquad \sigma^* = \frac{L_S}{2\pi G m_S c} \approx 1.53 g/m^2.$$

The quotient $\sigma = m/A$ is the sail loading parameter and parametrizes the performance of the Sail.

β	σ (g/m^2)	a_0 (mm/s^2)	Area (m^2)
0.01	153.0	0.059935	$\approx 8 \times 8$
0.02	76.5	0.119869	$\approx 12 \times 12$
0.03	51.0	0.179804	$\approx 14 \times 14$
0.04	38.25	0.239739	$\approx 16 \times 16$
0.05	30.6	0.359608	$\approx 20 \times 20$

Table 6.1: Relation between: β the sail lightness number, σ the inverse of the area-to-mass ratio of the satellite, a_0 the characteristic acceleration and A the sail area requirements for 10 kg of total mass [DSM$^+$05].

We call characteristic acceleration to the acceleration experienced by the sail-craft at 1 AU. Moreover, if we have a spacecraft mass of 10 kg we need a solar sail area of almost 14×14 m^2 for a sail lightness number $\beta = 0.03$. In Table 6.1 we can see, for different sail lightness numbers β, the corresponding to inverse of the area-to-mass ratio (σ), the characteristic acceleration (a_0) and the size of the solar sail for 10 kg of total spacecraft mass. This means that a sail lightness number $\beta = 0.03$ corresponds to a characteristic acceleration of 0.179804 mm/s^2. Taking into account the current technology capabilities, we shall focus on moderate values $\beta \in [0, 0.1]$. These are values for which SRP has a remarkable impact on the natural dynamics of a spacecraft in the Earth-Moon system. If we compare SRP acceleration with the Sun's (in the BCP, for simplicity) gravity acceleration we realize that the first is only a fraction (given by β) of the second. Therefore, a priory, it could seem that the contribution by Sun's gravity is much more important to the dynamics than the contribution by SRP. Nevertheless, this is not the case. Let us consider the series expansion of the Hamiltonian function of the BCP. The linear term is the same as the Coriolis term due to the motion of Earth-Moon barycentre but with opposite sign[3]. Therefore, the linear term and the Coriolis force cancel out and the contribution due to Sun's gravity starts at order two:

$$\frac{1}{a_S}\left(\frac{\rho}{a_S}\right)^2 P_2\left(\frac{\cos(\theta)x - \sin(\theta)y}{\rho}\right) \sim \mathcal{O}\left(\frac{m_S}{a_S^3}\right) \approx 0.0056,$$

while the acceleration due to SRP is of order $\mathcal{O}(\beta\frac{m_S}{a_S^2}) \approx 2.17\beta$. Recall that, here, P_2 is the second Legendre polynomial and $\rho = x^2 + y^2 + z^2$. Therefore, SRP dominates Sun's gravity in the Earth-Moon System.

Parameters α and δ: These parameters define the orientation of the sail in space. The angle α directs acceleration in the direction of the plane of motion of the primaries. The angle δ directs out-of-plane acceleration if it $\delta \neq 0$. In the case when $\delta = 0$ there is no out-of-plane acceleration. Therefore, the orbits that are confined in the plane of the primaries

[3]This has been developed in Chapter 5, Section 5.2.

stay confined when the sail is added. To study these confined motion **one can dispense with the vertical direction** and the system can be considered a two degrees and a half Hamiltonian system. Indeed, the discussion presented in Section 6.7 is done in terms of a four dimensional stroboscopic map.

It is easy to see that, for a fixed value of β, the magnitude of SRP acceleration is maximized at $\alpha = \delta = 0$, while the maximum out-of-plane acceleration is given by $\pm\delta_{max} = \pm\sin^{-1}(1/\sqrt{3})$. Both angles have physical sense when $\delta, \alpha \in [-\pi/2, \pi/2]$. If one of the two angles is set to $\pi/2$ or $-\pi/2$, SRP vanishes.

6.3 Preliminaries

In this section we summarize some of the information found in Chapter 5 that is to be used in the present chapter. This is done to keep this chapter as self-contained as possible and do not refer constantly to Chapter 5. We also explain the strategy to be followed to complete our study.

Let us set our mind in the context of the RTBP and remind that, as application of the Lyapunov centre theorem, we know that a family of periodic orbits (which can be parametrized by the period) grow along each elliptic direction related to each Lagrangian equilibrium point. The collinear points L_1, L_2 and L_3 have two elliptic directions and the triangular points have three of elliptic directions.

When the perturbation due to the gravity of Sun is considered, almost all (in the measure theory sense) these periodic orbits are replaced by two-dimensional invariant tori. Essentially, the periodic orbits gain the frequency of Sun. Anyhow, there is a set of these periodic orbits that remains being periodic when Sun's gravitational potential is considered. These orbits are the ones whose period is a (rational) multiple of the period of Sun, these are called **resonant orbits**. We focus on resonant orbits of low order, those only seem to appear in the vicinity of the collinear points L_1 and L_2.

Summarizing, there is a set of periodic orbits of the RTBP, close to the Lagrangian points L_1 and L_2, that can be continued as a T_S-periodic orbits to the QBCP. These computations can be found in [And98]. In this work the authors set labels for the orbits depending on the Lagrangian points which they are related to and their properties. When these orbits are continued from the RTBP to the QBCP several bifurcation points appear. That is, it is usual that a resonant orbit of the RTBP has several related orbits in the QBCP. The orbits of the QBCP are labeled taking into account these relations.

In Table 6.2 we summarize the given information. This Table has been also presented in Chapter 5. We repeat it here to ease the reading. We recall that, in the left column we show the label of each resonant orbit of the RTBP. Notice that these labels start with a zero. The

first character of each label indicates the libration point the orbit is associated with. The second character refers to the type of family: numbers identify orbits in the Lyapunov family and letters do it for orbits in the Halo family. For instance 12 is a Lyapunov trajectory near to L_1 while $2A^+$ is a Halo orbit related to L_2. The $\pm$ sign as super-index only appears in the Halo orbits. The $+$ stand for trajectories of the Halo family whose initial condition lie above the plane. The sign $-$ denotes the symmetric counterpart below the plane.

In the central columns, we show the order of the resonance and the number of bifurcating orbits appearing during the continuation. Lastly, in the right column, we show the orbits corresponding to the QBCP.

RTBP	RES	BIF	QBCP
012	1 : 2	2	12, 13
014	1 : 1	4	14, 15, 16, 17
018	1 : 1	4	18, 19, $1A^{\pm}$, $1B^{\pm}$
01C	1 : 3	2	$1C^{\pm}$, $1D^{\pm}$, $1N^{\pm}$
01E	1 : 3	2	$1E^{\pm}$, $1F^{\pm}$
022	1 : 2	4	22, 23, 24, 25
026	1 : 6	4	26, 27, 28, 29
02A	1 : 2	4	$2A^{\pm}$, $2B^{\pm}$, $2C^{\pm}$, $2D^{\pm}$
02E	1 : 3	2	$2E^{\pm}$, $2F^{\pm}$
026	1 : 4	2	$2G^{\pm}$, $2H^{\pm}$

Table 6.2: Continuation of the low order resonant orbits from the RTBP to the QBCP. The first column contains the label of the orbits corresponding to the RTBP. The second column contains the order of the resonance. The third columns contains number of bifurcating orbits. The fourth column contains the label of the orbits corresponding to the QBCP. See [And98] for more details. See text for the color code.

On the color code: We have added a color code to indicate the linear normal behaviour of each orbit. Labels in red stand for orbits of type saddle×centre×centre. Labels in green denote linear character of the kind saddle×saddle×centre. Labels in cyan denote totally hyperbolic orbits. The color black denotes totally elliptic orbits. The continuation for the orbits in yellow do not reach the homotopy level of the QBCP and, therefore, are not considered. This color code will be maintained during the whole manuscript. In the plots showing continuation curves, the points are colored according to this pattern. Notice that in other plots such as the ones in which we plot trajectories of the flow, we use different colors and they do not denote any kind of normal behaviour.

Dynamical equivalents of the libration points: The libration points are no longer equilibria in the QBCP nor the BCP. These points are replaced by periodic orbits with the same period as Sun. Usually, in the literature, these orbits are refereed as the **dynamical equivalents** of the Lagrangian points. Through this chapter, we shall referee to these equivalent orbits by the name of the corresponding equilibrium point in all the cases but not for the dynamical equivalents of the triangular points, indeed, there are three of them for each equilibria.

Orbits to be followed: In this chapter we do not keep track on how all the orbits in Table 6.2 evolve with respect to the parameters of the sail. We focus on the most relevant ones. Let us give some words on how we choose them. First of all most of the bifurcating orbits end up having trajectories which are close (in the phase space) to each other for any time. From these orbits which are similar, we select just one. On the other hand, there are orbits that are close to collision with one of the primaries (maybe both). These orbits lack of great interest as the effect of SRP is to drive them closer to the primaries but without a substantial change on their shapes. These quasi-colliding orbits are: 14, 15, 16, 17, 18, 19, $1A^{\pm}$, $1B^{\pm}$, $1E^{\pm}$, $1F^{\pm}$ 26, 27, 28, and 29 . We focus on the orbits L_1, 12, $1C^{\pm}$, $1N^{\pm}$, L_2, 22, $2A^{\pm}$, $2E^{\pm}$, $2G^{\pm}$ L_3, L_4 and L_5. The orbits which have not been mentioned are skipped as their trajectories are similar to one of the studied orbits. From a pack of similar orbits, all of them bifurcating from a certain resonant orbit of the RTBP, we select the one obtained by following the main branch in the continuation process.

Surfaces and sections: In this work we will move the angle δ near the collinear points L_1 and L_2 and the angle α to study the triangular points. As these two angles are not set different from zero at the same time, we are dealing with systems depending on two parameters in both cases (the corresponding angle and the effectivity). That is, for each periodic orbit of the QBCP (BCP) there is a surface of fixed points (of the stroboscopic map) in the AQBCP and ABCP parametrized by the orientation and the effectivity. We will study these surfaces by means of sections. That is, the families of curves obtained by cutting the surfaces by some subspace $\{\delta = \delta^+\}$, $\{\alpha = \alpha^+\}$ or $\{\beta = \beta^+\}$.

Main goal: The natural dynamics of both models, the AQBCP and the ABCP, is organized from their fixed points. This means that invariant structures with larger dimension are determined by the position and the normal behaviour of these fixed points. Therefore, it is crucial to understand how the dynamical equivalents of the Lagrangian equilibria are change, bifurcate and connect to each other when the parameters of the sail are moved. In other words, we want to understand the geometry of the surfaces of fixed points near each of the Lagrangian points.

6.4 Motion near L_1

In the present section we focus on how the periodic orbits L_1, 12, $1C^{\pm}$ and $1N^{\pm}$ change with respect to the parameters of the sail. We perform a continuation of each of these orbits with respect to the parameter β for a perpendicular sail ($\delta = 0$). Then we move the angle δ for fixed values of the β.

6.4.1 Continuation with respect to β

The following set of simulations goes as follows: We fix an orientation of the sail (most of the times we fix $\delta = 0$) and we continue the periodic orbits L_1, 12, $1C^{\pm}$ and $1N^{\pm}$ with respect to β. Let us check, first, how the dynamical equivalent of L_1 changes. When the sail is perpendicular to the direction of Sun ($\delta = 0$), there is no out-of-plane acceleration due to SRP. Therefore, L_1 remains a planar orbit for all values of β. As the value of β increases, the trace of the orbit becomes larger. Even though the trajectories get bigger in size, the growth with respect to β is slow.

In Figure 6.1 (a), we show trajectories corresponding to the continuation of L_1 (purple) and 12 (green) with respect to β. The continuation is started at $\beta = 0$ and it is stopped at

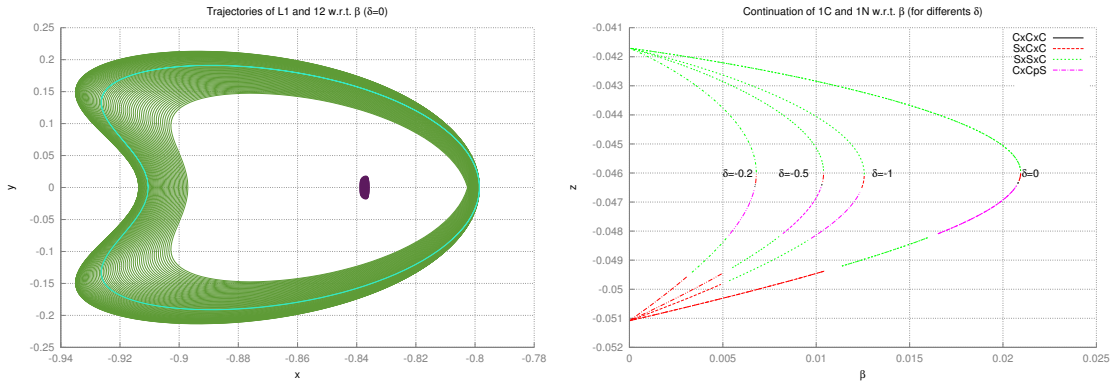

(a) (b)

Figure 6.1: **(a):** Trajectories corresponding to the continuation of L_1 and 12 with respect to β. The purple trajectories correspond to the dynamical equivalents of L_1 and the green trajectories correspond to the dynamical equivalents of 12. The blue curve denotes the trajectory 12. **(b):** Continuation with respect to β of $1C^+$ and $1N^+$ for the fixed values of $\delta = -0.2, -0.5, -1$ and 0. The angles are measured in radians.

the value $\beta = 1$. This maximal value of β is chosen in the seek for a clearer picture of the situation. As we mentioned, Figure 6.1 (a) also shows the dynamical equivalents of 12 for the same values of β. Here the situation is slightly different. First of all, the trajectories grow, becoming larger. Notice that this growth is limited by the presence of the primaries. For some value of β the dynamical equivalents of 12 start to decrease in size and, in fact, until they meet L_1 (at a value of $\beta \approx 4.2$ much larger than what is permitted taking into account the current technology and the ones we focus on in this chapter).

We do not show a characteristic curve for this continuation because the interesting phenomena in this continuation occurs for extremely large values of β. It is enough to mention that the periodic orbits L_1 and 12 are connected with respect to β through a saddle-centre bifurcation.

Let us see now how SRP affects the Halo orbit $1C^+$ and $1N^+$ (the situation of $1C^-$ and $1N^-$ is completely symmetric). In Figure 6.1, (b), it is displayed the continuation of $1C^+$ with respect to β for different values of δ. Notice that, each curve crosses the homotopy level $\{\beta = 0\}$ twice: $1C^+$ is the crossing point at the bottom, the one at the top is $1N^+$. The characteristic curves show several bifurcations. At the beginning the curves (red) start with saddle×centre×centre linear character. There is a period doubling bifurcation and the curves turn into saddle×saddle×centre. After a transition not seen in Figure 6.1, (b), due to the scale, the curves switch to centre×complex-saddle (magenta). Then the curve turns again into saddle×centre×centre. After a saddle-centre bifurcation the linear character switches finally to saddle×saddle×centre.

6.4.2 Continuation with respect to δ

Let us study how the fixed point corresponding to the periodic orbit L_1 changes with respect to δ. In Figure 6.2, (a), we show ten characteristic curves for fixed values of β from $\beta = 0.01$ to $\beta = 0.1$ (with constant step 0.01). The behaviour of all these curves is the same: First, the z value grows for $\delta \in (-\pi/2, -\delta_{max})$, where $\delta_{max} = \sin^{-1}(1/\sqrt{3})$. After reaching the homotopy level $\{\delta = -\delta_{max}\}$, the z value starts to decrease, crossing the plane of motion of the primaries. When the continuation curve reaches $\{\delta = \delta_{max}\}$ the z value increases until $\{\delta = \pi/2\}$, where the curve meets again L_1. This is the typical effect of SRP on the trajectories when the orientation of the sail changes, at least for small values of β.

If we look at the trajectories in the whole phase space, we notice that, for negative values δ, the trajectories are confined above the plane of motion of the primaries, while, for positive values, they lie below. The linear behaviour is the same for all the values of δ and all the characteristic curves: saddle×centre×centre. The maximal eigenvalue does not change substantially in any of these curves. We remark that the planar orbits near the geometrically defined L_1 are highly unstable, i.e. the maximal eigenvalues have extremely large moduli, in

this case, it is of order 10^8 (see Table 6.3). The effect of SRP on the stability of the orbits is treated in a more deep way in Section 6.6.

We discuss now the fate of 12 as the parameter δ changes. In Figure 6.2, (b), we show ten characteristic curves for fixed values of β from $\beta = 0.01$ to $\beta = 0.1$ (with constant step 0.01). The first thing to be said is that the plot shown in Figure 6.2, (b), can be misleading. We observe that, the fixed point corresponding to 12 is driven below the plane of motion of the primaries for negative values of δ while one expects the contrary. In Figure 6.3 we show the trajectories corresponding to the characteristic curve for $\beta = 0.01$. The curve in green is the one with $\delta = -\delta_{max}$, the solid one in blue corresponds to $\delta = 0$ (it is contained in the plane) and the purple one corresponds to $\delta = \delta_{max}$. The blue dashed solid curves are a sample of the curves corresponding to the rest of the initial conditions in the characteristic curve.

Notice that, even if the initial condition of the green curve lies below the plane, the trajectory is tilted up. Analogously, the purple curve is tilted down while the initial condition is above the plane. The interesting thing about this behaviour is that, the green and purple curves have a lot of the desirable properties of Halo orbits but lie much closer to the plane. Again, for reasonable values of β the impact of SRP is not strong enough to produce bifurcations. Henceforth, the stability type of all the fixed points of Figure 6.2 (b) (and the corresponding associated trajectories in Figure 6.3) is saddle×saddle×centre.

Let us analyze the continuation with respect to δ of the Halo orbits $1C^+$ and $1N^+$. The situation of their symmetric counterparts, $1C^-$ and $1N^-$ is completely analogous. For small

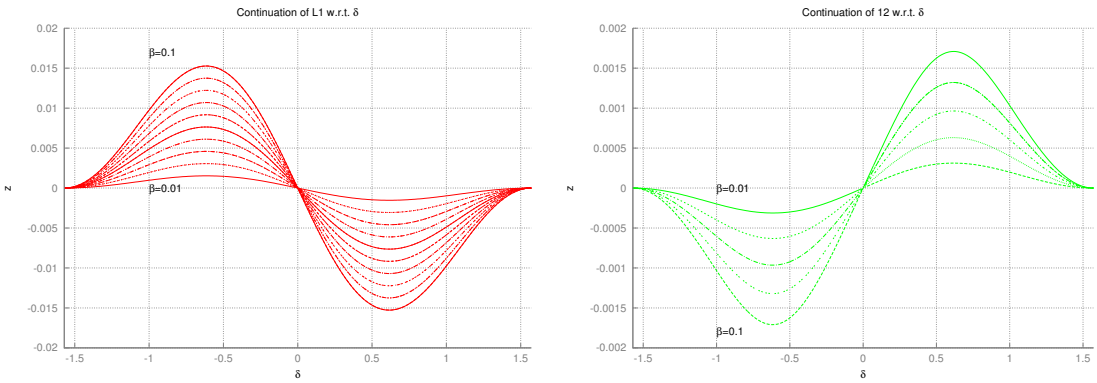

(a) (b)

Figure 6.2: **(a):** Continuations with respect to δ of L_1. The parameter β is fixed for values between 0.01 and 0.1. The stability type is saddle×centre×centre for all the fixed points. **(b):** Continuations with respect to δ of 12. The parameter β is fixed for values between 0.01 and 0.1. The stability type is saddle×saddle×centre for all the fixed points.

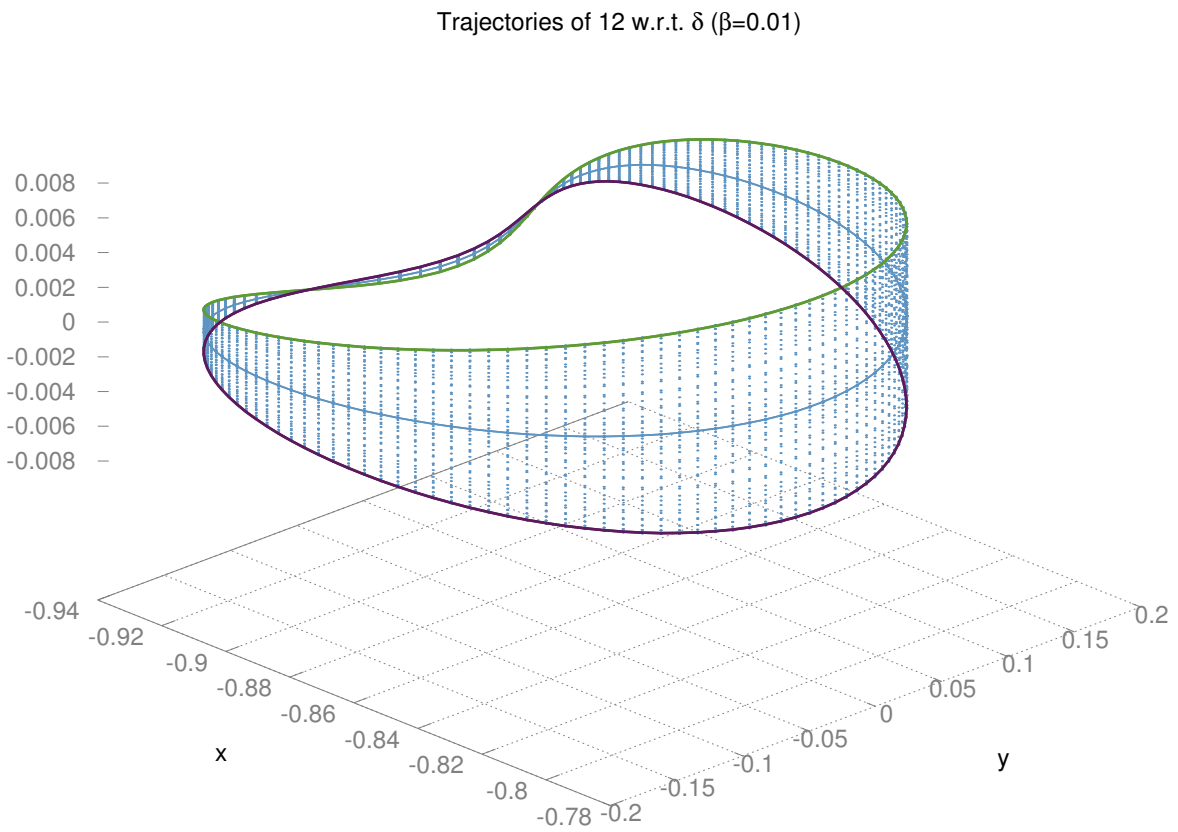

Figure 6.3: Trajectories corresponding to the characteristic curve of Figure 6.2 (b) for $\beta = 0.01$. The blue curve contained in $\{z = 0\}$ is the trace of orbit associated to $\delta = 0$. The green curve corresponds to the trajectory with $\delta = -\delta_{max}$. The purple curve to the trajectory with $\delta = \delta_{max}$. See the text for more details.

enough values of β, the effect of the sail's orientation is to move the orbits upwards (for negative values of δ) and downwards (for positive values of δ). Anyhow for $\beta > \beta^* \approx 0.078$ the situation is different. Indeed, if such is the case, the periodic orbits $1C^-$ and $1N^-$ are connected by continuation with respect to the parameter δ.

In Figure 6.4, (a), we display the characteristic curves for $\beta = 0.01, 0.02$ and 0.03 (we only show three curves because to put more does not add relevant information and the superposition of the curves makes the picture harder to read). One can observe that the curve is split in two connected components. The first of these two components is obtained by

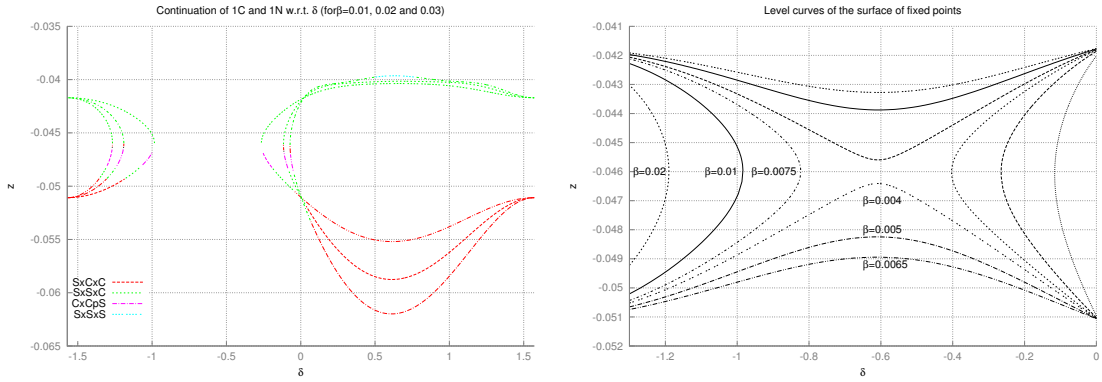

(a) (b)

Figure 6.4: **(a):** Continuations with respect to δ of $1C^+$ and $1N^+$. The parameter $\beta = 0.01, 0.02$ and 0.03. **(b):** Slices of the surface of fixed points connecting $1C^+$, $1N^+$. In this case, the (black) color do not represent any kind of stability behaviour.

continuation for negative values of δ (continuation forwards). Indeed, if we start at $1C^+$ and $\delta = -\frac{\pi}{2}$, we find fixed points for some range $\delta \in [-\frac{\pi}{2}, \delta^1_{tp}(\beta)]$, where $\delta^1_{tp}(\beta)$ is a value of δ, depending on β, for which the curve has a turning point (a saddle-centre bifurcation) and the continuation curve goes back to the homotopy level $\{\delta = -\frac{\pi}{2}\}$. Numerical evidences suggest that $|\delta^1_{tp}|$ is an increasing function of β. The stability type of the orbit changes along the curve. Orbit $1C^+$ is of type saddle×centre×centre, while $1N^+$ is of type saddle×saddle×centre. There is also a relevant range of δ-values for which the stability type of the curves is complex-saddle×centre. Another stability type appears to fulfill transitions between saddle×centre×centre and complex-saddle×centre (and viceversa): the totally elliptic. However it appears for ranges so small it cannot be observed in Figure 6.4 (a).

The second connected component is obtained by continuing $1C^+$ from $\{\delta = \frac{\pi}{2}\}$ to smaller values of δ (continuation backwards). We obtain new fixed points for $\delta \in \{\delta^2_{tp}(\beta), \frac{\pi}{2}\}$. Again δ^2_{tp} is a value of δ for which the characteristic curve encounters a turning point. The transition between stability types is similar to the one described for the first component of the curve. The simulations show, as well, that δ^2_{tp} is a decreasing function of β. We would like to notice that both pieces of the curve are, in fact, two different loops (there is a part of each component which does not appear in Figure 6.4 (a) because they take physically meaningless values of $\delta \notin [-\frac{\pi}{2}, \frac{\pi}{2}]$). The connected component obtained by continuation backwards, the one on the right in Figure 6.4 (a), is larger, and if β is small enough (as the values we show in Figure 6.4 (a)) it crosses $\{\delta = 0\}$. Notice that there are no fixed points for $\delta \in (\delta^1_{tp}, \delta^2_{tp})$. The length of this interval increases with β.

A geometrical point of view: To reach a better understanding of the situation described for the continuations of $1C^+$ and $1N^+$ we switch to a more geometrical point of view. As we move the parameters β and δ, we create a surface of fixed points. This surface is compact, with boundary, and embedded in the six-dimensional phase space. It also contains the fixed points $1C^+$ and $1N^+$ corresponding to the QBCP. This surface has a geometric saddle point. In Figure 6.4, (b), we show several level curves in β (continuation curves with respect to δ). Notice that the values of the horizontal axis range between -1.3 and 0. The saddle point is clearly observed.

6.5 Motion near L_2

In the present section we focus on how the periodic orbits L_2, 22 , $2A^{\pm}$, $2E^{\pm}$ and $2G^{\pm}$ change with respect to the parameters of the sail. As in the section devoted to L_1, we first measure the effect of the SRP when the sail is perpendicular to Sun. To do so, we perform a continuation of each of these orbits with respect to the parameter β for a perpendicular sail. Then we move the angle δ for fixed values of the β.

6.5.1 Continuation with respect to β

We focus first in the planar orbits. Let us fix $\delta = 0$ and continue L_2 and 22 with respect to β. As we pointed out before, the perpendicularity of the sail keeps these orbits to be planar for all the values of β. Unlike the case of L_1 and 12, the fixed points are not connected by continuation with respect to β (at least, for the values studied in this work). L_2 can be continued, however, to the orbit 24 of Table 5.2. We recall that orbit 24 bifurcates from 22 when it is continued from the RTBP to the QBCP and that their traces remain close for all time. In practical effects, they can be considered the same orbit. Again, the value of β is too large to be considered to practical purposes ($\beta \approx 4.2$). Being realistic on the values of β considered, we can only state that SRP changes the size and the shape of the periodic orbits L_2. In the case of 22 we have continued it for large values of β seeing small changes in the orbits besides becoming slightly larger. Similarly, SRP has not a remarkable impact on the Halo orbits $2A^{\pm}$ when the sail is perpendicular to Sun. Not even the size of the orbit is change substantially. We do not provide plots of these continuations as nothing interesting happens for realistic values of β.

The case of the Halo orbits $2E^{\pm}$ and $2G^{\pm}$ is a not much more interesting. Let us do, however, some comments. First of all, let us notice that these Halo orbits reach much higher values above (below) the plane of motion of the primaries than the orbits $2A^{\pm}$. Second, they pass much closer to Moon. With these two points under consideration, is to be expected some

difference. Indeed, SRP acts in $2E^{\pm}$ and $2G^{\pm}$ displacing the orbits towards the position of Moon and making their traces pass even closer. In fact, with relatively low values of β we can produce colliding trajectories from $2G^{\pm}$. The linear character of the orbits L_2, 22, $2E^{\pm}$ and $2G^{\pm}$ remains unchanged for all the explored values of β when the sail is perpendicular to Sun.

6.5.2 Continuation with respect to δ

We focus now on the continuation curves obtained by fixing β and changing δ. Let us start with L_2. As in the case of L_1, the effect of SRP to the fixed point L_2 is to move it above the plane (for negative values of δ) and below the plane (for positive values of δ).

See Figure 6.5 (a) for a sample of ten characteristic curves with β ranging from 0.01 to 0.1 with constant step-size. There we see how the fixed points corresponding to L_2 increase its z value, reaching a maximum at $\{\delta = -\delta_{max}\}$, then they decrease, crossing the plane at $\{\delta = 0\}$, reaching a minimum at $\{\delta = \delta_{max}\}$. Finally the fixed points return to the plane of motion of the primaries to meet the QBCP L_2 at the homotopy level $\{\delta = \frac{\pi}{2}\}$. The stability type of all the curves in Figure 6.5 (a) is saddle×centre× centre.

Let us describe the continuations of 22, $2A^+$ and $2A^-$. Notice that, in this case, $2A^+$ and $2A^-$ are named separately. For sufficiently large values of β, the three orbits are related by continuation and the characteristic curve is split in three connected components. We take a

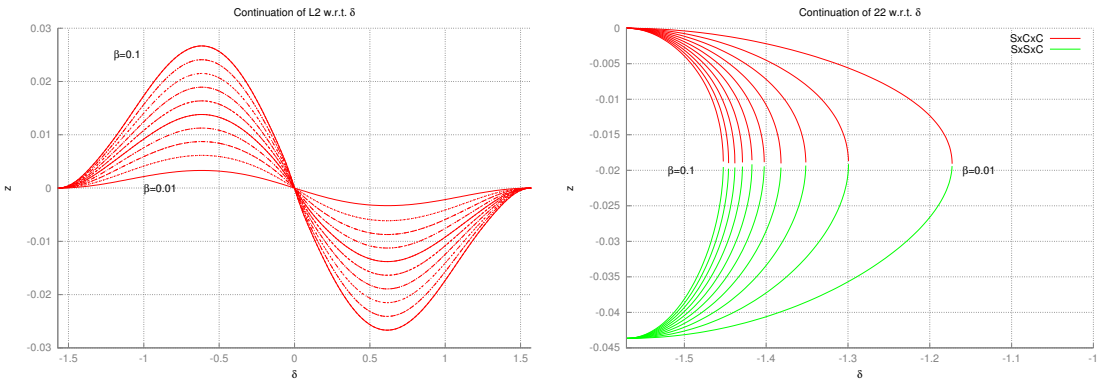

(a) (b)

Figure 6.5: **(a):** Continuation of the orbit L_2 with respect to δ for fixed values of β. These values of β range between 0.01 and 0.1 with constant step. **(b):** Continuation of the orbit 22 and $2A^-$ with respect to δ for fixed values of β. These values of β range between 0.01 and 0.1 with constant step.

look first at Figure 6.5 (b). This picture is a magnification of Figure 6.6 (a) and shows the continuation forwards of 22. We show a sample of ten characteristic curves for which the qualitative behaviour is the same: The method finds fixed points for $\delta \in (-\frac{\pi}{2}, \delta^3_{tp}(\beta))$. Again, $|\delta^3_{tp}|$ increases with β. The turning point corresponds to a saddle-centre bifurcation and the linear behaviour switches from saddle×saddle×centre to saddle×centre×centre. After the turning point, the continuation curve returns back to the homotopy level $\{\delta = \frac{\pi}{2}\}$. Again we see that the initial conditions of 22 move below the plane when we expect to move above and, again, it is a matter of initial conditions. The trajectories are, in fact, tilted up. Moreover, this continuation sets an homotopy from a planar orbit to a Halo one, which makes this particular continuation interesting.

Figure 6.6 (a) shows the complete picture. The small component on the left are the curves represented in Figure 6.5 (b). The other small component is the symmetric counterpart: A set of continuation curves (with β between 0.01 an 0.1) connecting 22 with $2A^+$ but by continuation backwards. Let us focus on the long component i.e. the continuation of $2A^+$ forward. These are the ten curves in Figure 6.6 (a) crossing from the homotopy level $\{\delta = -\frac{\pi}{2}\}$ to the homotopy level $\{\delta = \frac{\pi}{2}\}$. Again, the fixed values of β range from 0.01 to 0.1 with constant step-size. The qualitative behaviour of all these curves is the same. Let us describe it. The characteristic curves start for $\delta = -\frac{\pi}{2}$ at the QBCP $2A^+$. The z coordinate of the fixed points increases its value as $\delta \in (-\frac{\pi}{2}, -\delta_{max})$. For $\delta \in (-\delta_{max}, 0)$, the z value decreases but it is still positive. For $\delta = 0$ the characteristic curves cross the plane and meet a planar orbit. This planar orbit can be obtained also continuing 22 with respect to β when the sail is perpendicular to Sun. Notice that, before the characteristic curve crosses the plane, there is a saddle-centre bifurcation and the stability type changes form saddle×centre×centre to saddle×saddle×centre. After the characteristic curve crosses the plane, the z value keeps decreasing (it encounters another saddle-centre bifurcation) until it reaches the homotopy level $\{\delta = \delta_{max}\}$. These continuations establish homotopies between the orbits $2A^+$ and $2A^-$ i.e. the characteristic curves do not cross the plane of motion of the primaries again, it ends up at $2A^-$. As in the case of the continuations of $1C^+$ and $1N^+$, there is a geometrical interpretation of the shape of the continuation curves connecting 22, $2A^+$ and $2A^-$. There is a compact with boundary surface of fixed points that contains 22, $2A^+$ and $2A^-$. This surface has also a geometric saddle point at $\{z = 0, \delta = 0\}$. However, in this case, the saddle point is degenerated due to the symmetry of the vector-field given in (6.3).

Figure 6.6 (b) shows the continuation of $2G^+$ (the situation of $2G^-$ is analogous by symmetry) with respect to δ. Again the values of β range from 0.01 to 0.1 with constant step-size. The characteristic curve starts, for $\{\delta = -\frac{\pi}{2}\}$, at the QBCP $2G^+$. The z value of the characteristic curve increases for $\delta \in [-\frac{\pi}{2}, -\delta_{max}]$. A number of period doubling-halving processes take place in these curves. We name a period doubling-halving process the

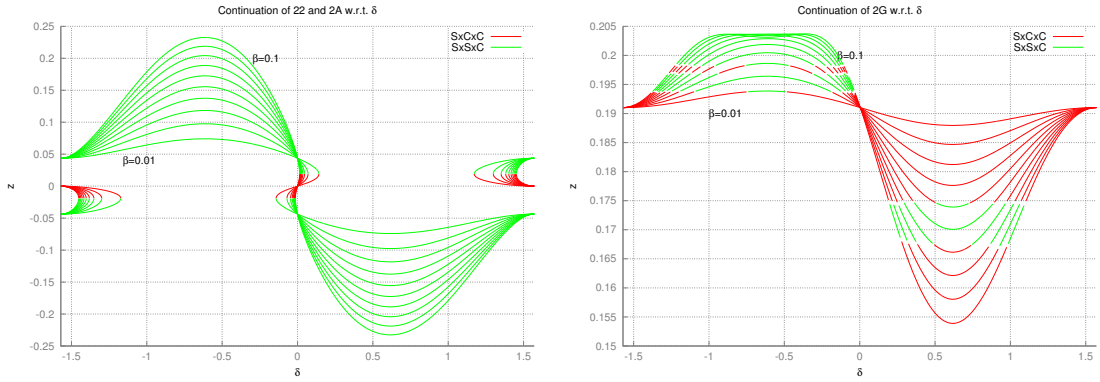

(a) (b)

Figure 6.6: **(a):** Continuation of the orbit 22, $2A^+$ and $2A^-$ with respect to δ for fixed values of β. These values of β range between 0.01 and 0.1 with constant step. **(b):** Continuation of the orbit $2G^+$ with respect to δ for fixed values of β. These values of β range between 0.01 and 0.1 with constant step. The situation for $2G^-$ is analogous.

mechanism for which a curve of fixed points undergoes a period doubling bifurcation and two families of 2-periodic points branch out and, after, the two branched families join together with the main one. All the changes of the stability type in Figure 6.6 (b) are produced by this kind of process. Notice that, for $\beta = 0.01$, the characteristic curve only undergoes to a single period doubling-halving process near to the homotopy level $\{\delta = \delta_{max}\}$.

As β increases, a second process can appear, in Figure 6.6 (b) it can be observed already for the curve corresponding to $\beta = 0.03$. For sufficiently small values of β we see the repeated pattern for which the z-value reaches its maximum at $\{\delta = -\delta_{max}\}$. However as β gets larger, the characteristic curve gets flat near $\{\delta = -\delta_{max}\}$. the curve corresponding to $\beta = 0.1$ even displays a local minimum. Notice that, while the z value of the fixed point is actually increasing, the maximal z value of the trajectory is not. This is because the lower part of these orbits is close to Moon and this is an obstacle for the orbits to be moved up. After reaching the plateau around the homotopy level $\{\delta = -\delta_{\max}\}$ the characteristic curve decreases its z value until it reaches $\{\delta = \delta_{\max}\}$ (passing through a period doubling-halving process). Then, it returns back to the original orbit for $\delta = \frac{\pi}{2}$.

We show, in Figure 6.7 (a), the trajectories corresponding to the characteristic curve for $\beta = 0.1$. The solid blue curve corresponds to $\delta = \pm\frac{\pi}{2}$ and it is the trajectory of $2G^+$ in the QBCP. The green trajectory is the one with $\delta = -\delta_{max}$ while the purple curve is the one with $\delta = \delta_{max}$. We observe how the size and the shape of $2G^+$ changes with respect to δ. Notice the difference in size between the green and purple trajectories. The value of β is the

same one for both.

We do not show any continuation with respect to the Halo orbits $2E^{\pm}$ because it is even more misleading than the ones in Figure 6.6 (b). Instead of that, we take a look at the trajectories directly. In Figure 6.7 (b) we show the trajectories corresponding to the continuation with respect to δ for the fixed value $\beta = 0.04$. The orange trajectory represents $2E^{+}$, the green trajectory is the one with $\delta = -\delta_{max}$ and the purple curve is the one with $\delta = \delta_{max}$. For all the values of β explored, the continuation takes $2E^{+}$ to itself. The orbits in this homotopy are large and pass close to the Moon (depicted in Figure 6.7 (b) as a black point). We do not observe changes in the stability type, it is totally elliptic for all the values of β and δ explored in this work.

6.6 On the stabilizing effect of SRP near the L_1 and L_2

We have been analyzing the different kind of resonant orbits and how they evolve with respect to the parameters of the sail. This study gives insight on potential usage of some of the orbits appearing in it, in view of hypothetical mission design. As almost all these orbits are unstable, the feasibility of such missions relies on station keeping.

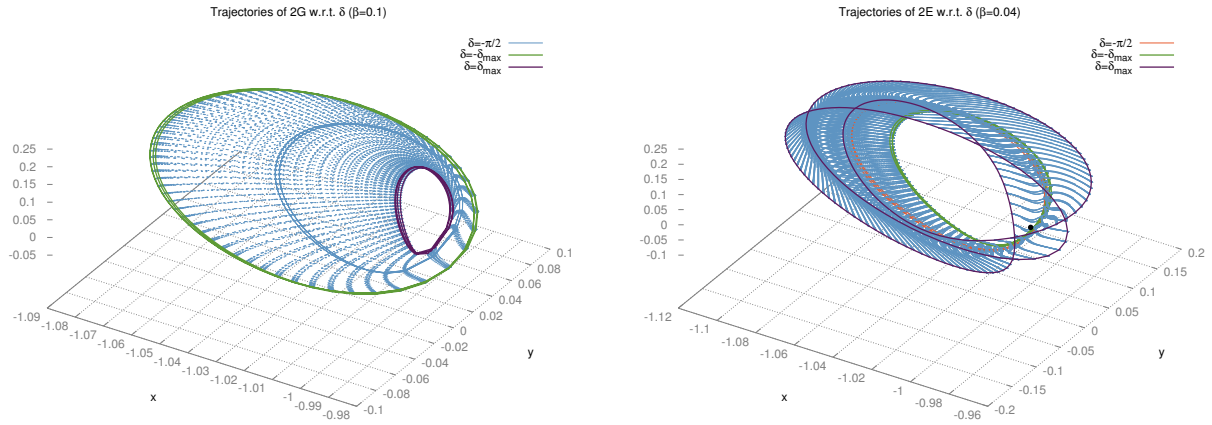

(a) (b)

Figure 6.7: **(a):** Trajectories corresponding to the characteristic curve with $\beta = 0.1$ of Figure 6.6 (b). The purple curve corresponds to $\delta = \delta_{max}$ and the green one to $\delta = -\delta_{max}$. See text for more details. **(b):** Trajectories corresponding to the continuation of $2E^{+}$ with respect to δ for $\beta = 0.1$. The purple curve corresponds to $\delta = \delta_{max}$ and the green one to $\delta = -\delta_{max}$. See text for more details.

A reasonable station keeping strategy requires the time span between maneuvers to be as large as possible. High hyperbolicity represents a thread to station keeping. The maximal eigenvalue of the Monodromy matrix (also called maximal Floquet exponent) related to each orbit gives an estimation on how small errors in the initial conditions of the orbits are propagated in a period of Sun. The larger the maximal Floquet exponent is, the more number of maneuvers in one period of Sun (around 29 days) are required to control the probe.

The natural motion around the Earth-Moon L_1 and L_2 points is highly unstable. In Table 6.3 we show the eigenvalues of the periodic orbits replacing L_1 and L_2 (of order 10^8 and 10^6 respectively) in the QBCP. Obviously, it would be mandatory to perform a large number of maneuvers to overcome such instability. Similar values hold for the maximal Floquet exponents of the planar resonant Lyapunov orbits 12 and 22. However, the resonant Halo orbits have much smaller maximal Floquet exponents. These out-of-plane orbits seem, in principle, more appealing as natural trajectories in which missions could be based on.

L_1	(real)	(imag)
1	460182151.57	0
2	−0.987151	0.159784
3	−0.963639	0.267205
L_2	(real)	(imag)
1	2397196.84	0
2	0.995818	0.0913562
3	0.917527	0.3976716

Table 6.3: Eigenvalues of the dynamical equivalents of L_1 and L_2. We only put three for each orbit. The rest are given by their inverses due to the symplectic character of the stroboscopic map.

The parameters of the sail establish connections between some of these orbits and, naturally, also does it with the corresponding Floquet exponents. In Figure 6.8 (a), we display the $\log_{10}$ of the maximal Floquet exponent related to the fixed points of the characteristic curve in Figure 6.1 (b) (the one with $\delta = 0$). The curve cuts the axis $\{\beta = 0\}$ in two points corresponding to the maximal Floquet exponent of $1C^+$ (the crossing between 1 and 1.5) and the maximal Floquet exponent of $1N^+$ (the crossing point between 2 and 2.5). The curve connects these two values and it reaches the horizontal axis where the maximal Floquet exponent is one. This range of parameters for which the $\log_{10}$ of the maximal Floquet exponent is zero represents, first the transition to complex saddle (totally elliptic points) and also the complex saddle points.

Notice that the points with complex saddle linear type are also unstable but they are

complex and the modulus is close to 1. We stress the dramatic decay of the maximal Floquet exponent appears for rather large values of β (larger than 0.1), maybe too large for the current technological capabilities. Anyhow, in our opinion, the values are not too large and should be taken into account for future missions: A solar sail permits us to find out-of-plane orbits with small instability. Let us stress that, in Figure 6.8 (a) the sail is perpendicular to Sun. To illustrate the effect the orientation of the sail has on the maximal Floquet exponents of orbits near L_2, we take the continuation curve of Figure 6.6 (a) corresponding to $\beta = 0.1$. This characteristic curve connects $2A^+$ and $2A^-$. Figure 6.8 (b) shows how the $\log_{10}$ of the maximal Floquet exponent changes with respect to δ.

The crossing of the curve with $\{\delta = -\frac{\pi}{2}\}$ is the maximal Floquet exponent of $2A^+$ while the crossing with $\{\delta = \frac{\pi}{2}\}$ corresponds to the maximal Floquet exponent of $2A^-$. By symmetry, the values of these two eigenvalues is the same. What Figure 6.8 (b) reveals is that being away from the plane gives better stabilization of the orbit with a sail. For orientation close to $-\delta_{max}$ and δ_{max} the $\log_{10}$ of the maximal Floquet exponent falls below 4 which means to lose two digits of accuracy less at each period of Sun. On the other hand, the orbits close to the plane are more unstable and the solar sail cannot prevent that. Indeed, at the centre of Figure 6.8 (b), for δ close to zero, we see how the $\log_{10}$ of the maximal Floquet exponent grows again to values as large as the ones associated to the original orbit and even bigger. Again, the value of β is taken a bit large for the current technology, but it is still suitable to illustrate the stabilizing effect of SRP near L_2.

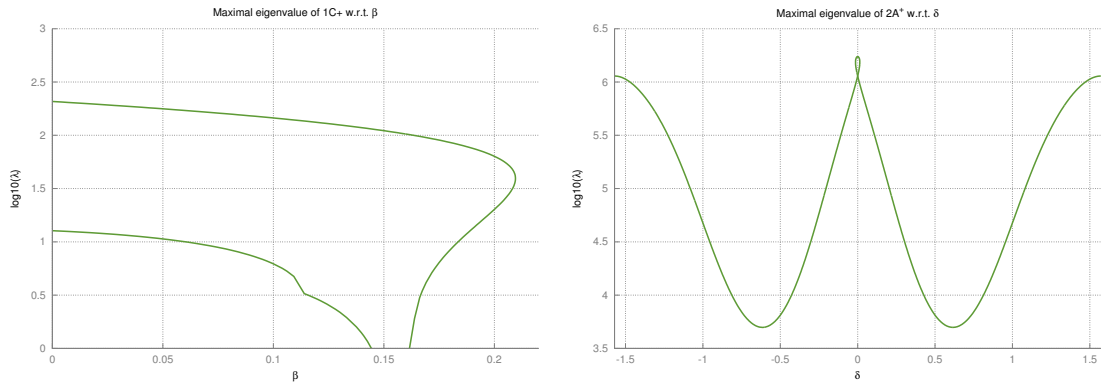

(a) (b)

Figure 6.8: **(a):** $\log_{10}$ of the maximal eigenvalue of the characteristic curve with $\delta = 0$ appearing in Figure 6.1 (b). **(b):** $\log_{10}$ of the maximal eigenvalue of the characteristic curve connecting $2A^+$ and $2A^-$ (with $\beta = 0.1$) appearing in Figure 6.6 (a).

6.7 Motion near L_3, L_4 and L_5

In this section we will be concerned with the motion of a solar sail near the triangular points and L_3. To fulfill this goal, we change the model to the ABCP. Indeed, as we have explained in Chapter 5, the BCP is suited (as suited as the QBCP) for the triangular points and more simple to work with. The reason why we study L_3 together with the triangular points will be clear by the exposition of the results. Indeed, there is a strong relation between L_3, L_4 and L_5. We shall be concerned on how these fixed points depend on the angle α. Therefore, during the present section, all the invariant objects to be studied are contained in the plane of motion of the primaries, $z = 0$, and we can dispense with the vertical motion and the system can be considered a two degrees and a half Hamiltonian system.

6.7.1 Continuation with respect to β

Let us focus first on the continuation of the periodic orbits with respect to the effectivity of the sail when the sail is fixed to be perpendicular to Sun's direction ($\alpha = 0$). Recall that the triangular points, in the BCP, are replaced by three periodic orbits with the same period as Sun. One of them unstable and the other two stable. As usual, we will work with the stroboscopic map, so, these orbits are seen as fixed points of the map. Again, we will use the name periodic orbit or fixed points indistinctly. Let us denote by $x_{4,1}$, $x_{4,2}$ and $x_{4,3}$ the coordinates of the three fixed points replacing the equilibrium point L_4 and by x_3 the coordinates of the fixed point replacing L_3. In a similar manner, $x_{5,1}$, $x_{5,2}$ and $x_{5,3}$ are named after L_5. In Figure 6.9 we display the continuation of the fixed points near L_3, L_4 and L_5 when the sail is perpendicular to Sun ($\alpha = 0$).

Let us consider the continuation of $x_{4,3}$ from $\beta = 0$ to positive values of the parameter. The curve of fixed points starts with elliptic linear behavior, for the value $\beta_1 \approx 6.3003 \times 10^{-5}$, a turning point takes place and the continuation curve goes back, with centre×saddle character, to $x_{4,1}$. Then, the homotopy level $\{\beta = 0\}$ is crossed and we find physically meaningless fixed points for which the value of β is negative. For $\beta \approx -5.4 \times 10^{-5}$, there is another turning point, the curve switches its linear behaviour to centre×centre again and goes all the way back to $\{\beta = 0\}$, it crosses this homotopy level at $x_{4,2}$. After that, the curve tracks fixed points with positive (and larger) values of the parameter. The situation described here and pictured in Figure 6.9, panel (b), may seem trivial in the sense that these events occur for extremely small values of the parameter but, anyhow, there are a few consequences worthy to point out.

- For $\beta = 0$, the model reduces to the BCP. There, we have three periodic orbits that replace the equilibrium point L_4. These orbits are connected by continuation with respect to β.

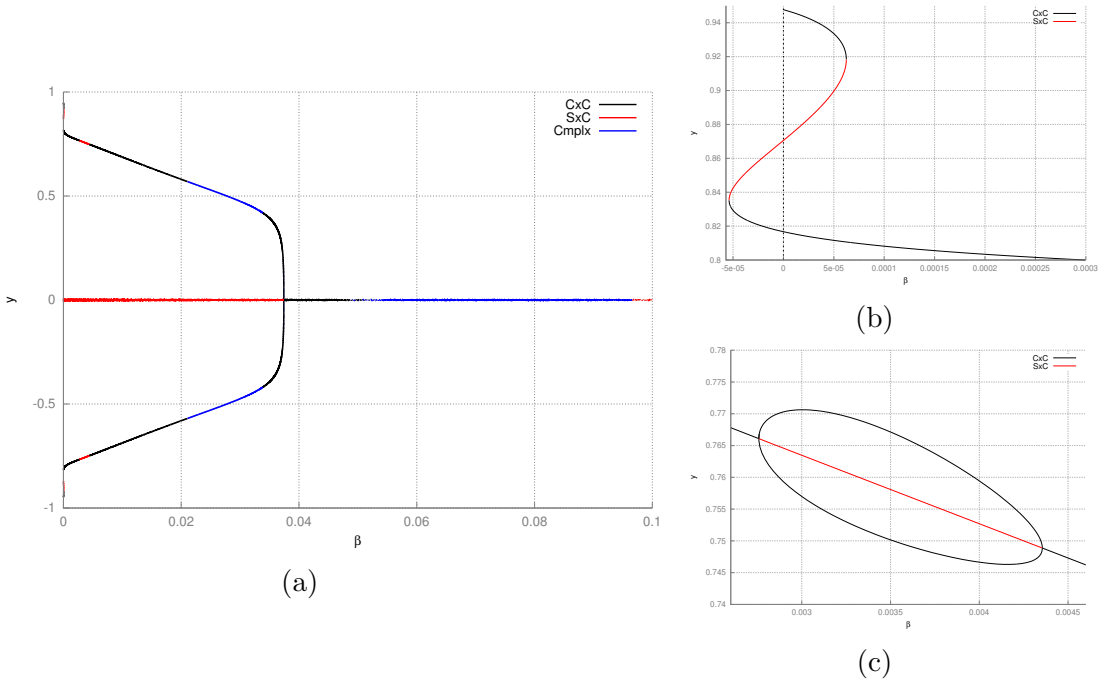

Figure 6.9: **(a):** Dynamical equivalents of L_3 , L_4 and L_4 for $\alpha = 0$. **(b):** Two consecutive saddle-centre bifurcations connecting $x_{4,1}$, $x_{4,2}$ and $x_{4,3}$ (magnification). **(c):** Period doubling-halving process (magnification). Horizontal axis: β. Vertical axis: y.

- For $\beta > \beta_1$ there is a single periodic orbit that replaces L_4. Hence, in any situation in which SRP plays a significant role, there is, one periodic orbit that replaces L_4.
- The values of β for which these saddle-centre bifurcation occur play an important role to determine whether the periodic orbits $x_{4,1}$, $x_{4,2}$ and $x_{4,3}$ are connected by continuation with respect to α or not.

The continuation curve keeps tracking fixed points for positive (and larger) values of β. For $\beta_2 \approx 0.0027$ the curve undergoes a period doubling bifurcation, that is, the main branch of the curve changes its linear behaviour from totally elliptic to centre×saddle and two new families of totally elliptic 2-periodic points branch from the bifurcation. There is a range of values of β for which the three families coexist until the value $\beta_3 \approx 0.004353$, where a period halving bifurcation occurs. The two period-doubled families merge with the main branch and the later changes its linear behaviour to centre×centre again. This period doubling-halving process is depicted in Figure 6.9, panel (c).

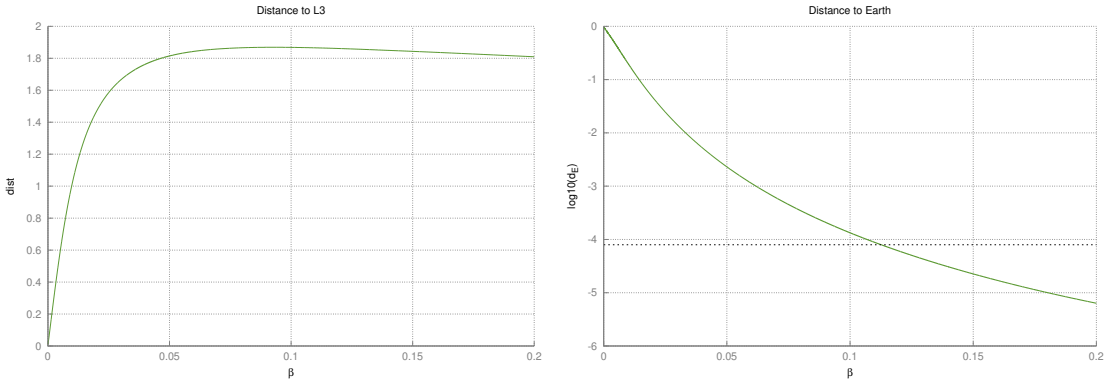

(a) (b)

Figure 6.10: **(a):** Horizontal axis: β, vertical axis: distance from the trajectory of the flow with initial condition $x_3(\beta)$ to the point L_3 **(b):** Horizontal axis: β, vertical axis: logarithm (to base 10) of the distance from the flow at $x_3(\beta)$ to Earth.

The curve of fixed points remains totally elliptic until $\beta_4 \approx 0.021067$ where it undergoes a Hamiltonian-Hopf bifurcation and its linear behaviour changes to complex instability. This bifurcation is produced when a pair of (non conjugated) eigenvalues collide at some point of the unit circle which is neither 1 nor -1 (Krein collision). The collision gives raise to 2-dimensional stable and unstable invariant manifold. Analogously to the period halving bifurcation, when $\beta_5 \approx 0.0338192$ the main branch of fixed points recovers the totally elliptic character due to another Krein collision. There is still another bifurcation to occur. Before describing it, let us remark some important points. As we have said, the system has a symmetry with respect to the $\{y = 0\}$ hyperplane. Consider now the continuation of x_3 with respect to β. Due to the symmetry, the y and p_x components of this family are always zero. For the value $\beta_6 \approx 0.037419$, the families of fixed points that raise from $x_{4,3}$, x_3 and $x_{5,3}$ merge in a single point. This (pitchfork) bifurcation is displayed Figure 6.9, panel (a). After the bifurcation (i.e. for $\beta > \beta_6$) only one fixed point, x_3, persists and its linear character switches to totally elliptic linear behaviour. For a range of values of β, x_3 is a linearly stable fixed point. For $\beta_7 \approx 0.05541$ there is a Hamiltonian-Hopf bifurcation and x_3 turns to complex instability. For $\beta_8 \approx 0.09052$ the eigenvalues merge again at the unit circle and the fixed point recovers totally elliptic character. It remains totally elliptic for a small range of values of β. For $\beta_9 \approx 0.09657$, one of the couples of eigenvalues gets out the unit circle through -1 (period doubling bifurcation) and the continuation curve goes to hyperbolic.

To describre the situation for $\beta > \beta_9$, we take a look at the fixed points as trajectories of the flow. These trajectories always wind around L_3, at least, once. The orbits of the

family keep increasing in size for growing values of β. To measure this growth we compute the distance of the projection to the xy-plane of the graph corresponding each trajectory to the L_3 point. That is, let $\varphi^3_\beta(t)$ be a trajectory that is obtained by continuation with respect to β from x_3 and define $\varphi^{3,xy}_\beta(t) = \pi_{xy} \circ \varphi^3_\beta(t)$. We compute $\|\varphi^{3,xy}_\beta - x_{L_3}\|_\infty$, where x_{L_3} are the coordinates of the equilibrium point L_3. One may observe that this distance tends to a constant (Figure 6.10, (a)). This is because the trajectories are getting close to Earth. It seems that this family of curves can be continued for all values of β and the trajectories will tend asymptotically to the singularity at Earth. However, at some point, our method has to stop because of the instability near the singularity. Physically, none of the trajectories which are closer to the singularity than the radius of Earth make sense. In Figure 6.10 (b) we display (logarithm of) the minimum distance between the trajectories and Earth (green curve). The dashed line represents the Earth's radius. We observe that, for $\beta_{10} \approx 0.110699$, the family of trajectories collides with the surface Earth and, therefore, the continuation can be stopped.

i		β_i	Type
β_1	$\approx$	6.300e-5	SC
β_2	$\approx$	2.753e-3	PD
β_3	$\approx$	4.353e-3	PH
β_4	$\approx$	2.106e-2	HH
β_5	$\approx$	3.381e-2	HH
β_6	$\approx$	3.741e-2	PF
β_7	$\approx$	5.541e-2	HH
β_8	$\approx$	9.052e-2	HH
β_9	$\approx$	9.657e-2	PD
β_{10}	$\approx$	1.106e-1	CE

Table 6.4: Values of β for which several types of bifurcations related to the continuation curve in Figure 6.9. Type code: SC stands for Saddle-Centre, PC for Period-Doubling, PH for Period-Halving, HH for Hamiltonian-Hopf, PF for Pitchfork. CE stands for Collision with Earth.

In Table 6.4 a summary of the bifurcations of the continuation curve show in Figure 6.9 is presented. The first column contain the names given to the values. The second column contains approximate values. The third column is a code for the type of bifurcation (see caption of the table). These labels are used in the next section to facilitate the discussion.

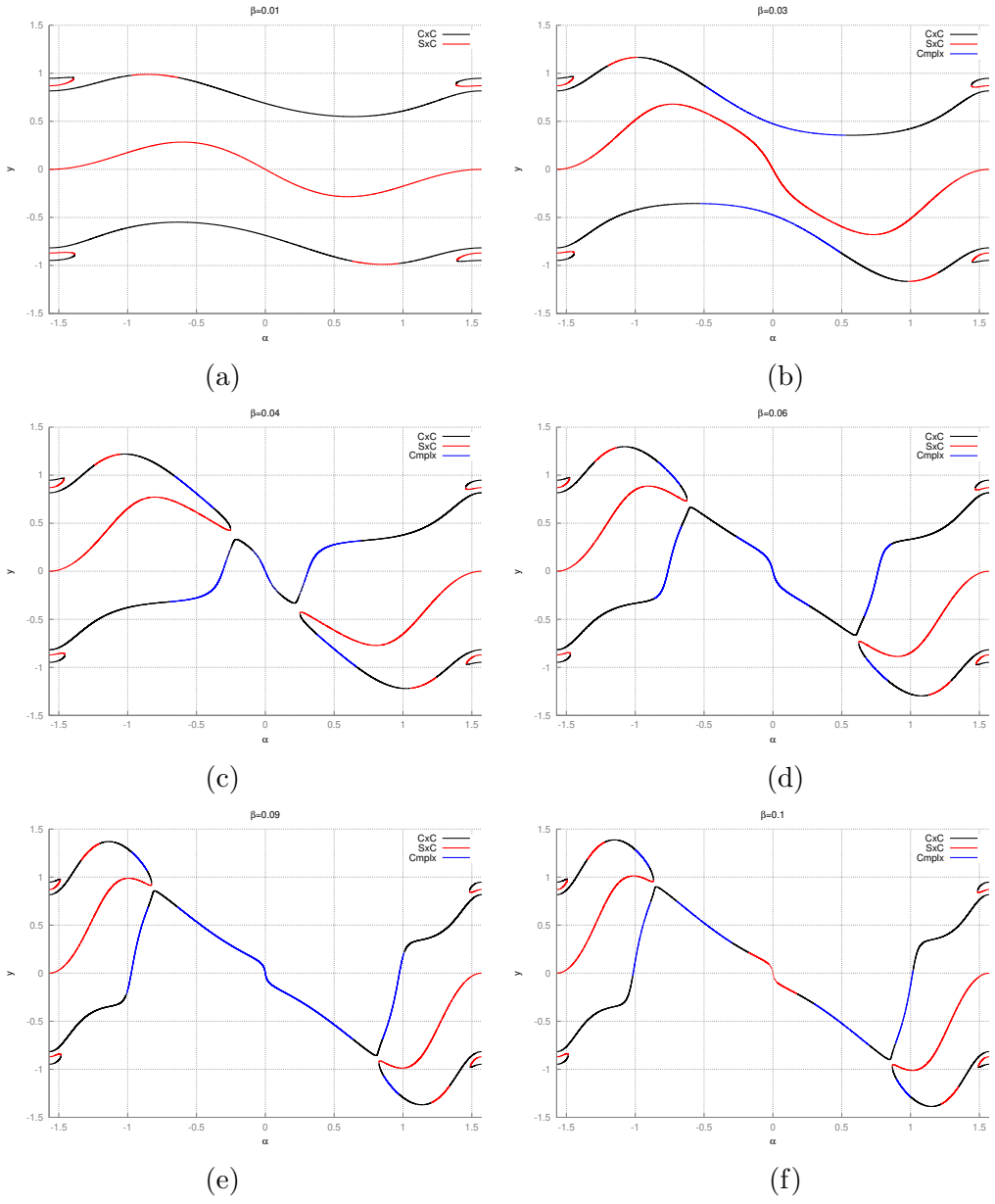

Figure 6.11: Dynamical equivalents of L_3, L_4 and L_3 (w.r.t. α) for a fixed value of β. **(a):** $\beta = 0.01$. **(b):** $\beta = 0.03$. **(c):** $\beta = 0.04$. **(d):** $\beta = 0.06$. **(e):** $\beta = 0.09$. **(f):** $\beta = 0.1$. Horizontal axis: α. Vertical axis: y.

6.7.2 Continuations with respect to α:

In Figure 6.11 we display continuations of the fixed points near L_3, L_4 and L_5 for some fixed values of β. We place α in the horizontal axis and y in the vertical one. The continuation curves of $x_{4,1}$, $x_{4,2}$, $x_{4,3}$, x_3, $x_{5,1}$, $x_{5,2}$ and $x_{5,3}$ are shown.

Fix $\beta > 0$ but smaller than β_1 and consider the continuation curves from each of the three periodic orbits near L_4 of the BCP. As α increases the fixed point moves a little bit from the original coordinates at the BCP. It reaches a maximum distance at $\alpha = 0$, and after, it goes back to the original coordinates. No change of linear stability happens. This description holds for the continuation of the three fixed points $x_{4,1}$, $x_{4,2}$ and $x_{4,3}$. The only difference is its linear stability: $x_{4,1}$ is hyperbolic while $x_{4,2}$ and $x_{4,3}$ are elliptic.

The three continuation curves merge into a single one for $\beta = \beta_1$. The result of this merging is that the three fixed points $x_{4,1}$, $x_{4,2}$ and $x_{4,3}$ are be connected by continuation with respect to α if $\beta > \beta_1$. The way they are connected is qualitatively the same in every case. If we start to track the curve of fixed points at $x_{4,3}$, we find some elliptic fixed points for $\alpha < -\pi/2$, then, at some value of α that depend on β, a saddle-centre bifurcation takes place and the curve goes back to the homotopy level $\{\alpha = -\pi/2\}$ where it meets the hyperbolic fixed point $x_{4,1}$. The curve keeps tracking hyperbolic fixed points for some (physically meaningless) values of $\alpha < -\pi/2$. After, another turning point (saddle-centre bifurcation) the curve gains linear stability again and goes back to the homotopy level $\{\alpha = -\pi/2\}$ where it meets $x_{4,2}$. From that moment, the curve tracks fixed points corresponding to $\alpha > -\pi/2$. Notice that, at each case, there is exactly one fixed point (near L_4) when α is larger than the value of the first saddle-centre point (which, we stress again, depend on the value of β we fix before the continuation). Then, for $\beta < \beta_1$, the curve reaches the homotopy level $\{\alpha = 0\}$ and, therefore, must go back to the original fixed points of the BCP again. We do not show any picture of the situation for $\beta < \beta_1$ as the values of β are very small. The fixed points $x_{4,1}$, $x_{4,2}$ and $x_{4,3}$ are connected in each panel of Figure 6.11. Notice that, due to the symmetries of the system, the same description holds for the dynamical equivalents of L_5.

For $\beta > \beta_2$ the continuation curve corresponding to L_4 and L_5 undergo a period doubling followed by a periodic halving as described in Section 6.7.1. The period doubling-halving process can be observed already in Figure 6.11, (a). Stress that this phenomenon happens for each $\beta > \beta_2$, in particular it can be observed at each panel of Figure 6.11.

For $\beta > \beta_4$ the curves corresponding to L_4 and L_5 undergo Hamiltonian-Hopf bifurcations. Again, the totally elliptic behaviour is recovered as discussed in Section 6.7.1. The first panel in Figure 6.11 in which fixed points of complex saddle type appear is panel (b). This double Hamiltonian-Hopf bifurcation is observed in each panel from (b) to (f).

For $\beta = \beta_6$ a degenerate pitchfork bifurcation takes place and the curves corresponding to

L_3, L_4 and L_5 merge in a point. Notice that, due to the symmetry verified by the surface of fixed points, $(\alpha, y) \mapsto (-\alpha, -y)$, the point in the surface corresponding to $\beta = \beta_6$ and $\alpha = 0$ is a saddle point of order two. Stress that, in this case, by saddle point we mean a geometric saddle, we are not refering to the linear character. For $\beta > \beta_6$ the dynamical equivalents of L_4 are connected with x_3 by continuation forwards and with the dynamical equivalents of L_5 by continuation backwards. This situation can be observed in Figure 6.11 from panel (c) to panel (f).

Let us hightlight the change on the qualitative behaviour observed between panels (b) and (c). Panel (b) corresponds to $\beta = 0.02 < \beta_6$. There, we observe three continuation curves that connect the dynamical equivalents of L_3, L_4 and L_5 with themselves. Indeed, the top curve of panel (b) corresponds to the continuation of $x_{4,1}$, $x_{4,2}$ and $x_{4,3}$. We have alredy argued that these points are connected to each other. Once it has connected the three dynamical equivalents of L_4, the curve starts to increase its y value until a maximum is reached. Then, the y value decreases, the curve crosses the homotopy level $\{\alpha = 0\}$ and keeps increasing until a minimum. Then, the curve increases its y value and crosses $\{\alpha = \pi/2\}$ at $x_{4,1}$, $x_{4,2}$ and $x_{4,3}$. The description for the dynamical equivalents of L_5 is the same one, taking into account the symmetries. The curve corresponding to x_3 also has a similar behaviour. In panel (c) the description is completely different. In this case, the continuation curve corresponding to L_4 and starting at $\{\alpha = -\pi/2\}$ does never reach the homotopy level $\{\alpha = 0\}$. Instead of that, it encounters a saddle-centre bifurcation, changes its linear character to hyperbolic and connects with x_3. The connection between the dynamical equivalents of L_4 and L_3 is the "tongue" on the left on panels (c)-(f). In a similar manner, L_3 and L_5 are connected through a saddle-centre bifurcation, that is the tongue on the right. The curve curve in the middle, crossing from the homotopy levels $\{\alpha = -\pi/2\}$ and $\{\alpha = \pi/2\}$ connects L_4 and L_5.

Notice that the curve connecting L_4 and L_5 in panel (f) is of type centre×saddle. This is because a period doubling bifurcation that takes place when $\beta > \beta_9$.

Topological description: For values of β which are smaller than β_5 there are three distinct curves of fixed points. The three curves merge for $\beta = \beta_4$ at $\{y = 0\}$ and this merging change the topology of the curves. Let us explain how. If we name $\mathbb{T}_\alpha = [-\pi/2, \pi/2]/\sim$, we can consider the curves of fixed points shown in Figure 6.11 lying in the cylinder $\mathbb{T}_\alpha \times \mathbb{R}^4$. Before the collision the three curves are homotopically non-trivial. Once the value β_4 is reached, the three curves merge into a single homotopically trivial curve of Fixed points.

Generally, before the collision we can observe three different curves of fixed points that start and end up at the same orbits of the BCP. The curves resulting from the collision give new connections between Lagrangian points. The curves that pass through L_3 have a

saddle-centre bifurcation which is γ^2-close[4] to the curve between them. This leads to two "tongues" that get smaller as β increase. The responsible for this separation of order γ^2 is, again, the inclusion of Sun's gravitational potential.

On the geometry of the phase space

In this section we take an effort to understand better the phase space around some Key periodic orbits selected from the continuations displayed in Figure 6.11. Observe first Figure 6.12. There we display pieces of the curves corresponding to $\beta = 0.03$ (a) and corresponding to $\beta = 0.04$ (b). These are selected to be paradigmatic examples of the situation before and after the (broken) pitchfork bifurcation. Notice that all these orbits correspond to $\alpha = -0.75$. The trajectories (in the flow) corresponding to orientations which are closer to perpendicular pass close to Earth and the dynamics around them is not very interesting.

We have named these periodic orbits as: $B1$, a totally elliptic orbit in Figure 6.12 (a), $B2$ an orbit of type centre×saddle in Figure 6.12 (a), $C1$ a totally elliptic orbit in Figure 6.12 (b), $C2$ an orbit of type centre×saddle in Figure 6.12 (b) and $C3$ a totally elliptic orbit in Figure 6.12 (b).

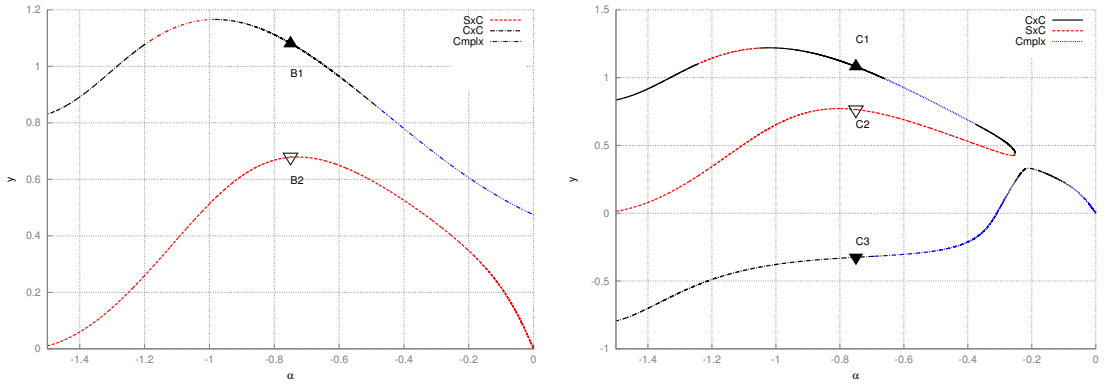

(a) (b)

Figure 6.12: **(a):** Magnification of panel (b) in Figure 6.11 ($\beta = 0.03$). **(b):** Magnification of panel (c) in Figure 6.11 ($\beta = 0.04$). In both plots: Horizontal axis: α. Vertical axis: y.

To study the geometry of the phase space near these fixed points we compute the families of invariant curves emerging from each elliptic direction. In all the cases, we fix that each invariant curve evaluated at $\theta = 0$ has the coordinate x of the fixed point. This is as the

[4]Recall that $\gamma = \frac{m_S}{a_S^3}$.

required extra condition for the computation of the invariant curves. See Chapter 3 for the suitable context for all these specifications.

Let us start by describing the phase-space near $B1$. As this fixed point is totally elliptic, there are two families of invariant curves, named $FB1A$ (Figure 6.13 (a)) and $FB1B$ (Figure 6.13 (b)), rising along each elliptic direction. These families have been computed up to order of truncation $N = 100$. This means that the last tori appearing in Figure 6.13 (a) and (b) need to be approximated by trigonometric polynomials of degree 100. This is also true for the rest of the families presented in this section. We do not claim that we have computed the whole of the families but the increasing truncation number mandatory to describe them provide numerical insight that the families are ending. Notice that both families have a diameter about a one tenth of unit. The family $FB1B$ displayed in Figure 6.13 (b) seems to get spiky by the last invariant curves. The shape of these curve suggest the existence of resonances nearby, therefore, this could be an explanation for the high number of harmonics needed to describe the last invariant curves. Anyhow, we have not explored further. The product of these two families give rise to the centre manifold of the fixed point $B1$.

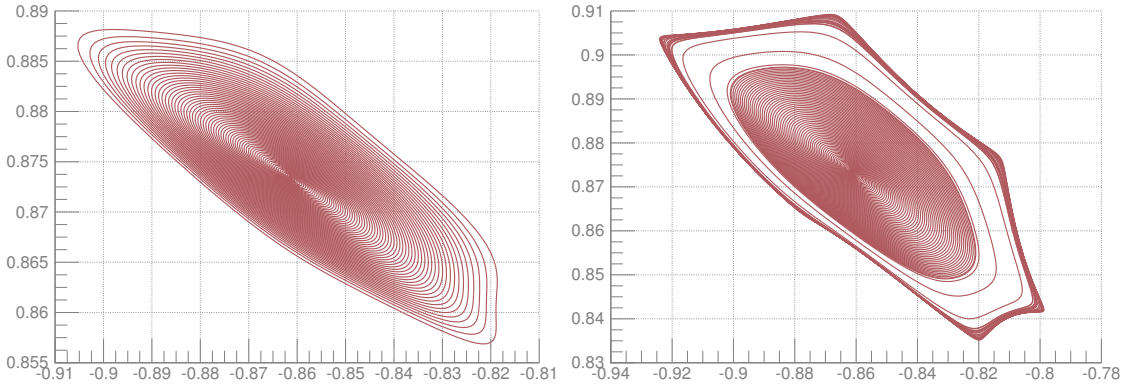

(a) (b)

Figure 6.13: **(a):** Family $FB1A$ of invariant curve surrounding the orbit $B1$. **(b):** Family $FB1B$ of invariant curve surrounding the orbit $B1$. Horizontal axis: x. Vertical axis: y.

In Figure 6.14 (a) we display the centre manifold related to the fixed point $B2$. Again, the last invariant curve in the plot needs truncation order $N = 100$ to be described. Besides from that, the shape of the invariant curves in this family is quite simple, close to circular. In Figure 6.14 (b) we display some points of the unstable manifold related to the unstable eigendirections of $B2$. The point in the plot represents the coordinates of $B2$ in the (x, y) plane. The manifold has been approximated up to order 16 and numerically grown. Not more than 4 iterates of points in the fundamental domain have been used. We can observe

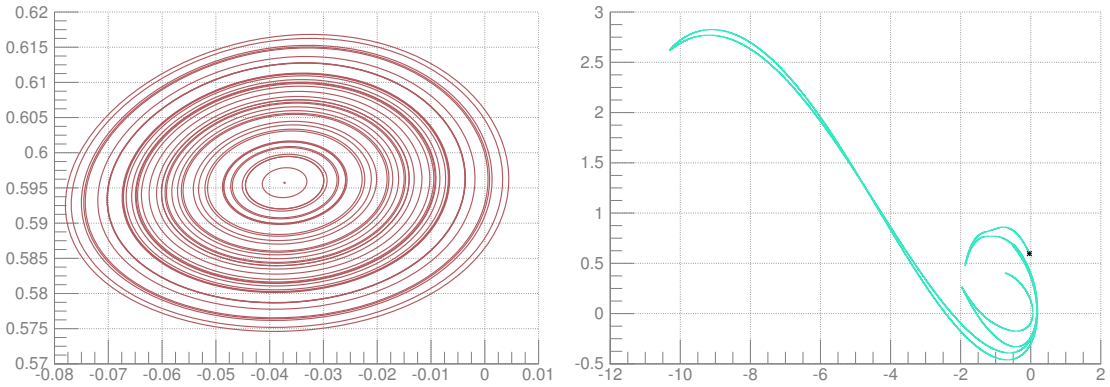

(a) (b)

Figure 6.14: **(a):** Centre manifold (family $FB2A$) related to the fixed point $B2$. **(b):** Unstable manifold $B2U$ related to the fixed point $B2$. Horizontal axis: x. Vertical axis: y.

in Figure 6.14 (b) how the manifold passes close to the L_4 triangular point, then it crosses the axis $\{y = 0\}$ initiating a long excursion that takes it further away from Earth and Moon. After this long excursion, the manifold returns back close to the coordinates of L_4.

Let us try to understand the extended phase-space of Figure 6.12 (b). The fixed points $C1$ and $C3$ are totally elliptic and their elliptic directions give rise to families of invariant curves, $FC1A$, $FC1B$, $FC3A$ and $FC3B$. The fixed point $C2$ is of type saddle×centre, therefore, its nearby motion is organized by a two-dimensional centre manifold, $FC2A$, a stable, $C2S$, manifold and an unstable $C2U$. In Figure 6.15 (a) and (b) we display the families $FC1A$ and $FC1B$ (respectively) related to the totally elliptic point $C1$. The panel (a) shows how the last invariant curve is slightly wrinkled showing why it is necessary many Fourier coefficients to describe it. Notice the difference between Figure 6.15 (a) and Figure 6.13 (a), its counterpart before the bifurcation. In Figure 6.15 (b) we cannot see any remarkable behaviour. The region of the phase-space occupied by this family is quite small and narrow.

In Figure 6.16 (a) we display the centre manifold related to the fixed point $C2$. Notice that a large region of the phase-space is occupied by this family. In panel (b) of the same Figure, we show the unstable manifold related to $C2$. Again, the manifold performs a long excursion, getting far away from Earth and Moon and crossing the horizontal axis. The computation is stopped because the angle between two consecutive points gets smaller than the epsilon machine in the standard double precision. This seem to suggest some kind of exponentially small phenomenon.

Finally, in Figure 6.17 we display the family $FC3A$ related to the fixed point $C3$. Although the point is totally elliptic and there is another family, $FCB3$, of invariant curves growing

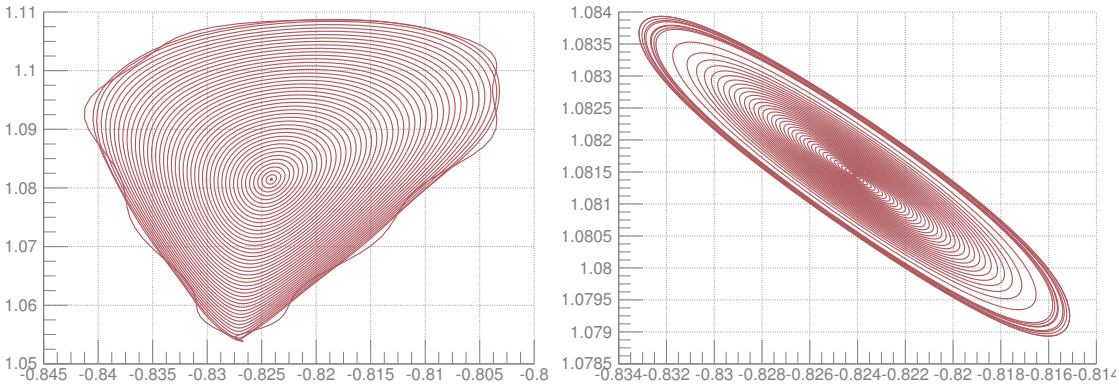

(a) (b)

Figure 6.15: **(a):** Family $FC1A$ of invariant curve surrounding the orbit $C1$. **(b):** Family $FC1B$ of invariant curve surrounding the orbit $C1$. Horizontal axis: x. Vertical axis: y.

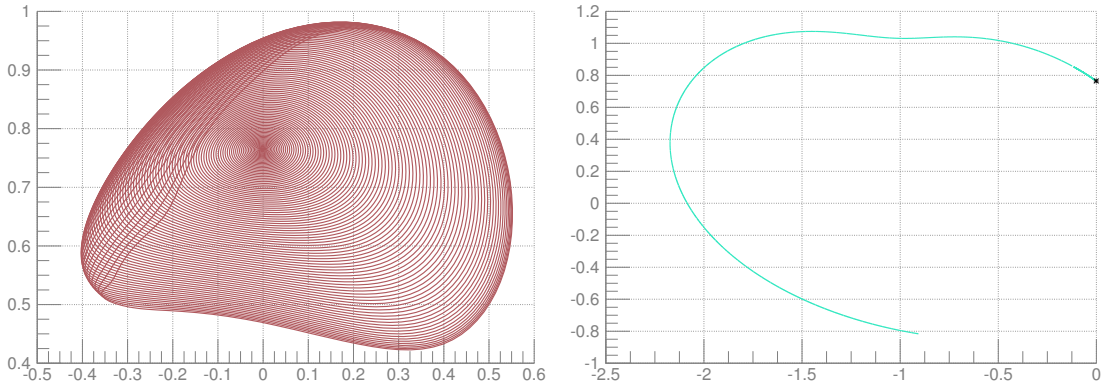

(a) (b)

Figure 6.16: **(a):** Centre manifold (family $FC2A$) related to the fixed point $C2$. **(b):** Unstable manifold $C2U$ related to the fixed point $C2$. Horizontal axis: x. Vertical axis: y.

from it, we do not display it here because it is very narrow and adds little information. With respect the family $FC3A$, we see that a relatively large region of the phase-space is occupied by it. Moreover the family is saddle-shaped.

6.8 On the effect of Sun's gravity

The goal of this section is to give some words on the consequences of adding Sun's gravity to the equations of motion. This, as it is pointed out before, is motivated by the fact that most of the works in the current literature do not include the gravitational effect of Sun. With this section we do not aim to repeat the study carried out in this chapter with a different model, but to highlight some differences that are worth to mention. To do so, we study the geometry of the surfaces of dynamical equivalents of the Lagrangian equilibria in the augmented RTBP, ARTBP for short. The illustrations in this chapter are much less detailed as our goal is just to provide evidences of substantial changes in the results. We claim that it should be taken into account in future studies (according to the goals). The topology of the surfaces of fixed points (near L_1 and L_2) is severely affected by the way Sun's gravity is introduced.

In the QBCP the motion of Sun is not circular and the model takes under consideration the non-constant distance between Earth and Moon, there are substantial disagreements in the gravitational forces acting on a small particle depending on the basis model (the BCP, the QBCP and the RTBP). Due to the properties of the QBCP, the acceleration due to SRP upon the sail used in the augmented model (AQBCP) has a small but noticeable disagreement with the solar sail acceleration considered in the augmented versions of the BCP and the RTBP.

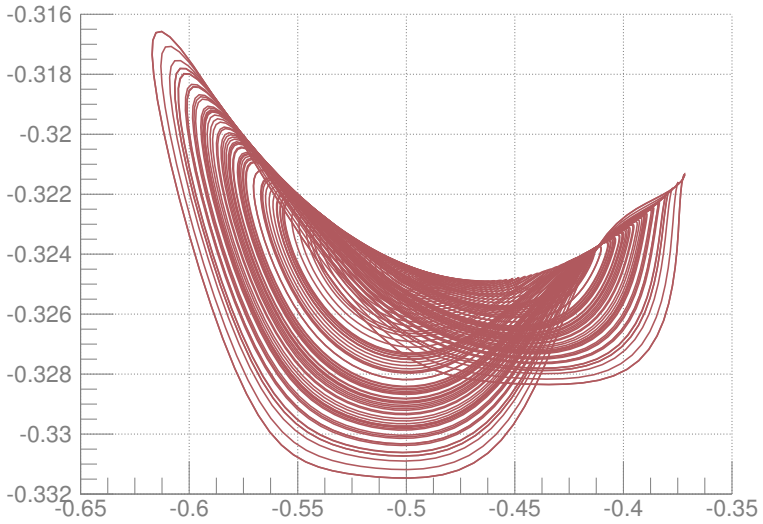

Figure 6.17: Family $FC3A$ associated to the fixed point $C3$. Horizontal axis: x. Vertical axis: y.

This is due to the periodic functions α_i's, see Remark 6.2.1. Indeed, in the BCP, SRP changes in time according to the assumption that Sun moves in a circular orbit (together with the centre of masses of the Earth-Moon system). The difference between the two models for the acceleration upon the sail is of order 10^{-3} and do not depend on the effectivity of the sail.

The ARTBP is, as the rest of the models studied in this chapter, a T_S periodic perturbation of the RTBP. The Hamiltonian system can be written as

$$H_{ARTBP} = H_{RTBP} + H_S(\alpha, \beta, \theta),$$

with $H_S(\alpha, 0, \theta) = 0$ and $H_S(\pm\frac{\pi}{2}, \beta, \theta) = 0$. As it is usual, the Lagrangian points are no longer equilibria but they are replaced by T_S-periodic orbits. Again, these periodic orbits may be seen as a fixed points of the stroboscopic map $P_{\alpha\beta}$. This model is the most widely used in the works related to the motion of solar sails in the Earth-Moon system[5].

The AQBCP, the ARTBP and the vicinity of L_1 and L_2

Let us compare first the AQBCP and the ARTBP. Notice that, as the QBCP captures some phenomena that are not included in the BCP nor the RTBP, it is to be expected the disparity of results to be more noticeable here. Let us start by giving a description of the results corresponding to the ARTBP near the Lagrangian point L_1.

Motion near L_1

As it is the case for the other models, there is a highly instability around this collinear point: The family of fixed points parametrized by the efficiency and the orientation of the sail are highly unstable as the ones in the AQBCP. In Figure 6.18 we display the continuation of L_1 as fixed point of the stroboscopic map with respect to δ for two fixed values of β (0.02 in (a) and 0.1 in (b)). The behaviour of the characteristic curve displayed in Figure 6.18 (a) is very similar to the one observed in the same simulation but performed in the AQBCP (see the set of characteristic curves displayed in Figure 6.2 (a)), The z-coordinate of the fixed point grows with δ until $\delta = -\delta_{max}$. For this orientation it is achieved the maximal value of z-coordinate. When δ grows larger than $-\delta_{max}$, the z-coordinate of the fixed point decreases rapidly with δ. The trajectory corresponding to $\delta = 0$ is confined in the plane of motion of the primaries. For $\delta > 0$, the fixed points are a mirror image through $z = 0$ of the ones for $\delta < 0$. The z-coordinate decreases (symmetrically) with respect to δ until a minimum value corresponding to δ_{max}. After this minimum, the characteristic curve goes back to L_1. The same description can be applied to the Lyapunov orbit 012 when it is continued with respect to δ for low values of β.

[5]See Section 6.1.2.

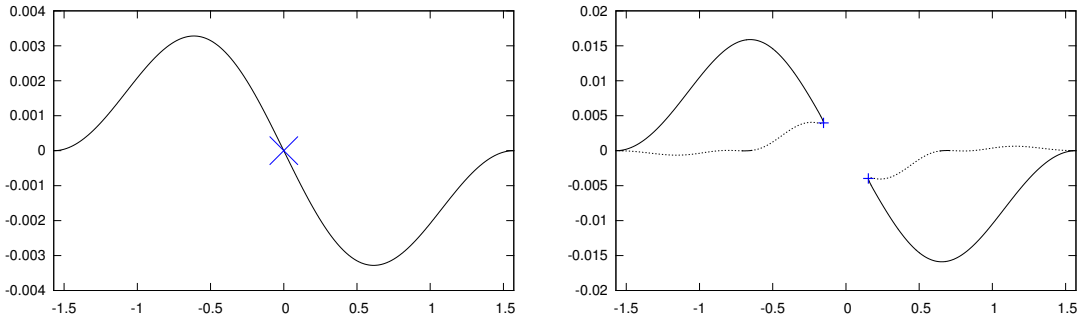

(a) (b)

Figure 6.18: Continuation of L_1 with respect to δ for a fixed value of β. **(a):** $\beta = 0.02$. **b**: $\beta = 0.1$. Horizontal axis: δ. Vertical axis: z.

This behaviour also been reported for L_1 and the Lyapunov orbit 12 in the AQBCP for all the values of β analyzed (Figure 6.2 (a) and Figure 6.2 (b) respectively).

Let us fix the value $\beta_{L_1} \approx 0.091889$. In Figure 6.18 (b) we display a typical plot for $\beta > \beta_{L_1}$ (in this case $\beta = 0.1$). We start a continuation from L_1 and $\delta = -\pi/2$. The z-coordinate grows to some maximum high at $-\delta_{max}$. For $\delta > \delta_{max}$ the z coordinate decreases rapidly in δ but, this time, the characteristic curve does not cross the homotopy level $\{\delta = 0\}$. There is a turning point and the stability changes to centre×saddle×saddle. After the turning point, characteristic curve goes back to the RTBP where it meets a the 012 resonant planar Lyapunov orbit. Notice that, in Figure 6.18 (b), it seems that the characteristic curve goes back to the same point it started. This is because we display the z-coordinate and the found orbit is planar. However, it can be observed that the linear normal behavior has changed, indeed, the solid line in Figure 6.18 (b) stands for centre×centre×saddle points and the dashed curve for centre×saddle×saddle points.

Notice the stark difference with the situation reported for the AQBCP. The saddle-centre bifurcation connecting the periodic L_1 and 12 has not been observed for the values of β considered in this work. The conclusion is that, the surface of fixed points (equivalents to L_1 and 12) parametrized by δ and β changes substantially depending on the chosen model. Similar results can be reported for other orbits (such as the Halo resonant orbits). Notice that this has a deep impact on the dynamics near the L_1 collinear point, as the invariant structures (invariant tori, unstable and stable manifolds) are organized from the fixed points.

Motion near L_2

Let us give some words on the continuation of L_2 as a T_S periodic orbit. We set, first, $\delta = 0$, that is, the sail is perpendicular to Sun. Therefore the acceleration due SRP has no out-of-plane component and the orbits are confined in the plane of motion of the primaries. As it is usual, we consider a mapping at period T_S and see the periodic orbits as fixed points of this map.

If we start at the coordinates of L_2, we trace some fixed points corresponding to increasing values of β. At $\beta_{L_2} \approx 0.01045$ the characteristic curve undergoes a saddle-centre bifurcation and the linear normal behaviour switches from saddle×centre×centre to saddle×saddle×centre. At the bifurcation point there is a turning point and the values of β decrease until $\{\beta = 0\}$ where it meets the planar 022 resonant Lyapunov orbit.

Recall that a similar situation hold for the AQBCP, where L_2 is connected by continuation by the orbit 24, a orbit bifurcating from 022 which is very close to. However, the turning point takes place for a large value of β (around 4.2), much larger than what can be achieved by a solar sail.

In the ARTBP, the families of fixed points reach lower values of β, that is, the turning point in the continuation with respect to β with a perpendicular sail happens before in the ARTBP. This means that there, for a perpendicular sail, there is no dynamical equivalent of L_2 for $\beta > \beta_{L_2}$. Let us consider the continuation of L_2 as a periodic orbit for fixed values of

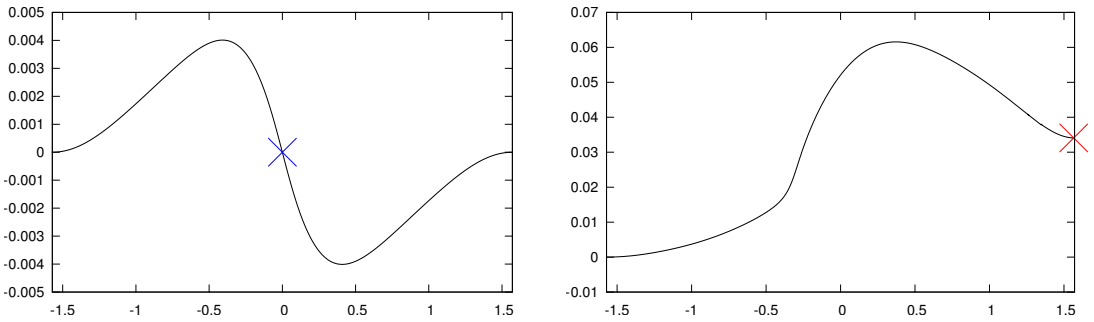

(a) (b)

Figure 6.19: Continuation of L_2 with respect to δ for a fixed value of β. **(a):** $\beta = 0.01$. **b**: $\beta = 0.02$. Horizontal axis: δ. Vertical axis: z.

β. If we fix $\beta < \beta_{L_2}$ and consider the characteristic curve obtained by continuing L_2 with respect to δ. The kind of behaviour is as we observe in Figure 6.19 (a). The characteristic curve starts at the coordinates of L_2 and $\delta = -\frac{\pi}{2}$. As δ increases, one finds some fixed points

with positive values of its z-coordinate. The maximum out-of-plane displacement is reached at δ_{max}. After this value of delta, the characteristic curve decrease its δ rapidly, and crossing the plane of motion of the primaries at $\delta = 0$. The characteristic curve is symmetric with respect to $\{z = 0\}$. Therefore, the orbits corresponding to positive values of δ are a mirror image through $z = 0$ of the ones for $\delta < 0$. If $\beta > \beta_{L_2}$ the situation is not the same. In Figure 6.19 (b) it is displayed the continuation for $\beta = 0.02$. The z-coordinate of the fixed points of this family grow up to a maximum high and then, they decrease again until the characteristic curve reaches the homotopy level $\{\delta = \pi/2\}$. At this point we find a trajectory of the RTBP. This time is not L_2 but the resonant vertical Lyapunov orbit $02A^-$.

Recall that in the case of the AQBCP, L_2 and 22 are never connected (L_2 is connected with 24 for large values of β) while 22 is connected with $2A^-$ by continuation forwards and with $2A^+$ by continuation backwards. Again, the geometry of the surface of fixed points is affected severely.

The ABCP, the ARTBP and the vicinity of L_3, L_4 and L_5

Let us move to the triangular points (and L_3). For the analysis of the dynamics around these points we have used the ABCP. Therefore, the comparison in for these Lagrangian points is done using the models ABCP and ARTBP. Recall that, in the BCP, the triangular points are replaced by three periodic orbits. Therefore, in the ABCP, we continue three fixed points for each triangular equilibrium point. While this, in qualitative terms, can be considered as a remarkable difference, these fixed points are connected for values of β that are not extremely small. This is translated into the small tongues near the triangular points observed in all plots in Figure 6.11. These, do not exist in the ARTBP.

Besides the difference in the number of dynamical replacements of the triangular points when SRP is very small, in both models, the ABCP and the ARTBP, we observe the same general situation. For a sails perpendicular to Sun, in the ARTBP, the periodic orbits from L_3, L_4 and L_5 merge into a Pitchfork bifurcation very similar to the one displayed in Figure 6.9 for the ABCP. In this case, however, the bifurcation happens for some bigger value of $\beta_{L_{345}} \approx 0.045$. For values of the effectivity larger $\beta_{L_{345}}$, a single curve of fixed points persist. The actual orbits corresponding to these fixed points pass close to the Earth until, for some value of β, an encounter with Earth's surface occurs. This impact leads to a natural limit for the useful range of lightness number values to navigate between L_3, L_4 and L_5. We would like to stress that the ABCP provides a lower bound of this value. Since this bound is smaller it would be technically achievable earlier.

In Figure 6.20 we display continuations with respect to α for some fixed values of β. Figure 6.20 has to be compared with 6.11. The first thing to be observed is that, in the ARTBP, the bifurcations connecting L_3, L_4 and L_5 happen for a larger values of β, larger

than $\beta_{L_{345}}$. The qualitative behaviour is also changed. Notice that, after the bifurcation, L_4 and L_5 remain connected.

In fact, the characteristic curves connect L_3 with L_4 and L_5 via a perfect Pitchfork bifurcation. In the case of the ABCP, the symmetry of the Pitchfork is broken by higher order terms of Sun's gravitational potential, hence, we observe imperfect bifurcations when Sun's gravity is included. The tongues connecting the Lagrangian points are slightly bigger in the case of the ARTBP. Despite this topological changes, one could compare the shapes and sizes between bifurcation diagrams in Figures 6.20 and 6.11 and conclude that the behaviour is quite similar. If one takes a look on the linear normal behaviour, the models show to be different enough to vindicate the use of the ABCP. Not taking into account Sun's gravity leads to an extra symmetry which is not realistic. Due to the existence of this symmetry, the three Lagrangian points L_3, L_4 and L_5 remain connected for all values of β. We would like to remark that this triple connection is obviously not persistent under the most relevant perturbation in the Earth-Moon system (which is Sun's gravity). Therefore, not including Sun's gravity relies in a model that does not capture well a qualitatively important property of the problem.

One last thing to be reminded is that including Sun's gravity does not increase the complexity of the model, at least from the mathematical point of view. All, the ARTBP, the ABCP and the AQBCP are periodic time dependent perturbations of the RTBP, they all are Hamiltonian and the simplest invariant objects that exist are periodic orbits with period T_S. If one do not take into account the number of operations needed to evaluate the vector-field, there is no practical gain in excluding Sun's gravity.

6.9 Some concluding remarks

In this chapter we have studied the dynamical equivalents of the Lagrangian equilibrium points for a solar sail moving in the Earth-Moon system. In particular, we have focused on the dependence of these dynamical equivalents upon the parameters related to the orientation and the effectivity of the sail.

We have taken Sun's gravity under consideration. Restricted models for the motion of the primaries, the QBCP and the BCP, have been augmented to include the effect of Solar Radiation Pressure. The resulting models are Hamiltonian systems with periodic time dependence. The period of both Hamiltonian is the period of Sun. As far as we know, this is the first time in the literature these particular model have been used. We have studied how different periodic orbits (with the same period as Sun) of the QBCP and the BCP change with respect to the parameters of the sail. Let us stress that, these are the simplest invariant objects of the system. We have used the stroboscopic map to see these periodic orbits as

fixed points. As the sail depends on two parameters, the orientation and the effectivity, each of the Lagrangian equilibria has a surface of dynamical equivalents embedded in the phase space. We have studied the geometry and topology of these surfaces by computing sections. These sections are obtained by using the continuation method. We have identified geometric properties of some of the surface. In particular these particular surfaces have a saddle point (maybe degenerate due to symmetries of the vectorfield involving the orientation of the sail). These geometrical properties have a deep impact on the dynamics of the systems in terms of existence, linear character and trace of each orbit for a given value of the parameters.

We also report the effect SRP has on the maximal Floquet exponent of some orbits near the Lagrangian points L_1 and L_2. Among the non-planar resonant Halo orbits we studied in this work, there is a subset of them which can be stabilized i.e. the maximal Floquet exponent can be reduced as much as desired using suitable parameters of the sail. The value of the effectivity required to accomplish that is a little bit larger than the current technological capabilities, around 0.02. The impact of SRP on the large hyperbolicity of the planar orbits is not remarkable. Therefore, these Halo orbits (besides the natural properties that make them interesting) are the ones suitable to be used in mission design as station keeping strategies are reliable. Indeed, the small instability permit to reduce the number of maneuvers to be performed on time.

Finally, we give some words on the impact that taking under consideration the gravity of Sun has. We do not repeat the study for the case in which Sun's gravity is not considered but, we spot some differences that, in our opinion, are enough to vindicate the use of a model taking Sun's gravity under consideration.

6.10 Technical details

All the integrations have been done by means of a Taylor method. The demanded accuracy for the computations related to periodic orbits and invariant tori has been 10^{-15}. We have used jet transport to obtain the solution of the first order variational equations. We also have used multiple shooting to cope with the huge propagation of errors the systems display near the collinear points L_1 and L_2. A maximum of four sections have been required. The values of the parameters for the BCP can be found in Section 5.5.

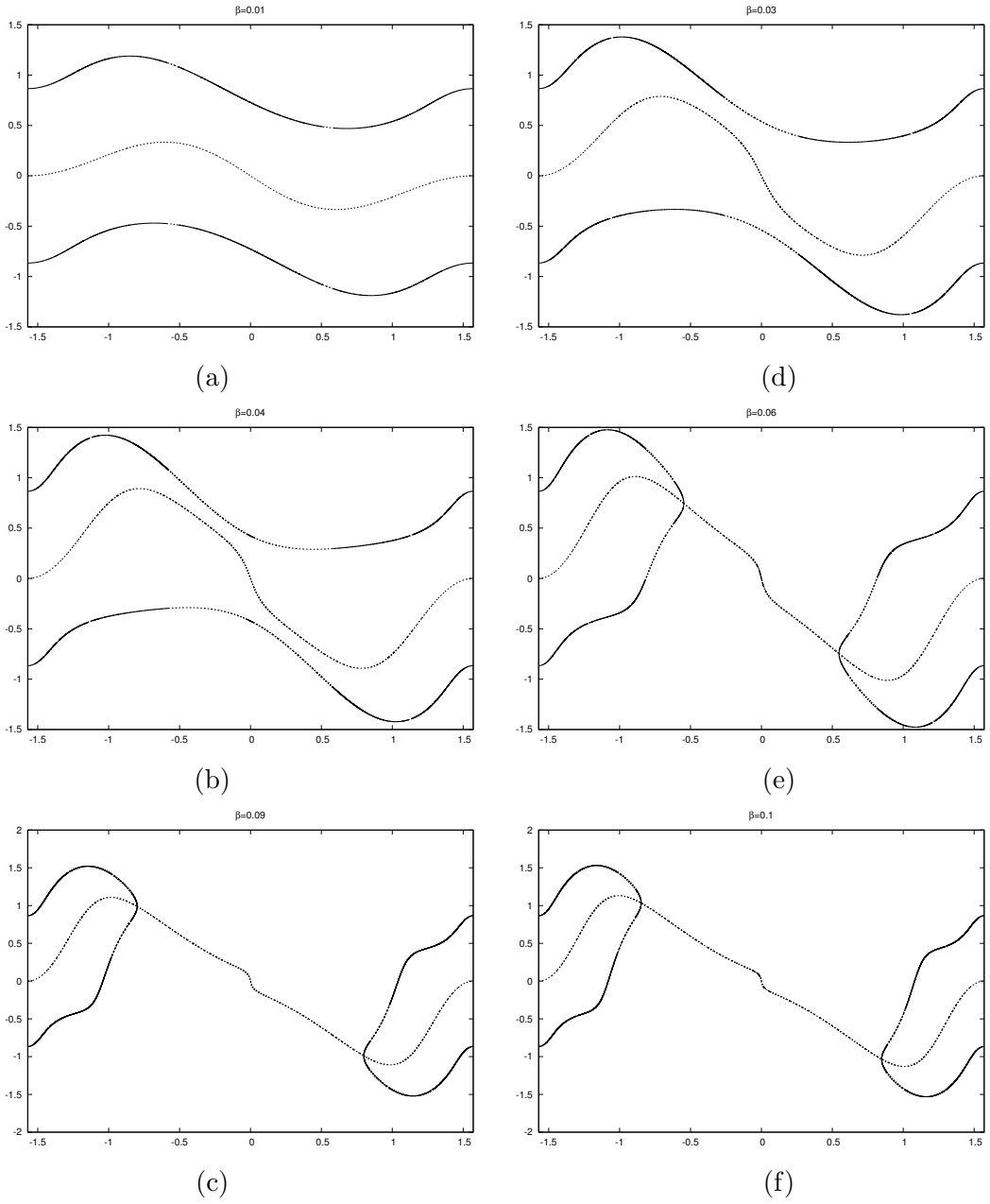

Figure 6.20: Dynamical equivalents of L_3, L_4 and L_3 (w.r.t. α) for a fixed value of β. **(a):** $\beta = 0.01$. **(b):** $\beta = 0.03$. **(c):** $\beta = 0.04$. **(d):** $\beta = 0.06$. **(e):** $\beta = 0.09$. **(f):** $\beta = 0.1$. Horizontal axis: α. Vertical axis: y.

"It's the questions we can't answer that teach us the most. They teach us how to think. If you give a man an answer, all he gains is a little fact. But give him a question and he'll look for his own answers."

Patrick Rothfuss, The Wise Man's Fear

7

On Kordylewsky clouds

The presence of Trojan asteroids near the triangular points of the Sun-Jupiter system leads to a natural question: Are there similar objects in the vicinity of the Earth-Moon triangular points? The first work in the scientific literature addressing this question appeared in 1961 when the polish astronomer K. Kordylewsky published a paper [Kor61] in which he reports the presence of a region populated with small particles near the triangular point L_5 at the Earth-Moon system. During the subsequent years, several authors tried to reproduce the observations of Kordylewsky with positive [Roa75] and negative [FV80, FV82, Win89] results. This ambivalence of results put the existence of Kordylewsky clouds, that is the name that concentration of dust received, under the shadow of doubt. The letter by R. G. Roosen and C. L. Wolf [RW69] (1969) opened the debate to the scientific community has been lurching between the existence and non-existence of these clouds. It is clear that the existence of these regions cannot be followed by analogy with the existence of Trojan asteroids. Indeed, the RTBP seems to be a reasonable[1] model for the Sun-Jupiter system as these bodies represent more than the 99 percent of the total mass of the solar system and, hence, perturbations due to the gravitational fields of other planets should not be very relevant. On the other hand, the motion in the Earth-Moon system is severely affected by the presence of Sun, as we have discussed in Chapter 5. The first paper proposing a model for the study of the libration clouds [Poh64] , considered, however, a modified Kepler problem with Earth as central mass. This work, due to Pohle, was published in 1964, 5 years before the letter by

[1]Nevertheless, more complete models have been studied, see [GJL05, GJR04, GJ01, GJ04, RGJ05, RG06].

Roosen and Wolf. The models got more complicated as the controversy increased. Katz, in 1975 [Kat75], presented a numerical study using a model considering Sun's gravitational field together with Earth's and Moon's. In this model, Sun is frozen at infinity but this suffices to capture the unstable nature of the Earth-Moon triangular points. It is also remarkable that the author considered the importance of Solar Radiation Pressure (SRP) in the problem. Indeed, as the libration clouds are to be formed by small particles, SRP should be considered as a relevant force. In 1979, Burns, Lamy and Soter [BLS79] published a seminar paper on the effect of different kinds of radiation forces on small particles in the solar system. In this work it is analyzed how SRP affects the dynamics of dust. The other radiation forces studied in this work are the solar wind, the Poynting-Robertson effect and the Yarkowsky effect. Other references concerning the relation between SRP and dust are [KOM02, Vin09]. Even if the role of SRP seems to be remarkable to explain Kordyleswky clouds, most of the works do not take into account SRP (see [SS15] addressing directly the problem of libration clouds). Besides the paper by Katz, the first study of the dynamics near the Earth-Moon libration points that takes under consideration SRP is the content of this chapter published as a proceeding in 2015 [JCFJ15]. In 2017, Sal'mikove and Stepanov published a paper in which a density function of the libration clouds is derived from numerical simulations using the same model we use here (to be specified in next section).

In Chapter 5 we analyze carefully the impact of Sun's gravity near the triangular points of the Earth-Moon system. A fact that is discussed in that chapter, is that the Coriolis acceleration compensates the first order of Sun's potential (in the vectorfield). The aim of the present chapter is to illustrate that, while Sun's gravity is relevant enough to produce bifurcations near the triangular points, when SRP is considered it has a more relevant role than what may be expected, because of that cancellation. This fact has been relevant in Chapter 6, where it is shown that SRP stabilizes the dynamical equivalent of the triangular point L_4 for very small values of β. However, we think that it is interesting to emphasize the role of SRP in the Earth-Moon systems through a problem that has an appealing (and rather controversial) history.

It is true that the role of SRP on the problem of the existence of Kordylewsky clouds has been considered but not from the dynamical systems point of view. And, moreover, the most recent work [SBBH18], the authors state that SRP can be neglected. We do not state that the results we are going to present confront their claim, as the model we use here is not the same one used in [SBBH18], and, moreover the results in the present chapter should be contrasted in more accurate models[2].

Summarizing, in this chapter we study the role of SRP in the out-of-plane stability regions found in [Jor00] for the BCP, that is, we look for practically stable motions around the triangular points. The first idea that pops on our mind when confronting this problem is to

[2]See Chapter 9 for a more detailed explanation.

select a dense ($6D$) grid of points around a triangular point and integrate initial conditions on the grid for a long time spans. Then, we construct a stability regions with the points that, after the integration, remain close to the triangular point. At the first hurdle, one can understand why this is not a promising strategy: the grid in the phase space has to be 6 dimensional which entails enormous numerical costs. In order to decrease the dimension of the grid, we take advantage on the skeleton of the dynamics. We remark that we follow the same strategy as in [Jor00] but taking SRP under consideration. We stress that our study is not completely adapted to the skeleton of the dynamics when SRP is activated, but our goal is to find out the fate of those out-of-plane effective stability regions reported in [Jor00]. While We also examine the dynamics in the plane as SRP has a huge impact on it.

7.1 Some remarks on the Model

In Chapter 5 we discuss the Bicircular Problem (BCP) and focus on the motion of a test particle near the triangular points. Let us give a summary, for selfcontainedness of the present chapter, to the most relevant facts of the model. We assume Earth and Moon to revolve, around its common centre of masses, describing a circular orbit. At the same time, the centre of masses of the Earth-Moon system revolve together with Sun, around the barycentre of the system, describing again a circular orbit. We are interested on the motion of a test particle subject to the gravitational forces of Earth, Moon and Sun as well as SRP. We take a synodical frame of reference so that Earth and Moon are fixed on the horizontal axis x. The plane (x, y) contains the motion of the primaries. The unit of distance is the distance between Earth and Moon, the unit of mass is the sum of Earth's and Moon's masses and the unit of time is taken so that the period of Earth and Moon around its centre of masses is 2π. In these units the universal gravitation constant equals to one. Let us denote by μ the mass of Moon, m_S the mass of Sun, ω_S the mean angular velocity of Sun in these synodic coordinates and a_S the distance between Sun and the Earth-Moon barycentre. SRP is included in the equations of the BCP and the resulting model is a Hamiltonian System with three degrees of freedom. In positions-momenta coordinates, it has the Hamiltonian function:

$$\begin{aligned} H = &\frac{1}{2}(p_x^2 + p_y^2 + p_z^2) + yp_x - xp_y - \frac{1-\mu}{r_{PE}} - \frac{\mu}{r_{PM}} \\ &- \frac{m_S(1-\beta)}{r_{PS}} - \frac{m_S}{a_S^2}(y\sin\theta - x\cos\theta). \end{aligned} \tag{7.1}$$

where $r_{PE}^2 = (x-\mu)^2 + y^2 + z^2$, $r_{PM}^2 = (x-\mu+1)^2 + y^2 + z^2$, $r_{PS}^2 = (x-x_S)^2 + (y-y_S)^2 + z^2$, $x_S = a_S\cos\theta$, $y_S = -a_S\sin\theta$, $\theta = \omega_S t$ and β is, the lightness number, a parameter associated to the magnitude of SRP. Notice that we do not truncate the potential of SRP in this Hamiltonian. Therefore, while is is close to, the system in this chapter is not the same as the one used in Chapter 6 for the motion of a perpendicular sail near the triangular points.

In Chapter 6 we provide a long discussion on how to include SRP in the BCP and (QBCP), the resulting models are said to be the augmented versions of the ones studied in Chapter 5 . This nomenclature is useful in that chapter as we are constantly addressing to different models and comparing them. In this chapter we only deal with Hamiltonian system (7.1) and, therefore, we avoid these names.

In this chapter SRP is considered to act on a spherical particle which is equivalent to take out the angles in the equations of Chapter 6 considering the orientation to be always perpendicular. If the angles no longer play a role, there is no need to cut the expansion of SRP to keep the Hamiltonian character of the model. For that reason, β appears in a coefficient multiplying the mass of Sun in equation (7.1).

Notice that we can split the Hamiltonian function in three parts:

$$H(X,\theta,\beta) = H_{RTBP}(X) + H_{SG}(X,\theta) + H_{SRP}(X,\theta,\beta), \tag{7.2}$$

here X denotes the phase space variables. The first part, H_{RTBP}, is the Hamiltonian of the Earth-Moon RTBP, the second part is describes the contribution of Sun's gravitational field and a Coriolis acceleration, together with the first part, they conform the Hamiltonian of the BCP. The last term takes into account the effect of SRP and depends on the parameter β, the lightness number, which, we recall, represents the ratio between the acceleration due SRP and the solar gravity. When $\beta = 1$ the effects of SRP and Sun's gravity cancel each other.

In some situations (such as the two body problem and the RTBP, see, for instance, [LC15]) it is frequent to say that the particle feels a reduced gravity, as if Sun were lighter. This is not the situation here, where, while it's true that the magnitude of Sun's gravitational potential is reduced due SRP, the centre of mass of the Earth-Moon system keeps moving according to the real mass of Sun and therefore, the Coriolis force exerted on the particle is not canceled out.

As we mentioned in the introduction, the main point of the present chapter is to illustrate something that is discussed in Chapter 5: The Coriolis acceleration, cancels out the linear term of Sun's gravitational potential of equation (7.1). Therefore, the term of lowest order in the perturbation, once SRP is turned on, is $\beta\frac{m_S}{a_S^2}(x\sin\theta - x\cos\theta)$. For $\beta = \mathcal{O}(1/a_S) = 10^{-3}$, the magnitude of SRP is already comparable to the one of Sun's gravity. For larger values, SRP is the most important term in the perturbation. As β increases, the role of the Coriolis term takes importance. When SRP and Sun's gravity cancel out (at $\beta = 1$), the only remaining term in the perturbation is the Coriolis acceleration.

The parameter β depends on the area, the mass and the reflectivity of the particle. For a perfectly absorbing spherical body this coefficient can be approximated [BFM94] by $\beta \approx 0.2/r$, where r is the radius of the particle in micrometers. Reflectivity increases the value of β. In this chapter, we handle extremely small values of β. The smallest value of β we

work with is 5×10^{-5}. The possible radii corresponding to this β range from 400 micrometers for perfectly absorbing bodies to 3.7 centimeters for perfectly reflecting bodies. Notice that, having a collection of particles with the same density and reflectivity (for instance, particles composed with the same material), the parameter β can be used to classify them. As a matter of fact, this reveals the importance of studying the impact of SRP for low values of β.

Let us notice that SRP is not the only relevant force that could be considered in this study. In other works, another relevant forces (such as the solar wind drag and the Poynting-Robertson drag) have been included [LC15, Sri99].

When $\beta = 0$ the model reduces to the well known BCP: Near the triangular points, the perturbation due to Sun's gravity is relevant enough to produce a bifurcation on L_4. It is replaced by three periodic orbits, one small and unstable and two larger and stable. Due to the presence of the unstable periodic orbit, the neighborhood of L_4 is no longer stable. Recall that this is a feature that BCP shears with the real system (by real systems we mean the model that takes into account the whole solar system, where the trajectories of the masses are given by the JPL ephemeris), and the reason we use it to study the motion near the Earth-Moon triangular points.

The third term of the Hamiltonian is a new periodic perturbation with the same period as Sun, so, if we set $\beta > 0$, the periodic orbits corresponding to the BCP are changed.

7.2 Periodic orbits for low values of β

Let us recall that, in Chapter 5 we have named the dynamical equivalents of the triangular points as $PO1$, $PO2$ and $PO3$. We recover these names in the subsequent discussion.

Let us consider Hamiltonian system (7.1) with $\beta > 0$. The Implicit Function Theorem assures that, under generic conditions, the periodic orbits of the BCP can be continued with respect to β. We focus on the periodic orbits near L_4. Let us consider, as usual, the stroboscopic map (P_β) at time $T_S = 2\pi/\omega_S$, where ω_S is the frequency of Sun. Periodic orbits of period $2\pi/\omega_S$ appear as fixed points of P_β.

In Figure 7.1 we display the curve of fixed points corresponding to the continuation, with respect to β, of the dynamical equivalents of the triangular points in the BCP. The curve crosses $\beta = 0$ three times (corresponding the three periodic orbits near L_4 of the BCP). The numerical continuation uses $PO3$ as initial condition. We observe that $PO3$ can be continued (as a fixed point of P_β) for low positive values of β. Eventually the curve finds a turning point (changing from stable to unstable) and returns back to $PO1$. After another turning point, the curve regains stability and crosses again $\beta = 0$ at $PO2$. After that, the curve keeps tracking fixed points with positive values of β. Stress that fixed points with negative values of β do not

have physical meaning but they are helpful to see that the three fixed points corresponding to the BCP are connected by the curve. All this process happens extremely fast in β (see the magnification in Figure 7.1). Let $\beta^1 < 5 \times 10^{-4}$ be the value of for which the characteristic

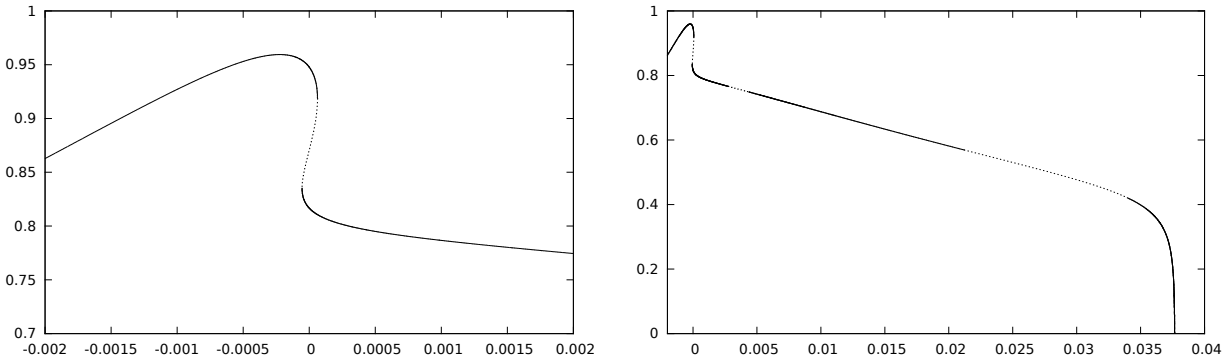

(a) (b)

Figure 7.1: Numerical continuation of the periodic orbits $PO1$, $PO2$ and $PO3$. Horizontal axis: β. Vertical axis y. **(a):** Magnification for small values of β. **(b):** Continuation for $y > 0$.

curve has the first touring point. For $\beta > \beta_1$, there is a single dynamical equivalent of L_4, that is, there is exactly one fixed point continuing from $PO3$. The curve keeps going until it reaches the horizontal axis at $\beta_2 < 0.038$. There, the characteristic curve undergoes a pitchfork bifurcation, and the branch corresponding to L_4 joints with the ones corresponding to L_3 and L_5. For $\beta > \beta_2$ there exist a unique dynamical replacement for L_3, L_4 and L_5 which is totally elliptic right after the bifurcation but it changes its linear behaviour as β keeps increasing. Finally, the trajectory (in the flow) corresponding to this unique dynamical replacement collides with Earth. The qualitative description of this continuation is the same as the one described in Chapter 6 for a perpendicular sail. Notice that, there, the higher order terms of SRP are neglected. The qualitative agreement between the results vindicates, somehow, the choice of the model in Chapter 6.

In Figure 7.1, continuous line stands for stable periodic orbits while the dashed line stands for unstable ones. We observe several changes of stability, they are product of the bifurcations. For $\beta \approx 2.74 \times 10^{-3}$, the characteristic curve undergoes a period doubling bifurcation. The main branch switches from stable to unstable and it creates two families of stable 2-periodic fixed points that eventually merge with the main branch in a period halving bifurcation. For $\beta \approx 2.114 \times 10^{-3}$, the characteristic curve undergoes a Hamiltonian-Hopf bifurcation and the main branch changes to complex instability. At this point it is essential

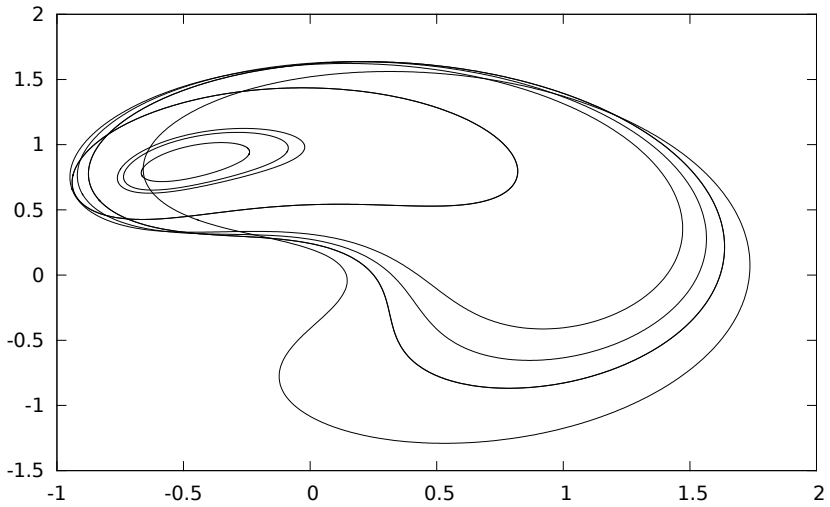

Figure 7.2: Dynamical equivalents of L_4 for some values of β. See text for more details. Horizontal axis: x. Vertical axis: y.

to take a look at the actual orbits of the system. Figure 7.2 shows trajectories for the values $\beta = 0$ (PO3), $\beta = 6\times10^{-5}$, $\beta = 6.3\times10^{-5}$, $\beta = 2.74\times10^{-3}$, $\beta = 1.67\times10^{-2}$, $\beta = 2.11\times10^{-2}$, $\beta = 1.27\times10^{-2}$ and $\beta = 3.39\times10^{-2}$. The trajectories increase dramatically in size with respect to β. The main objective of this chapter is to study the motion of particles near the geometrical L_4 and, as we see in Figure 7.2, the orbits already cross the horizontal axis for very small values of β. Indeed, the largest four trajectories in Figure 7.2 correspond to values of β of order 10^{-2}, and are the ones that cross the horizontal axis. This implies that the skeleton of the dynamics has moved too much for our interests for that magnitude of values of β. This will be crucial in Section 7.3.1 when we choose the values of $\beta$to be used to compute vertical invariant tori. This is not a novelty as the same phenomenon is illustrated in Chapter 6. However, there we are much more concerned in the geometry of the surface of fixed point and the size of the trajectories in the flow is not discussed at all. As we already pointed out, this huge impact of small values of β is the reason that pushed us to undertake this study.

7.3 Vertical families of $2D$ invariant tori

We have seen that, in the BCP[3], there are three vertical (Cantor) families of $2D$-invariant tori ($VF1$, $VF2$ and $VF3$) rising from the periodic orbits ($PO1$, $PO2$ and $PO3$) near the triangular points. One of their frequencies is always ω_S, the frequency of the periodic perturbation due to Sun. These tori can be regarded as the dynamical equivalents of the vertical Lyapunov periodic orbits of the RTBP. The main goal of this chapter is to study the stability regions near L_4 induced by elliptic tori. On one hand, the stability region associated to $VF2$ is small, narrow and does not reach high values of (z, p_z) amplitude. For that reason we focus on how $VF3$ changes with respect to β. On the other hand, we have seen in Section 7.2 that, for larger values of β, the dynamically equivalent periodic orbits (and so the invariant tori) are far from being in a neighborhood of L_4. For that reason we select small values of β such that, as in the case of periodic orbits, are enough to produce important changes on the size of the tori.

Let P_β be the Poincaré map appearing in Section 7.2. Notice that the vertical invariant tori of system (7.1), which have ω_S as one of its frequencies, appear as invariant curves of P_β. As we have seen in Chapter 3, approximations of invariant curves can be regarded as zeros of functions defined in large dimensional spaces. Hence we can use a continuation method to find these zeros. There is, however, a remarkable difference: while the families of periodic orbits depend smoothly on the parameter, the families of invariant tori are defined in a Cantor set of frequencies with gaps corresponding to resonances. Nevertheless, these gaps are usually very small.

7.3.1 Computation of vertical families of invariant tori

The computations go as follows. First, we compute the family $VF3$ of the BCP. Once we have this family, we select three different values of p_z (later will be clear how this determines a torus in the family) which approximates the maximal amplitude in z. Then we continue each of these tori with respect to β.

Let us recall first how to start the computation of the vertical families of invariant tori in the BCP. As we have stressed, there is a family of tori for each periodic orbit. We focus on the $VF3$ corresponding to $PO3$. Let $\tilde{x} \in \mathbb{R}^6$ be the coordinates of $PO3$ as a fixed point of P_0 and let $v = v_r \pm \sqrt{-1} v_i$ be the (normalized) eigenvectors corresponding to the vertical mode of $\tilde{x}$. Consider the circle:

$$\varphi(\theta) = \tilde{x} = h(v_r \cos(\theta) + v_i \sin(\theta)),$$

[3]See Chapter 5.

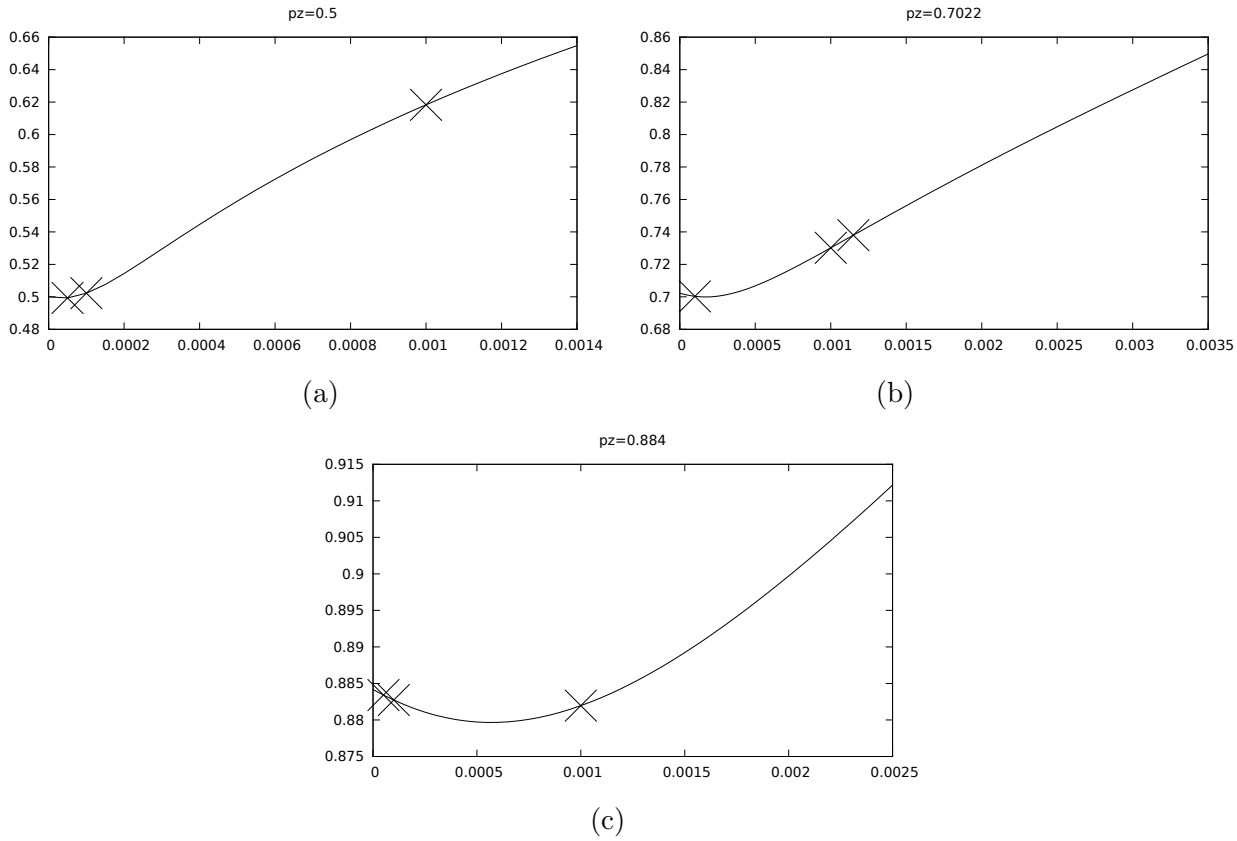

Figure 7.3: Continuation of some tori of $VF3$ with respect to β. Horizontal axis displays β and vertical axis displays p_z. **(a):** Continuation of the torus of $VF3$ given by $p_z = 0.5$. **(b):** Continuation of the torus of $VF3$ given by $p_z = 0.7022$. **(c):** Continuation of the torus of $VF3$ given by $p_z = 0.884$.

where h is a small parameter. Name $\tilde{\omega}$ the vertical frequency of $\tilde{x}$. We propose as a prediction (to be corrected by means of a Newton method) for the first invariant curve φ with frequency $\omega = \tilde{\omega} \mp \alpha$. Here, α is again a small parameter. The $\mp$ stands because the real invariant curves only exit for frequencies either larger or smaller than $\tilde{\omega}$ (we do not know in advance). If we fail in the choice of the sign, the method may not converge (depending on the size of h). Then, we only need to change the sign and restart the computation. Recall that, in order to have uniqueness on our equations, we have to add some extra condition. This condition could be chosen generically but in this case we adapt the condition to our problem. Since each torus cuts the $\{z = 0\}$ plane, we force them to do it at $\theta = 0$. Notice that there are two

points where the torus cuts the $\{z = 0\}$ plane, we choose the one with $p_z > 0$[4]. The rest of the procedure is to continue this first torus with respect to the vertical frequency until it reaches a desired value of p_z (at $\{z = 0\}$). To do so, it is convenient to construct the prediction by interpolating for some of the previous tori. In Figure 7.3 we display some continuations of invariant tori. The horizontal axis shows the value of β while in the vertical axis p_z. The panel, (a), displays the continuation of the torus on the $VF3$ identified by $p_z = 0.5$. The continuations goes up to $\beta = 1.4 \times 10^{-3}$ with tori increasing in p_z monotonically. The last tori reaches $p_z \approx 0.66$. In the plot on panel (b), the curve starts at the torus of $VF3$ identified by $p_z = 0.7$ and, for $\beta = 0.0035$, reaches the amplitude 0.86. Finally, in the picture on the bottom, it is displayed the continuation of the torus in $VF3$ identified by $p_z = 0.885$. At the beginning p_z decreases until a minimum (located at $\beta \approx 5 \times 10^{-4}$) and from that point they increase until the value 0.915 for $\beta = 0.0025$.

We observe that, as in the case of periodic orbits, the tori grow their amplitude rapidly in β. In fact the last tori of the plot on the bottom is almost as away from L_4 as from Earth.

7.4 Effective stability regions

It is well known that normally elliptic lower dimensional tori induce a nearby region of effective stability. That is, the time a point needs to escape from a neighborhood of the torus increases exponentially with the inverse of the distance to the torus. Our aim in this section is to estimate the size and the shape of the regions of effective stability induced by the tori computed in Section 7.3

We explain briefly in Chapter 5 how to compute these regions of practical stability. Let us retake these discussion giving more details. The regions of effective stability are regions of the phase space in which the initial conditions do not escape for a long time. There is an obvious issue with this definition to be solved before performing any practical computation, that is, how much is a long time. In general, this quantity is chosen according to the problem and also is limited by the assumable computational cost. As the goal of this chapter is to study the stability regions appearing in [Jor00], we take the same maximal integration time as in there, which is 15000 Moon revolutions, let us call this time T_m[5].

The next step to follow is to select a grid of initial conditions in the phase space. We will be more precise on the grid when explaining the computations. Each of these initial conditions is integrated T_m units of time.

At each integration step, we check if the particle is closer to Earth or Moon than their corresponding radius. In the units of the model we use, the radius of Earth is about 0.017

[4]With this extra condition, to fix a value of p_z identifies uniquely a torus in the family.

[5]Notice that, by definition, $T_m = 2\pi 15000$

units and the radius of Moon is about 0.0045 units. If such a thing happens, we decide that the particle has collided with the corresponding primary and stop the integration. The criterion to decide whether the particle escapes from the system or not is the crossing with the subspace $\{y = -0.5\}$. Notice that we start the integrations in the vicinity of the triangular point L_4 in the upper semi-plane $\{y > 0\}$.

The initial conditions are taken as follows. First, we select a torus in a vertical family of invariant curves. This torus, as we have imposed in the computation, cuts the plane of motion of the primaries at $\theta = 0$ with positive vertical momentum. Let us use the coordinates in which the torus cuts the plane and produce a two dimensional grid in which the plane (x, y). The initial conditions to be integrated are obtained by selecting point on the grid to fill the values of x and y. The remaining coordinates are set to be the coordinates for which the torus cuts the plane of motion of the primaries.

As we explain in Chapter 5, the two dimensional grid in the (x, y) is taken in polar coordinates in the centred at Earth:

$$\begin{cases} x_{ij} = r_i \cos \alpha_j + \mu, & r_i = 1 + ih_r, \\ y_{ij} = r_i \sin \alpha_j, & \alpha_j = 2\pi j h_\alpha, \end{cases}$$

where h_r (selected such that ih_r ranges form 0.5 to 1.) and h_α (selected such that jh_α ranges -0.5 to 0.5) are used to control the density of the grid.

In Figures 7.4, 7.5 and 7.6 we display the remaining points of the grid after an integration of T_m units of time for some fixed values of β: 5×10^{-5}, 1×10^{-4},1×10^{-3}, 1.5×10^{-3}, 2×10^{-3}. The coordinates (ρ, α) are selected according to what it is explained in Chapter 5.

In Figure 7.4 we display some of the effective stability regions induced by the tori of the curve at the top of Figure 7.3. The first region (on the top) corresponds to the stability region for $\beta = 0$, one of the stability regions found on BCP. The remaining regions, from top to bottom, correspond respectively to $\beta = 5\times10^{-5}, 1\times10^{-4}, 1\times10^{-3}$. We see that the region increases as β decreases. For the last value of β, the region has almost disappeared. In Figure 7.5 we display the stability regions corresponding to the tori of the curve at the middle of Figure 7.3. Here the stability region is larger for $\beta = 5\times10^{-5}, 1\times10^{-4}, 1\times10^{-3}$. The region is almost gone for $\beta = 2\times10^{-3}$. In Figure 7.6 we display stability regions corresponding to the tori of the curve at the bottom of Figure 7.3. Its size decreases with β. For $\beta = 1.5\times10^{-3}$ no point subsists after 15000 Moon revolutions.

7.5 Some concluding remarks

This is a preliminary work on the effect of SRP on the out-of-plane effective stability regions of the BCP. The numerical experiments suggest that these regions are not close to L_4 for

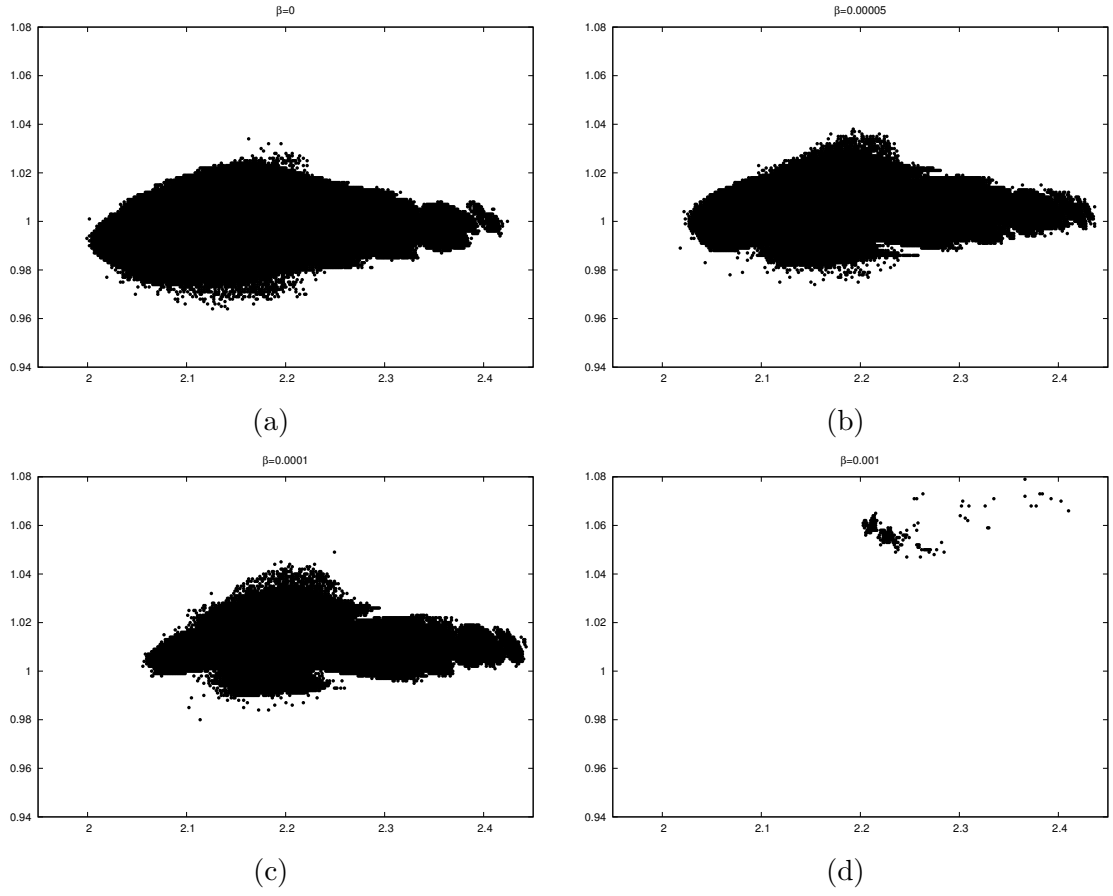

Figure 7.4: Remaining points near the tori in Figure 7.3 **(a)**. Horizontal axis: α. Vertical axis r. From (a) to (d): $\beta = 0$, 5×10^{-5}, 10^{-4}, 10^{-3}. See text for more details.

moderate values of β. This would imply that the motion of small particles (such as space dust and small asteroids), even with small values of β, have no stable dynamics near L_4. Without precipitating conclusions (there is still much work to do), our results seem to indicate that it is improbable to find particles with values of $\beta > 10^{-2}$ (space dust) trapped near the triangular points. On the other hand, we find that particles with smaller values (corresponding to bigger objects) do have effective stable regions near the triangular points. These regions are located outside the Earth-Moon plane, for high values of the coordinate z.

Stress again that the parameter β we use to characterize the magnitude of SRP depends on the mass, the area and the reflectivity of the particle. Therefore some of the work to do is to catalog the objects in space according to β.

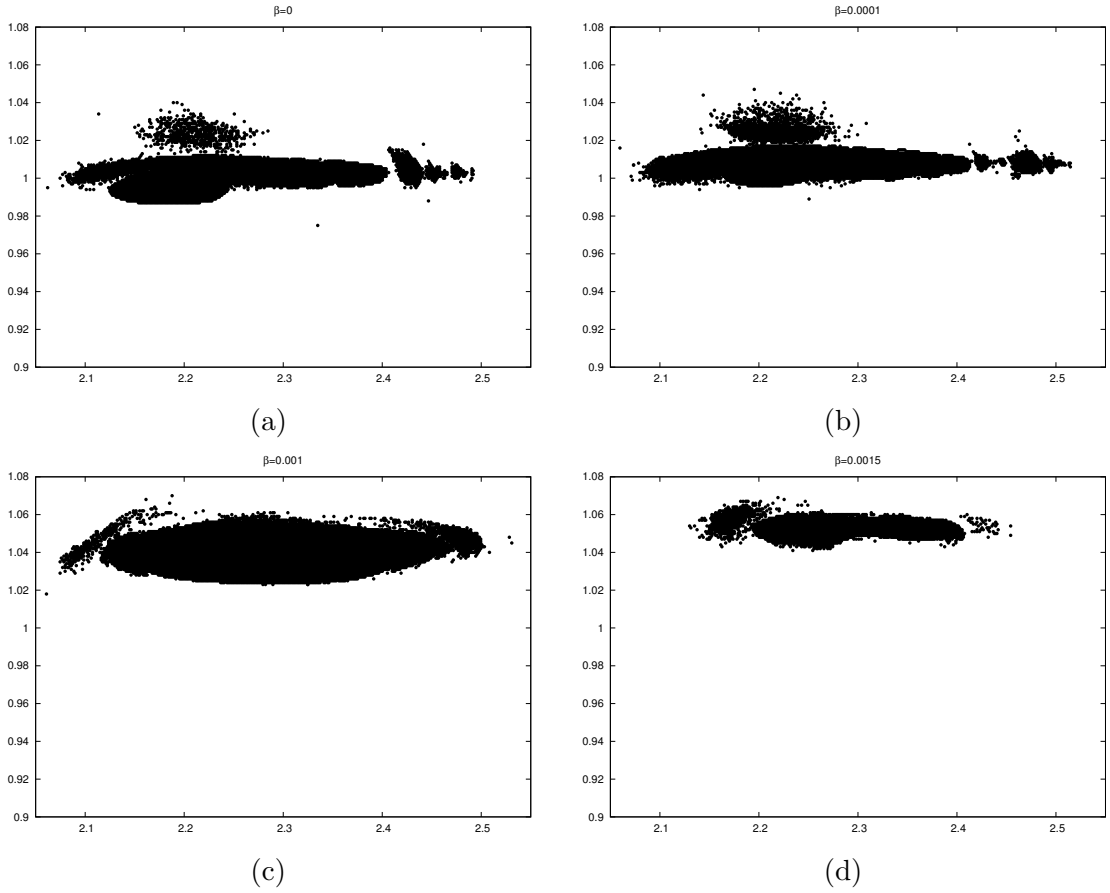

Figure 7.5: Remaining points near the tori in Figure 7.3 **(b)**. Horizontal axis: α. Vertical axis r. From (a) to (b): $\beta = 0$, 10^{-4}, 10^{-3}, 1.5×10^{-3}. See text for more details.

Let us finish by remarking some future work to do. The results on this intermediate model have to be tested in the real Solar System. Moreover, as we already have mentioned, there are some other forces (solar wind, Poynting-Robertson drag) to be included in future explorations.

7.6 Technical details

All the integrations have been done by means of a Taylor method. The demanded accuracy for the computations related to periodic orbits and invariant tori has been 10^{-15}. The values

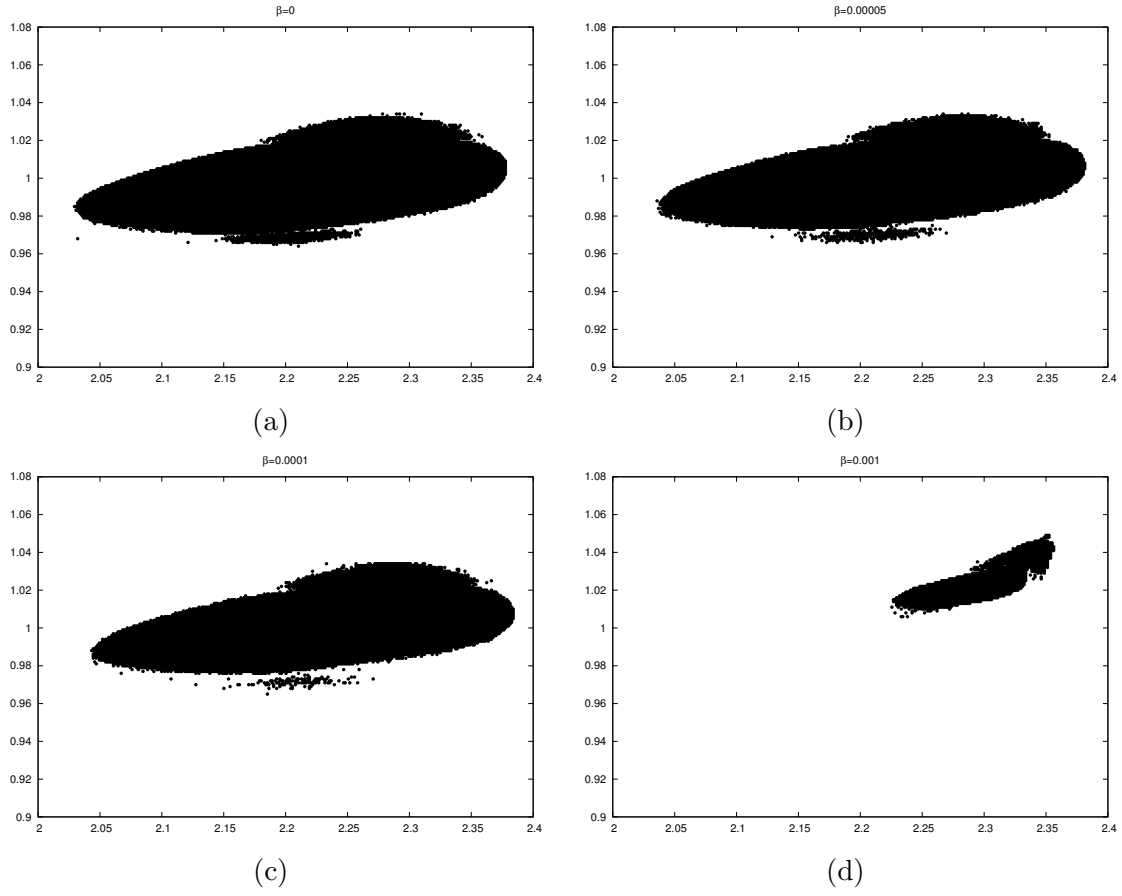

Figure 7.6: Remaining points near the tori in Figure 7.3 **(c)**. Horizontal axis: α. Vertical axis r. From (a) to (b): $\beta = 0$, 5×10^{-5}, 10^{-4}, 10^{-3}. See text for more details.

of the parameters for the BCP can be found in Section 5.5.

"Without order nothing can exist-without chaos nothing can evolve."

Oscar Wilde

8

Electron dynamics in atoms driven by strong laser fields

The idea of using collision of particles to probe the structure of atoms dates back to 1906 with the "scattering" experiment by Ernest Rutherford. It consisted in shooting nuclei of He (α particles) to a mica film from a long distance. These α particles get deflected and scattered. The scattering experiment provided empirical evidences to understand the structure of the atoms. During the XX century, a large number of examples vindicates collisions between particles as an essential tool to discover the fundamental building blocks of nature.

While scattering experiments give a small amount of information regarding atoms (such as the existence of their nuclei and their size), one needs more refined techniques to get a more detailed understanding on the fine atomic structure, for instance, the atomic orbitals (see [GC07, MCZ$^+$08, BXD$^+$12, ASM18]) or the electron dynamics during chemical reactions (see [BLJHE12]). The use of strong laser pulse probe the atoms and molecules at their own timescale: the attosecond[1] ($10^{-18}s$, the typical timescale in atoms). To do so, one uses the electrons of the target itself to probe its own structure (pump-probe technique). This is, sometimes, refereed to as "half-scattering". The electrons are teared of the target by a strong lased field and then go far away (ionize). The configuration of the ionized atom provides information of the target. In particular, most of the imaging techniques use recollisions, [MCZ$^+$08, BXD$^+$12].

[1]The attosecond is defined so that the period of the electron of a Hydrogen atom at its ground state is 24.

The recollision physics is an emerging field, transversal to collision physics and optics, see [Cor93, Cor14]. The typical situation recollision physicists are concerned with is the one in which a laser field excites an electron enough so the gained acceleration causes the electron to abandon the atomic core (ionizes), see [YI01, AD08]. After an excursion away from the atom, the electron is captured again by its parent ion. From the classical point of view, a highly energetic laser is to be used to transfer enough kinetic energy to an electron for this to leave the core. However, the phenomenon known as the quantum tunneling allow electrons to find its way through the potential barrier even if the particle travels not fast enough to overcome it, see [AGK$^+$92]. After the tunneling, however, the electronic dynamics behaves in a classical way. In this sense, the model is said to be semi-classical because, while the main forces acting upon the electron are modeled in a classical manner [BGK$^+$02, LHP$^+$13], some physical assumption made to interpret the model comes from quantum mechanics.

There are several works studying this phenomenon from the dynamical systems point of view: [MCU10, KCUM14, KMCU14, NCUW15, MKCU12]. The model we use to deal with recollisions is Hamiltonian with periodic time dependence. The model consists on two main forces: the Coulomb interaction between the ion and the electron and a periodic laser field. Near the core, this model can be regarded as a periodic perturbation of a central force-problem. The energy of the laser acts as a perturbation parameter. When the laser is turned off, the system is integrable. The model displays a classical KAM picture: As the laser is turned on most of the invariant curves subsists when its energy is small. It remains, then, a region near the nucleus of the atom with a large measure of invariant tori carrying with quasi-periodic inner dynamics. Notice that, as the laser turns on, the system gains half a degree of freedom and, therefore, the dimension of the phase space is increased by one. The same thing happens with the quasi-periodic invariant structures provided that they satisfy some non-resonance condition with respect to the frequency of the laser field. The simplest invariant objects are periodic orbits. The phase space is organized by the invariant objects attached to these periodic orbits and, moreover, there exist some key periodic orbits whose invariant manifolds drive most of the interesting recollision trajectories within the model.

In this chapter we investigate whether the recollision scenario established in the one dimensional configuration space, see [KCUM14], persists or not to higher dimensions. A little bit of physical context is given in Section 8.1. There, the fundamental physical concepts to play a role in the present chapter are developed. Some mathematically-oriented alternative definitions are also given just to make clear what we are measuring in the numerical experiments. In Section 8.2 we review some basic facts on the one dimensional case. We explain the underlying dynamics behind the well-known recollision scenario for this case. In particular we focus on two periodic orbits, $\mathcal{O}_1$ and $\mathcal{O}_2$, whose unstable (stable) invariant manifolds drive most of the recolliding trajectories. The literate usually identifies $\mathcal{O}_1$ (and very similar orbits) to the one with a bigger role in the recollision scenario while $\mathcal{O}_2$ receives

less attention. This is because the properties of recolliding orbits driven by $\mathcal{O}_1$ are better suited to capture the pattern drawn by typical recolliding trajectories. In Section 8.3 we investigate, finally, the role of the transversal direction. We show that periodic orbit $\mathcal{O}_1$ is no longer relevant in this situation, as the hyperbolicity along the transversal direction is large and nearby orbits escape fastly. On the other hand, the extra normal direction to $\mathcal{O}_2$ is elliptic. This makes this orbit to drive a lot of recolliding trajectories by means of its centre-unstable manifold. This mechanism is essentially different to the one revisited in Section 8.2 as the transversal direction is indispensable for these kind of recollisions to occur. Finally, we close this chapter with Section 8.4, containing remarks that report on some inconclusive work leading to questions to be dealt with in the near future, and with Section 8.4, devoted to technical details.

This is a joint work with J. Dubois, C. Chandre, S. A. Berman and T. Uzer.

8.1 Physical context

A recollision, in the sense of this chapter, is the process an electron undergoes when, due to some external forcing, it is kicked out of the atomic core and, after an excursion away from its parent ion, it returns with high kinetic energy. Usually, this excitation is given by a lased field. When an electron leaves the core, the atom acquires positive charge. This process is called **ionization**. Obviously for a recollision to occur, it is mandatory the atom to ionize in the first place. Positively charged atoms are produced when some amount of energy is transferred to a bound electron. This energy is provided by a collision with other charged particles of photons. From the classical point of view, in order to ionize, the energy an electron carries must be large enough to overcome the potential barrier induced by the laser field. However, there is a mechanism called **quantum tunneling** in which the electron passes through the potential barrier because of the wave nature of the electron itself, see Figure 8.1. The larger the energy is, the larger the probability of tunneling is as the barrier to tunnel through is thinner. In practice, tunneling ionization is observed when the atom is excited by strong laser pulses. The process in which a bounded electron is ionized due to the absorption of more than one photon from a lased field is called **multiple ionization**.

After the ionization, the electron goes far away from the core and it is assumed that its motion is driven by the lased field. This assumption is known as Strong Field Approximation as it neglects the role of Coulomb potential. Anyhow, the electron may return close to the ion. In that case, the ion and the electron are attracted to each other according to Coulomb's law. If the velocity of the electron is low enough, it can be captured again by the atom. The process in which two electrical carriers neutralize each other, is known as **recombination**.

Remark 8.1.1. *In a recombination, the recolliding wave-package returns to the core emitting*

a photon of frequency I_p+K due to energy conservation law. Here I_p is the ionization potential of the atom and K is the kinetic energy of the electron at the recombination.

In the situation described in the previous paragraph, after the tunnel ionization, there is an ion (positive carrier) and an electron (negative carrier) that neutralize each other (recombine) as the electron is re-captured by the atom. Summarizing: It is common in the literature to describe recollisions as processes with three different stages:

1. Tunneling ionization,
2. motion under under Strong Field Approximation (SFA),
3. return to the core.

Yet, this is a simplified explanation that is able to capture some qualitative aspects of the phenomenon but fails to hit experimental data in several situations. It is still a valuable model to understand the mechanisms of recollision.

Recollision mechanisms are interesting because they help us in our understanding of atomic structure. The recombination after recollision is able to trigger remarkable phenomena such as break-up of atomic bounds and high-harmonic generation. For all these reasons recollision is sometimes refereed as the keystone of the strongfield physics.

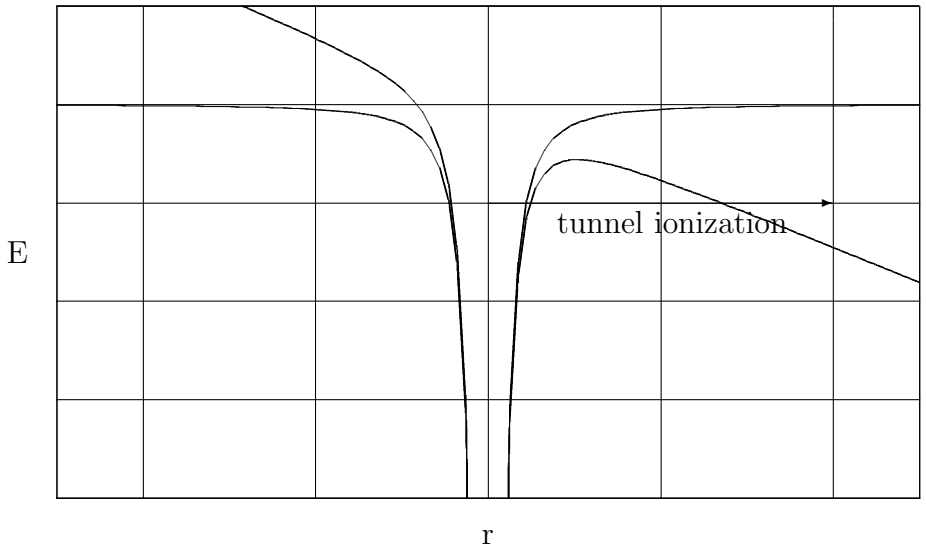

Figure 8.1: Quantum tunnel.

Remark 8.1.2. *High-harmonic generation is a process in which a target (let us think of an atom) receives the impact of a laser with some frequency ω. After the recombination, the atom emits a photon of frequency $n\omega$ for some integer n.*

The three step scenario described above is semi-classical in the sense that it requires tunneling ionization and classical motion in the SFA. Recall that, in the SFA, one neglects the Coulomb interaction between the ion and the electron. If we allow the motion of the electron to take place in a $1D$ space, the dynamics of such electron is given by the Hamiltonian function

$$H(x, p_x.t) = \frac{p_x^2}{2} + E_0 x \cos(\theta), \tag{8.1}$$

where $\theta = \omega t + \varphi$, ω is the frequency of the lased field, φ its initial phase and E_0 its amplitude. As the laser acts along the $\{y = 0\}$, the x-direction is called **polarization direction**. The lased field is modeled by a simple periodic function as a first approach. However, there are more complicated models in the literature that consider some envelope to the laser or taking into account the magnetic effects. Solutions of system (8.1) can be explicitly found in a closed formula:

$$x(t) = x_0 - \frac{E_0}{\omega^2}\cos\varphi + \left(p_{x,0} + \frac{E_0}{\omega}\sin\varphi\right)t + \frac{E_0}{\omega^2}\cos(\omega t + \varphi).$$

An electron that moves according this set of solutions tends to return to its parent ion due to the periodic term while it is pushed away by the secular term, the so-called **momentum drift**. This combination leads to a perfect setting for recolliding trajectories to occur. The success of the SFA model is ascribed to the determination of the cut-off energy in the High Harmonic Generation (see [KSK92, MKG93, AD08]) spectra based on the calculation of the maximum kinetic energy (varying the initial phase and the return in time) an electron can bring back to the core:

$$\max_t = \frac{p_x^2(t)}{2} = 3.17 U_p.$$

Obviously such a simple model neglects a lot of relevant effects, in particular, the Coulomb interaction [YI01]. Coulomb interactions make its presence known in many phenomena. If we add the soft Coulomb potential, the motion of the electron is described by the Hamiltonian

$$H(x, p_x, \theta) = \frac{p_x^2}{2} - \frac{1}{\sqrt{x^2+1}} + E_0 x \cos\theta.$$

Here the picture is much more interesting. The behaviour of the system displays a (well understood) recollision mechanism that shall be explained in full detail in Section8.2. It is no so clear what happens in the spatial case:

$$H(x, y, z, p_x, p_y, p_z\theta) = \frac{1}{2}\left(p_x^2 + p_y^2 + p_z^2\right) - \frac{1}{\sqrt{x^2+y^2+z^2+1}} + E_0 x \cos\theta. \tag{8.2}$$

In both cases, the model to be used is a Hamiltonian systems with periodic time dependence and can be handled by means of the stroboscopic map.

8.1.1 A definition of recolliding trajectory

To make clear the quantities we are going to measure in the numerical simulations performed in this chapter, we provide, in the following lines, some mathematically rigorous definitions. These should be taken not as a substitute of the physical concepts which are handled in the literature but as an agreement of the observables used in this work to study the phenomenon of recollisions from a dynamical systems point of view.

Let us consider the evolutive process associated to the system induced by the Hamiltonian (8.2). This flow has $\mathbb{R}^6 \times \mathbb{R}$ as phase space. Call the subspace spanned by the position variables the **configuration space**. The intuitive definition of recollision we give in the previous section depends on the size of the atomic core. That is, assuming the atom to be placed at the origin, the distance to it for which we consider an electron to collide with the core, depends on the atom. Therefore, a rigorous definition of recollision should depend on the atom.

Definition 8.1.3 (Recolliding trajectory)**.** *Consider the Hamiltonian system given by (8.2). Let $r > 0$ be a real number and $B_r(0)$ a closed ball centred at the origin of the configuration space. A trajectory $\phi \in \mathcal{C}^\omega(\mathbb{R}, \mathbb{R}^6)$ of the system is said to be r-recolliding if there exist three real numbers $t_0 < t_1 < t_2$ such that $\phi(t_0), \phi(t_2) \in B_r(0)$ and $\phi(t_1) \notin B_r(0)$.*

A trajectory for which exist $t_0 \leq t_1$ with $\phi(t_0) \in B_r(0)$ and $\phi(t_1) \notin B_r$ is said to be an **ionizing trajectory**. If, for $j \geq 1$, there exist a set $\{t_l\}_{l=0}^{2j+1}$ such that $t_l \in B_0$ for l even and $t_l \notin B_0$ if l is odd, then we say that the trajectory ϕ displays a recollision chain of order $k = 2j + 1$. The time $t = t_k$ is called **ionization delay**. If $k = \infty$, we say that the orbit ϕ is **perfectly recolliding**. These definitions can be translated to the trajectories of the stroboscopic map.

8.2 One dimensional configuration space

This section is a summary of some known facts of the situation when the electron is allowed to move in a one dimensional space. Let us recall that the one-dimensional case is described by the Hamiltonian function

$$H(x, p_x, \theta) = \frac{p_x^2}{2} - \frac{1}{\sqrt{x^2 + 1}} + E_0 x \cos\theta. \tag{8.3}$$

From now on and until the rest of the chapter, we assume $\varphi = 0$.

8.2.1 Global aspects of the phase space

Let us fix $E_0 = 0$. The electron is only affected by the Coulomb potential and the system is integrable. The origin, an elliptic equilibrium point, is surrounded by periodic orbits, if an electron starts its motion far enough from the origin is not captured, so it escapes. As we turn the laser on ($E_0 > 0$) the system loss its integrability as gains half a degree of freedom. Notice that, for x small enough, the system is close to integrable. As the phase space is periodically perturbed, the periodic orbits gain, generically, the frequency of the perturbation. In this case, the equilibrium at the origin is replaced by a periodic orbit and most of the periodic orbit in the non-linear centre become two-dimensional invariant tori. As in any time periodic system, the dynamics can be studied by using the stroboscopic map. In this case, the mapping at period is an Area Preserving Map. If E_0 is small most of the region near the origin is occupied by invariant curves. An increment of the laser energy leads to the progressive destruction of invariant curves according to the Diophantine condition satisfied by their frequencies. The destruction of invariant curves is caused by the birth of hyperbolic periodic orbits. The invariant manifolds of these periodic orbits intersect transversely and the phenomena known as heteroclinic tangle occurs. The intersection between stable and unstable manifolds lead to small chaotic regions that tend to grow as E_0 increases.

As the splitting of the manifolds grow with the energy of the laser, chaotic regions start to be noticeable and relevant. The dynamics becomes a synthesis between quasi-periodic and chaotic behaviour. If in the integrable case there is no place for recolliding trajectories, the effect of the laser opens a new perspective on the possibility of such trajectories to appear.

In [NCUW15] the authors suggest a relation between ionization probability and the size of the chaotic region. To do so, they compute the probability of recollision with respect to the laser energy. They also estimate the size of the chaotic region around the core. The simulations show that the size of the chaotic layers change with respect to E_0 similarly to the way recollision probability does it. This suggest a strong relation between chaotic and recolliding orbits. In [MKCU12] this relation and some key ideas are also discussed. The conclusion is that the number of recollisions has a strong sensitivity on initial conditions. Other observables that are also sensible to initial conditions can be used to get some insight on the dynamical mechanisms that drive recollisions. In this chapter we use the final distance to the core after an integration of some laser cycles as this, in practice, provides cleaner plots-

Depending on the radius of the atom selected to decide whether a trajectory is recolliding or not, the chaotic region should provide sets with many recolliding trajectories. Indeed, if the core intersects with the chaotic zone (and the second is not strictly contained in the first), the transitivity of the chaotic trajectories shall enter and leave the core infinitely many times, in other words, those trajectories would be perfectly recolliding. Obviously, any invariant curve whose trace enters and leave the atomic core is also a perfectly recolliding trajectory.

However, this scenario supposes the energy to be sufficiently large and the core to be small. For realistic values of r and E_0, the chaotic zone is contained inside the core, therefore none of the chaotic trajectories is recolliding. This should not discard a positive correlation between chaos and a high number of recolliding trajectories as we will see later. A typical situation for realistic values of the parameters is the one shown in Figure 8.2. There, the energy is not large enough to produce relevant chaotic zones. Mechanisms of recollision, in which the trajectories go far away from the core, seem to be more interesting from the physical point of view.

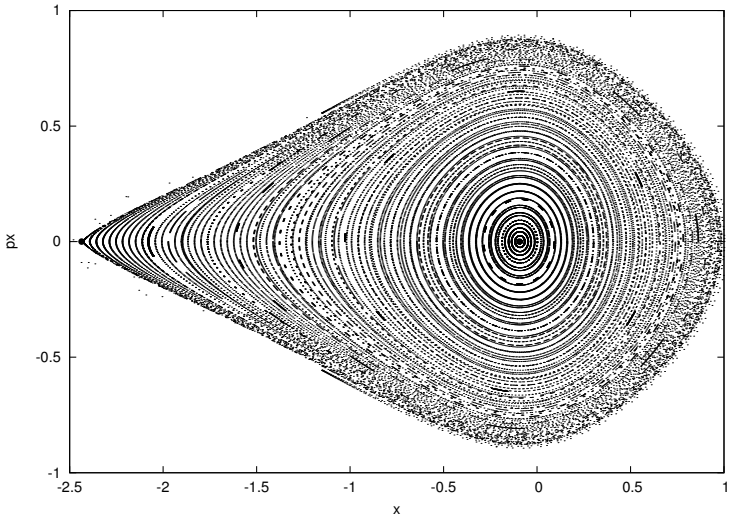

Figure 8.2: Phase portrait of Hamiltonian 8.3. The black bullets indicate the periodic orbit at the origin and $\mathcal{O}_2$.

8.2.2 The classical recollision scenario

The goal is to describe how the skeleton of the dynamical system drives the recolliding trajectories. Before performing a methodological study of the invariant objects of the system, we start with a rather simple simulation. We take a dense grid of initial conditions in the (x, p_x) plane. For each initial condition, we integrate the flow 10 laser cycles. For each trajectory, we count the number of recollisions, and the ionization delay (the last time the particle leaves the core), and the final distance to the core. The radius considered to count collisions and ionizations is $r = 5$. The color pattern of Figure 8.4 display the final distance for a grid of initial conditions in (x, p_x) in log-scale and a very an intricate pattern can be

observed. We do not show the plots for the other two observables because the patterns obtained with the number of recollisions and the ionization delay are very similar but not so clean. The three indicators we have chosen are sensitive with respect to the initial conditions, therefore this first simulation shows some correlation between chaotic motion and recollisions.

The next task is to identify the invariant objects that are responsible from the observed patterns. The simplest invariant objects in Hamiltonian (8.3) are periodic orbits with period which is a multiple of the one of the laser. These orbits appear as periodic points of the stroboscopic map. Most of these orbits can be continued from trajectories of the integrable system that are in resonance with the exciting frequency. In the literature, two periodic orbits are observed to play a fundamental role in the recollision scenario. The first one, call it $\mathcal{O}_1$, is obtained from a perfectly recolliding orbit in the SFA model, see panel (a) in Figure 8.3. The initial guess to refine orbit $\mathcal{O}_1$ is $(x_0, 0)$ where $x_0 = E_0\omega^{-2}$. This orbit is centred at the origin ans it is hyperbolic. The unstable eigenvalues is about 2.3 atomic units, therefore it is slightly unstable. Stress that orbit $\mathcal{O}_1$ is a perfectly recolliding orbit itself: During time, the trajectory enters and leave the core infinitely many times. By continuity of the flow with respect to the initial conditions, orbits near $\mathcal{O}_1$ tend to mimic its trace while escaping along the unstable direction. The fact that hyperbolicity of $\mathcal{O}_1$ is not large plays also an important role as trajectories take relatively long times to escape following the unstable manifold. The Recolliding Periodic Orbits are called, for shortness, RPO. In the literature, this kind of orbits, especially $\mathcal{O}_1$, has been seen as the most appealing objects from which ensemble a dynamical explanation of recolliding trajectories.

The second interesting orbit we will study, $\mathcal{O}_2$ is also centred at the origin, see panel (b) in Figure 8.3. Unlike $\mathcal{O}_1$, the trace of $\mathcal{O}_2$ does not go far from the core and it cannot be considered a RPO. The linear behaviour of $\mathcal{O}_2$ is also hyperbolic but the unstable eigenvalue is slightly larger, about 7.7 atomic units. Notice also that, in one limit cycle, the periodic orbit does many turns around the origin. This is significant because a nearby orbit mimicking the trace of $\mathcal{O}_2$ but escaping through the unstable direction may recollide a lot of times but with a lower kinetic energy.

To have a better understanding on how periodic orbits $\mathcal{O}_1$ and $\mathcal{O}_2$ drive the recolliding trajectories of the system, we return to the stroboscopic map. The invariant manifolds of $\mathcal{O}_1$ and $\mathcal{O}_2$, fixed points under the dynamics of the stroboscopic map, are the key ingredient for the recollision scenario. The coordinates of $\mathcal{O}_1$ are shown in Figure 8.4 with a black cross, while the coordinates of $\mathcal{O}_2$ are shown with a golden cross.

In Figure 8.4 we also show the stable and unstable manifolds related to both, $\mathcal{O}_1$ and $\mathcal{O}_2$, in the stroboscopic map. The first thing to notice is that these manifolds resemble the colored pattern given by the final distance to the core. The stable manifold of $\mathcal{O}_1$ and the stable manifold of $\mathcal{O}_2$ are close to each other and contribute to form the pattern. Both manifolds take long excursions away from the core while they keep returning to wander around the

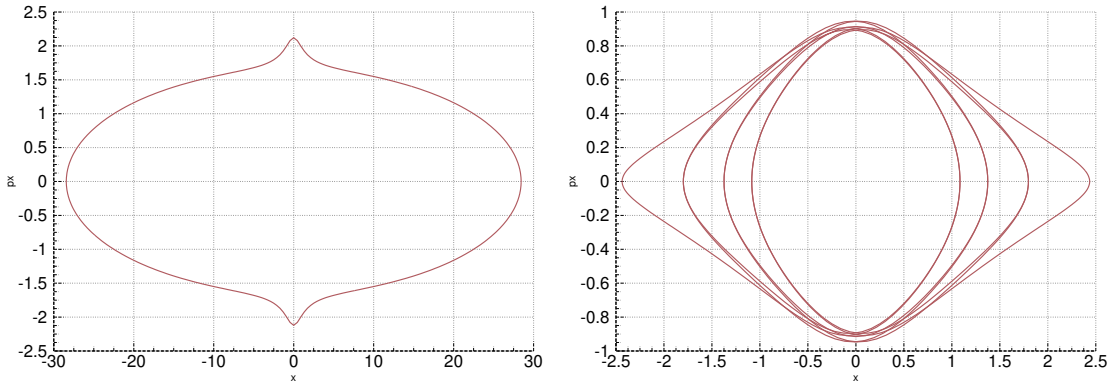

(a) (b)

Figure 8.3: **(a):** Trace of $\mathcal{O}_1$. **(b):** Trace of $\mathcal{O}_2$. Horizontal axis: x. Vertical axis y.

quasi-periodic region for long times. It is clear why orbits shadowing these stable invariant manifolds are driven to recollision. It is remarkable that the unstable (light grey) and stable (green) manifolds of $\mathcal{O}_2$ split infinitely many times in a homoclinic tangle which is observed without putting any effort. The influence of this tangle in the dynamics is noticeable since it brings a notable amount of chaotic behavior, a necessary condition for a likely recollision picture.

A dynamical description of the mechanism

Let us give an accurate description of the main ingredients playing a role in the recollision mechanism from the dynamical systems point of view. For realistic values of the parameters, the system is not so far from integrable near the core and most of the quasi-periodic motion near the atomic nucleus persists. However, far enough from the core, the splitting of separatrices associated to the stable and unstable manifolds of $\mathcal{O}_2$ (and $\mathcal{O}_1$) is large. By large we mean noticeable and detectable with the standard double precision. The complicated patterns displayed by the tangle is an essential ingredient for the scenario. Indeed, the invariant manifolds of $\mathcal{O}_1$ and $\mathcal{O}_2$ go away from the core and return back as they form the heteroclinic tangle. Notice, in Figure 8.4 how these invariant manifolds enclose regions with positive Lebesgue measure of the phase space are driven to follow the intricate pattern of the manifolds and, hence, recolliding many times as well. Notice that the dimensions of the objects are crucial here. We need the enclosed regions of the phase space that are driven by the manifolds to be of positive Lebesgue measure in order to get a relevant mechanism.

One last thing to be pointed out is that there is no way to decide which one is the periodic

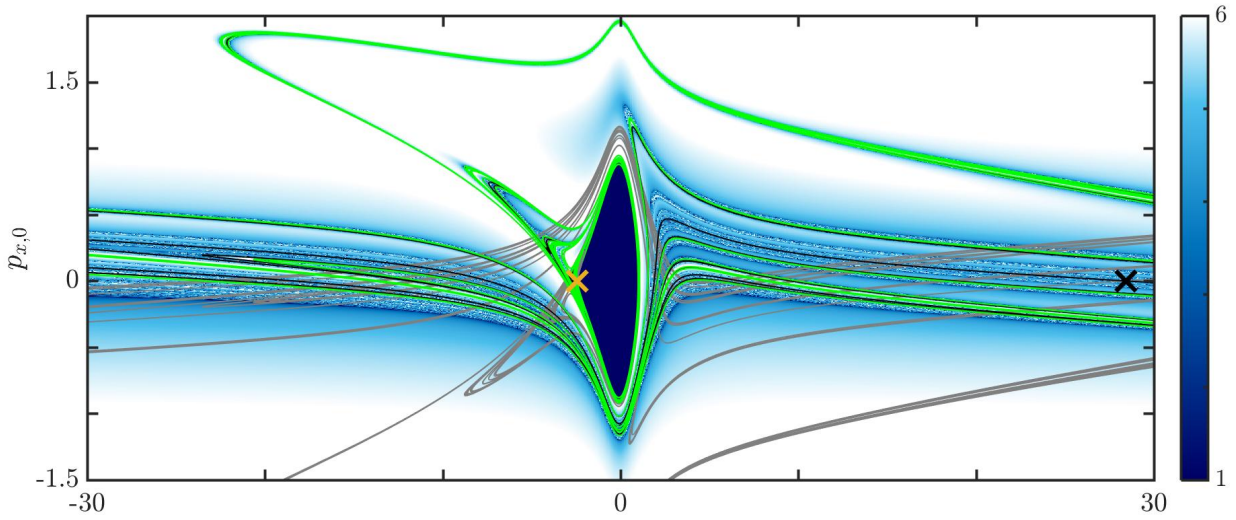

Figure 8.4: The color pattern shows the final distance to the ionic core for each initial condition after 100 periods of the laser. We also show the stable manifold (green) of $\mathcal{O}_2$, the unstable manifold (black) of $\mathcal{O}_1$, the unstable manifold of $\mathcal{O}_2$ (light grey) and the stable manifold (dark gray) of $\mathcal{O}_1$.

orbit that drives the recollisions. They both do it. However, as $\mathcal{O}_1$ is a recolliding orbit itself, it has received much more attention in the literature.

8.3 Higher dimensional configuration space

In this section we take an effort to study how the recollision scenario in the one-dimensional configuration space generalizes to the two dimensional configuration space.

Let us be a bit more precise on what do we mean by using the word "generalization". The dynamical mechanism leading to recollisions explained in the last chapter depends on the linear character of some periodic orbits and the dimensionality. That is, there are two hyperbolic periodic orbits whose invariant manifolds separate the phase space. The complicated trace displayed by the manifold encloses many initial conditions (regions of positive Lebesgue measure) and tends to move away from the core and return back. The initial conditions which are enclosed by the intricate pattern of the manifold are forced to recollide inevitably. To apply the previous argument to the two-dimensional configuration space, we need an invariant manifold of codimension one with respect to the (four dimensional) phase space. This,

obviously, discards one unstable/stable invariant manifolds related to fixed point. Therefore, one must ask which kind of object is the one taking the role of the one-dimensional invariant manifolds. To address this question we have to seek for and invariant object (of the right dimension, 3) leading to many recolliding trajectories. This is, then, the sense we give to the word generalization in this chapter.

We focus, until the end of the chapter, in the system induced by the Hamiltonian function

$$H(x, y, p_x, p_y, \theta) = \frac{p_x^2 + p_y^2}{2} - \frac{1}{\sqrt{x^2 + y^2 + 1}} + E_0 \cos\theta.$$

Recall that we have introduced the angular coordinate $\theta = \omega t + \varphi$. The first thing to be pointed out about this system is that the subspace $\mathcal{I} = \{y = 0, p_y = 0\}$ is invariant under the dynamics. Hence, the recollision picture explained in the preceding section for the one-dimensional case is still valid in this particular invariant subspace. Anyhow, there are interesting questions to address: Is there any other recolliding scenario holding out of the invariant subspace $\mathcal{I}$? Are $\mathcal{O}_1$ and $\mathcal{O}_2$ the periodic orbits that drive that particular scenario? Let us take a look to a general picture of the phase space under the dynamics of the stroboscopic map. When the transverse direction is considered, the fixed point at the origin remains totally elliptic. This guarantees a whole region of $(2D)$ invariant tori carrying quasi-periodic motion near the origin. This is to be expected and those trajectories represent the motion of electrons trapped in the core. Unlike in the one-dimensional space, this region is no longer stable in the strong sense of Lyapunov. Arnold diffusion is expected to happen and this could lead to electrons ionizing and recolliding. This process of diffusion is too slow to be interesting for realistic purposes. Indeed, the experiments do not take more than a few laser cycles. Therefore, despite Arnold diffusion is interesting from a theoretical point of view and in other applications, it should be discarded here as a relevant mechanism leading to recollisions. In fact, while the quasi-periodic region is not stable and the maximal invariant tori do not separate the phase space, it is effectively stable. The tori are sticky and trajectories nearby take a long time to depart from the proximity of them. Therefore, we have to look for candidates out of this region of quasi-periodic motion. The obvious ones are $\mathcal{O}_1$ and $\mathcal{O}_2$. These, we remember, are hyperbolic orbits in the direction of the polarization and, along the transverse direction $\mathcal{O}_1$ is also hyperbolic while $\mathcal{O}_2$ is elliptic.

The fate of $\mathcal{O}_1$

Let us focus first in $\mathcal{O}_1$, the RPO that has received more attention in the literature. Once the transversal direction is considered, $\mathcal{O}_1$ becomes a saddle×saddle fixed point of the stroboscopic map. Eigenvalues of the monodromy matrix are displayed in Table 8.1.

Because there are two unstable eigenvalues, the unstable invariant manifold is two dimensional, see Figure 8.5. Notice the size of λ_1 and λ_2 in Table 8.1. There is a strong

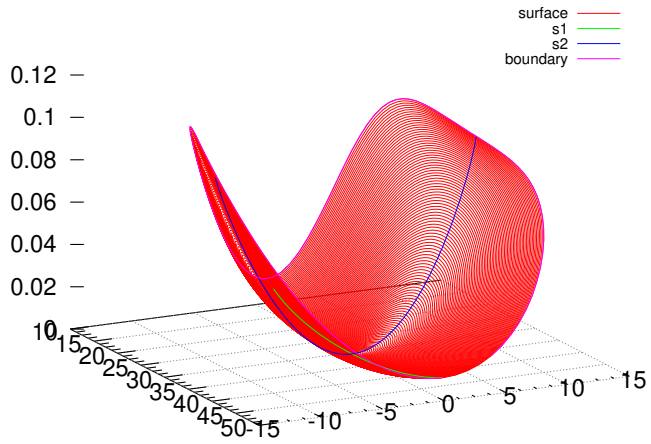

Figure 8.5: Unstable manifold of $\mathcal{O}_1$. We display the x and y coordinates at the basis. The vertical direction is the kinetic energy: $\frac{1}{2}\left(p_x^2 + p_y^2\right)$.

λ_1	λ_1^{-1}	λ_2	λ_2^{-1}
2.192456350299	0.4561094225951	1059.89237974	0.0009434920178

Table 8.1: Eigenvalues related to the orbit $\mathcal{O}_1$. The orbit is regarded as a fixed point of the stroboscopic map and, hence, the eigenvalues are computed for the differential of such map.

unstable direction and a weak unstable direction. The weak one is the direction contained in the invariant subspace, the one whose related invariant manifold drive most of the recolliding orbits in the $1D$ case. The strongly unstable direction appears as cause of adding the transversal (to the polarization laser) direction. Therefore, the dynamics near the periodic orbit $\mathcal{O}_1$ is dominated by the strongly unstable direction which is transversal to $\mathcal{I}$. Because of the magnitude of the strong eigenvalue, most of the trajectories nearby the fixed point get expelled away from the atom and do not return back, at least, in a few laser cycles. It is possible, however to find thin strips close to the invariant subspace $\mathcal{I}$ with a lot of recolliding trajectories. This can be done in the following way: Let

$$W : \Lambda_1 \times \Lambda_2 \mapsto \mathbb{R}^4,$$

(with Λ_1 and Λ_2 intervals containing the origin) a parameterization of the unstable invariant manifold related to $\mathcal{O}_1$. This parameterization verifies the following invariance equation:

$$f(W(s_1, s_2)) = W(\lambda_1 s_1, \lambda_2 s_2).$$

Then, choosing the value of s_2 sufficiently small, the strong unstable manifold needs many iterates to dominate the motion of this particular initial condition. Moving s_1 we will obtain a curve on the two dimensional unstable invariant manifold that moves close to the invariant subspace $\mathcal{I}$. Moreover, it is mimicking the intersection of the two dimensional invariant manifold with the subspace $\mathcal{I}$. This intersection turns to be the unstable manifold associated to λ_1 and, as we showed in the previous section, leads to many recolliding trajectories.

This inherit mechanism of recollision is not satisfactory at all. In the first place, the stark difference between the magnitudes of the eigenvalues will cause the strips to be very thin and the electron to go away from the invariant subspace rapidly. The strong unstable direction is attracting when the motion is restricted to the two dimensional manifold. Moreover, the codimension of the unstable manifold is two. This means that it does not separate the phase space, as it happened in the one-dimensional case. This does not make these recolliding trajectories invalid but less relevant from the physical point of view. Therefore, $\mathcal{O}_1$ which is the key periodic orbit in the one-dimensional case becomes less relevant when the transversal direction is considered. Notice that this already answers one of the questions we wanted to address in this chapter. The recollision mechanism holding in the one-dimensional case still exists in the two-dimensional case but it is not as relevant because of it drives a not significant amount of initial conditions to recollision.

The fate of $\mathcal{O}_2$: A new recollision scenario

The periodic orbit $\mathcal{O}_2$ has stability character of type saddle$\times$centre. The hyperbolic direction is contained in the invariant subspace $\mathcal{I}$ and it has been studied in the previous section, when dealing with the one-dimensional case. The elliptic direction is transversal to the polarization of the laser. In Table 8.2 we display the eigenvalues related to the orbit $\mathcal{O}_2$ regarded as a fixed point of the stroboscopic map. From the elliptic direction it grows a family of invariant

λ_1	λ_1^{-1}	$\mathrm{re}(\lambda_2)$	$\mathrm{im}(\lambda_2^{-1})$
7.746266605845e+00	1.290944465099e-01	2.190712620606e-01	9.757088613613e-01

Table 8.2: Eigenvalues related to the orbit $\mathcal{O}_2$. The orbit is regarded as a fixed point of the stroboscopic map and, hence, the eigenvalues are computed for the differential of such map.

curves parametrized by the frequency ν. The family collapses into $\mathcal{O}_2$ as the frequency tends to the natural frequency of the fixed point. In Figure 8.6 we display the continuation curve from the fixed point. Each invariant curve is identified by its y-value when the angular

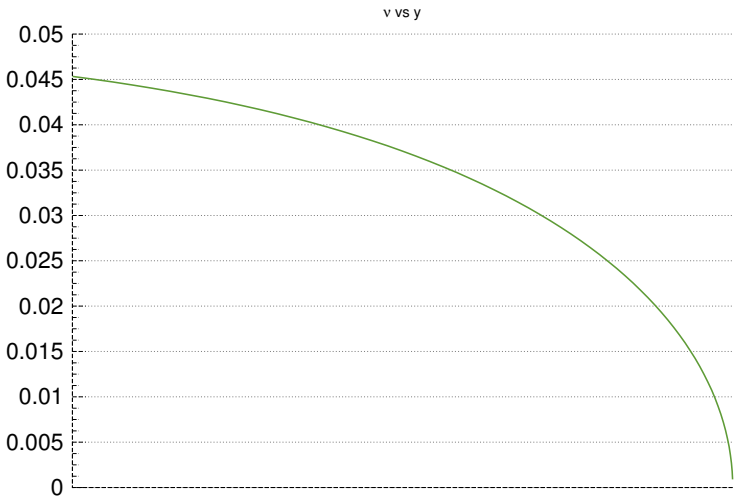

Figure 8.6: Invariant curves on the centre manifold of $\mathcal{O}_2$. Horizontal axis: ν. Vertical axis: y.

variable is set to zero. For this value of the angle, the x coordinate of the invariant curve is fixed at the x-coordinate of $\mathcal{O}_2$ as the extra condition to overcome the lack of uniqueness of the Fourier representation for invariant curves of autonomous skew-products.

The continuation is stopped when the truncation order of the Fourier series used to describe the curves reaches the value $N = 100$. The numerical evidences suggest that the family of invariant curves does not live on much further.

The family of invariant curves is displayed in Figure 8.7. Several projections are shown in the different panels. Let us start describing panel (a), the x vs y projection. The invariant curves grow towards the origin along the horizontal axis. In the vertical one, the family achieves its maximal amplitude fastly. As the family grows to its end, the invariant curves look more tilted towards the origin. The panel (b) corresponds to the projection on the invariant subspace $\mathcal{I}$. There is not much to say besides the invariant curves look close to circles extending around the origin. The panel (c), in which we display the projection of the family into (y, p_y), looks very similar to panel (a) so we do not describe it again. Finally, in panel (d), we observe the projection on the (y, p_y) plane. In this case it can be observed that the family grows in the y direction (starting from zero) as the maximal value of p_x increases. Notice that, in all the invariant curves of the family, the kinetic energy is small.

The family of invariant curves described in the previous paragraph is the centre manifold attached to $\mathcal{O}_2$. All the curves of the family have the same linear character as the fixed point

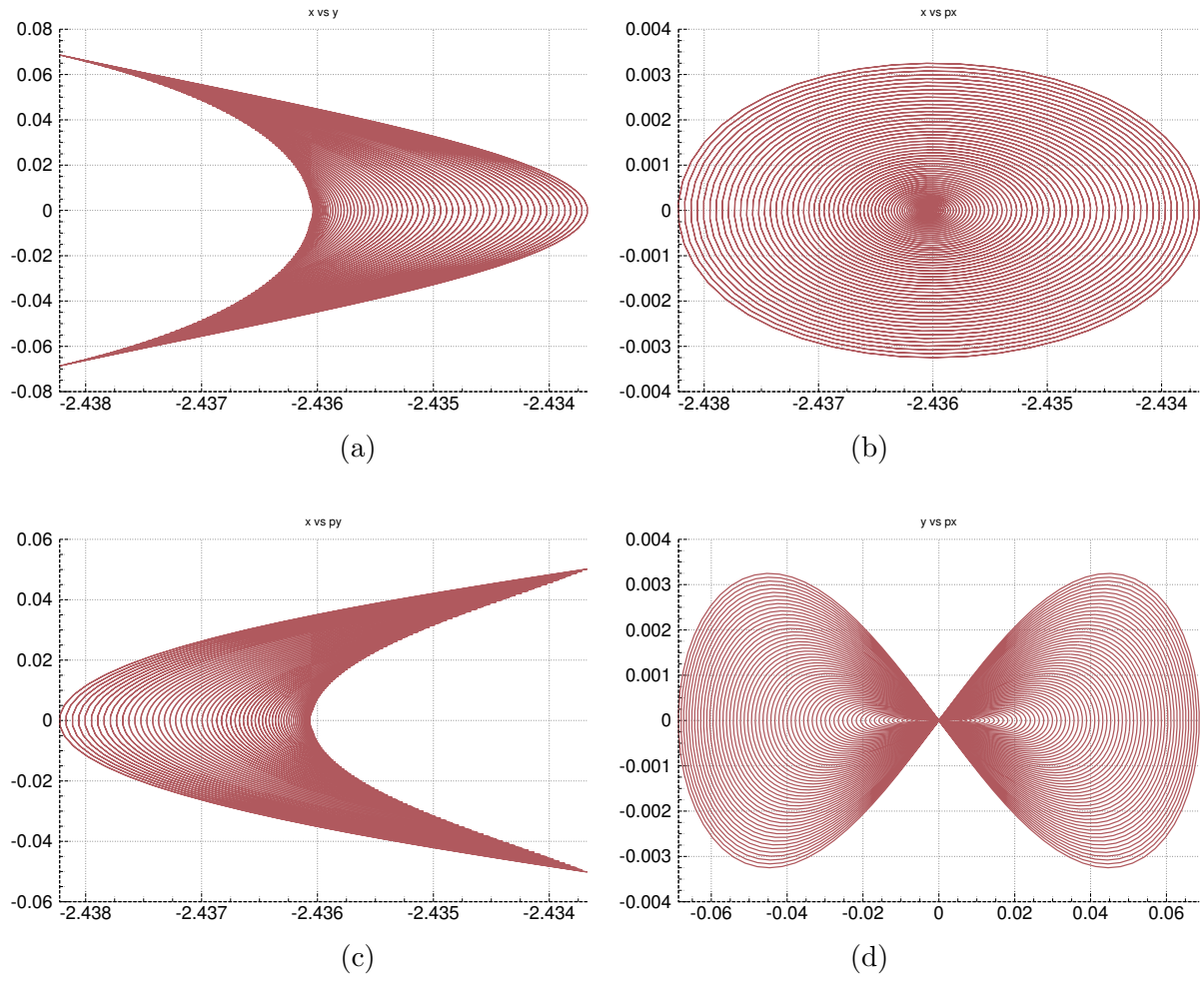

Figure 8.7: Centre manifold related to $\mathcal{O}_2$. We display several projections. **(a):** x vs y. **(b):** x vs p_x. **(c):** x vs p_y. **(d):** y vs p_x.

i.e. they have a hyperbolic direction. This means there are stable and unstable invariant manifolds departing from each curve. The union of the invariant curves and their unstable manifolds conform the centre-stable manifold and the centre-unstable manifold of $\mathcal{O}_2$. Pieces of the centre-stable manifold (green) and centre-unstable manifold (red) are depicted in Figure 8.8. This Figure is obtained from iterating a suitable grid from the linear approximation of the invariant manifolds obtained by computing the corresponding eigenfunctions related to each invariant curve as explained in Chapter 3. The centre-stable manifold, stands out as the best candidate to drive generic recolliding trajectories for initial data out of the invariant

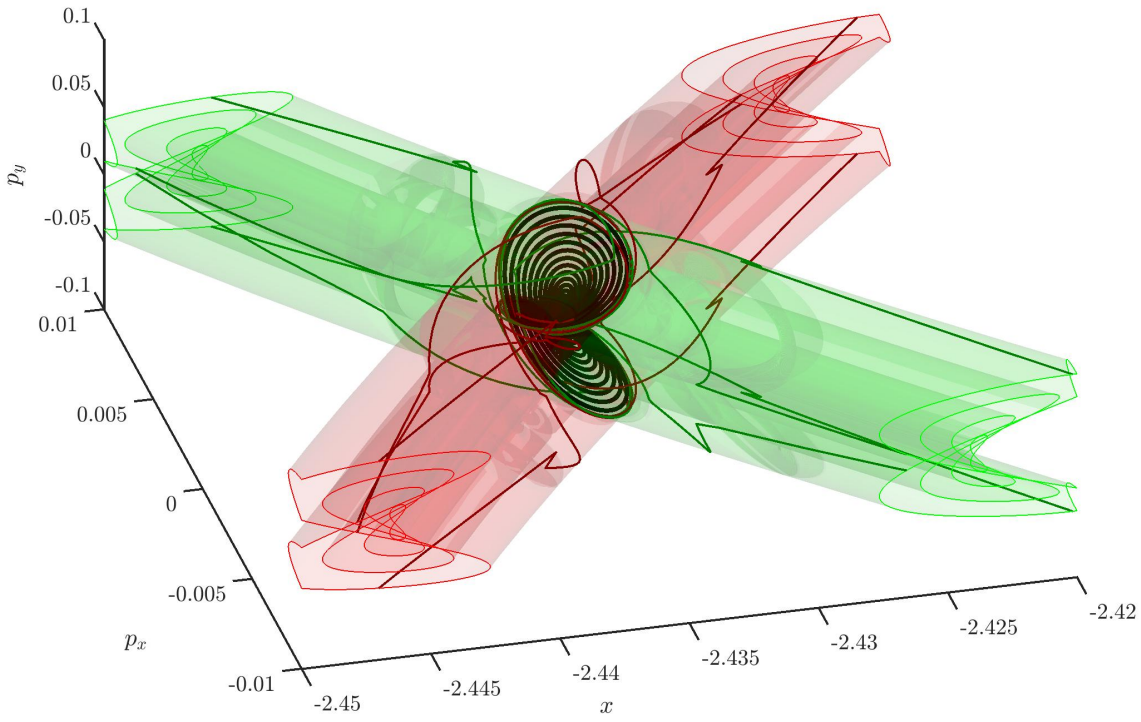

Figure 8.8: Pieces of the centre-unstable manifold (red) and the centre-stable manifold (green) related to $\mathcal{O}_2$. The black curves are some invariant curves in the centre manifold, see Figure 8.7. The dark colored curves are paths contained in the centre-unstable manifold (red) and contained in the centre-stable manifold (green).

subspace $\mathcal{I}$. Indeed, in first place it has codimension one, therefore intersects the configuration space in a curve, a picture very similar to the one obtained in the one dimensional case. The color pattern appearing in Figure 8.9 is given also by the final distance, in log-scale, to the core after an integration of 10 periods of the laser. In this case, the grid of initial conditions is taken in the plane $\{y = p_x = 0\}$. The black dots are points of the intersection between the centre-stable manifold of O_2 and the plane $\{y = p_x = 0\}$. The intersection fits the colored pattern.

We also measure the role the centre-unstable manifold in the new recollision scenario, we

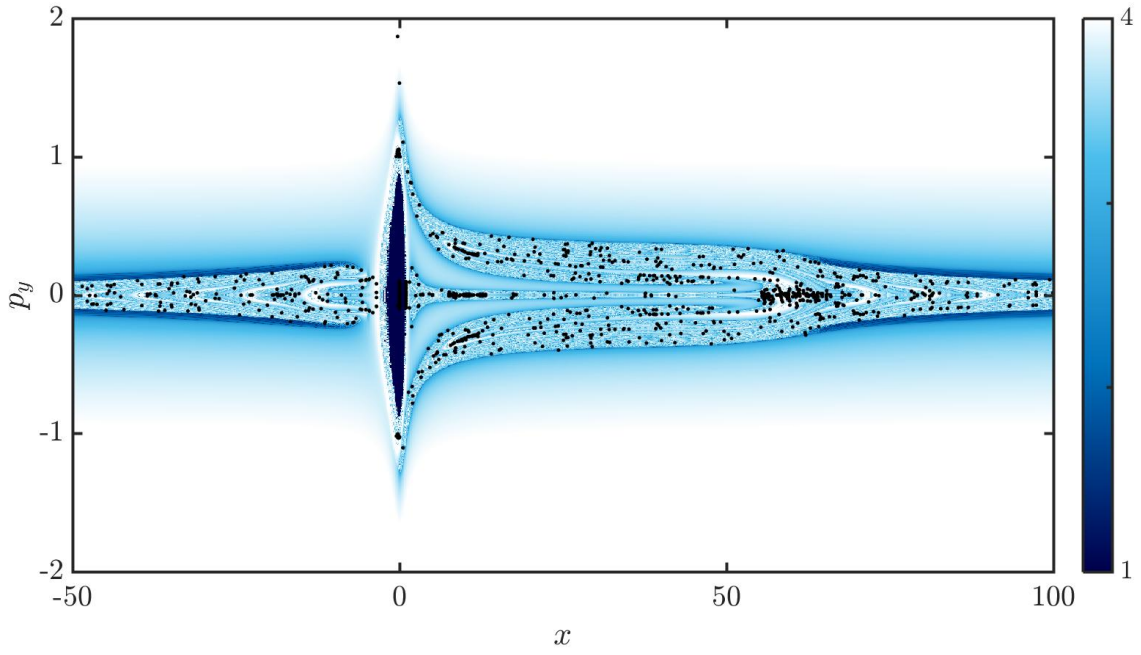

Figure 8.9: The color pattern shows the final distance to the ionic core for each initial condition after 10 periods of the laser. The black dots show the intersection of the centre-stable manifold related to $\mathcal{O}_2$ with the plane $\{y = 0, p_x = 0\}$.

perform the following experiment: For each point of a grid in the centre-unstable manifold we integrate 10 laser cycles. At each step of integration we check out whether the trajectory is inside or outside the atomic core (determined by a ball of radius $r = 5$ centred at the origin). Each time the trajectory enters to the core we count it as a recollision. Obviously the same orbit can have multiple recollisions, what we call a recolliding chain. After the orbit reaches ten laser cycles, we print, in a file, the initial data, the number of recollisions and some control quantifiers. In Figure 8.10 we display the results of this simulation. The different panels stand for the different projections: (a): x vs y, (b): x vs p_x, (c): x vs p_y, (d): y vs p_x. Notice that most of points are black, this means that the initial condition recollides once and ionizes. Largest degree of recollision chains is 7. The circles denote recolliding orbits of degree 4 or larger. Notice that while the recolliding chains appear, more or less, in all the grid, they are more dense close to the fixed point $\mathcal{O}_2$. We also would like to stress that only about the 50% the initial conditions, the ones being closer to the fixed point, recollide.

A typical recolliding trajectory with initial condition in the centre-unstable manifold

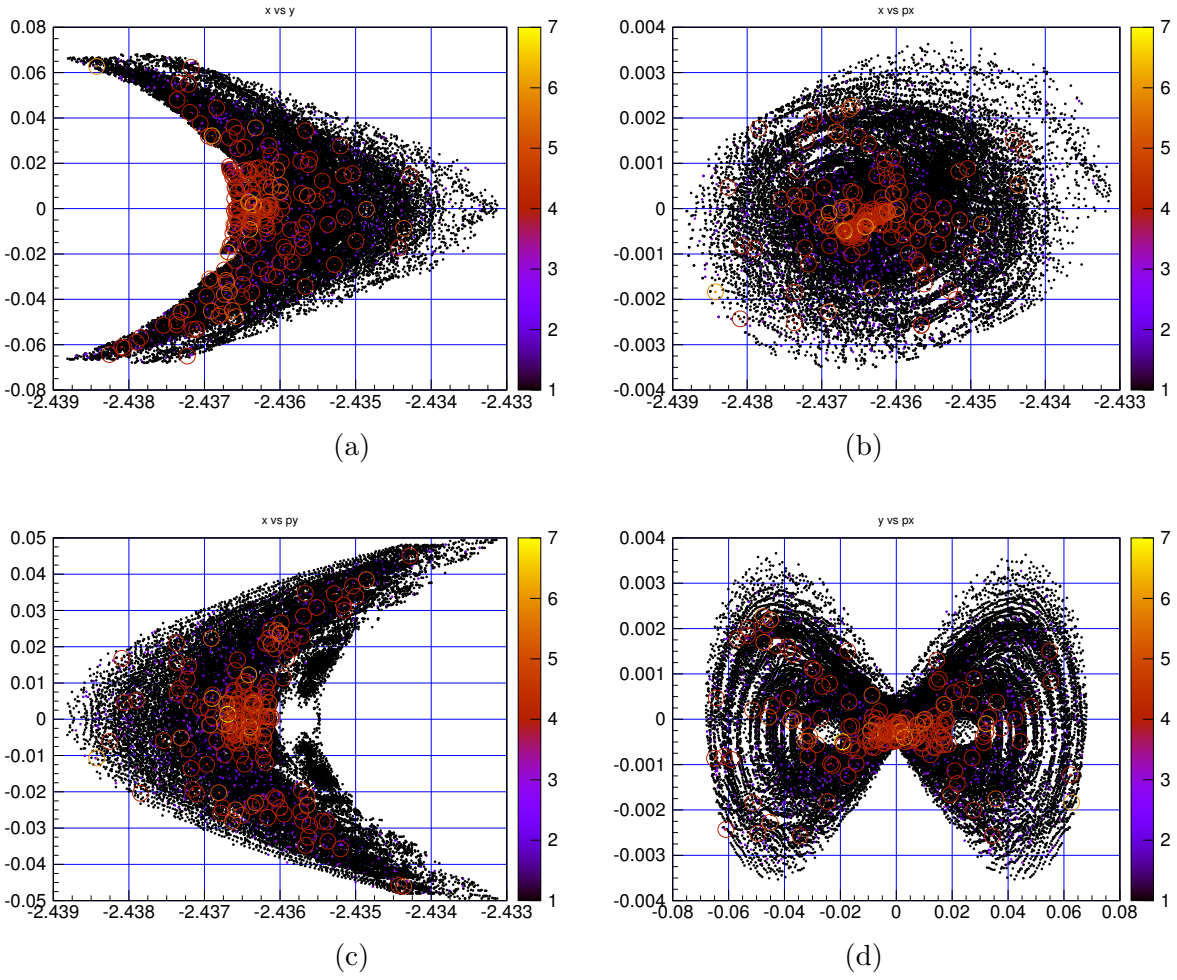

Figure 8.10: Recolliding initial conditions for the grid displayed in Figure 8.8. The color displays the number of recollisions found in 10 laser cycles. The circles show the initial conditions displaying a recollision chain of degree 4 or larger. We show several projections. **(a):** x vs y. **(b):** x vs p_x. **(c):** x vs p_y. **(d):** y vs p_x.

behaves in the following way: First it wanders around the core, shadowing the quasi-periodic trajectories on the centre manifold. As the times goes on, the trajectory detaches from the centre manifold and takes a long excursion away from the core. Then, it returns back to the core with an incremented kinetic energy, this process may be repeated a number of times until a last ionization takes place. Stress again that we have only integrated the initial conditions for ten laser cycles. For larger times, most of the recolliding chains in Figure 8.10 increase

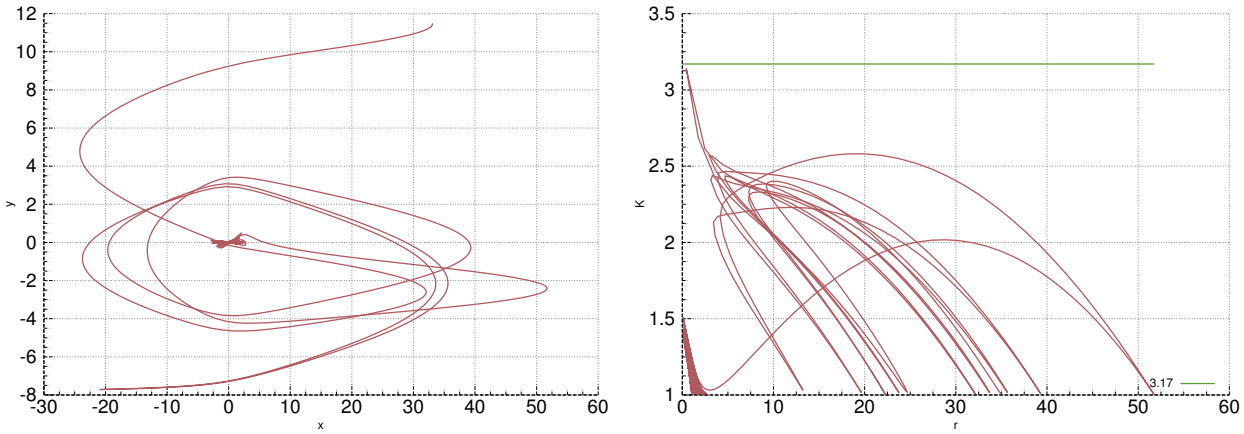

(a) (b)

Figure 8.11: Orbit displaying a recolliding chain of degree 5 for $r = 5$. **(a):** x vs y. **(b):** radius vs kinetic energy

their degree.

In Figure 8.11 we display a particular orbit undergoing a recolliding chain of degree 7. In panel (a) we show the projection on the (x, y) plane. It is interesting to see that the orbit goes far from the horizontal axis, at 8 atomic units before recolliding and ionizing for last time. Therefore, this particular recollision scenario is not close to the one known for the one-dimensional case, therefore it is a result of considering the transversal direction to the polarizing one. In panel (b) we display the radius of the trajectory (in the configuration space) against the kinetic energy. The trajectory recollides (in may times) with a larger kinetic energy than the one it has at the beginning, at the centre-unstable manifold. The green horizontal line corresponds to the value $3.17U_p$, being U_p the average kinetic energy of the electron in the lased field, the theoretical maximal kinetic energy an electron can bring back to the core. It is remarkable that, the trajectory almost reaches these value. Let us say that the maximal kinetic energy of the trajectory is achieved inside (for realistic values of the parameters) the core, at $r \approx 0.4$.

Let us compose a general picture of this new recollision scenario: We have collected numerical evidences that the centre-stable manifold of $\mathcal{O}_2$ displays a complicated pattern in the phase space. Notice that the intersection of the centre-stable manifold with the invariant subspace $\mathcal{I}$ is the invariant manifold in green appearing in Figure 8.4. Moreover the number of black points found in the grid of Figure 8.9 assures that the complicated behaviour extends on the whole phase space. The manifold has the correct dimension: It separates the phase

space, and hence, regions of initial conditions with positive measure are compelled to follow that patter for long periods. These initial conditions are driven to recollide with the atomic core.

Let us summarize the whole picture, explaining how the classical one dimensional scenario generalizes to the two dimensional one.

1. There are two periodic orbits, $\mathcal{O}_1$ and $\mathcal{O}_2$, in the invariant subspace $\mathcal{I}$ corresponding to the one dimensional configuration space. Their stable and unstable manifolds drive recolliding trajectories. Notice also stable manifold of $\mathcal{O}_2$ and the unstable manifold of $\mathcal{O}_1$ are very close to each other. Therefore, it is not possible to distinguish which one drives the recollisions.

2. The intersection of the centre-stable and centre-unstable manifolds of $\mathcal{O}_2$ with $\mathcal{I}$ recover the manifolds of $\mathcal{O}_2$ restricted to $\mathcal{I}$.

3. The initial conditions out of the invariant subspace corresponding to the one dimensional case are driven also by the center-stable manifold of $\mathcal{O}_2$. Therefore, the scenario of the center-stable manifold of $\mathcal{O}_2$ driving the recolliding trajectories is consistent in both the one dimensional and the two dimensional case.

4. Notice that the transversal direction to the $\mathcal{O}_1$ is strongly hyperbolic. Any electron close to $\mathcal{O}_1$ and out of the invariant subspace will be pushed away from the ionic core.

5. For an invariant object to drive a set of initial conditions with a positive Lebesgue measure, it has to be three-dimensional. Therefore, a totally hyperbolic periodic orbit cannot structure generic recollisions.

8.4 Some concluding remarks

In this chapter we have investigated the role of invariant manifolds in the physical process known as recollision. The main novelty is the mechanism discovered when the electron is allowed to move in the two dimensional space. While the guiding invariant manifolds in the one dimensional case are one dimensional, the ones presented in this chapter are three dimensional: They are the centre-stable and the centre-unstable manifolds of some periodic orbit of type centre×saddle. As far as we know, there is no mention in the literature about this mechanism of recollision. It is also relevant how this invariant manifold intersects with certain subspaces. Numerical evidences suggest that the patters drawn by recolliding initial conditions out of the invariant subspace $\mathcal{I}$ are recovered by the intersection of the centre-stable manifold of $\mathcal{O}_2$ with the corresponding subspace in which we take initial conditions.

However we are positive that, with more effort and time, we should come out with more solid numerical evidences of that fact. These ideas will be developed a little bit more in Chapter 9.

The model we have used has a very simple expression for the perturbing laser. More involved forms can be used to get more realistic approximations. In particular, there exist models in the literature in which the laser polarize both the x and the y directions. A natural question to answer in further works is how these more complicated models affect the recollision mechanism discovered here. Again, we shall be giving more details of that in Chapter 9, at this point we would like to remark that some partial results show that, in the case of the circularly polarized lased field, the recollision mechanism presented in this chapter still holds.

8.5 Technical details

In all the integrations, we have used a Taylor method with variable order and step-size. The demanded accuracy for the standard double precision has been 10^{-16}. We have used multiple accuracy in the computation of the two dimensional invariant manifold appearing in Figure 8.5. See Chapter 2 for more details. The computations in multiple accuracy have been done using the library MPFR. The LAPACK library has also been used for some computations related to linear algebra. The rest of the programs have been written by the authors in C and C++ languages from the scratch. Table 8.3 contains the values of the parameters used for the computations. To recover the numerical experiments performed in this chapter use these values for the vectorfield as well as the value $r = 5$ to consider a trajectory to be recolliding according to Definition 8.1.3.

ω	E_0	φ
5.84e-02	9.245687210802669e-02	0.

Table 8.3: Values of the parameters used in this chapter.

9

Conclusions and outlook

This thesis is a compendium of strategies to deal with periodic time dependent Hamiltonian systems and some specific problems that can be formulated in terms of those systems. The spirit of the dissertation is to highlight the computation and understanding of the skeleton of the dynamics i.e. the invariant objects and its usage on specific problems coming from applied sciences.

In order to deal with periodic time depending Hamiltonian systems, we have taken advantage on a methodology that has been developed worldwide, and especially in Barcelona, during the last decades. This methodology results from the interaction between theoretical arguments, numerical simulations and the modeling and study of, let us say, real life problems.

A large part of the work behind this dissertation is the development of specialized software. Some of those programs are not new (in the sense that other authors have implemented the same algorithm) but the design is.

Contributions and further work

The contents of this dissertation cover a variety of topics. While contents of **Part I** can be regarded as a toolbox to cope with problems arising in **Part II**, they represent a goal by itself.

Normal forms and Lie series method

In Chapter 1 we deal with the numerical implementation of the Lie series method for periodic time dependent Hamiltonian systems.

The software to compute normal forms (recall that we include centre manifolds there, thought centre manifold reduction is not properly a normal form) is, by far, the piece of software that has been taken more time to be developed. The main novelty of this software is its design, taking advantage on the public domain library FFTW3 to build an efficient arithmetic of Fourier series and, taking into account the computation times, the implementation has been successful. We have used this tool to compute the centre manifold related to the periodic orbit that replaces L_1 in the BCP. Stress that, by means of this tool, we have reduced a Hamiltonian of three and a half degrees of freedom to an Area Preserving Map (APM) catching relevant information about the dynamics such as the bifurcation giving rise to Halo orbits which, in the BCP, are not periodic but quasi-periodic with two basic frequencies.

The reduction to an APM has been only possible because we have chosen to kill time dependence of the Hamiltonian. Notice that this can be problematic as small divisors appear in the computation when removing the harmonics of the surviving monomials. A consequence of the existence of these extra small divisors is that the radius of convergence of the reduced Hamiltonian is smaller. Notice that in the centre manifold reduction for autonomous systems involves no small divisors and, therefore, to kill time dependence can lead into a less useful method[1]. A solution for this is not to remove time dependence, at least completely. Indeed, one could choose to not kill the harmonics that lead to small divisors and reduce the Hamiltonian only by a degree of freedom. This would certainly avoid the struggle with small divisors in the case of the centre manifold and also in the case of complete normal forms, which do display small divisors in the autonomous case as well, prevent the process to deal with these extra small divisors arising from killing time dependence. To visualize the remaining Hamiltonian would be harder in this case, as it would be mandatory to cope with a fourth dimensional symplectic map (the stroboscopic map associated to the reduced Hamiltonian). However, there are some cases in which it is not necessary a visualization, and, moreover there are techniques that permit us to visualize phase spaces of four dimensions. To investigate the benefits of not removing time dependence is a line to be followed in a near future.

Another natural line to follow is to adapt Lie series method to the computation of normal forms around quasi-periodic motion. This has been done previously. There are a couple of main difficulties to overcome when doing this. The first one is the Floquet change: Indeed,

[1]We would like to stress that, in the case of the centre manifold of L_1, small divisors have not been a problem, as they appear at high order

as we have pointed out in Chapter 4, not all quasi-periodic motion is reducible to constant coefficients and even thought there are a large number of situations in which the reducibility can be assured, the computation of the Floquet Change is much more involved than in the periodic case. The second difficulty to be dealt with is the appearance of internal resonances (and small divisors) that can lead to even smaller radii of convergence. With all this regards, it has been shown that the Lie series method can be useful as well to compute normal forms around quasi-periodic motion and we add this line as the outscope of this thesis as well.

One last, and rather obvious, direction to follow is to apply the Lie transformation method to other problems. We will give some words on the specific problems appearing in this dissertation when giving the corresponding conclusions and outlook.

The parameterization method in stroboscopic maps

In Chapter 2 we deal with high order expansions of stroboscopic maps and its applications to the computation of invariant manifolds in the framework of the parameterization method.

To produce a high order expansion of a stroboscopic map, we use a technique called **jet transport** i.e. we take advantage on automatic differentiation to transport the jet, i.e. the the set of derivatives, of the flow with respect to the initial conditions. The software we have developed is based on a Taylor method in which the standard double precision arithmetic is replaced by one of polynomials. The code is written so several arithmetic, dealing at each case with a different number of variables, can be interchanged. Depending on the goal to fulfill, number of variables of the polynomial arithmetic changes. In this dissertation we have applied this ideas to two main applications.

First, when the arithmetic of polynomials is the same one as the phase space, we can use jet transport to compute the solutions of the variational equations of any order. We have taken advantage on this to compute the differential matrices of the different stroboscopic maps appearing in the physical problems of Part II. The main benefit of doing that is to avoid tedious handmade computations of the variational equations, computations in which it is easy to make mistakes and some effort is to be put in checking the correctness of these formulae.

The other application of jet transport we have worked on is the computation of high order approximations of stable and unstable invariant manifolds related to fixed points of stroboscopic maps in the context of the parameterization method. We have implemented the software to compute one and two dimensional stable and unstable manifolds. The benefits of having high order approximations of such manifolds are several. In the first place, we need less iterates to grow numerically the manifolds, which leads to more efficient codes and, therefore, to get a larger piece of the manifold in the same amount of time. On the other hand we have seen that, in some situations, the dynamics far away from the fixed points is

less harmful in terms of error propagation. High order parameterization allow us to start certain computations far away from the fixed points.

These techniques allow us to tackle many other different problems, some of them, with a little bit more effort. Essentially we can adapt any procedure in the context of the parameterization method. Let us mention some of them that we expect to cover in the future.

We have worked with stroboscopic maps because it is the natural object to deal with in the context of periodically time dependent systems, but, we could apply these ideas to spatial Poincaré sections. The implementation is harder than the case of stroboscopic maps as one has to compute the projection of the jets on the Poincaré section, but, it can be done without any major problems to be expected.

Another interesting thing to be done is to adapt our software to cope with complex saddles, that is, to compute stable and unstable manifolds of fixed points whose eigenvalues are complex out of the unit circle. We have encountered fixed point with this kind of linear character in this thesis. The computation of invariant manifolds of complex saddles can be regarded as the computation of a two dimensional real manifold. In any case, it is a matter of adapting the algorithms of two dimensional manifolds (for the real computation) or the one dimensional manifolds (for the complex computation). Notice that these high order expansions of complex saddles could help us to understand better some geometrical aspects of the Hamiltonian-Hopf bifurcations that are now being considered.

The third direction of further development we want to address is normal forms. Indeed, we can develop a counterpart of the computations presented in Chapter 1 but in stroboscopic/Poincaré maps. To work with stroboscopic maps and the parameterization method has several advantages in terms of efficiency and the computation of the Floquet change is not to be done. However, it has a main shortcoming: unstable dynamics cannot be avoided. Indeed, the fact that the periodic orbit that replaces L_1 in the BCP has an unstable eigenvalue of order 10^8 represents no problem in the most computation of the centre manifold shown in Chapter 1[2]. In the case of performing the normal form directly on the stroboscopic map the error propagation induced by large unstable eigenvalues is to be dealt with some strategy such as multiple precision or parallel shooting. This is, in our opinion, a very interesting direction to follow.

One last thing to say is that all of these computations can be generalized to the case of higher invariant manifolds. For instance, invariant curves. For instance, the method to produce the linear approximation of the whiskers related to invariant curves presented in Chapter 3 can be generalized to high order by means of the techniques we have presented here. The main difficult we have to overcome is that the arithmetic to replace the standard double precision in the Taylor method must be an arithmetic of Taylor-Fourier series. Notice that combining source code developed for Chapter 1 and Chapter 2 we can solve this problem

[2]It complicates a little bit the Floquet Change.

easily. In fact, the programs to handle Taylor-Fourier series are already coded.

Complex skew-products

In Chapter 4 we deal with invertible and linear skew-products (also known as cocycles) on the complex plane, this being motivated by the linearization around invariant curves. We provide a linear and topological classification of invertible linear skew-products of the complex plane. The class in which each of the belongs to, provided suitable hypotheses are satisfied, is determined by the Lyapunov exponent and the winding number of the cocycle around the origin of the complex plane. This classification also leads to a characterization of non-reducibility in this context, indeed, non-reducible systems are the ones whose winding number around the origin is different from zero. This kind of non-reducibility is called essential as the cocycle is prevented from being reducible due to a topological obstruction. The classification in presented in Chapter 4 gives a complete description of invertible linear skew-products.

We also study the dependence of the Lyapunov exponent with respect to parameters. We give a rigorous proof on the loss of smoothness of the Lyapunov exponent when a change of winding number takes place (the system passes thought non-invertible) when the parameter is moved. In particular we show that the Lyapunov exponent is smooth as long as the cocycle is invertible and only continuous at the value of the parameters for which the cocycle is non-invertible.

Affine systems can be used to understand the dependence of invariant curves on the parameters of the systems, therefore are they seem to be the natural step to take after having a complete understanding of linear systems. The classification for linear systems can be extended to affine systems as long as they have an invariant curve, hence, it is natural to study mechanism of destruction of invariant curves in affine systems. We have shown that, for a particular non-reducible skew product, the destruction of a certain invariant curve seems to be pathological, it displays a fractalization process, when the system transits from attracting to repelling. The remarkable thing about this part of the chapter is that, despite the system is extremely simple, the behaviour of the invariant curve as it gets destructed is quite complicated.

There are several directions to follow in this particular area. First of all, the linear and topological classifications seem to be extendable to non-invertible skew-products as well. On the other hand, we believe that the fractalization process we have shown in a non-reducible example cannot happen for a generic class of reducible systems. To find a proof for this fact would be interesting.

A more ambitious direction to follow is to go to non-linear dynamics. In this case the possible scope is so wide that it is hard to select specific possibilities to introduce here. Let us mention some of them.

It seems that there is a relation with the wild winding process introduced in Chapter 4 and other breakdown mechanism such as the fractalization mechanism also presented in Chapter 4 and other alternative definitions. To investigate the relations between these different definitions essentially means to find out if one of these definitions imply the others in some particular context. Also it would be interesting to study non-linear maps displaying this kind of behavior.

Strange Nonchaotic Attractors have been an appealing topic for researches investigating skew-products in the real case. Several parts of the argument to show the existence of SNA for the real one dimensional case subsist for the complex case. However, the set of hypotheses requires the skew-product to be pinched, which is not generic in the complex plane, and other hypotheses, like monoticity (this does not even make sense in the complex plane). Therefore it would be interesting to study what are the relevant hypotheses that lead to the existence of SNA in the complex plane. In particular, a good question to answer is if invertible skew-products can display SNA in the complex plane.

Solar sails in the Earth-Moon system

In Chapter 6 we study the motion of a solar sail in the Earth-Moon system taking under consideration the gravitational effects of Earth, Moon and Sun. As far as we known, this is the first time the effect of Sun's gravity on a solar sail moving in the Earth-Moon system has been taken into account in a simplified model[3]. We manage two main models according if the sail is close to the collinear points L_1 and L_2 or the triangular points and L_3. These two models are obtained from including the effect of the Solar Radiation Pressure (SRP) on the sail in the Quasi-Bicircular Problem (L_1 and L_2) and the Bicircular Problem (L_3, L_4 and L_5)[4]. The modified models depend on three parameters, two that determine the orientation of the sail and one that captures its effectivity.

Chapter 6 studies how the dynamical equivalents of the libration points (and some resonant orbits) change when the parameters of the sail are moved. These dynamical equivalents are periodic orbits with the same period as Sun. By means of a stroboscopic map, we reduce the problem to the study of the geometry of surfaces of fixed points. There is a number of connections between several fixed points when these parameters are moved. Notice that this is the reason we use the Bicircular Problem to study the motion near L_3, as it cannot be separated from the motion near L_4 and L_5. Moreover, we have reported on a bifurcation which is degenerate due to the symmetries of the system. We have also studied the invariant manifolds attached to some of the fixed points that replace the libration points L_3, L_4 and

[3]There are simulations for a solar sail in the Earth-Moon system considering the whole solar system. Therefore, the effect of Sun's gravity has been considered before, but not specifically addressed.

[4]These two models are discussed deeply in Chapter 5.

L_5.

The end of the Chapter is devoted to the comparison with a model in which Sun's gravity is not taken under consideration. We provide this comparison as most of the literature uses this simplified model. We have reported remarkable differences in the geometry of the surfaces of fixed points, especially near the collinear points L_1 and L_2.

There is much further work to be done in this problem. First of all, the technology to compute normal forms and centre manifolds by means of the Lie transformation method is to be applied in this problem. In particular, it would be interesting to analyze how the SRP affects the bifurcation that leads to Halo orbits. Indeed, if the sail is not perpendicular to Sun, SRP breaks the pitchfork bifurcation that originates Halo orbits. This is to be done in a near future.

Other line to follow is to explore new models for the solar radiation pressure acceleration. In particular we could consider the sail to be not perfectly reflecting. Moreover there is another kind of solar sails, named oscillating sails, in which the effectivity (or the orientation) depends periodically in time. If that extra frequency is not commensurable with Sun's, the phase space of the system becomes more complicated, as the simplest invariant objects are invariant tori.

Solar Radiation Pressure and the Kordylewsky clouds

In Chapter 7 we study how stability out-of-plane stability regions appearing near the triangular points of the BCP behave when Solar Radiation Pressure (SRP) is considered. As we have explained, the reason to consider SRP is that the bodies that are to be expected in those places are dense concentrations of space dust, the so-called Kordylewsky clouds. The numerical computations reveal that the regions of practical stability far away of the triangular points as the effect of SRP gets larger. The reason why this happens is the dynamical equivalents of the triangular points moving towards L_3. In fact, these three dynamical equivalents are merged in a pitchfork bifurcation, and, therefore, there is only one periodic orbits that replaces L_3, L_4 and L_5 if the SRP acceleration is large enough. Stress also that this unique periodic orbit gets closer and closer as the lightness number increases, ending up with a colliding trajectory. Even thought after the bifurcation the periodic orbit is totally elliptic, most of the initial conditions are captured by Earth.

As Chapter 7 is a preliminary study on the problem, there is much work to do regarding this topic. First of all, we have not explored how these effective stability regions move around the phase space. Moreover, the effect of SRP has, for low values of the lightness number, is to stabilize the periodic orbits that replace the triangular points, therefore, it makes sense to look for stability regions in the plane. Moreover, in the RTBP, there is numerical evidence that the invariant object that determines the boundary of the stability region around the

triangular points is the centre-unstable manifold of the collinear point L_3. A similar study can be undertaken in the BCP (with or without adding SRP) to determine if this still holds when Sun's gravity is considered. This is one of the most interesting applications for the computation of high order centre-unstable manifolds by means of the parameterization method in the stroboscopic maps we refereed to some paragraphs above.

A last thing this type of study requires is to contrast all these stability regions in the real solar system. This can be done by means of JPL ephemeris or with a many body problem with the solar system parameters.

Recollision mechanisms

In Chapter 8 we use the software presented in Chapter 3 to identify a generic recolliding scenario for an electron detached from a core under the effect of a laser pulse in the two-dimensional configuration space. We have collected numerical evidences that regions of the phase space with positive Lebesgue measure are driven to multiple recollisions by the centre-stable and centre-unstable manifolds of some key periodic orbit close to the core. Notice that, even the initial conditions we found start close to the ionic parent, they take long excursions and recollide many times in ten laser cycles. Moreover, the kinetic energy these initial conditions bring back to the core is larger than the one they had at the beginning of the integration. This recollision mechanism is different from the, well-known one happening in the one-dimensional configuration space and, as far as we know, it has not been reported in the literature.

The reason why we say that regions of positive Lebesgue measure are driven to recollision is that codimension one invariant manifolds recollide many times. As these objects separate the phase space, initial conditions enclosed by the manifolds are to be driven by it. However, these results can be enhanced remarkably.

First of all, we have not estimated the region of initial conditions that is driven to recollision by the manifold. This measure could be estimated by several methods but a bigger pieces of the driving centre-unstable manifold would help to do it more efficiently. Therefore, a natural path to follow is to get a larger piece of the manifold and this can be obtained by means of the parameterization method applied to the stroboscopic map. Moreover intersections with certain sub-spaces can be utilized to visualize the regions where there are more recolliding initial conditions and the ones in which these initial conditions recollide a large number of times.

Self-criticism

Let me change to first person for these last words of the concluding chapter. This dissertation is the result of five years of hard work, lack of sleeping and a tremendous amount of coffee. I would like to share some final thoughts regarding the motivations that took me to follow the particular approach presented in this dissertation.

This thesis tackles several aspects related to the invariant manifolds of Hamiltonian systems with periodic time dependence and also some applications. A natural general criticism to this dissertation is that it goes wide instead of deep. That is, there are many questions and problems faced and, in several of them, the explorations do not go further inside of those problems. While this is true and a legit appreciation, I would like to point out that I am aware of it and that this approach is completely intentional.

The purpose of any PhD dissertation is the author taking contact with the world of scientific research. In this regard, the work behind this thesis has helped me to master a number of different techniques that can be used the face many problems in applied dynamical systems and to get into some theoretical issues that, if possible, are to be developed in the following years. The learning of the methodology applied in this work will be essential for my career and, consequently, I think that the main purpose of this work is well accomplished.

I noticed, in the early months of the PhD program, how lucky I was to work on my thesis in the Barcelona group of dynamical systems. I have been surrounded by many top researchers that, each one at his own extent, helped to develop and enlarge the legacy of Carles Simó. During all these years an ambition of learning these many techniques and take as much as I could from these professionals has grown inside me. Honestly speaking, I have been trying to see myself worthy of help carrying this legacy.

While I am moderately proud of my work, I am aware of several things that I could be done much better. Maybe the most important negative consequence of the approach I have followed is the lack of published papers. I know, nowadays, ending up the PhD with only one or two references is a bad situation. That is a penalty I will have to pay. However, there is a number of papers in preparation that will be publishable in a short period of time if everything goes correctly. I feel that I have done very little and I let much more to be done. This is the nature of research itself and it is, probably, a good new as I am provided with problems to work on for several years. Knowing that other challenges will appear and some of these problems will be moved to some dark closed in my mind, I hope I will, at least, face most of the further work I mentioned in this chapter.

Bibliography

[AC09] Ll. Alsedà and S. Costa. On the definition of strange nonchaotic attractor. *Fund. Math.*, 206:23–39, 2009.

[AD08] P. Agostini and L. F. DiMauro. Atoms in high intensity mid-infrared pulses. *Contemporary Physics*, 49(3):179–197, 2008.

[AFJ+08] E.M. Alessi, A. Farrés, À. Jorba, C. Simó, and A. Vieiro. Efficient usage of self validated integrators for space applications. Ariadna final report, contract no. 20783/07/nl/cb, ESTEC (European Space Agency), 2008.

[AGK+92] M. Ammosov, P. Golovinsky, I. Kiyan, V. Krainov, and V. Ristic. Tunneling ionization of atoms and atomic ions in an intense laser field with a nonhomogeneous space–time distribution. *J. Opt. Soc. Am. B*, 9(8):1225–1230, Aug 1992.

[Ahl66] L.V. Ahlfors. *Complex Analysis ... 2nd Ed.* International series in pure and applied mathematics. McGraw-Hill, 1966.

[AMR17] L. Alsedà, J.M. Mondelo, and D. Romero. A numerical estimate of the regularity of a family of strange non-chaotic attractors. *Physica D: Nonlinear Phenomena*, 347:74 – 89, 2017.

[And98] M.A. Andreu. *The quasi-bicircular problem.* PhD thesis, Univ. Barcelona, 1998.

[And02] M.A. Andreu. Dynamics in the center manifold around L_2 in the quasi-bicircular problem. *Celestial Mech.*, 84(2):105–133, 2002.

[Arn63a] V.I. Arnold. Proof of A.N. Kolmogorov's theorem on the preservation of quasi-periodic motions under small perturbations of the Hamiltonian. *Russian Math. Surveys*, 18(5):9–36, 1963.

[Arn63b] V.I. Arnold. Small denominators and problems of stability of motion in classical and celestial mechanics. *Russian Math. Surveys*, 18(6):85–191, 1963.

[Arn64] V.I. Arnold. Instability of dynamical systems with several degrees of freedom. *Soviet Math. Dokl.*, 5:581–585, 1964.

[Arn74] V.I. Arnold. *Équations différentielles ordinaires*. Mir, Moscou, 1974.

[Arn78] V.I. Arnold. *Mathematical Methods of Classical Mechanics*. Springer, New York, 1978.

[AS00] M.A. Andreu and C. Simó. The quasi-bicircular problem for the Earth-Moon-Sun parameters. Preprint, 2000.

[ASM18] M. Abu-Samha and L. Madsen. Probing atomic and molecular targets by intense bicircular counter-rotating laser fields. *Journal of Physics B: Atomic, Molecular and Optical Physics*, 51, 05 2018.

[BB79] J. V. Breakwell and J. V. Brown. The 'halo' family of 3-dimensional periodic orbits in the earth-moon restricted 3-body problem. *Celestial mechanics*, 20(4):389–404, Nov 1979.

[BBCG96] M. Berz, C. Bischof, G.F. Corliss, and A. Griewank, editors. *Computational Differentiation: Techniques, Applications, and Tools*. SIAM, Philadelphia, Penn., 1996.

[BCCG92] C.H. Bischof, A. Carle, G.F. Corliss, and A. Griewank. ADIFOR: Automatic differentiation in a source translation environment. In Paul S. Wang, editor, *Proceedings of the International Symposium on Symbolic and Algebraic Computation*, pages 294–302, New York, 1992. ACM Press.

[BFM94] C. Beaugé and S. Ferraz-Mello. Capture in exterior mean-motion resonances due to poynting-robertson drag. *Icarus*, 110(2):239 – 260, 1994.

[BGK+02] W. Becker, F. Grasbon, R. Kopold, D. Milosevic, G. Paulus, and H. Walther. Above-threshold ionization: From classical features to quantum effects. *Advances in Atomic, Molecular, and Optical Physics*, 48:35–98, 12 2002.

[BGMO16] E. Barrabés, G. Gómez, J. M. Mondelo, and M. Ollè. Pseudo-heteroclinic connections between bicircular restricted four-body problems. *Monthly Notices of the Royal Astronomical Society*, 462(1):740–750, 2016.

[Bje09] K. Bjerklöv. SNA's in the quasi-periodic quadratic family. *Comm. Math. Phys.*, 286(1):137–161, 2009.

[BKSF59] L.M. Beda, L.N. Korolev, N.V. Sukkikh, and T.S. Frolova. Programs for automatic differentiation for the machine BESM. Technical Report, Institute for Precise Mechanics and Computation Techniques, Academy of Science, Moscow, USSR, 1959. (In Russian).

[BLJHE12] W. Becker, X. Liu, P. Jo Ho, and J. Eberly. Theories of photoelectron correlation in laser-driven multiple atomic ionization. *Reviews of Modern Physics*, 84:1011–1043, 07 2012.

[BLS79] J. A. Burns, P. L. Lamy, and S. Soter. Radiation forces on small particles in the solar system. *Icarus*, 40(1):1 – 48, 1979.

[BMGLD17] B. L. Bihan, J. J. Masdemont, G. Gómez, and S Lizy-Destrez. Invariant manifolds of a non-autonomous quasi-bicircular problem computed via the parameterization method. *Nonlinearity*, 30(8):3040, 2017.

[BOS18] Nicola Baresi, Zubin P. Olikara, and Daniel J. Scheeres. Fully numerical methods for continuing families of quasi-periodic invariant tori in astrodynamics. *The Journal of the Astronautical Sciences*, 65(2):157–182, Jun 2018.

[Bou97] J. Bourgain. On Melnikov's persistency problem. *Math. Res. Lett.*, 4(4):445–458, 1997.

[Bro68] R.A. Broucke. *Periodic Orbits in the Restricted Three-body Problem with Earth-moon Masses*. JPL technical report. Jet Propulsion Laboratory, California Institute of Technology, 1968.

[Bro71] R. Broucke. Solution of the N-Body Problem with recurrent power series. *Celestial Mech.*, 4(1):110–115, 1971.

[BWZ70] D. Barton, I.M. Willers, and R.V.M. Zahar. The automatic solution of ordinary differential equations by the method of Taylor series. *Computer J.*, 14(3):243–248, 1970.

[BXD+12] C. Blaga, J. Xu, A. DiChiara, E. Sistrunk, K. Zhang, P. Agostini, T. Miller, L. Dimauro, and C. Lin. Imaging ultrafast molecular dynamics with laser-induced electron diffraction. *Nature*, 483:194–7, 03 2012.

[CC82] G.F. Corliss and Y.F. Chang. Solving ordinary differential equations using Taylor series. *ACM Trans. Math. Software*, 8(2):114–144, 1982.

[CC94] Y.F. Chang and G.F. Corliss. ATOMFT: Solving ODEs and DAEs using Taylor series. *Computers and Mathematics with Applications*, 28:209–233, 1994.

[CFdlL03a] X. Cabré, E. Fontich, and R. de la Llave. The parameterization method for invariant manifolds I: Manifolds associated to non-resonant subspaces. *Indiana Univ. Math. J*, 52(2):283–328, 2003.

[CFdlL03b] X. Cabré, E. Fontich, and R. de la Llave. The parameterization method for invariant manifolds II: Regularity with respect to parameters. *Indiana University Mathematics Journal*, 52(2):329–360, 2003.

[CFdlL05a] X. Cabré, E. Fontich, and R. de la Llave. The parameterization method for invariant manifolds III: Overview and applications. *Journal of Differential Equations*, 218(2):444 – 515, 2005.

[CFdlL05b] X. Cabré, E. Fontich, and R. de la Llave. The parameterization method for invariant manifolds. III. Overview and applications. *J. Differential Equations*, 218(2):444–515, 2005.

[CJ00] E. Castellà and À. Jorba. On the vertical families of two-dimensional tori near the triangular points of the Bicircular problem. *Celestial Mech.*, 76(1):35–54, 2000.

[Cor93] P. B. Corkum. Plasma perspective on strong field multiphoton ionization. *Phys. Rev. Lett.*, 71:1994–1997, Sep 1993.

[Cor95] G.F. Corliss. Guaranteed error bounds for ordinary differential equations. In M. Ainsworth, J. Levesley, W. A. Light, and M. Marletta, editors, *Theory of Numerics in Ordinary and Partial Differential Equations*, pages 1–75. Oxford University Press, Oxford, 1995. Lecture notes for a sequence of five lectures at the VI-th SERC Numerical Analysis Summer School, Leicester University, 25 - 29 July, 1994.

[Cor14] P. Corkum. Recollision physics. *Phyricsl Today*, 64:36–41, 03 2014.

[CRR64] J. Cronin, P.B. Richards, and L.H. Russell. Some periodic solutions of a four-body problem. *Icarus*, 3:423–428, 1964.

[DDDW97] W.C. Ding, H. Deutsch, A. Dinklage, and C. Wilke. Observation of a strange nonchaotic attractor in a neon glow discharge. *PHYSICAL REVIEW E*, 55(3):3769–3772, 1997.

[dlLGJV05] R. de la Llave, A. González, À. Jorba, and J. Villanueva. KAM theory without action-angle variables. *Nonlinearity*, 18(2):855–895, 2005.

[DS92] A. Delshams and T.M. Seara. An asymptotic expression for the splitting of separatrices of the rapidly forced pendulum. *Comm. Math. Phys.*, 150:433–463, 1992.

[DSM+05] B. Dachwald, W. Seboldt, M. Macdonald, G. Mengali, A.A. Quarta, C.R. McInnes, L. Rios-Reyes, D.J. Scheeres, B. Wie, M. Görlich, et al. Potential Solar Sail Degradation Effects on Trajectory and Attitude Control. In *AIAA Guidance, Navigation, and Control Conference and Exhibit*, volume 6172, 2005.

[Eli88] L.H. Eliasson. Perturbations of stable invariant tori for Hamiltonian systems. *Ann. Sc. Norm. Super. Pisa, Cl. Sci.*, 15(1):115–147, 1988.

[Far70] R.W. Farquhar. *The Control and Use of Libration-point Satellites*. NASA TR R. National Aeronautics and Space Administration, 1970.

[FGJ+18] A. Farrés, J. Gimeno, Á. Jorba, M. Jorba-Cuscó, N. Miguel, and M. Zou. The parametrization method on Poincaré sections. Preprint, 2018.

[FH12] J.-Ll. Figueras and A. Haro. Reliable computation of robust response tori on the verge of breakdown. *SIAM J. Appl. Dyn. Syst.*, 11(2):597–628, 2012.

[FH15] J.-L. Figueras and A. Haro. Different scenarios for hyperbolicity breakdown in quasiperiodic area preserving twist maps. *Chaos*, 25(12):123119, 16, 2015.

[FH16] J.-L. Figueras and Á. Haro. A note on the fractalization of saddle invariant curves in quasiperiodic systems. *Discrete and Continuous Dynamical Systems - S*, 9(1937-1632-2016-4-1095):1095, 2016.

[FHL+07] L. Fousse, G. Hanrot, V. Lefèvre, P. Pélissier, and P. Zimmermann. Mpfr: A multiple-precision binary floating-point library with correct rounding. *ACM Trans. Math. Softw.*, 33(2), June 2007.

[FJ97] M. Frigo and S. G. Johnson. The fastest fourier transform in the west. Technical report, Massachusetts Institute of Technology, Cambridge, MA, USA, 1997.

[FJ05] M. Frigo and S.G. Johnson. The design and implementation of fftw3. *Proceedings of the IEEE*, 93:216 – 231, 03 2005.

[FJ08a] A. Farrés and À. Jorba. A dynamical system approach for the station keeping of a solar sail. *J. Astronaut. Sci.*, 56(2):199 – 230, 2008.

[FJ08b] A. Farrés and À. Jorba. Solar sail surfing along families of equilibrium points. *Acta Astron.*, 63:249–257, 2008.

[FJ10a] A. Farrés and À. Jorba. Dynamics of a solar sail near a halo orbit. Preprint, 2010.

[FJ10b] A. Farrés and À. Jorba. On the high order approximation of the centre manifold for ODEs. *Discrete Contin. Dyn. Syst. Ser. B*, 14(3):977–1000, 2010.

[FJ10c] A. Farrés and À. Jorba. Periodic and quasi-periodic motions of a solar sail close to SL_1 in the Earth-Sun system. *Celestial Mech.*, 107(1-2):233–253, 2010.

[FJJC15a] A. Farrés, À. Jorba, and M. Jorba-Cuscó. On the solar sail periodic orbits near the earth-moon libration points. In *Proceedings of the XXIV Congress on differential equations and applications*, Cádiz, Spain, 8–12 June 2015.

[FJJC15b] A. Farrés, À. Jorba, and M. Jorba-Cuscó. On the solar sail periodic orbits near the earth-moon libration points. In *Proceedings of the XXIV Congress on differential equations and applications*, Cádiz, Spain, 8–12 June 2015.

[FK73a] R. W. Farquhar and A. A. Kamel. Quasi-periodic orbits about the translunar libration point. *Celestial mechanics*, 7(4):458–473, Jun 1973.

[FK73b] R.W. Farquhar and A.A. Kamel. Quasi-periodic orbits about the translunar libration point. *Celestial Mech.*, 7(4):458–473, 1973.

[FR81] V. Franceschini and L. Russo. Stable and unstable manifolds of the Hénon mapping. *J. Statist. Phys.*, 25(4):757–769, 1981.

[FT18] J.-L. Figueras and T.O. Timoudas. Sharp $\frac{1}{2}$-Hölder continuity of the Lyapunov exponent at the bottom of the spectrum for a class of Schrödinger cocycles. Preprint, 2018.

[FV80] R. A. Freitas and F. Valdes. A search for natural or artificial objects located at the earth-moon libration points. *Icarus*, 42(4):442–447, 1980.

[FV82] R. A. Freitas and F. Valdes. A search for objects near the earth-moon lagrangian points. *Icarus*, 53(11):453–457, 1982.

[Gab03] F. Gabern. *On the dynamics of the Trojan asteroids*. PhD thesis, Univ. de Barcelona, 2003.

[GC91] A. Griewank and G.F. Corliss, editors. *Automatic Differentiation of Algorithms: Theory, Implementation, and Application*. SIAM, Philadelphia, Penn., 1991.

[GC07] K. Gaffney and H. Chapman. Imaging atomic structure and dynamics with ultrafast x-ray scattering. *Science (New York, N.Y.)*, 316:1444–8, 07 2007.

[GDF+89] A. Giorgilli, A. Delshams, E. Fontich, L. Galgani, and C. Simó. Effective stability for a Hamiltonian system near an elliptic equilibrium point, with an application to the restricted three body problem. *J. Differential Equations*, 77:167–198, 1989.

[GG78] A. Giorgilli and L. Galgani. Formal integrals for an autonomous Hamiltonian system near an equilibrium point. *Celestial Mech.*, 17:267–280, 1978.

[GG85] A. Giorgilli and L. Galgani. Rigorous estimates for the series expansions of Hamiltonian perturbation theory. *Celestial Mech.*, 37:95–112, 1985.

[Gib60] A. Gibbons. A program for the automatic integration of differential equations using the method of Taylor series. *Comp. J.*, 3:108–111, 1960.

[GJ01] F. Gabern and À. Jorba. A restricted four-body model for the dynamics near the Lagrangian points of the Sun-Jupiter system. *Discrete Contin. Dyn. Syst. Ser. B*, 1(2):143–182, 2001.

[GJ04] F. Gabern and À. Jorba. Generalizing the Restricted Three-Body Problem. The Bianular and Tricircular Coherent Problems. *Astron. Astrophys.*, 420:751–762, 2004.

[GJ05] F. Gabern and À. Jorba. Effective computation of the dynamics around a two-dimensional torus of a Hamiltonian system. *J. Nonlinear Sci.*, 15(3), 2005.

[GJL05] F. Gabern, À. Jorba, and U. Locatelli. On the construction of the Kolmogorov normal form for the Trojan asteroids. *Nonlinearity*, 18(4):1705–1734, 2005.

[GJMS91a] G. Gómez, À. Jorba, J. Masdemont, and C. Simó. Quasiperiodic orbits as a substitute of libration points in the solar system. In A.E. Roy, editor, *Predictability, Stability and Chaos in N-Body Dynamical Systems*, pages 433–438. Plenum Press, 1991.

[GJMS91b] G. Gómez, À. Jorba, J. Masdemont, and C. Simó. A quasiperiodic solution as a substitute of l_4 in the Earth-Moon system. In *Proceedings of the 3rd International Sysmposium on Spacecraft Flight Dynamics*, pages 35–41, ESTEC, Noordwijk, Holand, 1991. ESA Publications Division.

[GJMS91c] G. Gómez, À. Jorba, J. Masdemont, and C. Simó. Study refinement of semi-analytical Halo orbit theory. ESOC contract 8625/89/D/MD(SC), final report, European Space Agency, 1991. Reprinted as *Dynamics and mission design near libration points. Vol. III, Advanced methods for collinear points*, volume 4 of World Scientific Monograph Series in Mathematics, 2001.

[GJMS93] G. Gómez, À. Jorba, J. Masdemont, and C. Simó. Study of Poincaré maps for orbits near Lagrangian points. ESOC contract 9711/91/D/IM(SC), final report, European Space Agency, 1993. Reprinted as *Dynamics and mission design near libration points. Vol. IV, Advanced methods for triangular points*, volume 5 of World Scientific Monograph Series in Mathematics, 2001.

[GJMS01] G. Gómez, À. Jorba, J. Masdemont, and C. Simó. *Dynamics and mission design near libration points. Vol. IV, Advanced methods for triangular points*, volume 5 of *World Scientific Monograph Series in Mathematics*. World Scientific Publishing Co. Inc., 2001.

[GJR04] F. Gabern, À. Jorba, and P. Robutel. On the accuracy of restricted three-body models for the Trojan motion. *Discrete Contin. Dyn. Syst. Ser. B*, 11(4):843–854, 2004.

[Gle02] P. Glendinning. Global attractors of pinched skew products. *Dyn. Syst.*, 17(3):287–294, 2002.

[GLMS85] G. Gómez, J. Llibre, R. Martínez, and C. Simó. Station keeping of libration point orbits. ESOC contract 5648/83/D/JS(SC), final report, European Space Agency, 1985. Reprinted as *Dynamics and mission design near libration points. Vol. I, Fundamentals: the case of collinear libration points*, volume 2 of World Scientific Monograph Series in Mathematics, 2001.

[GLMS01] G. Gómez, J. Llibre, R. Martínez, and C. Simó. *Dynamics and mission design near libration points. Vol. I, Fundamentals: the case of collinear libration points*, volume 2 of *World Scientific Monograph Series in Mathematics*. World Scientific Publishing Co. Inc., 2001.

[GM01] G. Gómez and J.M. Mondelo. The dynamics around the collinear equilibrium points of the RTBP. *Phys. D*, 157(4):283–321, 2001.

[GMS97] G. Gómez, J.J. Masdemont, and Simó S. Lissajous orbits around halo orbits. *Adv. in the Astronautical Sciences*, 95:117–134, 1997.

[GOPY84] C. Grebogi, E. Ott, S. Pelikan, and J.A. Yorke. Strange attractors that are not chaotic. *Phys. D*, 13(1-2):261–268, 1984.

[Gra74] S. Graff. On the conservation of hyperbolic invariant tori for Hamiltonian systems. *J. Differential Equations*, 15(1):1–69, 1974.

[Gri00] A. Griewank. *Evaluating Derivatives*. SIAM, Philadelphia, Penn., 2000.

[HC17] J. Heiligers and M. Ceriotti. Orbital dynamics of an oscillating sail in the earth-moon system, 2017.

[HCL+16] A. Haro, M. Canadell, A. Luque, J.-M. Mondelo, and J.-Ll. Figueras. *The Parameterization Method for Invariant Manifolds. From Rigorous Results to Effective Computations*, volume 195 of *Applied Mathematical Sciences*. Springer-Verlag, 2016.

[HdlL06] À. Haro and R. de la Llave. Manifolds on the verge of a hyperbolicity breakdown. *Chaos*, 16(1):013120, 8, 2006.

[Her83] M.R. Herman. Une méthode pour minorer les exposants de Lyapounov et quelques exemples montrant le caractère local d'un théorème d'Arnol'd et de Moser sur le tore de dimension 2. *Comment. Math. Helv.*, 58(3):453–502, 1983.

[HH94] J.F. Heagy and S.H. Hammel. The birth of strange nonchaotic attractors. *Physica D: Nonlinear Phenomena*, 70(1):140 – 153, 1994.

[HHNC14] J. Heiligers, S. Hiddink, R. Noomen, and McInnes C. Solar sail periodic orbits in the earth-moon three-body problem. In *Proceedings of the 65th International Astronautical Congress*, Toronto, Canada, 26–30 September 2014.

[HHNM15a] J. Heiligers, S. Hiddink, R. Noomen, and C. R. McInnes. Solar sail lyapunov and halo orbits in the earth-moon three-body problem. *Acta Astronautica*, 116:25 – 35, 2015.

[HHNM15b] J. Heiligers, S. Hiddink, R. Noomen, and C. R. McInnes. Solar sail lyapunov and halo orbits in the earth–moon three-body problem. *Acta Astronautica*, 116:25 – 35, 2015.

[HL14] G.H. Hardy and J.E. Littlewood. Some problems of diophantine approximation. *Acta Mathematica*, 37(1):193–239, 1914.

[HL05a] À. Haro and R. de la Llave. A parameterization method for the computation of invariant tori and their whiskers in quasiperiodic maps: numerical algorithms. Preprint, 2005.

[HL05b] À. Haro and R. de la Llave. A parameterization method for the computation of invariant tori and their whiskers in quasiperiodic maps: numerical implementation and examples. Preprint, 2005.

[HL07] À. Haro and R. de la Llave. Spectral theory and dynamical systems. Preprint, contained in the file `ftp://ftp.ma.utexas.edu/pub/papers/llave/spectral.pdf`, 2007.

[HLS09] G. Huguet, R. de la Llave, and Y. Sire. Fast numerical algorithms for the computation of invariant tori in hamiltonian systems. Preprint, 2009.

[HMP16a] J. Heiligers, M. Macdonald, and J. S. Parker. Extension of earth-moon libration point orbits with solar sail propulsion. *Astrophysics and Space Science*, 361(7):1–20, 2016.

[HMP16b] J. Heiligers, M. Macdonald, and J. S. Parker. Extension of earth-moon libration point orbits with solar sail propulsion. *Astrophysics and Space Science*, 361(7):1–20, 2016.

[HMP18] J. Heiligers, M. Macdonald, and J. S. Parker. Novel solar-sail mission concepts for high-latitude earth and lunar observation. *Journal of Guidance, Control, and Dynamics*, 41(1):212–230, 2018.

[Hoe01] J. Hoefkens. *Rigorous numerical analysis with high order Taylor methods*. PhD thesis, Michigan State University, 2001.

[Hol18] P. Holoborodko. Mpfr c++. http://www.holoborodko.com/pavel/mpfr/, 2008-2018.

[HS06] À. Haro and C. Simó. To be or not to be a SNA: That is the question. Preprint, 2006.

[HTL09] X. Hou, J. Tang, and L. Liu. On utilization of solar sails in triangular libration point missions in the earth-moon system. *Transactions of the Japan society for aeronautical and space sciences, aerospace technology japan*, 8(ists27):1–5, 2009.

[Hua60] S.S. Huang. *Very restricted four-body problem.* NASA technical note. National Aeronautics and Space Administration, 1960.

[HXSW15] X. Y. Hou, X. Xin, D. J. Scheeres, and J. Wang. Stable motions around triangular libration points in the real earth–moon system. *Monthly Notices of the Royal Astronomical Society*, 454(4):4172–4181, 2015.

[IS90] D.H. Irvine and M.A. Savageau. Efficient solution of nonlinear ordinary differential equations expressed in S-system canonical form. *SIAM J. Numer. Anal.*, 27(3):704–735, 1990.

[Jäg03] T.H. Jäger. Quasiperiodically forced interval maps with negative Schwarzian derivative. *Nonlinearity*, 16(4):1239–1255, 2003.

[Jäg07] T.H. Jäger. On the structure of strange non-chaotic attractors in pinched skew products. *Ergodic Theory Dynam. Systems*, 27(2):493–510, 2007.

[JCFJ15] M. Jorba-Cuscó, A. Farrés, and À. Jorba. A study on the effect of solar radiation pressure on the stability region near the earth-moon triangular points. In *Proceedings of the 66th International Astronautical Congress*, Jerusalem, Israel, 12–16 October 2015.

[JCFJ16a] M. Jorba-Cuscó, A. Farrés, and À. Jorba. Periodic and quasi-periodic motion for a silar sail in the earth-moon system. In *Proceedings of the 67th International Astronautical Congress*, Guadalajara, México, 26–30 September 2016.

[JCFJ16b] M. Jorba-Cuscó, A. Farrés, and À. Jorba. Periodic and quasi-periodic motion for a silar sail in the earth-moon system. In *Proceedings of the 67th International Astronautical Congress*, Guadalajara, México, 26–30 September 2016.

[JCFJ18] M. Jorba-Cuscó, A. Farrés, and À. Jorba. Solar sail resonant periodic orbits in the augmented earth-moon quasi-bicircular problem. In *Proceedings of the 69th International Astronautical Congress*, Bremen, Germany, 1–5 October 2018.

[JLZ99] À. Jorba, R. de la Llave, and M. Zou. Lindstedt series for lower dimensional tori. In Simó [Sim99], pages 151–167.

[JM99a] À. Jorba and J. Masdemont. Dynamics in the centre manifold of the collinear points of the Restricted Three Body Problem. *Phys. D*, 132:189–213, 1999.

[JM99b] À. Jorba and J. Masdemont. Nonlinear dynamics in an extended neighbourhood of the translunar equilibrium point. In Simó [Sim99], pages 430–434.

[JMAT18] A. Jorba, J.M. Muñoz-Almaraz, and J. C. Tatjer. On non-smooth pitchfork bifurcations in invertible quasi-periodically forced 1-d maps. *Journal of Difference Equations and Applications*, 24(4):588–608, 2018.

[JNOT07] À. Jorba, C. Núñez, R. Obaya, and J.C. Tatjer. Old and new results on strange nonchaotic attractors. *Internat. J. Bifur. Chaos Appl. Sci. Engrg.*, 2007.

[JO04] À. Jorba and M. Ollé. Invariant curves near Hamiltonian-Hopf bifurcations of four-dimensional symplectic maps. *Nonlinearity*, 17:691–710, 2004.

[JO09] À. Jorba and E. Olmedo. On the computation of reducible invariant tori on a parallel computer. *SIAM J. Appl. Dyn. Syst.*, 8(4):1382–1404, 2009.

[Jor99] À. Jorba. A methodology for the numerical computation of normal forms, centre manifolds and first integrals of Hamiltonian systems. *Exp. Math.*, 8(2):155–195, 1999.

[Jor00] À. Jorba. A numerical study on the existence of stable motions near the triangular points of the real Earth-Moon system. *Astron. Astrophys.*, 364(1):327–338, 2000.

[Jor01] À. Jorba. Numerical computation of the normal behaviour of invariant curves of n-dimensional maps. *Nonlinearity*, 14(5):943–976, 2001.

[JPN10] À. Jorba and E.-M. Pérez-Nueno. Propagation of the uncertainty region for a particle around the Earth. Final report, Deimos Space SL, 2010.

[JS92] À. Jorba and C. Simó. On the reducibility of linear differential equations with quasiperiodic coefficients. *J. Differential Equations*, 98:111–124, 1992.

[JS94] À. Jorba and C. Simó. Effective stability for periodically perturbed Hamiltonian systems. In J. Seimenis, editor, *Hamiltonian Mechanics: Integrability and Chaotic Behaviour*, volume 331 of *NATO Adv. Sci. Inst. Ser. B Phys.*, pages 245–252. Held in Toruń, Polland, 28 June–2 July 1993. Plenum, New York, 1994.

[JT08] À. Jorba and J.C. Tatjer. A mechanism for the fractalization of invariant curves in quasi-periodically forced 1-D maps. *Discrete Contin. Dyn. Syst. Ser. B*, 10(2-3):537–567, 2008.

[JV97a] À. Jorba and J. Villanueva. On the normal behaviour of partially elliptic lower dimensional tori of Hamiltonian systems. *Nonlinearity*, 10:783–822, 1997.

[JV97b] À. Jorba and J. Villanueva. On the persistence of lower dimensional invariant tori under quasi-periodic perturbations. *J. Nonlinear Sci.*, 7:427–473, 1997.

[JV98] À. Jorba and J. Villanueva. Numerical computation of normal forms around some periodic orbits of the Restricted Three Body Problem. *Phys. D*, 114(3-4):197–229, 1998.

[JZ05a] À. Jorba and M. Zou. A software package for the numerical integration of odes by means of high-order taylor methods. *Experimental Mathematics*, 14(1):99–117, 2005.

[JZ05b] À. Jorba and M. Zou. A software package for the numerical integration of ODEs by means of high-order Taylor methods. *Exp. Math.*, 14(1):99–117, 2005.

[Kat75] J. I. Katz. Numerical orbits near the triangular lunar libration points. *Icarus*, 25(2):356–359, 1975.

[KCUM14] A. Kamor, C. Chandre, T. Uzer, and F. Mauger. Recollision scenario without tunneling: Role of the ionic core potential. *Physical review letters*, 112:133003, 04 2014.

[Kel96] G. Keller. A note on strange nonchaotic attractors. *Fund. Math.*, 151(2):139–148, 1996.

[KH95] A. Katok and B. Hasselblatt. *Introduction to the modern theory of dynamical systems*, volume 54 of *Encyclopedia of Mathematics and its Applications*. Cambridge University Press, Cambridge, 1995.

[Khi97] A. Ya. Khinchin. *Continued fractions*. Dover Publications, Inc., Mineola, NY, russian edition, 1997. With a preface by B. V. Gnedenko, Reprint of the 1964 translation.

[KMCU14] A. Kamor, F. Mauger, C. Chandre, and T. Uzer. How key periodic orbits drive recollisions in a circularly polarized laser field. *Physical Review Letters*, 25:253002, 07 2014.

[Knu98] D.E. Knuth. *The art of computer programming. Vol. 2*. Addison-Wesley, Reading, MA, 1998.

[Kol54] A.N. Kolmogorov. On the persistence of conditionally periodic motions under a small change of the Hamilton function. *Dokl. Acad. Nauk. SSSR*, 98(4):527–530, 1954.

[KOM02] H. Kimura, H. Okamoto, and T. Mukai. Radiation pressure and the poynting–robertson effect for fluffy dust particles. *Icarus*, 157(2):349 – 361, 2002.

[Kor61] K. Kordylewski. Photographic observations of the libration point l_5 of the earth-moon system. *Acta Astronautica*, 11(165):165–169, 1961.

[KSK92] J. L. Krause, K. J. Schafer, and K. C. Kulander. High-order harmonic generation from atoms and ions in the high intensity regime. *Phys. Rev. Lett.*, 68:3535–3538, Jun 1992.

[Lan95] S. Lang. *Introduction to Diophantine Approximations*. Springer books on elementary mathematics. Springer, 1995.

[LC15] C. Lhotka and A. Celletti. The effect of poynting-robertson drag on the triangular lagrangian points. *Icarus*, 250:249 – 261, 2015.

[LHC18] Y. Liu, J. Heiligers, and M. Ceriotti. Loosely-displaced geostationary orbits with hybrid sail propulsion. *Aerospace Science and Technology*, 79:105 – 117, 2018.

[LHP+13] A. S. Landsman, C. Hofmann, A. N. Pfeiffer, C. Cirelli, and U. Keller. Unified approach to probing coulomb effects in tunnel ionization for any ellipticity of laser light. *Phys. Rev. Lett.*, 111:263001, Dec 2013.

[LJ] R. Llave and À. Jorba. Regularity properties of cener manifolds and applications. Preprint.

[LKK+15] J. F. Lindner, V. Kohar, B. Kia, M. Hippke, J. G. Learned, and W. L. Ditto. Strange nonchaotic stars. *Phys. Rev. Lett.*, 114:054101, Feb 2015.

[LN02] R. de la Llave and P. Nikola. Regularity of conjugacies between critical circle maps: an experimental study. *Experiment. Math.*, 11(2):219–241, 2002.

[Mac11] M. Macdonald. Solar sailing: applications and technology advancement. In Jason Hall, editor, *Advances in Spacecraft Technologies*, page Chapter 2. InTech, February 2011. This is an open-source book.

[Mar90] C. Marchal. *The three-body problem*. Elsevier, 1990.

[McI93] C. R. McInnes. Solar sail trajectories at the lunar l2 lagrange point. *Journal of Spacecraft and Rockets*, 30(6):782–784, 1993.

[McI99] C.R. McInnes. *Solar Sailing: Technology, Dynamics and Mission Applications*. Springer-Praxis, 1999.

[MCU10] F. Mauger, C. Chandre, and T. Uzer. Recollisions and correlated double ionization with circularly polarized light. *Phys. Rev. Lett.*, 105:083002, Aug 2010.

[MCZ+08] M. Meckel, D. Comtois, D. Zeidler, A. Staudte, D. Pavicic, H. C Bandulet, H. Pépin, J-C. Kieffer, R. Dörner, D. M Villeneuve, and P. Corkum. Laser-induced electron tunneling and diffraction. *Science (New York, N.Y.)*, 320:1478–82, 07 2008.

[MH92] K.R. Meyer and G.R. Hall. *Introduction to Hamiltonian Dynamical Systems and the N-Body Problem*. Springer, New York, 1992.

[MKCU12] F. Mauger, A. Kamor, C. Chandre, and T Uzer. Delayed double ionization as a signature of hamiltonian chaos. *Phys. Rev. E*, 85:066205, 06 2012.

[MKG93] J. J. Macklin, J. D. Kmetec, and C. L. Gordon. High-order harmonic generation using intense femtosecond pulses. *Phys. Rev. Lett.*, 70:766–769, Feb 1993.

[MMSM94] C.R. McInnes, A.J.C. McDonald, J.F.L. Simmons, and E.W. MacDonald. Solar sail parking in restricted three-body system. *Journal of Guidance, Control and Dynamics*, 17(2):399–406, 1994.

[Mon01] J.M. Mondelo. *Contribution to the study of Fourier methods for quasi-periodic functions and the vicinity of the collinear libration points*. PhD thesis, Univ. Barcelona, 2001.

[Moo66] R.E. Moore. *Interval Analysis*. Prentice-Hall, Englewood Cliffs, N.J., 1966.

[Mos62] J. Moser. On invariant curves of area-preserving mappings of an annulus. *Nachr. Akad. Wiss. Göttingen Math.-Phys. Kl. II*, 2:1–20, 1962.

[MS86] K. R. Meyer and D. S. Schmidt. The stability of the Lagrange triangular point and a theorem of Arnold. *J. Differential Equations*, 62(2):222–236, 1986.

[Nau12] U. Naumann. *The art of differentiating computer programs*, volume 24 of *Software, Environments, and Tools*. Society for Industrial and Applied Mathematics (SIAM), Philadelphia, PA, 2012. An introduction to algorithmic differentiation.

[NCUW15] M. J. Norman, C. Chandre, T. Uzer, and P. Wang. Nonlinear dynamics of ionization stabilization of atoms in intense laser fields. *Phys. Rev. A*, 91:023406, Feb 2015.

[Nir71] L. Nirenberg. A proof of the Malgrange preparation theorem. In *Proceedings of Liverpool Singularities—Symposium, I (1969/70)*, pages 97–105. Lecture Notes in Mathematics, Vol. 192. Springer, Berlin, 1971.

[NJC99] N.S. Nedialkov, K.R. Jackson, and G.F. Corliss. Validated solutions of initial value problems for ordinary differential equations. *Appl. Math. Comput.*, 105(1):21–68, 1999.

[NK96] T. Nishikawa and K. Kaneko. Fractalization of a torus as a strange nonchaotic attractor. *Phys. Rev. E*, 54:6114–6124, Dec 1996.

[OGH09] M. T. Ozimek, D. J. Grebow, and K. C. Howell. Design of solar sail trajectories with applications to lunar south pole coverage. *Journal of Guidance, Control, and Dynamics*, 32(6):1884–1897, 2009.

[PF95] A. Pikovsky and U. Feudel. Characterizing strange nonchaotic attractors. *Chaos (Woodbury, N.Y.)*, 5:253–260, 04 1995.

[PMR98] A. Prasad, V. Mehra, and R. Ramaskrishna. Strange nonchaotic attractors in the quasiperiodically forced logistic map. *Phys. Rev. E*, 57(2):1576–1584, 1998.

[PNR01a] A. Prasad, S. Negi, and R. Ramasawmy. Strange nonchaotic attractors. *International Journal of Bifurcation and Chaos*, 11(02):291–309, 2001.

[PNR01b] A. Prasad, S.S. Negi, and R. Ramaswamy. Strange nonchaotic attractors. *Internat. J. Bifur. Chaos Appl. Sci. Engrg.*, 11(2):291–309, 2001.

[Poh64] F. V. Pohle. A dynamical model for kordylewsky cloud satellites. *AIAA Journal*, 2(10):1818–1820, 1964.

[Pon07] M. Ponce. Local dynamics for fibred holomorphic transformations. *Nonlinearity*, 20(12):2939–2955, 2007.

[Pös89] J. Pöschel. On elliptic lower dimensional tori in Hamiltonian systems. *Math. Z.*, 202(4):559–608, 1989.

[Ral81] L.B. Rall. *Automatic Differentiation: Techniques and Applications*, volume 120 of *Lecture Notes in Computer Science*. Springer Verlag, Berlin, 1981.

[RG06] P. Robutel and F. Gabern. The resonant structure of Jupiter's Trojan asteroids – I. Long-term stability and diffusion. *Mon. Not. R. Astron. Soc.*, 372:1463–1482, 2006.

[RGJ05] P. Robutel, F. Gabern, and A. Jorba. The observed Trojans and the global dynamics around the Lagrangian points of the Sun-Jupiter system. *Celestial Mech.*, 92(1-3):53–69, 2005.

[Ric80] D.L. Richardson. A note on a Lagrangian formulation for motion about the collinear points. *Celestial Mech.*, 22(3):231–236, 1980.

[Roa75] J. R. Roach. Counterglow from the earth-moon libration points. *Planetary and Space Science*, 23(1):173 – 181, 1975.

[Rüs76] H. Rüssmann. On optimal estimates for the solutions of linear difference equations on the circle. *Celestial Mech.*, 14(1):33–37, 1976.

[RW69] R. G. Roosen and C. L. Wolf. Are the libration clouds real? *Nature*, 224(8):571, 1969.

[SBA+11] T. Sweetser, S. Broschart, V. Angelopoulos, G. Whiffen, D. Folta, M. Chung, S. J. Hatch, and M. Woodard. Artemis mission design. *Space Science Reviews*, 165:27–57, 09 2011.

[SBBH18] J. Slíz-Balogh, A. Barta, and G. Horváth. Celestial mechanics and polarization optics of the kordylewski dust cloud in the earth-moon lagrange point l_5 - i. three-dimensional celestial mechanical modelling of dust cloud formation. *Monthly Notices of the Royal Astronomical Society*, 480(4):5550–5559, 2018.

[SBBH19] J. Slíz-Balogh, A. Barta, and G. Horváth. Celestial mechanics and polarization optics of the kordylewski dust cloud in the earth-moon lagrange point l_5 -part ii. imaging polarimetric observation: new evidence for the existence of kordylewski dust cloud. *Monthly Notices of the Royal Astronomical Society*, 482(1):762–770, 2019.

[Sch98] D. J. Scheeres. The restricted hill four-body problem with applications to the earth–moon–sun system. *Celestial Mechanics and Dynamical Astronomy*, 70(2):75–98, Feb 1998.

[SGJM95] C. Simó, G. Gómez, À. Jorba, and J. Masdemont. The Bicircular model near the triangular libration points of the RTBP. In A.E. Roy and B.A. Steves, editors, *From Newton to Chaos*, pages 343–370, New York, 1995. Plenum Press.

[SH16] R. Sood and K. C. Howell. L4 , L5 solar sail transfers and trajectory design: Solar observations and potential earth trojan exploration. In *Proceedings of the 26th AAS/AIAA Space Flight Mechanics Meeting*, 2016.

[Sim89] C. Simó. Estabilitat de sistemes Hamiltonians. *Mem. Real Acad. Cienc. Artes Barcelona*, 48(7):303–348, 1989.

[Sim90] C. Simó. On the analytical and numerical approximation of invariant manifolds. In D. Benest and C. Froeschlé, editors, *Modern methods in celestial mechanics*, pages 285–330. Ed. Frontières, 1990.

[Sim96] C. Simó. Effective computations in Hamiltonian dynamics. In *Mécanique céleste*, volume 1996 of *SMF Journ. Annu.*, page 23. Soc. Math. France, Paris, 1996.

[Sim98] C. Simó. Effective computations in celestial mechanics and astrodynamics. In V.V. Rumyantsev and A.V. Karapetyan, editors, *Modern Methods of Analytical Mechanics and their Applications*, volume 387 of *CISM Courses and Lectures*. Springer Verlag, 1998.

[Sim99] C. Simó, editor. *Hamiltonian Systems with Three or More Degrees of Freedom*. NATO Adv. Sci. Inst. Ser. C Math. Phys. Sci. Held in S'Agaró, Spain, 19–30 June 1995. Kluwer Acad. Publ., Dordrecht, Holland, 1999.

[Sim01] C. Simó. Global dynamics and fast indicators. In H.W. Broer, B. Krauskopf, and G. Vegter, editors, *Global analysis of dynamical systems*, pages 373–389, Bristol, 2001. IOP Publishing.

[SM09a] J. Simo and C. R. McInnes. Solar sail orbits at the earth-moon libration points. *Communications in Nonlinear Science and Numerical Simulation*, 14(12):4191 – 4196, 2009.

[SM09b] J. Simo and C. R. McInnes. Solar sail orbits at the earth–moon libration points. *Communications in Nonlinear Science and Numerical Simulation*, 14(12):4191 – 4196, 2009.

[SM10a] J. Simo and C. R. McInnes. Designing displaced lunar orbits using low-thrust propulsion. *Journal of Guidance, Control, and Dynamics*, 33(1):259–265, 2010.

[SM10b] J. Simo and C. R. McInnes. Displaced solar sail orbits: Dynamics and applications. *Advances in the Astronautical Sciences*, 136(2):14–17, 2010.

[Sri99] R. Srikanth. Physical interpretation of the poynting-robertson effect. *Icarus*, 140(1):231 – 234, 1999.

[SS15] T. V. Sal'nikova and S. Y. Stepanov. Mathematical model of formation of kordylewski cosmic dust clouds. *Duklady Physics*, 60(7):323–326, 2015.

[SSST13] C. Simó, P. Sousa-Silva, and M. Terra. Practical stability domains near $L_{4,5}$ in the restricted three-body problem: Some preliminary facts. In Santiago Ibáñez, Jesús S. Pérez del Río, Antonio Pumariño, and J. Ángel Rodríguez, editors, *Progress and Challenges in Dynamical Systems*, pages 367–382, Berlin, Heidelberg, 2013. Springer Berlin Heidelberg.

[Sta97] J. Stark. Invariant graphs for forced systems. *Phys. D*, 109(1-2):163–179, 1997.

[Ste56] J.F. Steffensen. On the restricted problem of three bodies. *Danske Vid. Selsk. Mat.-Fys. Medd.*, 30(18):17, 1956.

[Ste57] J.F. Steffensen. On the problem of three bodies in the plane. *Mat.-Fys. Medd. Danske Vid. Selsk.*, 31(3):18, 1957.

[Sun18] V. Sundararajan. Overview and technical architecture of india's chandrayaan-2 mission to the moon. In *Proceedings of the AIAA Aerospace Sciences Meeting*, Kissimmee, US, 8–12January 2018.

[SV87] M.A. Savageau and E.O. Voit. Recasting nonlinear differential equations as S-systems: a canonical nonlinear form. *Math. Biosci.*, 87(1):83–115, 1987.

[Sze67] V. Szebehely. *Theory of Orbits*. Academic Press, 1967.

[UMH+13] S. Uenohara, T. Mitsui, Y. Hitara, T. Morie, Y. Horio, and K. Aihara. Experimental distinction between chaotic and strange nonchaotic attractors on the basis of consistency. *Chaos*, 23(5), 2013.

[Vin09] D. Vinković. Radiation-pressure mixing of large dust grains in protoplanetary disks. *Nature*, 459(14):227–229, 2009.

[VKCG10] R. Vondrak, J. Keller, G. Chin, and J. Garvin. Lunar reconnaissance orbiter LRO: Observatrions for Lunar exploration and science. *Space Science Reviews*, 150(1):7–22, Jan 2010.

[Wen64] R. E. Wengert. A simple automatic derivative evaluation program. *Comm. ACM*, 7(8):463–464, 1964.

[WH11a] G. Wawrzyniak and K. C. Howell. Generating solar sail trajectories in the earth-moon system using augmented finite-difference methods. *International Journal of Aerospace Engineering*, page 13 pages, 2011. Article ID 476197.

[WH11b] G. Wawrzyniak and K. C. Howell. Investigating the design space for solar sail trajectories in the earth-moon system. *The Open Aerospace Engineering Journal*, 4(1):26–44, 2011.

[WH11c] G. Wawrzyniak and K. C. Howell. Numerical techniques for generating and refining solar sail trajectories. *Advances in Space Research*, 48(11):1848 – 1857, 2011. Solar Sailing: CONCEPTS, TECHNOLOGY, AND MISSIONS.

[Win89] M. Winiarski. Photographic observations of the cloud in the neighbourhood of libration point l_5 of the earth-moon system. *Earth, Moon and Planets*, 47(2):193–215, 1989.

[WN63] J. Wei and E. Norman. Lie Algebraic Solution of Linear Differential Equations. *Journal of Mathematical Physics*, 4:575–581, April 1963.

[YI01] G. L. Yudin and M. Y. Ivanov. Physics of correlated double ionization of atoms in intense laser fields: Quasistatic tunneling limit. *Phys. Rev. A*, 63:033404, Feb 2001.